Atomic layer deposition of tantalum, hafnium and gadolinium nitrides

By

Ziwen Fang

A thesis submitted for the degree of Doctor of Philosophy (Ph.D) in accordance with the requirements of the University of Liverpool

Submitted August 2011

Abstract

This research describes the development of ALD processes for the deposition of nitride materials including tantalum, hafnium and gadolinium nitrides. Ta and Hf nitrides are of significant interests for sub-100nm silicon based electronic devices, while Gd nitride may be exploitable in future spintronic devices. ALD has been established a key manufacturing tool in microelectronics, the development of ALD processes for these nitrides are essential for future manufacturing of electronic devices and can benefit future manufacturing of spintronic devices. In the current research, these nitrides were deposited using ALD and the films were characterised using MEIS, AES, XRD, TEM, SEM, AFM, and a four point probe.

Ta nitride films were grown at temperatures ranging from 200°C to 375°C using ALD with Pentakis(dimethylamino)tantalum, $Ta(NMe_2)_5$ as the metal source and either ammonia or monomethyl-hydrazine (MMH) as a nitrogen co-reactant. Self-limiting behaviour was observed for both ammonia and MMH processes, with growth rates of 0.6 and 0.4 Å/cycle respectively at 300°C. Films deposited using ammonia were found to have a mono-nitride stoichiometry with a cubic microstructure and resistivities as low as 70 mΩ.cm. In contrast, films deposited using MMH were found to be nitrogen rich Ta_3N_5 with an amorphous microstructure and high resistivities (>4 Ω.cm). A QCM was used to measure mass gain and loss during the cyclic ALD processes and the data was used in combination with MEIS to elucidate the $Ta(NMe_2)_5$ absorption mechanisms.

For Hf nitride, films were firstly deposited using thermal ALD with tetrakis(dimethylamino)hafnium, $Hf(NMe_2)_4$ and ammonia between 100 and 400°C. Self-limiting behaviour was observed, however, the films exhibit a low density and were prone to oxidation during post-deposition exposure to air. A comparison between thermal and PE ALD was then made at 300°C with tetrakis(ethylmethylamino)hafnium, $Hf(NEtMe)_4$ as the metal source and either molecular or plasma-cracked ammonia as a nitrogen source. PEALD allows shorter purge time, which significantly reduces the cycle length; PEALD also results in higher film density. The densities of the films deposited by PEALD and thermal ALD were found to be 11.6 and 9.7 g/cm^3 respectively. Mass spectroscopy indicates that the process characteristics in PEALD are attributed to the nature of the co-reactants, namely, radicals of hydrogen and nitrogen. Their high reactivity and short life time are responsible for the resulted high density and the short required purge time. All films deposited were found to be insulators and with an amorphous microstructure. The films deposited by PEALD remain amorphous and stable with no interactions between Hf and Si after vacuum annealing up to 800°C.

Gd nitride films were successfully deposited using a cyclic PEALD based process. The deposition was carried out with tris(methylcyclopentadienyl)gadolinium, $Gd(MeCp)_3$, and remote nitrogen plasma exposure, separated by argon pulses. Films were deposited at temperatures between 150 and 300°C and capped with Ta nitride to prevent post deposition oxidation. Gd nitride with a 1:1 Gd:N ratio, low oxygen incorporation (5%), good thickness uniformity (95%), an amorphous microstructure and smooth surface (Ra.=~0.7nm) have been deposited. Deposition with tris(silylamide)gadolinium, $Gd\{N(SiMe_3)_2\}_3$, and either ammonia or MMH was also investigated. Although the process using ammonia was unsuccessful due to the insufficient reactivity of ammonia, the results show that a reaction between $Gd\{N(SiMe_3)_2\}_3$ and MMh does take place. $Gd\{N(SiMe_3)_2\}_3$ was found to be a self-limiting precursor, however, the as deposited films were found to be $GdSi_xO_y$. The silicon incorporation was attributed to partial breakdown of silylamine groups, where the oxygen incorporation was attributed to the possible tetrahydrofuran (THF) contamination in the precursor.

Acknowledgements

I would like to thank the following.

Dr. R. J. Potter (University of Liverpool) for his supervision, support, ideas, discussions, and guidance.

Prof. P. R. Chalker (University of Liverpool) for his supervision and advice.

Dr. M. Werner (University of Liverpool) for his guidance of MEIS experiments and data interpretation.

Dr. T. Noakes and Dr. P. Bailey (CCLRC Daresbury Laboratory) for providing technical support during the MEIS experiments.

Prof. H. Jeon (Hanyang University, Korea) and Dr. G. Critchlow (Loughborough University) for providing AES results.

Dr. R. Murray (University of Liverpool) for providing TEM results and discussions in EDX spectra.

K. Dawson (University of Liverpool) for providing SEM measurements and discussions in EDX spectra.

Dr. P. Marshall (University of Liverpool) for his guidance and discussions in ellipsometry measurements.

Dr. H. Aspinall and Dr. P. Williams (University of Liverpool) for their discussions and profound knowledge in chemistry.

Dr. N. Pham, P. King, and S. Hindley, D. Atkinson (University of Liverpool) for results discussions.

Dr. Q. Fang and Dr. C. Hodson (Oxford Instruments Plasma Technology) for the reactor technical support.

The Engineering and Physical Sciences Research Council for their financial support.

And finally to my dear wife Yunwei and my family for their encouragements and support.

Publications

1. Ziwen Fang, Helen C. Aspinall, Rajesh Odedra and Richard J. Potter, 'Atomic layer deposition of TaN and Ta_3N_5 using pentakis(dimethylamino)tantalum and either ammonia or monomethylhydrazine', Journal of Crystal Growth, (2011) doi:10.1016/j.jcrysgro.2011.07.012

2. Ziwen Fang, Paul A. Williams, Hyeongtag Jeon, Richard J. Potter, 'Plasma enhanced atomic layer deposition of gadolinium nitride', publication pending, (2011)

Contents

Abbreviations

ALD	Atomic layer deposition
AFM	Atomic force microscope
Ra	Arithmetical mean roughness
AES	Auger electron spectroscopy
BIL	Bottom interface layer
CVD	Chemical vapour deposition
CMOS	Complementary metal oxide semiconductor
DRAM	Dynamic random access memory
EDX	Energy dispersive X-ray spectroscopy
ICP	Inductively coupled plasma
ITRS	International technology roadmap for semiconductors
MFC	Mass flow controller
MRAM	Magnetic random access memories
MEIS	Medium energy ion scattering
MOS	Metal oxide semiconductor
MOSFET	Metal oxide semiconductor field effect transistor
MBE	Molecular beam epitaxy
MMH	Monomethylhydrazine
PDMAT	Pentakis(dimethylamino)tantalum
PEMAT	Pentankis(ethylmethylamino)tantalum
PVD	Physical vapour deposition
PEALD	Plasma enhanced atomic layer deposition
PLD	Pulsed laser deposition
PZT	Piezoelectric transducers
QCM	Quartz crystal microbalance
RF	Radio frequency
RE	Rare earth
REN	Rare earth nitrides
RBS	Rutherford backscattering spectroscopy
SEM	Scanning electron microscope
TIL	Top interface layer
TEM	Transmission electron microscope
TFEL	Thin film electroluminescent displays
TMA	Trimethylaluminum

TBTDET	(Tertbutylimido)tris(diethylamido)tantalum
TDMAH	Tetrakis(diemethylamino)hafnium
TEMAH	Tetrakis(ethylmethylamino)hafnium
THF	Tetrahydrofuran
TGA	Thermogravimetric analysis
TEA	Toroidal electrostatic analyzer
UV	Ultraviolet
VLSI	Very large scale integration
XRD	X-ray diffraction

Chapter 1. Introduction

The research in this thesis describes atomic layer deposition (ALD) processes for the manufacture of tantalum, hafnium and gadolinium nitrides. Ta and Hf nitrides are transition metal nitrides, which are of significant interest for sub-100nm silicon devices for the microelectronic industry. Gd nitride is a member of the rare-earth nitrides family, these are a group of materials which are largely untapped, but have potential to be used for spintronic devices. Since the two material groups have different properties and applications, the motivations and objectives are presented separately in the following sections.

Transition metal nitrides, such as Ta and Hf nitrides are highly refractory and have high thermal stability, good chemical resistance, superior hardness, good adhesion property, and can have low electrical resistivity.[1] Both Ta and Hf nitrides have two main stoichiometric phases, mono nitrides and nitrogen rich nitrides, where the former are electrical conductors (resistivity < 200 μΩ.cm),[2,3] and the latter are highly resistive (resistivity > 6 Ω.cm).[4,5] Thin films of these nitrides have been identified as good candidates for diffusion barriers[6,7] and gate electrodes[8,9] in microelectronics. Due to the high resistivities of nitrogen rich nitrides, which significantly increase power consumption and heat generation of electronic devices, conductive mono nitrides are currently desirable.[10] Control over stoichiometry is therefore, essential during the deposition processes. The conventional ways to deposit these nitrides are physical based deposition techniques and chemical vapour deposition (CVD). Although these techniques can control the stoichiometry and deposit high quality films on plane substrates, they are not well suited to coating complex structures.[11]

With the continuous downscaling of electronic devices, increasingly high aspect ratio 3D structures are being employed.[12] To fully implement the applications of the Ta and Hf nitrides, conformal coatings on these structures are required, which has raised a significant challenge for the conventional deposition techniques.

ALD is a deposition technique relying on self-limiting surface reactions and has fascinating features including, precise thickness control, large area uniformity, batch process capability, and conformality over complex structures.[13,14] Nitride deposition using ALD can therefore overcome the challenges associated with the continuous downscaling of microelectronic devices. However, to date, ALD studies of Ta and Hf nitrides have been very limited and in addition, the control of stoichiometry has been a challenge for thermal ALD. The early part of this thesis deals with these issues and the following objectives are identified:

- To find the optimum growth conditions for self-limiting ALD deposition of Ta and Hf nitrides.
- To control nitride stoichiometry using different nitrogen containing co-reactants.
- To determine how growth conditions affect the film composition, crystal structure, thermal stability and electrical properties. Use analytical tools including MEIS, XRD, TEM, SEM, EDX, and a four point probe to investigate these properties.
- To gain an understanding of the reactions/mechanisms involved in the ALD process using in-situ analytical techniques such as quartz crystal microbalance (QCM) and mass spectrometry in addition to the ex-situ characterisations.

Rare-earth nitrides are a group of materials that possess a unique combination of magnetic and electronic properties. A number of rare-earth nitrides (GdN,[15-21] DyN,[22] SmN[22] and ErN[23]) are classified as ferromagnetic semiconductors. Among them, GdN has attracted most attention due to its high Curie temperature (~70K) and large magnetic moment ($7\mu_B/Gd^{3+}$).[15-19] The magnetism of GdN arises from the highly localized 4*f* electron shell of the Gd metal,[15-19] while the electronic property is determined by the itinerant s-d electrons.[24] Ferromagnetic semiconductors are very rare, and this unique combination has made GdN extremely attractive for spintronic devices.[15-19]

To data, only a handful of papers are available on the deposition of GdN, which is perhaps due to the challenges involved in the processes. Gadolinium has a high affinity to oxygen, which means that even trace levels of oxygen impurities during the deposition would lead to oxide formation.[25] In addition, GdN films can convert to oxide when exposed to air at ambient temperature within a few tens of seconds.[25] Unfortunately, Gd oxide is antiferromagnetic and is of no use in spintronics.[26,27] It is therefore anticipated that GdN may be exploitable in spintronics if it can be made with high purity. Despite these difficulties, GdN has been deposited using MBE,[25,28] PVD,[29,30] PLD,[18] and very recently using CVD.[31,32] Comparing to these techniques, ALD offers high conformability, large area uniformity and sub-nanometre thickness control.[13,14] ALD has been established as a key manufacturing tool in the microelectronic industry,[12] and a successful ALD process for GdN may benefit the future manufacturing of spintronic devices. However to date, no ALD studies on rare-earth nitrides has been reported, and the possibility of depositing such challenging materials using ALD remains unclear. The latter part of this thesis is dedicated to answering this question and the following objectives are identified:

- Use self-limiting ALD processes to deposit GdN films that are suitable for further explorations in spintronics.
- To determine how growth conditions affect the film composition, crystal structure, and surface roughness using EDX, MEIS, AES, XRD, and AFM.

The remainder of this thesis is organized as follows. Chapter 2 provides background to the research work and includes an overview of nitride materials and their major applications. ALD is also reviewed from first principles through to practical applications and in particular, nitride ALD processes are discussed. In chapter 3, the growth processes and analytical techniques used throughout this thesis are described. Chapter 4 presents the results and discussions of the thermal ALD processes of Ta nitride. Chapter 5 investigates the plasma enhanced ALD for the deposition of Hf nitride and a direct comparison has been made to the thermal ALD. In Chapter 6, a pioneering search for the suitable ALD processes of GdN is presented, which demonstrates the deposition of GdN using a PEALD based process for the first time. Finally, chapter 7 concludes the major outcomes of this research work, and also gives the suggestions of the possible future work.

Reference

1. R. A. Fischer, H. Parala, *Metal-organic Chemical Vapour Deposition of Refractory Transition Metal Nitrides*. In *Chemical Vapour Deposition: Precursors, Processes and Applications*, A. C. Jones, M. L. Hitchman, Eds. Royal Society of Chemistry: Cambridge, p 413 (2009).

2. R. Araujo, X. Zhang, H. Wang, *Journal of Electronic Materials* **37**, 1828-1831 (2008).

3. H. Y. Yu, H. F. Lim, J. H. Chen, M. F. Li, C. X. Zhu, C. H. Tung, A. Y. Du, W. D. Wang, D. Z. Chi, D. L. Kwong, *Ieee Electron Device Letters* **24**, 230-232 (2003).

4. K. Hieber, *Thin Solid Films* **24**, 157-164 (1974).

5. J. S. Becker, E. Kim, R. G. Gordon, *Chemistry Of Materials* **16**, 3497-3501 (2004).

6. W. L. Yang, W. F. Wu, D. G. Liu, C. C. Wu, K. L. Ou, *Solid-State Electronics* **45**, 149-158 (2001).

7. K. L. Ou, *Microelectronic Engineering* **83**, 312-318 (2006).

8. S. Consiglio, W. X. Zeng, N. Berliner, E. T. Eisenbraun, *Journal Of The Electrochemical Society* **155**, H196-H201 (2008).

9. I. De, D. Johri, A. Srivastava, C. M. Osburn, *Solid-State Electronics* **44**, 1077-1080 (2000).

10. C. Lee, Y. L. Kuo, *Jom* **59**, 44-49 (2007).

11. S. M. Rossnagel, H. Kim, I. Ieee, *From PVD to CVD to ALD for interconnects and related applications*. Ieee Computer Soc: Los Alamitos, p 3-5 (2001).

12. International Technology Roadmap for semiconductors (ITRS). http://www.itrs.net/ (accessed 2010).

13. M. Leskelä, M. Ritala, *Thin Solid Films* **409**, 138-146 (2002).

14. M. Ritala, J. Niinistö, *Atomic Layer Deposition*. In *Chemical Vapour Deposition: Precursors, Processes and Applications*, A. C. Jones, M. L. Hitchman, Eds. Royal Society of Chemistry: Cambridge, p 164 (2009).

15. C. Meyer, B. J. Ruck, J. Zhong, S. Granville, A. R. H. Preston, G. V. M. Williams, H. J. Trodahl, *Physical Review B* **78**, 174406 (2008).

16. D. X. Li, Y. Haga, H. Shida, T. Suzuki, Y. S. Kwon, G. Kido, *Journal of Physics: Condensed Matter* **9**, 10777 (1997).

17. D. X. Li, Y. Haga, H. Shida, T. Suzuki, *Physica B: Condensed Matter* **199-200**, 631-633 (1994).

18. B. M. Ludbrook, I. L. Farrell, M. Kuebel, B. J. Ruck, A. R. H. Preston, H. J. Trodahl, L. Ranno, R. J. Reeves, S. M. Durbin, *Journal of Applied Physics* **106**, 063910 (2009).

19. F. Natali, N. O. V. Plank, J. Galipaud, B. J. Ruck, H. J. Trodahl, F. Semond, S. Sorieul, L. Hirsch, *Journal of Crystal Growth* **312**, 3583-3587 (2010).

20. S. Granville, B. J. Ruck, F. Budde, A. Koo, D. J. Pringle, F. Kuchler, A. R. H. Preston, D. H. Housden, N. Lund, A. Bittar, G. V. M. Williams, H. J. Trodahl, *Physical Review B* **73**, 235335 (2006).

21. H. J. Trodahl, A. R. H. Preston, J. Zhong, B. J. Ruck, N. M. Strickland, C. Mitra, W. R. L. Lambrecht, *Physical Review B* **76**, 085211 (2007).

22. A. R. H. Preston, S. Granville, D. H. Housden, B. Ludbrook, B. J. Ruck, H. J. Trodahl, A. Bittar, G. V. M. Williams, J. E. Downes, A. DeMasi, Y. Zhang, K. E. Smith, W. R. L. Lambrecht, *Physical Review B - Condensed Matter and Materials Physics* **76**, 245120 (2007).

23. T. A. Yamamoto, T. Nakagawa, K. Sako, T. Arakawa, H. Nitani, *Journal of Alloys and Compounds* **376**, 17-22 (2004).

24. C. M. Aerts, P. Strange, M. Horne, W. M. Temmerman, Z. Szotek, A. Svane, *Physical Review B* **69**, 045115 (2004).

25. J. W. Gerlach, J. Mennig, B. Rauschenbach, *Applied Physics Letters* **90**, 061919 (2007).

26. R. J. Gambino, T. R. McGuire, H. A. Alperin, S. J. Pickart, *Journal of Applied Physics* **41**, 933-934 (1970).

27. P. Wachter, E. Kaldis, *Solid State Communications* **34**, 241-244 (1980).

28. M. A. Scarpulla, C. S. Gallinat, S. Mack, J. S. Speck, A. C. Gossard, *Journal of Crystal Growth* **311**, 1239-1244 (2009).

29. F. Leuenberger, A. Parge, W. Felsch, K. Fauth, M. Hessler, *Physical Review B* **72**, 014427 (2005).

30. E. Shalaan, H. Schmitt, *Optics Communications* **260**, 588-594 (2006).

31. A. P. Milanov, T. B. Thiede, A. Devi, R. A. Fischer, *Journal of the American Chemical Society* **131**, 17062-17063 (2009).

32. J. R. Brewer, Z. Gernhart, H. Y. Liu, C. L. Cheung, *Chemical Vapor Deposition* **16**, 216-219 (2010).

Chapter 2. Literature review

This chapter focuses on two major topics that are related to the research project, nitrides and Atomic Layer Deposition (ALD). Nitride materials including transition metal nitrides and rare-earth metal nitrides are reviewed and their thin film applications are introduced. ALD is reviewed from first principles to practical applications and in particular, nitride ALD processes are discussed. The aim of this chapter is to provide an overview and specific reviews dedicated to TaN_x, HfN_x and GdN are provided in chapter 4, chapter 5, and chapter 6 respectively.

2.1 Introduction to nitrides

This thesis describes the ALD coatings of tantalum, hafnium and gadolinium nitrides. Tantalum and hafnium nitrides are transition metal nitrides, while gadolinium nitride is a member of the rare-earth nitride family. Before introducing the deposition techniques, it is worthwhile to introduce these materials and their applications.

2.1.1 Transition metal nitrides and applications

Transition metal nitrides (M = Ti, Zr, Hf, V, Nb, and Ta) can be considered as interstitial alloys, where nitrogen atoms nest in the interstices of the metal lattice.[1] To hold metal and nitrogen atoms together, three types of bonding including ionic, covalent, and metallic bonds are involved.[1] Ionic and covalent bonds are responsible for metal-to-nitrogen connections, while metallic bonds are responsible for metal-to-metal connections. Due to the high overall bond energy (between ~13 and ~16 eV)[1] and a mixture of three types of bonding, transition metal nitrides can

exhibit both ceramic and metallic characteristics. They are highly refractory and have high thermal stability, good chemical resistance, superior hardness, good adhesion property, and can have low electrical resistivity.[2]

As a consequence of these properties, thin films of transition metal nitrides are employed for many applications such as hard coatings,[3-5] corrosion and abrasion resistant layers,[6,7] and decorative coatings.[8,9] They are also used for photonic applications such as photocatalysis,[10] and photoelectrolysis.[11] Furthermore, Ti,[12,13] Hf,[14] Zr[15] and Nb[16] nitrides have been reported as high transition temperature superconductors. In microelectronics, transition metal nitrides are used as diffusion barriers,[17-27] gate electrodes[28-32] and work function tuning layers[33-38] (Figure 2.1). Metal oxynitrides have also been investigated as the gate dielectric material in Metal Oxide Semiconductor (MOS) devices.[39] Because the aim of this thesis is to develop ALD processes for Ta and Hf nitrides, which are mainly used in microelectronics as diffusion barriers[20,22,24,27,40-44] and gate electrodes,[30,45,46] these applications are discussed in more detail below.

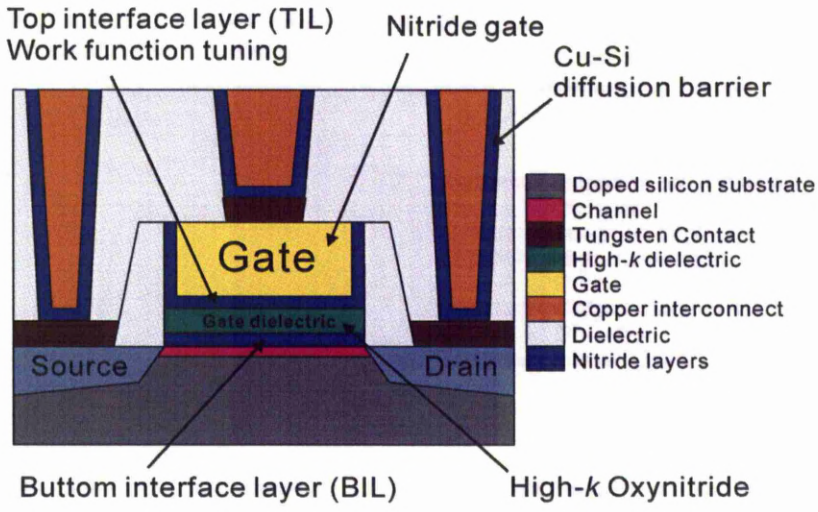

Figure 2.1 A schematic of Metal Oxide Semiconductor Field Effect Transistor (MOSFET) indicating places that nitrides can be used (filled in blue).

Diffusion barriers – The continual down scaling of MOS based silicon electronics is a demanding field of active research for thin film materials. The international technology roadmap for semiconductors (ITRS) indicates that new materials are required to enable 45nm node and smaller MOS devices.[47] Copper has attracted a significant interest and has already been employed as an interconnect material because of the low resistivity (1.67 μΩ.cm) and high electron-migration resistance.[48,49] However, copper-silicon diffusion occurs above 200°C and forms highly resistive copper silicide (Cu_3Si).[48-50] This is detrimental to devices because resistive interconnects would lead to high power consumption and heat generation, the device would even fail if current cannot pass through the interconnects.

To stop the diffusion, an effective diffusion barrier layer between copper and silicon is essential. The barrier material must have high thermal stability, good adhesion, chemical inertness to copper and silicon, and preferably low resistivity.[24] Previous reports show that the diffusion takes place primarily along grain boundaries and therefore, amorphous or nanocrystalline microstructures are desirable.[24,51] Transition metals[25,52,53] and metal nitrides[2,27] have been investigated for this application. TiN has been the most thoroughly studied and the Cu/TiN/Si structure is reported to be stable up to 600°C.[42,54-57] TaN is considered to be a better candidate as the Cu/TaN/Si structure was reported to be stable up to 700°C.[20,22,24,27,40-42] Thin films of HfN also successfully inhibited the Cu-Si formation up to 700°C.[43,44] The barrier characteristic of ZrN[58] and NbN[18] have both remained up to 550°C.

In addition to the Cu-Si barrier layer, nitrides can also be used as a diffusion barrier in the gate stack (Figure 2.1). Previous studies have shown that internal oxidation of silicon occurs above 500°C between silicon and high-k dielectrics such as HfO_2.[59,60]

A thin layer SiO_2 is formed near the channel, which not only affects the overall equivalent oxide thickness,[59] but also decreases the channel mobility.[60] Nitride has been demonstrated to suppress this oxidation and therefore can be used as a bottom interface layer (BIL) (Figure 2.1).[59,60] In addition, nitrides can also be used between the high-k dielectric and the gate as a top interface layer (TIL), which can prevent internal oxidation of the gate electrode.[61,62]

Gate electrode and work function tuning - Silicon dioxide has been used as the gate dielectric in Metal Oxide Semiconductor Field Effect Transistor (MOSFET).[63] However, as the dimensions of the device have been aggressively scaled down, the leakage current through the gate dielectric has significantly increased and this reduces device performance.[47] To maintain the low leakage current with a similar capacitance, high permittivity (k) materials were used instead of silicon dioxide. Silicon oxy-nitride was used in the 100nm node devices, and a hafnium based oxide has been employed in the Intel 45nm node devices.[47]

To accommodate the change into hafnium based oxide, other modifications are required to the gate stack. Polycrystalline silicon has been used as the gate electrode material; however, it is not compatible with high-k dielectrics. Defects at the poly-Si/HfO_2 interface give rise to Si-Hf bonds, which lead to Fermi-level pinning[64,65] and result in high threshold voltage.[65] In addition, the downscaling of MOS devices also leads to a significant increase of depletion capacitance in the polycrystalline silicon at the interface with the gate dielectric.[65] The increase has been mainly attributed to the fringing gate field,[66-68] which is schematically illustrated in Figure 2.2. With a shorter gate length, the depletion due to fringing fields at gate side walls contributes more to the overall depletion in poly-silicon. This

decreases the overall capacitance and impairs device performance. To allow further downscaling of the devices, alternative gate materials are needed.[69]

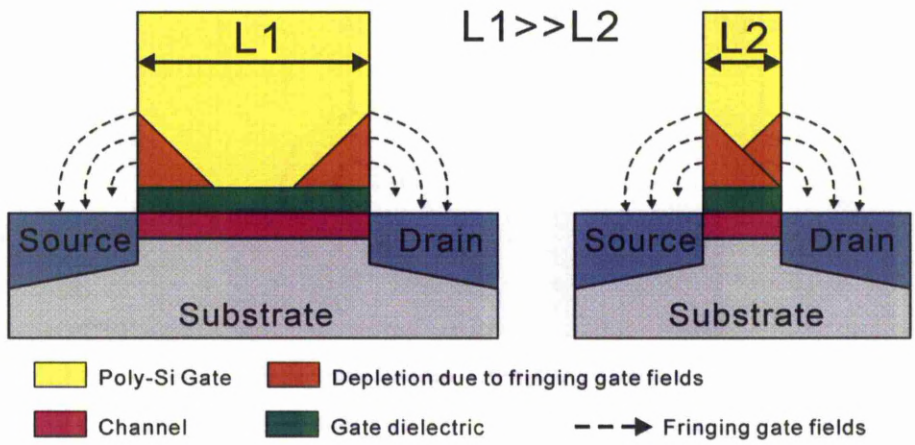

Figure 2.2 A schematic illustration of the depletion region in poly-silicon gate due to fringing gate fields.

It was anticipated that metal gates are needed alongside the introduction of high-*k* dielectrics to overcome these challenges, and this has been implemented in the Intel 45nm node devices.[47] The candidates must have low resistivity, high thermal stability, and chemical inertness to the high-*k* layer. The metallic nature would eliminate the depletion layer, the high thermal stability would reduce the interactions to the high-*k* layer and hence can avoid Fermi-level pinning.[35] In addition, the candidates must also have an appropriate work function to match the operation of the silicon channel.[63] The optimal work function for the operation of n-MOS and p-MOS is near to the silicon conduction band (~4eV) and valence band (~5eV) respectively.[70,71]

Transition metal nitrides offer all these properties and more importantly, their work functions are tuneable within the range between 4 and 5eV. The effective work functions of TaN_x and HfN_x increase from ~4 to ~4.5 eV by adding nitrogen to the

metal.[35] Most transition metal mono nitrides have a mid-gap work function,[2] but can be altered by appropriate doping. The work functions of HfN and TaN have been reduced to ~4eV by doping lanthanide elements (La, Tb, Er, or Yb),[35,36,72,73] this is suitable for the use in n-MOS. The work functions of TaN and TiN have also been tuned up to ~5eV by doping aluminium,[35,74] making them good candidates for the p-MOS gate electrode. Previous papers have successfully used TiN,[75-77] TaN[78,79] and HfN[31,32] gate electrodes in HfO_2 based MOS devices and therefore, transition metal nitrides are promising candidates for gate electrodes and can fulfil the challenges raised by the introduction of high-*k* dielectrics.

2.1.2 Rare-earth (Lanthanide) nitrides and applications

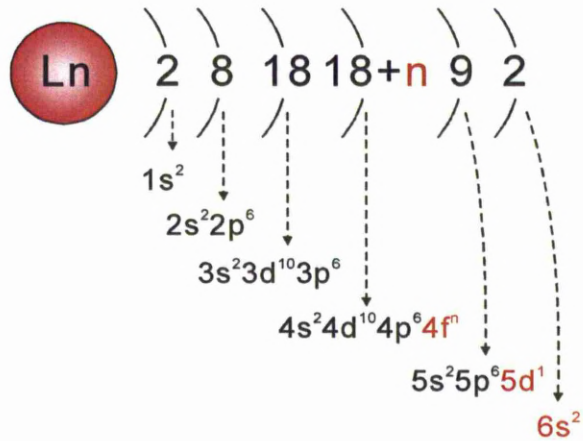

n	0	1	2	3	4	5	6	7	8	9	10	11	12	13	14
	La	Ce	Pr	Nd	Pm	Sm	Eu	Gd	Tb	Dy	Ho	Er	Tm	Yb	Lu

Figure 2.3 Electron configuration of Lanthanide, n is the number of electrons in the 4f shell. The valence electrons are displayed in red.

Rare Earth (RE), also known as lanthanide, is a group of elements with their 4*f* electron shell progressively filled from 0 to 14 (Figure 2.3).[80] The majority of these metals (except Yb, Eu and Ce) exhibit magnetic properties.[81] Before introducing RE nitrides, it is worth explaining the origin of the magnetism in RE metals.

Magnetism describes a phenomenon that materials attract or repulse other materials. Magnetic forces arise from the movement of electrically charged particles. An electric current moving through a wire is a typical example, and the resulting magnetic force can be determined by the 'right hand rule'. In atomic scale, an electron is considered to rotate around the atomic nucleus, which can be considered equivalent to a current flow, resulting in a magnetic moment along the axis of rotation.

There is more than one electron in an atom and the magnetic moments of an electron pair cancel out. For an atom to exhibit any magnetic moment there must be at least one unpaired electron. Electrons in a completed filled shell or subshell pair together and a magnetic moment is impossible. Only atoms that have partially filled electron shells would give rise to unpaired electrons and have a magnetic moment. In most elements across the periodic table, although the outer shells are partially filled, electrons are not stable and tend to participate in bonding, which can eliminate any magnetism. The *d* and *f* electron shells are protected by outer shells, meaning that the unpaired electrons in these levels are stable and can give rise to a magnetic moment.

In RE metals (Figure 2.3), the 4*f* electron shell is progressively filled but highly localized, meaning that there is little chance for these electrons to directly participate in bonding.[81] The unpaired electrons in this level are the origin of the magnetism of RE elements.[81-84] When a RE element forms compounds, three itinerant electrons in the 5d and 6s levels are responsible for bonding and depending on the bonding structure, the electronic property of the compound may vary.[81] In RE metals, the metallic bonds lead to conductive metal behaviour,[85] in RE compounds, the electronic properties are affected by the interactions between the metal to the adjacent element.[81]

RE nitrides (REN) can inherit the magnetism of RE metals but alter the electronic property. A number of REN are classified as ferromagnetic semiconductors.[86] GdN has been most thoroughly studied and has been confirmed to process both ferromagnetic[87-91] and semiconducting[90-93] properties. DyN,[94] SmN,[87,94] ErN[95] have also been found to be ferromagnetic semiconductors. PmN[96] and EuN[97,98] have been found to show half-metallicity in the ferromagnetic state. HoN and TbN are also ferromagnetic but unfortunately, no electronic property has been investigated.[95] Among these REN, GdN has attracted most interest because of its high magnetic moment ($7\mu_B/Gd^{3+}$) and relatively high Curie temperature (~70K).[87-91] Materials that combine ferromagnetism with either semiconducting or half-metallic properties are extremely rare, and can be exploited in spintronic devices.[87-91,99,100]

Spintronics - In microelectronics, the charge of the electron has been used as a method of determining the 'on' and 'off' binary states in MOS devices. To convey this information, a sufficient number of charges must be supplied and detected. With a continuous downscaling of MOS devices following Moore's law,[47] the detection of these charges will become more challenging. Spintronic devices exploit the spin of the carriers in addition their charge to register 'on' and 'off' states, researchers in spintronics have predicted that it is possible to detect one spin polarized electron.[101] This makes spintronics strong candidates for the next generation logic devices, however, a major challenge in integrating spin-based devices with charge-based ones is to find suitable materials that are both ferromagnetic and semiconducting.[102]

REN have these properties and can fulfil this challenge in spintronics.[87-91,99,100,103,104] Unfortunately, to date, no study has been available for REN based spintronic devices. The lack of work is perhaps due to the significant challenges associated with the

deposition of these materials. RE elements such as gadolinium have a high affinity to oxygen, which means that even trace levels of oxygen impurities during the deposition would lead to oxide formation.[99] In addition, GdN can convert to oxide when exposed to air at ambient temperature within a few tens of seconds.[99] Unfortunately, oxygen contamination will largely inhibit the magnetism of GdN and therefore,[105,106] it is essential to deposit high quality nitride films with low oxygen incorporation. Although no REN has been used in spintronic devices, other RE based materials have been previously employed. EuS,[107] which is also a ferromagnetic semiconductor with a Curie temperature of 16.6K and a magnetic moment of 3.5 μ_B/EuS, has been successfully functioned as a spin filter.[108] GdN is more advantageous to EuS in terms of the curie temperature (~70K) and the magnetic moment (7 μ_B/GdN)[87-91] and therefore, GdN may be exploitable in spintronics if it can be prepared with high purity.

2.2 Deposition techniques

The adoption of any material for applications in microelectronics is heavily dependent on a well controlled thin film deposition technique. The deposition method employed must produce high quality, uniform, pinhole free films with the desired stoichiometry and thickness. In many modern devices, the films must be conformal over high aspect ratio features, such as the trench structures in Dynamic Random Access Memory (DRAM) cells[45] and in copper interconnects.[47] The thermal budget of the deposition process may also be an important consideration when temperature sensitive parts of the device have been formed prior to deposition.[109]

All deposition techniques rely on two steps, source transportation and deposition. The source may be a solid, liquid or vapour, however; vapour is generally preferred for transportation, because it is easy to transfer to the surface and easy to control. The vapour of a solid or liquid can be obtained by heat or other means of energy input such as electron beam, photon, or ion bombardment. Film deposition is then achieved by interacting this vapour with substrates, and depending on the type of interactions, they are categorized into physical based deposition and chemical based deposition. In physical based deposition techniques, films are deposited by absorption of vapour phase sources, the substance that is to be deposited as a film is transported from the source. In chemical based deposition techniques, films are deposited by chemical reactions of vapour phase sources, the precursors of the reactions are transported. In reality however, it is difficult to distinguish one from the other. In nitride deposition using techniques such as molecular beam epitaxy (MBE),[99] pulsed laser deposition (PLD),[90] and evaporative deposition,[104] the metal source is transported and nitride films are formed by reacting the metal source in a nitrogen rich atmosphere. Although chemical reactions are involved in the deposition, these techniques are classified as physical based deposition.

2.2.1 Physical based deposition

Physical based deposition techniques are widely used to prepare thin films and to study intrinsic material properties. Techniques such as MBE, PLD, evaporative deposition, and sputtering often operate under high vacuum, with pressures ranging from 10e-3 mTorr to 10e-6 mTorr.[110] This is to provide a long mean free path of molecules, so that they can travel in space without being scattered.[111] A high background pressure would also contribute to film impurities from ambient

elements[112,113] and from the working gas such as argon.[114] In addition, high vacuum allows the use of in-situ analytical tools such as electron diffraction[115] and Auger electron microscopy,[116] which provide vital information during deposition. While these techniques can deposit high quality films on planar substrates, they are not well suited for conformal coatings onto high aspect ratio trench structures.[117] This is because when the mean free path is high, vapour tends to travel in a straight line and results in low deposition on trench walls.[117] Poor conformality is the major drawback of physical based deposition techniques and makes them unsuitable for deposition onto complex structures. These structures often occur in electronic device and are also being progressively scaled down,[45,47] raising even more challenges.

2.2.2 Chemical based deposition

Chemical based deposition techniques such as chemical vapour deposition (CVD) rely on chemical reactions and they can operates over a wide pressure range from high vacuum[118] to atmosphere pressure.[119] The high deposition pressure reduces the mean free path of precursor molecules so that they are scattered at all directions and can reach most surfaces. The deposition is then relying on chemical reactions between precursors. The reactions may occur at both gas phase and on substrate surface, contributing to a significant enhancement in conformality compared with physical based deposition.[117,120] To allow an efficient deposition with minimum contamination, the chemical reactions need to be carefully designed. This is done by selecting appropriate chemical species that allow a reaction from gaseous precursors to the desired solid with gaseous by-products. In the deposition of GaN for example (Eq.2.1),[121] a reaction between trimethylgallium and ammonia is initiated, resulting

in solid GaN and gaseous methane, which minimises carbon and hydrogen contaminations in the film.

$$Ga(CH_3)_3(g) + NH_3(g) \rightarrow GaN(s) + 3CH_4(g) \quad \text{(Eq. 2.1)}$$

Most CVD reactions are thermodynamically endothermic and therefore,[122] activation energy is required and often supplied in the form of heat (thermal CVD),[122] light (photo-assisted CVD[123]) or plasma (plasma-enhanced CVD[124]). Heat is the most conventional energy, however, thermal CVD can be disadvantageous when temperature sensitive parts have already been formed in the substrates prior to the process. In such cases, low temperature deposition is required. To effectively reduce deposition temperatures, photo-assisted and plasma-enhanced CVD have been developed to supply the required energy, and proven to yield high quality films.[8] A wide range of materials such as metals, semiconductors, oxides, nitrides and carbides have been successfully deposited,[122] many CVD processes are employed in manufacture of modern electronic and optoelectronic devices.[47]

2.3. Atomic Layer Deposition

ALD, also known as atomic layer epitaxy (ALE), was originally developed by Suntola et al. 30 years ago to deposit highly uniform layers over large areas for thin film electroluminescent (TFEL) displays.[125] Since then, ALD has been increasingly exploited as a thin film deposition technique for microelectronics.[47] Meanwhile, ALD is also used in optoelectronics,[126] micro-electromechanical systems,[127,128] catalysis[129] and protective coatings.[130] ALD is a deposition technique developed from CVD, but unlike CVD, ALD relies exclusively on surface driven reactions between two or more gaseous precursors. This is achieved by alternating doses of

precursors with inert gas purges in between to prevent gas phase reactions.[131,132] ALD is a self-limiting process and provides Angstrom scale thickness control, large area uniformity,[125] excellent conformality on high aspect ratio structures,[133] and virtually pin-hole free coatings.[134] ALD has been successfully used in the deposition of metals,[135] oxides,[136-139] nitrides,[61,140-142] and carbides.[143]

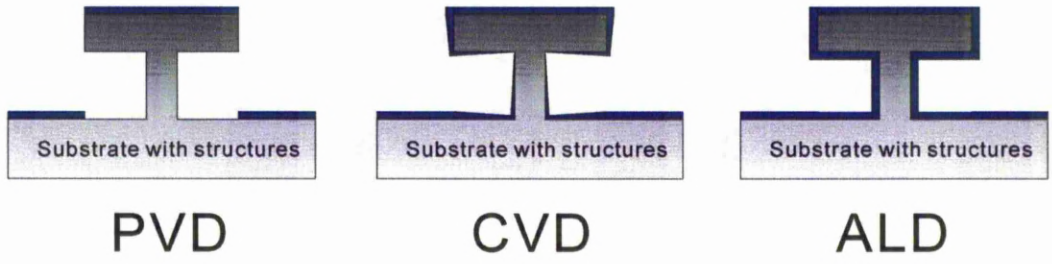

Figure 2.4 Schematic illustration of film (filled in blue) conformality on complex structures when using physical vapour deposition (PVD), CVD and ALD.[144]

Compared to physical based deposition techniques and CVD, the major advantage of ALD is conformality and this is schematically illustrated in Figure 2.4.[144] It can be seen that no film can be deposited under the complex structure when using physical based deposition due to the line of sight effect. Some improvements can be made by CVD, but a significant improvement is made by ALD for fully conformal coatings on complex structures. As a deposition process, ALD has been reviewed for many times, the purpose of this section is to provide an overview for nitride ALD processes and for other materials, readers are directed to references.[145-149]

2.3.1. Principle

ALD relies on cyclic surface reactions between absorbed chemical species, and these are schematically illustrated in Figure 2.5. A typical ALD cycle involves the following four steps, (a) precursor dose, (b) precursor purge, (c) co-reactant dose and

(d) co-reactant purge. (a) During the precursor dose, a pulse of reactive metal precursor is introduced into the reactor, and is chemisorbed onto the surface via reactions with hydrogen containing surface species such as –OH or –NH groups. In most ALD processes the chemisorption is saturative, meaning that only a limited number of precursor molecules can absorb on the surface.[148] (b) An inert gas purge is then introduced and carries away all excess precursor molecules and reaction by-products in the gas phase. This purge, sometimes replaced by pumping, should leave the chamber with no reactive species and the substrate with absorbed precursor. (c) Co-reactants are then introduced to form the targeting material by reacting with surface precursor molecules. This reaction can also provide surface groups that are also needed for the next pulse of precursor. (d) An inert gas purge is finally provided, removing all excess co-reactants and by-products in the gas phase. This completes an ALD cycle and prepares the reaction chamber ready for the next cycle.

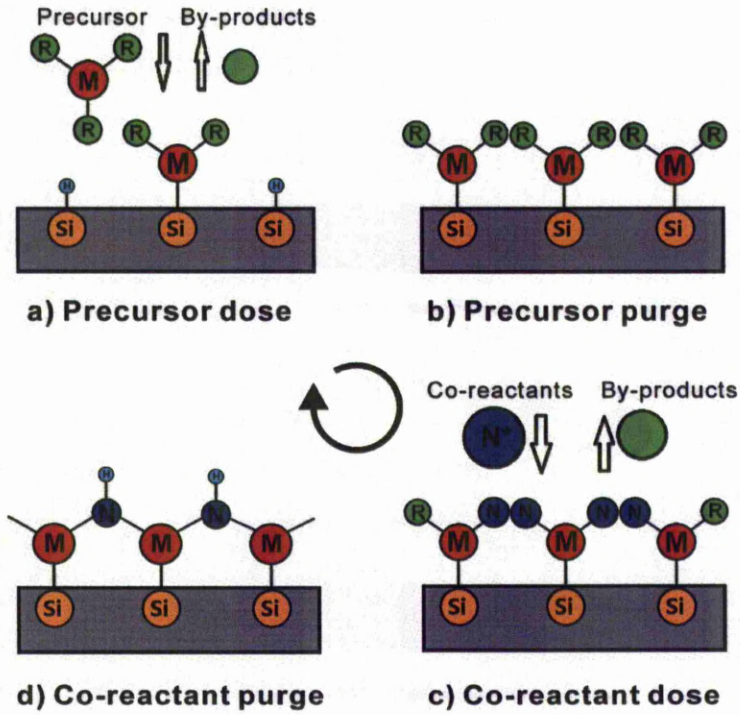

Figure 2.5 A schematic illustration of one ALD cycle for nitride deposition.

Just like CVD, the reactions involved in ALD may be assisted by different types of energy. There have been thermal ALD,[149] photo-assisted[150] and plasma-enhanced ALD.[151] Thermal ALD is the most conventional process, while the other two processes provide extra energy, which can enhance the reactions and reduce the deposition temperature. Room temperature process has been demonstrated using UV enhanced ALD for the deposition of ZrO_2,[150] where the thermal process using the same precursor requires deposition temperatures higher than 200°C.[152] Similar low temperature processes have also been demonstrated using plasma-enhanced ALD compared to thermal ALD.[153,154]

2.3.2 Features – self-limiting behaviour

In one ALD cycle, the resulting deposition remains constant regardless of the dose received, given the dose is high enough to achieve saturation. Unlike CVD, the growth rate in ALD is defined as the thickness gain per cycle (Å/cycle) instead of per time, and the overall film thickness is determined by the number of cycles applied. This self limited growth using surface absorption is a unique feature of ALD and is called self-limiting behaviour.

Self-limiting behaviour is verified by monitoring the growth rate as a function of precursor or co-reactant doses. However, before conducting this experiment, the purge length must be established to ensure that no gas phase reaction occurs and the deposition relies solely on surface reactions (Figure 2.6a). When the purge length is insufficient, precursor and co-reactant doses overlap and CVD-like deposition can occur. If the purge length is extended, precursor and co-reactant doses are separated and the deposition relies purely on surface reactions. The length of purge required is

dependent on the chamber volume, chamber geometry, pump capacity, purge flow, the type of precursors/co-reactants, and the deposition temperature used.

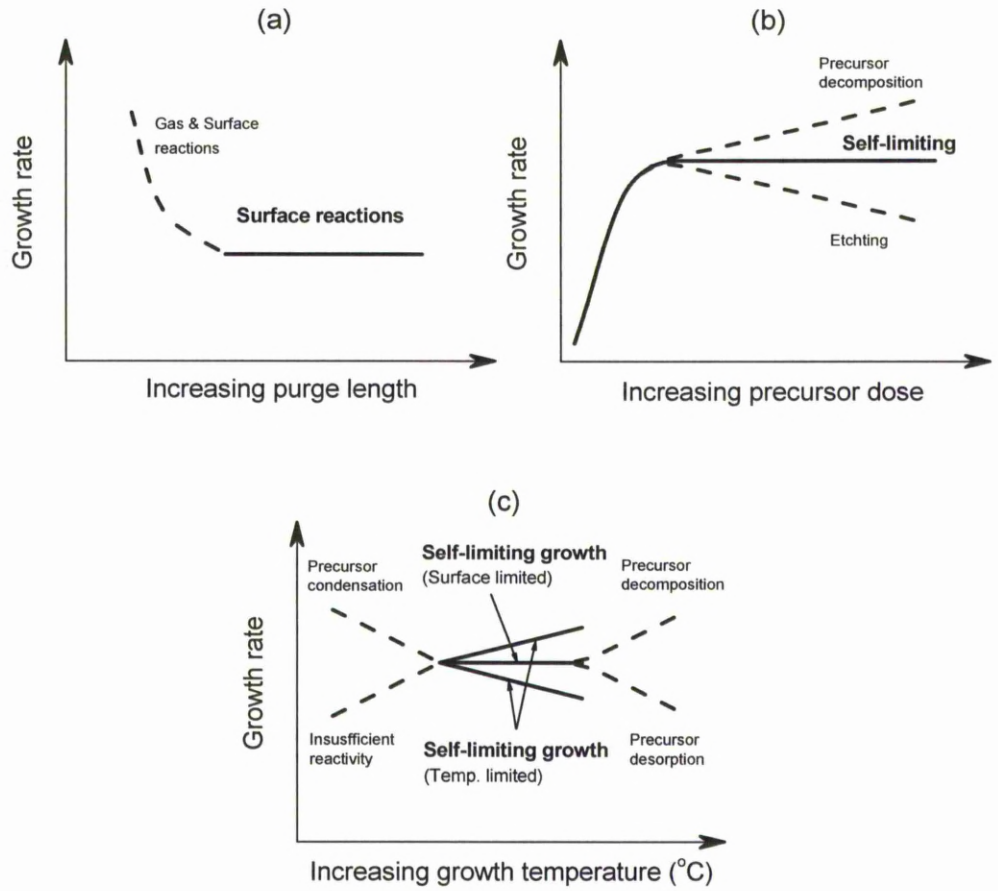

Figure 2.6 Growth rate in ALD as a function of (a) purge length, (b) precursor/co-reactant doses and (c) growth temperature.

Once the purge time has been established, self-limiting behaviour can be verified by monitoring the growth rate as a function of increasing precursor doses (Figure 2.6b). The growth rate initially increases with the dose and self-limits when the dose is sufficient to saturate the deposition area. It is this feature that gives rise to high uniformity and excellent conformality in ALD. Ideally, ALD produces one monolayer per cycle, however, in practice, due to steric hindrance of precursor/co-reactant molecules and perhaps limited surface sites, the growth rate often falls below one

monolayer per cycle.[148] In practice, it is also possible to have either increasing or decreasing growth rate in the saturation region (Figure 2.6b). The increase is due to decomposition of the precursor molecule. The decomposition may be driven by thermal energy that the deposition temperature is too high.[155] It may also be driven by chain reactions when using particular precursors such as alkoxide, where the ligands may undergo β-hydride elimination.[156] This reaction releases additional sites that can react with incoming precursors, resulting in an increase in growth rate and inhibiting self-limiting behaviour.[156] The decrease of growth rate in the saturation region is due to etching.[157] Both precursor decomposition and etching should be minimised if possible to achieve self-limiting deposition.

In ALD, a constant growth rate is often observed within a temperature range, which is known as the ALD temperature window (Figure 2.6c).[141,158,159] This is attributed to surface limited reactions when sufficient energy is supplied to activate reactions but not high enough for thermal decomposition. There have also been cases when the growth rate is dependent on temperature,[160] and this is due to the unfavoured reaction thermodynamics at low temperatures. However, self-limiting behaviour has been reported in both cases and therefore,[141,158-160] a temperature window is not essential for ALD. Nevertheless, an ALD window is advantageous as high film uniformity can be achieved even if there are small temperature differences across the substrate. An ALD window is also advantageous when depositing doped or nanolaminate materials to facilitate a match in the deposition temperature between two or more processes.

In practice, the growth rate is often affected by temperature when operating within the zones of precursor condensation,[146] decomposition,[161] desorption[162] and insufficient reactivity (Figure 2.6c).[160] Precursor condensation may lead to

absorption of multiple layers of precursor molecules.[145] The molecules buried underneath are less likely to have a reaction with the co-reactant and therefore, the film can be contaminated by elements from the precursor ligands.[145] Thermal decomposition at higher temperatures destroys self-limiting behaviour and leads to CVD-like processes, the as deposited films can also be contaminated by elements from the precursor ligands.[161] The desorption and insufficient reactivity would inhibit the growth rate and largely reduce the throughput, in the worst case, no film could be deposited.[163] As a result, the effects mentioned above should be minimised if possible for the deposition of high quality films in a self-limiting manner.

The self-limiting behaviour raises fascinating features for ALD. Firstly, film thickness is precisely controlled by the number of ALD cycles. The surface limited deposition also results in large area uniformity[125] and batch process capability.[164] In addition, conformal coatings have been achieved on high aspect ratio (>700:1 trench diameter 65nm)[133] and powder[165] structures when sufficient precursor molecules and time are given to allow them reaching the coating surfaces. Pin-hole free films with high density have been deposited,[134] and finally ALD processes are easy to scale-up because the surface chemistry involved in small area deposition and large area deposition is identical. All these features can be achieved by optimising growth conditions within the self-limiting region, and no complex control of gas flux homogeneity is required.

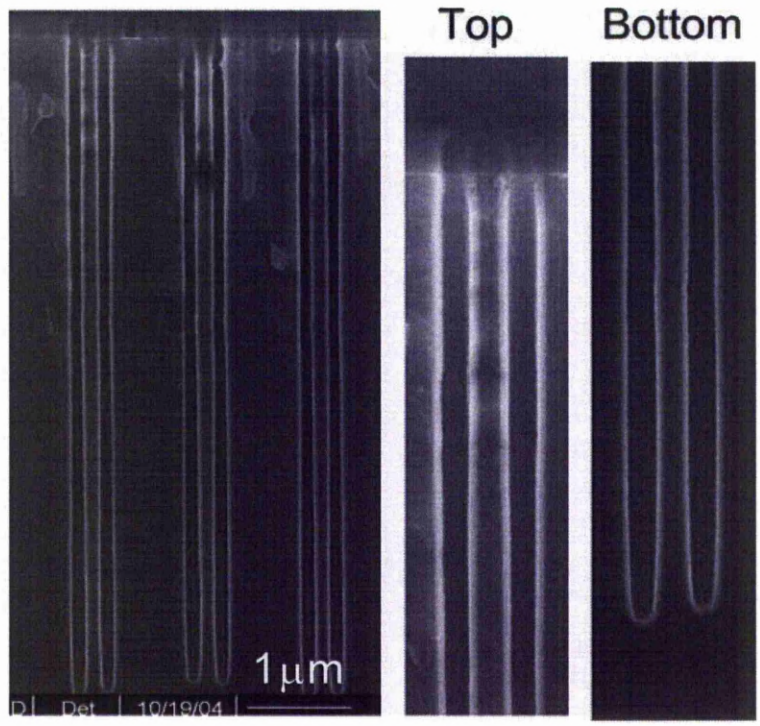

Figure 2.7 SEM micrograph of a 40:1 aspect ratio trench coated with 28nm Y_2O_3, thickness variation is less than 5% between top and bottom of the trench.[166]

As emphasised before, the major advantage of ALD is conformal coating and this has been illustrated in previous ALD studies.[166] Figure 2.7 shows Y_2O_3 films (28nm) deposited by ALD on trench structures with an aspect ratio of 40:1 (trench diameter ~100nm). The SEM micrograph confirms that the thickness variation of the film at the top and bottom of the trench is less than 5%, showing a good conformality.

The major limitation of ALD is the relative low throughput compared with CVD and physical based deposition techniques. A deposition rate of 100nm/hour is quite common for ALD, which is one or two magnitudes slower than CVD and other physical based deposition techniques.[145] However, this low growth rate is not necessarily a limiting factor for industry as multiple samples (150 wafers) can be simultaneously coated hence allowing a high throughput batch process.[167]

2.3.3 Nitride ALD

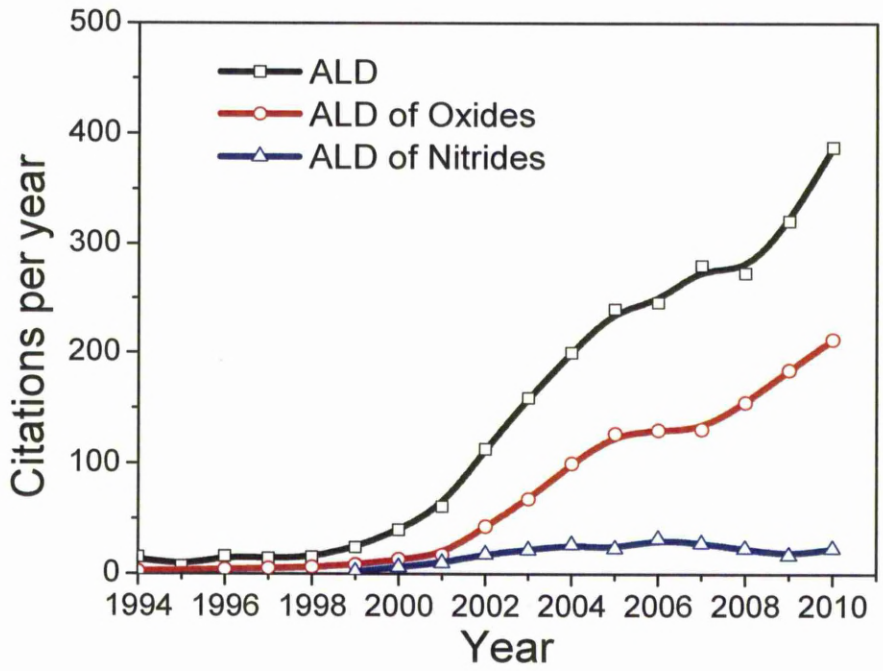

Figure 2.8 Citation numbers per year for ALD, oxide ALD and nitride ALD papers, data retrieved from ISI web of knowledge.

The number of published papers on ALD has increased significantly since 2000 (Figure 2.8), this has largely been driven by its potential applications for producing high-*k* dielectrics in MOS devices. While considerable work has been carried out on thin film oxides such as Hf,[137,138] Ta,[168] Gd,[155] and Pr[156] oxides, which have potential applications as high-k dielectrics, little has been reported about their nitride counterparts (Figure 2.8). For example, in 2010, only 23 papers report on ALD of nitride compared with 212 papers for oxides.

This apparent lack of work on ALD of nitrides is perhaps largely due to the significant challenges associated with nitride ALD. The main obstacle to the formation of nitrides is their significantly lower thermodynamic stability compared with the corresponding oxides. Table 2.1 summarizes the bond dissociation energy,

D^{o}_{298}, for selected metal-to-nitrogen and metal-to-oxygen bonds in diatomic molecules. It can be seen the metal-to-nitrogen bond is always weaker than the metal-to-oxygen bond, indicating that these nitrides are less stable than the corresponding oxides. This is probably due to a higher electronegativity of oxygen than nitrogen, with a value of 3.44 and 3.04 respectively on the Pauling scale.[169] In any nitride deposition process, trace levels of oxygen species in the reaction chamber, precursors, co-reactants or carrier gases can lead to preferential oxide reactions and hence oxygen contamination in films.[170] Therefore, it is critical to ensure a leakage free chamber and high purity sources of precursors, co-reactants and carrier gases prior to any nitride ALD.

	Bond dissociation energy, D^{o}_{298} (kJ/mol)	
	M-N	**M-O**
Ta	476	839
Hf	535	801
Ti	476	666
Zr	565	766
V	523	637
La	519	798
Ce	519	790
Y	477	714

Table 2.1 Bond dissociation energy of metal to nitrogen and metal to oxygen bonds in diatomic molecules. Data are obtained from CRC handbook of chemistry and physics.[169]

2.3.3.1 Metal precursors

The success of ALD relies heavily on appropriate chemical reactions. Precursor chemistry is one of the most active research fields in ALD and has been extensively reviewed in papers[147,148] and text books.[132,145] The requirements for precursors in nitride ALD are summarized in Table 2.2. They are divided into essential properties and desirable properties because in practice, not all requirements can be fulfilled simultaneously and properties listed in the latter group may be sacrificed.

Essential properties	Desirable properties
• High volatility • Thermal stability • High reactivity • No dissolution into substrates • Oxygen free ligands • High purity	• Unreactive volatile by-products • Inexpensive • Easy to synthesize and handle • Non toxic • No etching

Table 2.2 Summary of precursor requirements for nitride ALD.

High volatility is essential for ALD precursors as it gives high flux of precursor molecules and provides an efficient dosing. Precursors such as Trimethylaluminum (TMA) has a vapour pressure of ~10 Torr at 20°C and is considered as a highly volatile precursor.[171] In some cases, the precursor volatility is insufficient at room temperature and heating is required to achieve adequate vapour pressure. For example, in the industrial ALD process of HfO_2 using $HfCl_4$,[172] the precursor needs to be heated at ~200°C to achieve good vapour pressure that is suitable for deposition.[173] However, to choose the optimum temperature for precursor transportation is not straight forward and requires some optimisations. Vapour pressure measurements investigate the pressure of heated substances, and high temperatures lead to volatility (Figure 2.9a).[174] Although increased temperature enhances the vapour pressure, it can cause problems if the precursor starts to decompose or change phase. These effects result in poor stability and short life-time for precursors, in addition, thermal decomposition also affects self-limiting behaviour and leads to CVD-like reactions and contaminated films. Thermogravimetric analysis[175] (TGA) measures the weight loss of precursors as a function of increasing temperature and is indicative of a decomposition regime (Figure 2.9b).[176] In this experiment, the precursor with a given weight is placed onto a microscale in an inert atmosphere, the temperature of the microscale is ramped up at a given rate (typically 5-10°C/min) and the weight of the precursor is recorded at each temperature. The

decrease in the weight is indicative of thermal decomposition or a phase changing process. The general rule for selecting a transpiration temperature is to aim for high vapour pressure but with low weight loss as measured by TGA.

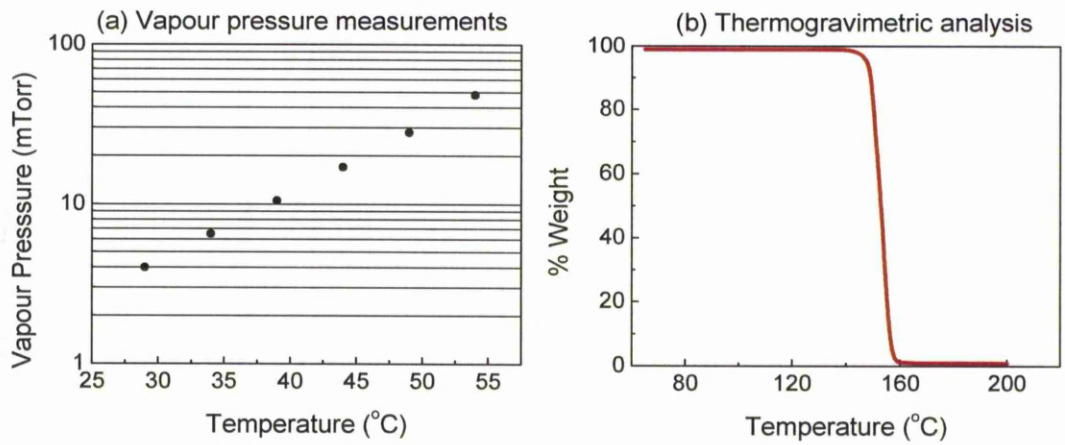

Figure 2.9 (a) vapour pressure measurements for $Ta(NMe_2)_5$[174]; (b) a typical thermogravimetric analysis data for ALD precursors.

Surface reactions in ALD are very similar to reactions involved in CVD and many CVD precursors have been proven to work in the ALD mode.[147] Aggressive reactions are required in ALD to ensure a fast formation of desired material and therefore, ALD reactions should have a Gibbs free energy change as negative as possible.[145] By-products released from deposition should be unreactive and volatile so they can be efficiently removed during the purge step.

For nitride ALD, precursors must be oxygen free, both in terms of ligand structure and purity to avoid preferential oxide formation. Previous theoretical work has demonstrated that the reaction between $Hf(NMe_2)_4$ and water is spontaneous, however the reaction between $Hf(NMe_2)_4$ and ammonia is endothermic.[170,177] This means that if there are oxygen species in the reactor, they can be easily incorporated in the film. Once an oxide is formed, any nitride formation would be extremely difficult. The nitridation from HfO_2 to HfO_xN_y using ammonia requires temperatures higher than

700°C,[178,179] the required temperature would be higher if the targeting materials are stoichiometric nitrides. Thus, the precursors used for nitride reaction must be oxygen free.

ALD deposition of transition metal nitrides has previously been reported using various metal precursors. The halide precursors including metal fluorides,[180] chlorides,[18,157,181], and bromides[17] have been most widely studied, however, these tend to form corrosive hydrogen halide by-products, which can damage deposition equipment. Halide precursors also require relatively high deposition temperatures (>400°C) to prevent halide incorporation.[181] This is because metal-halogen bonds are stronger than metal-nitrogen bonds and consequently,[182] substantial energy is required to convert halides into nitrides. To overcome these challenges, alkylamide based precursors such as dimethylamides,[183] ethylmethylamides,[184] diethylamides,[58] and tertbutylamides[160] have been developed and used in nitride ALD. Alkylamides allow lower deposition temperature because they undergo a transamination-like reaction with co-reactants such as ammonia.[185] Transamination reactions, as suggested by the name, refer to exchange reactions that transfer the amine group from one molecule to another, which facilitates nitride formation when alkylamide precursors are used with nitrogen hydrides such as ammonia.[186] Gas phase transamination has been well understood for nitride CVD[185] and similar surface reactions are evident in ALD.[187] Carbon and hydrogen are potential impurities with alkylamide precursors; however, efficient transamination-like reactions exchange the alkylamide group with ammonia and therefore, these contaminants can be inhibited. Carbon content as low as 2% have has reported in TaN_x films deposited with pentakis(dimethylamino)tantalum and ammonia at 275°C.[183]

2.3.3.2 Co-reactants

Co-reactants, sometimes referred as non-metal precursors, are as important as metal precursors to ensure aggressive and efficient reactions in nitride ALD. Ammonia is the most widely used nitrogen containing co-reactant and has been proven successful in the ALD of TiN,[75,188] HfN_x,[189] TaN_x,[161,181,183] NbN,[18] ZrN,[140] WN,[190] and MoN.[188] Hydrazines are another class of nitrogen co-reactants and offer superior reactivity to ammonia.[191] The high reactivity originates from the weak N-N bond (ΔH^o=287 kJ/mol) compared to the N–H bond in ammonia (ΔH^o=461 kJ/mol).[191] The reactivity has been demonstrated in the ALD of TaN_x, where a lower process temperature was achieved using hydrazines compared with ammonia.[109,160] Molecular N_2 and H_2 have been used in CVD as nitrogen co-reactants at high temperatures (~1000°C),[192] unfortunately, this approach is not well suited to ALD because such high temperatures would lead to thermal decomposition of precursors. Plasma-enhanced (PE) ALD uses the extra energy supplied by a plasma and can effectively reduce deposition temperature. PEALD has been used for the deposition of TaN_x,[151,157,193] TiN,[194] and HfN[28,159,195] from a mixed plasma of N_2 and H_2 gases. This approach gives added control over nitride stoichiometry; the reduction power of hydrogen radicals allows the deposition of elemental metal,[135] the addition of nitrogen radicals results in a wide range of stoichiometric nitrides subject to the H_2/N_2 partial pressure.[157] Pure hydrogen plasma has also been used for the deposition of mono-nitrides of HfN,[28] TaN,[56,196] and TiN[197] when alkylamide precursors were used. Pure N_2 plasma has also been used for the deposition of Hf_3N_4,[159] TiN[198], and ZrN[58] with alkylamide precursors. And ammonia plasma has been used for the deposition of WN,[199] AlN[200] and TiN.[198,201]

2.3.4 ALD reactors

ALD was developed from CVD and they share many common features including reactor hardware. This section discusses the main components that are involved in ALD reactors, and for a detailed description of CVD reactors, readers are directed to reference[202]. Typical ALD reactors have the following basic components, a vacuum pump, a reaction chamber, a substrate holder, and, precursor/gas delivery systems.

2.3.4.1 Pumps

ALD operates over a wide pressure range from high vacuum[203] to atmosphere pressure[204] and mechanical pumps are most widely used for ALD reactors. Mechanical pumps form a vacuum by trapping gas molecules from the chamber and subsequently moving them to exhaust, repeated cycling of this process can achieve pressures in the range of 10e-3 Torr. There have been two general categories for mechanical pumps, according to whether they require lubricants during operation. 'Wet' pumps such as rotary vane pump (Figure 2.10a) involve friction and require oil lubricants. Oils are volatile species and oil back-streaming can be an issue for 'wet' pumps because it leads to contamination of the reaction chamber and films. A liquid nitrogen trap (Figure 2.10b) can be used between pump and reactor to condense back-streamed oil vapour. Alternatively, mechanical frictions can be minimised or even eliminated by proper designing of pumping mechanisms so that no oil lubricant is needed. These pumps are classified as 'dry' pumps and some typical designs such as diaphragm pumps and screw pumps are shown in Figure 2.10. 'Dry' pumps are generally preferred to the 'wet' variants for ALD because they do not have oil back streaming problems; turbo pumps are also used where high vacuum is required.[117]

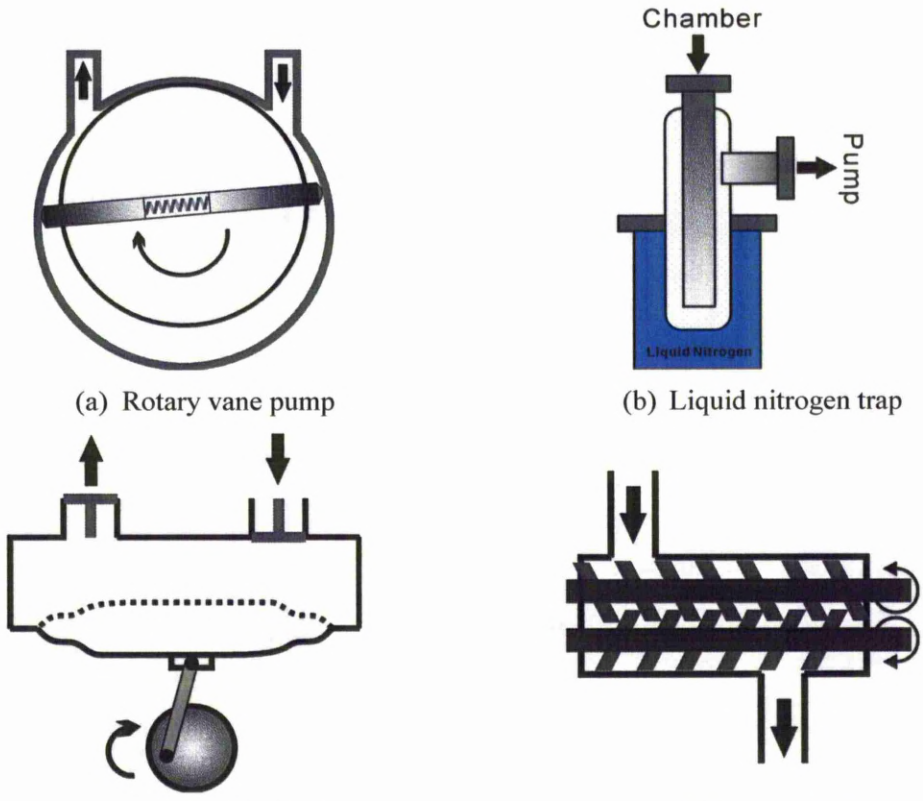

(a) Rotary vane pump (b) Liquid nitrogen trap

(c) Diaphragm pump (d) Screw pump

Figure 2.10 Schematic illustrations of (a) rotary vane pump, (b) liquid nitrogen trap, (c) diaphragm pump and (d) screw pump.

2.3.4.2 Chamber and substrate holder

The reaction chamber is another component to ensure a clean deposition environment. Leaks must be minimised because most ALD precursors are air sensitive, for nitride deposition, this is more critical since a trace level of oxygen containing species in the chamber will be incorporated in the films. A leak-up rate test is a quick and cost-effective way to examine chamber leakage. The leak of a chamber can be quantified by monitoring the pressure rise when the chamber is isolated from the pump using a valve. A pressure rise of 1 mTorr/min is considered good sealing by Becky et al.[140] in the deposition of HfN_x and should be ensured prior to deposition. Other tools such as a helium based leak detector may be used to identify the source of leakage.

ALD relies on surface reactions and therefore, a highly uniform temperature profile is required for substrate surfaces. In ALD reactors, resistance based heating coils are often used embedded in a substrate holder to achieve uniform heating. Thermo couples are generally used to measure temperatures; by employing a thermal couple heating coils at multiple locations, a temperature profile can be monitored and optimised. In batch process reactors, the heating are usually provided in the form of tube furnace with resistance coils embedded in furnace walls, which can provide uniform heating.[167]

2.3.4.3 Precursor delivery methods

Precursor doses should be controlled with high accuracy and repeatability. This is because hundreds or even thousands of ALD cycles may be used to deposit a film. Although ALD is self-limiting, it is desirable to minimise precursor usage and to avoid waste – this is important on the basis of cost and environmental grounds. It is therefore important to accurately control precursor dose. Precursor delivery manifold should be designed with care. Cold and hot spots should be avoided because they lead to precursor condensation and decomposition respectively. In addition, laminar flow is desired for precursor transportation because it is easy to control. Dead space introduces turbulent flows and should be avoided during the design of the manifold.

The dosing method employed is very much dependent on precursor volatility. The dose of gaseous precursors is controlled by mass flow controllers (MFCs). Precursors with high volatility may be dosed via vapour draw, whereas precursors with relatively lower vapour pressure may be dosed via a bubbling process with the help of additional inert gas flow.

Gaseous precursors - The dose of gaseous precursors is often controlled by MFCs (Figure 2.11). Standard MFCs use feedback control of a leak valve to achieve the desired flow rate. The flow rate is measured by the temperature difference along a heated sample tube where laminar flow is established for a known gas, and the relation is written in Eq. 2.2. Leak valves in MFCs are not designed to close fully and a downstream valve is required to either turn 'on' or 'off' the flow. In practice, the dose is often controlled by a fixed flow rate with a variable flow time, or vice versa.

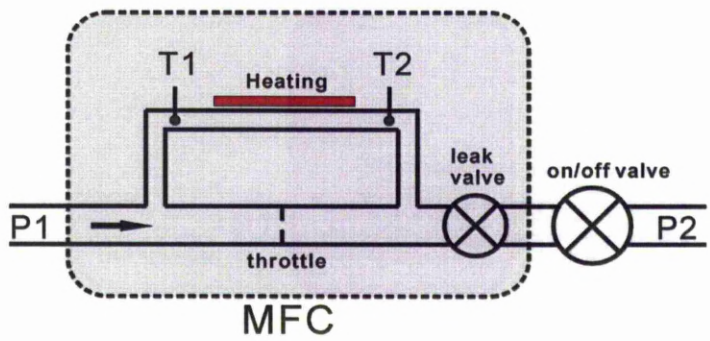

Figure 2.11 Working principle of a MFC (P_1 must be greater than P_2 to establish the flow).

$$Q = \frac{T_2 - T_1}{BC_p} \qquad \text{(Eq. 2.2)}$$

Where Q is the flow rate (standard cubic centimetre per minute); B is the calibration constant; C_p is the heat capacity of a known gas.

Vapour draw - In vapour draw (Figure 2.12a), the precursor vapour pressure is a lot higher than the chamber pressure and consequently, the vapour is drawn from the bubbler to the chamber when the valve opens. TMA is a good example for vapour draw, it has a vapour pressure of ~10 Torr at ambient temperature and the working pressures of ALD reactors are typically below ~0.5 Torr. The dose is controlled by the valve opening time and the required dose can be established using the saturation-plot

mentioned in Figure 2.6b. The valve should have a response time below 20ms and a life over millions of cycles to ensure accurate control with high repeatability.[205] Such low response time is required to accommodate highly volatile precursors such as TMA to minimise the waste of precursor. Pneumatically driven diaphragm valves (Figure 2.13) can fulfil this requirement and are widely employed for ALD reactors. The major limitation for these valves is the operation temperature, which is limited to 200°C due to the plastic valve seat used.

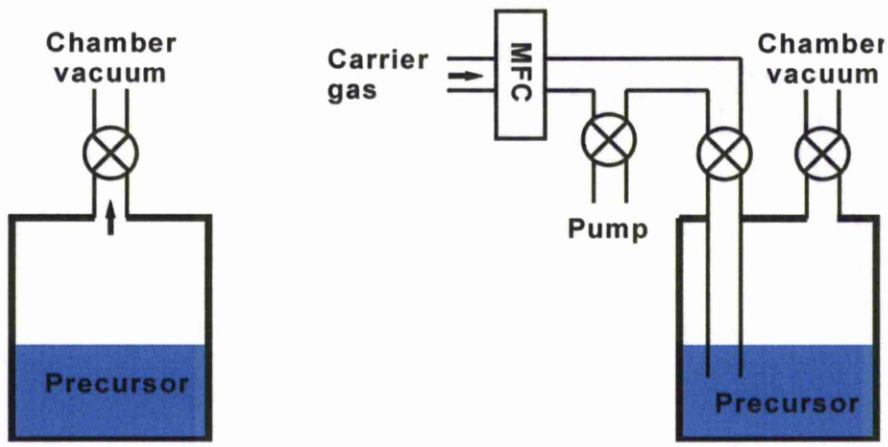

(a) Vapour draw (b) Bubbling

Figure 2.12 Schematic illustrations for precursor transportation using (a) vapour draw and (b) bubbling.

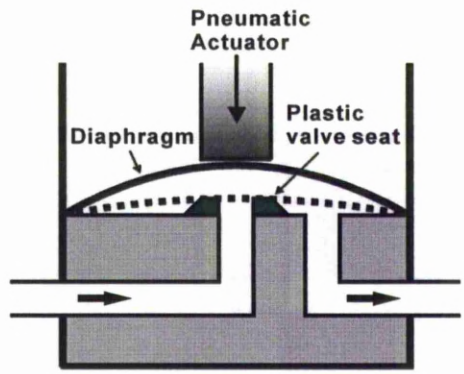

Figure 2. 13 A schematic illustration of a diaphragm valve.

Bubbling - Bubbling is often used when the vapour pressure is not sufficient to compete with chamber pressure, but still high enough to have surface reactions. It is also used even when the vapour pressure is high to enhance transportation. An inert gas flow, usually nitrogen or argon, is used as a carrier gas to transport the precursor vapour (Figure 2.12b). The dose is determined by both bubbling time and flow rate of the inert gas. A fast response is also required in this method and diaphragm valves are generally used. However, the operation of a leak valve in MFCs is slow and can take 1-2s to activate, which dramatically reduces the response. This has been solved by an additional by-pass line to a pump, where the flow is established prior to dosing.

The methods described above are limited to the tolerance of diaphragm valve seat (200°C) and are not suitable for high temperature transportations. Low volatility precursors must transport at higher temperatures, and precursor delivery systems such as 'inert gas valving system'[145] and 'liquid injection system'[156] have been developed for this purpose. These methods are not employed in the current study and readers are directed to references[145,156] for the full descriptions.

2.4 References

1. H. O. Pierson, *Handbook of Refractory Carbides and Nitrides*. William Andrew Publishing/Noyes: New Jersey, U.S.A., (1996).

2. R. A. Fischer, H. Parala, *Metal-organic Chemical Vapour Deposition of Refractory Transition Metal Nitrides*. In *Chemical Vapour Deposition: Precursors, Processes and Applications*, A. C. Jones, M. L. Hitchman, Eds. Royal Society of Chemistry: Cambridge, p 413 (2009).

3. B. Subramanian, R. Ananthakumar, M. Jayachandran, *Vacuum* **85**, 601-609 (2010).

4. S. Veprek, S. Reiprich, *Thin Solid Films* **268**, 64-71 (1995).

5. J. Musil, *Surface & Coatings Technology* **125**, 322-330 (2000).

6. D. E. Wolfe, B. M. Gabriel, M. W. Reedy, *Surface & Coatings Technology* **205**, 4569-4576 (2011).

7. E. Alkhateeb, R. Ali, S. Virtanen, N. Popovska, *Surface & Coatings Technology* **205**, 3006-3011 (2011).

8. K. L. Choy, *Progress in Materials Science* **48**, 57-170 (2003).

9. N. Vershinin, K. Filonov, B. Straumal, W. Gust, I. Wiener, E. Rabkin, A. Kazakevich, *Surface & Coatings Technology* **125**, 229-232 (2000).

10. M. Tabata, K. Maeda, M. Higashi, D. Lu, T. Takata, R. Abe, K. Domen, *Langmuir* **26**, 9161-9165 (2010).

11. X. Feng, T. J. LaTempa, J. I. Basham, G. K. Mor, O. K. Varghese, C. A. Grimes, *Nano Letters* **10**, 948-952 (2010).

12. H. G. Leduc, B. Bumble, P. K. Day, B. H. Eom, J. S. Gao, S. Golwala, B. A. Mazin, S. McHugh, A. Merrill, D. C. Moore, O. Noroozian, A. D. Turner, J. Zmuidzinas, *Applied Physics Letters* **97**, 102509 (2010).

13. K. Makise, H. Terai, M. Takeda, Y. Uzawa, Z. Wang, *Ieee Transactions on Applied Superconductivity* **21**, 139-142 (2011).

14. S. Yamanaka, K.-i. Hotehama, H. Kawaji, *Nature* **392**, 580-582 (1998).

15. I. Hase, Y. Nishihara, *Physical Review B* **60**, 1573 (1999).

16. A. Z. Tuleushev, Y. Z. Tuleushev, V. N. Volodin, *Physics of Metals and Metallography* **94**, 490-495 (2002).

17. P. Alen, M. Juppo, M. Ritala, T. Sajavaara, J. Keinonen, M. Leskela, *Journal of The Electrochemical Society* **148**, G566-G571 (2001).

18. P. Alén, M. Ritala, K. Arstila, J. Keinonen, M. Leskelä, *Thin Solid Films* **491**, 235-241 (2005).

19. R. A. Araujo, X. H. Zhang, H. Y. Wang, *Journal of Vacuum Science & Technology B* **26**, 1871-1874 (2008).

20. S. L. Cho, K. B. Kim, S. H. Min, H. K. Shin, S. D. Kim, *Journal of The Electrochemical Society* **146**, 3724-3730 (1999).

21. K. I. Choi, B. H. Kim, S. W. Lee, J. M. Lee, In *Characteristics of ALD-TaN thin films using a novel precursors for copper metallization, Interconnect Technology Conference, 2003. Proceedings of the IEEE 2003 International*, 129-131 (2003).

22. A. E. Kaloyeros, *Journal of The Electrochemical Society* **146**, 170-176 (1999).

23. A. E. Kaloyeros, X. Chen, S. Lane, H. L. Frisch, B. Arkles, *Journal of Materials Research* **15**, 2800-2810 (2000).

24. A. E. Kaloyeros, E. Eisenbraun, *Annual Review of Materials Science* **30**, 363-385 (2000).

25. H. Kim, J. C. Cabral, C. Lavoie, S. M. Rossnagel, *Journal of Vacuum Science & Technology B: Microelectronics and Nanometer Structures* **20**, 1321-1326 (2002).

26. T. Oku, E. Kawakami, M. Uekubo, K. Takahiro, S. Yamaguchi, M. Murakami, *Applied Surface Science* **99**, 265-272 (1996).

27. S. C. Sun, *CVD and PVD transition metal nitrides as diffusion barriers for Cu metallization*. Ieee: New York, p 243-246 (1998).

28. S. Consiglio, W. X. Zeng, N. Berliner, E. T. Eisenbraun, *Journal Of The Electrochemical Society* **155**, H196-H201 (2008).

29. M. Kadoshima, K. Akiyama, K. Yamamoto, H. Fujiwara, T. Yasuda, T. Nabatame, A. Toriumi, *Journal of Vacuum Science & Technology B* **23**, 42-47 (2005).

30. W. W. Wang, T. Nabatame, Y. Shimogaki, *Microelectronic Engineering* **85**, 320-326 (2008).

31. H. Y. Yu, J. F. Kang, C. Ren, J. D. Chen, Y. T. Hou, C. Shen, M. F. Li, D. S. H. Chan, K. L. Bera, C. H. Tung, D. L. Kwong, *Ieee Electron Device Letters* **25**, 70-72 (2004).

32. H. Y. Yu, H. F. Lim, J. H. Chen, M. F. Li, C. X. Zhu, C. H. Tung, A. Y. Du, W. D. Wang, D. Z. Chi, D. L. Kwong, *Ieee Electron Device Letters* **24**, 230-232 (2003).

33. P. Majhi, H. C. Wen, K. Choi, H. Alshareef, C. Huffman, B. H. Lee, *Proceedings of Technical Papers - IEEE VLSI-TSA International Symposium on VLSI Technology* 105-106 (2005).

34. W. P. Bai, S. H. Bae, H. C. Wen, S. Mathew, L. K. Bera, N. Balasubramanian, N. Yamada, M. F. Li, D. L. Kwong, *IEEE Electron Device Letters* **26**, 231-233 (2005).

35. X. P. Wang, A. E. J. Lim, H. Y. Yu, M. F. Li, C. Ren, W. Loh, C. X. Zhu, A. Chin, A. D. Trigg, Y. C. Yeo, S. Biesemans, G. Q. Lo, D. L. Kwong, *IEEE Transactions on Electron Devices* **54**, 2871-2877 (2007).

36. C. Ren, B. B. Faizhal, D. S. H. Chan, M. F. Li, Y. C. Yeo, A. D. Trigg, N. Balasubramanian, D. L. Kwong, *Thin Solid Films* **504**, 174-177 (2006).

37. H. Luan, H. N. Alshareef, H. R. Harris, H. C. Wen, K. Choi, Y. Senzaki, P. Majhi, B. H. Lee, *Applied Physics Letters* **88**, 142113 (2006).

38. R. Jha, J. Lee, P. Majhi, V. Misra, *Applied Physics Letters* **87**, 223503 (2005).

39. T. Das, C. Mahata, G. K. Dalapati, D. Z. Chi, G. Sutradhar, P. K. Bose, C. K. Chia, S. Y. Chiam, J. S. Pan, Z. Zhang, C. K. Maiti, *Semiconductor Science and Technology* **25**, 125009 (2010).

40. T. Laurila, K. Zeng, J. K. Kivilahti, J. Molarius, T. Riekkinen, I. Suni, *Microelectronic Engineering* **60**, 71-80 (2002).

41. K. Holloway, P. M. Fryer, C. Cabral, J. M. E. Harper, P. J. Bailey, K. H. Kelleher, *Journal of Applied Physics* **71**, 5433-5444 (1992).

42. C. Lee, Y. L. Kuo, *Jom* **59**, 44-49 (2007).

43. K. L. Ou, *Microelectronic Engineering* **83**, 312-318 (2006).

44. I. A. Khorin, Y. I. Denisenko, V. N. Gusev, A. A. Orlikovsky, A. E. Rogozhin, V. I. Rudakov, A. G. Vasiliev, *Hf-based barrier layers for Cu-metallization*. In *International*

Conference on Micro- and Nano-Electronics 2009, K. A. Valiev, A. A. Orlikovsky, Eds. Spie-Int Soc Optical Engineering: Bellingham, Vol. 7521 (2010).

45. N. Ramaswamy, V. Ananthan, D. Hwang, R. Iyer, C. Mouli, A. McTeer, S. Tang, K. Parekh, T. Owens, Y. P. Kim, N. Palaniappan, J. Li, S. Groothuis, G. Haller, S. Wang, In *Metal Gate Recessed Access Device (RAD) for DRAM Scaling, IEEE Workshop on Microelectronics and Electron Devices*, 42-44 (2007).

46. W. W. Wang, T. Nabatame, Y. Shimogaki, *Thin Solid Films* **498**, 75-79 (2006).

47. International Technology Roadmap for semiconductors (ITRS). http://www.itrs.net/ (accessed 2010).

48. S. P. Murarka, R. J. Gutmann, A. E. Kaloyeros, W. A. Lanford, *Thin Solid Films* **236**, 257-266 (1993).

49. J. Torres, *Applied Surface Science* **91**, 112-123 (1995).

50. C. K. Hu, J. M. E. Harper, *Materials Chemistry and Physics* **52**, 5-16 (1998).

51. J. F. Kang, H. Y. Yu, C. Ren, N. Sa, H. Yang, M.-F. Li, D. S. H. Chan, X. Y. Liu, R. Q. Han, D.-L. Kwong, *Journal of The Electrochemical Society* **154**, H927-H932 (2007).

52. K. Holloway, P. M. Fryer, *Applied Physics Letters* **57**, 1736-1738 (1990).

53. H. Ono, T. Nakano, T. Ohta, *Applied Physics Letters* **64**, 1511-1513 (1994).

54. K.-C. Park, K.-B. Kim, *Journal Of The Electrochemical Society* **142**, 3109-3115 (1995).

55. H. C. Chen, B. H. Tseng, M. P. Houng, Y. H. Wang, *Thin Solid Films* **445**, 112-117 (2003).

56. H. C. M. Knoops, L. Baggetto, E. Langereis, M. C. M. van de Sanden, J. H. Klootwijk, F. Roozeboom, R. A. H. Niessen, P. H. L. Notten, W. M. M. Kessels, *Journal of The Electrochemical Society* **155**, G287-G294 (2008).

57. Y. H. Shin, Y. Shimogaki, *Science and Technology of Advanced Materials* **5**, 399-405 (2004).

58. S. Cho, K. Lee, P. Song, H. Jeon, Y. Kim, *Japanese Journal of Applied Physics* **46**, 4085-4088 (2007).

59. L. V. Goncharova, M. Dalponte, T. Feng, T. Gustafsson, E. Garfunkel, P. S. Lysaght, G. Bersuker, *Physical Review B* **83**, 115329 (2011).

60. M. L. Green, D. Brasen, K. W. Evans-Lutterodt, L. C. Feldman, K. Krisch, W. Lennard, H.-T. Tang, L. Manchanda, M.-T. Tang, *Applied Physics Letters* **65**, 848-850 (1994).

61. H. Kim, *Journal of Vacuum Science & Technology B: Microelectronics and Nanometer Structures* **21**, 2231-2261 (2003).

62. J.-S. Park, S.-W. Kang, H. Kim, *Journal of Vacuum Science & Technology B: Microelectronics and Nanometer Structures* **24**, 1327-1332 (2006).

63. E. W. A. Young, S. Mantl, P. B. Griffin, *Silicon MOSFETs-Novel Materials and Alternative Concepts*. In *Nanoelectronics and Information Technology*, R. Waser, Ed. Wiley-VCH: Weinheim, p 361 (2005).

64. C. C. Hobbs, L. R. C. Fonseca, A. Knizhnik, V. Dhandapani, S. B. Samavedam, W. J. Taylor, J. M. Grant, L. G. Dip, D. H. Triyoso, R. I. Hegde, D. C. Gilmer, R. Garcia, D. Roan, M. L. Lovejoy, R. S. Rai, E. A. Hebert, H. H. Tseng, S. G. H. Anderson, B. E. White, P. J. Tobin, *Ieee Transactions on Electron Devices* **51**, 978-984 (2004).

65. C. C. Hobbs, L. R. C. Fonseca, A. Knizhnik, V. Dhandapani, S. B. Samavedam, W. J. Taylor, J. M. Grant, L. G. Dip, D. H. Triyoso, R. I. Hegde, D. C. Gilmer, R. Garcia, D. Roan, M. L. Lovejoy, R. S. Rai, E. A. Hebert, H. H. Tseng, S. G. H. Anderson, B. E. White, P. J. Tobin, *Ieee Transactions on Electron Devices* **51**, 971-977 (2004).

66. C. H. Choi, P. R. Chidambaram, R. Khamankar, C. F. Machala, Z. P. Yu, R. W. Dutton, *Ieee Electron Device Letters* **23**, 224-226 (2002).

67. N. R. Mohapatra, A. Dutta, M. P. Desai, V. R. Rao, S. Ieee Computer, *Effect of fringing capacitances in sub 100 nm MOSFET's with high-K gate dielectrics*. Ieee Computer Soc: Los Alamitos, p 479-482 (2001).

68. D. N. Pattanayak, J. G. Poksheva, R. W. Downing, L. A. Akers, *Ieee Transactions on Components Hybrids and Manufacturing Technology* **5**, 127-131 (1982).

69. G. D. Wilk, R. M. Wallace, J. M. Anthony, *Journal of Applied Physics* **89**, 5243-5275 (2001).

70. T. Kauerauf, B. Govoreanu, R. Degraeve, G. Groeseneken, H. Maes, *Solid-State Electronics* **49**, 695-701 (2005).

71. I. De, D. Johri, A. Srivastava, C. M. Osburn, *Solid-State Electronics* **44**, 1077-1080 (2000).

72. C. Ren, D. S. H. Chan, X. P. Wang, B. B. Faizhal, M. F. Li, Y. C. Yeo, A. D. Trigg, A. Agarwal, N. Balasubramanian, J. S. Pan, P. C. Lim, A. C. H. Huan, D. L. Kwong, *Applied Physics Letters* **87**, 073506 (2005).

73. J. D. Chen, X. P. Wang, M. F. Li, S. J. Lee, M. B. Yu, C. Shen, Y. C. Yeo, *Ieee Electron Device Letters* **28**, 862-864 (2007).

74. H. C. Wen, S. C. Song, C. S. Park, C. Burham, G. Bersuker, K. Choi, M. A. Quevedo-Lopez, B. S. Ju, H. N. Alshareef, H. Niimi, H. B. Park, P. S. Lysaght, P. Majhi, B. H. Lee, R. Jammy, P. Japan Soc Appl, *Gate first metal-aluminum-nitride PMOS electrodes for 32nm low standby power applications*. Japan Society Applied Physics: Tokyo, p 160-161 (2007).

75. F. Fillot, T. Morel, S. Minoret, I. Matko, S. Maîtrejean, B. Guillaumot, B. Chenevier, T. Billon, *Microelectronic Engineering* **82**, 248-253 (2005).

76. A. Kerber, E. A. Cartier, *Ieee Transactions on Device and Materials Reliability* **9**, 147-162 (2009).

77. M. Lukosius, C. Wenger, S. Pasko, H. J. Mussig, B. Seitzinger, C. Lohe, *Chemical Vapor Deposition* **14**, 123-128 (2008).

78. C. Henkel, S. Abermann, O. Bethge, P. Klang, E. Bertagnolli, *Impact of sputter deposited TaN and TiN metal gates on ZrO(2)/Ge and ZrO(2)/Si high-k dielectric gate stacks*. Ieee: New York, p 197-200 (2009).

79. J. Kwon, Y. J. Chabal, *Applied Physics Letters* **96**, 151907 (2010).

80. International Union of Pure and Applied Chemistry (IUPAC). http://www.iupac.org/ (accessed 2010).

81. J. Rhyne, T. McGuire, *IEEE Transactions on Magnetics* **8**, 105-130 (1972).

82. G. Busch, P. Junod, O. Vogt, F. Hulliger, *Physics Letters* **6**, 79-80 (1963).

83. T. R. M. R. J. Gambino, *Proceedings of the seventh rare earth research conference, Coronado, California* **1**, 233-236 (1968).

84. R. Didchenko, F. P. Gortsema, *Journal of Physics and Chemistry of Solids* **24**, 863-870 (1963).

85. R. V. Colvin, S. Legvold, F. H. Spedding, *Physical Review* **120**, 741-745 (1960).

86. C. G. Duan, R. F. Sabirianov, W. N. Mei, P. A. Dowben, S. S. Jaswal, E. Y. Tsymbal, *Journal of Physics-Condensed Matter* **19**, 315220 (2007).

87. C. Meyer, B. J. Ruck, J. Zhong, S. Granville, A. R. H. Preston, G. V. M. Williams, H. J. Trodahl, *Physical Review B* **78**, 174406 (2008).

88. D. X. Li, Y. Haga, H. Shida, T. Suzuki, Y. S. Kwon, G. Kido, *Journal of Physics: Condensed Matter* **9**, 10777 (1997).

89. D. X. Li, Y. Haga, H. Shida, T. Suzuki, *Physica B: Condensed Matter* **199-200**, 631-633 (1994).

90. B. M. Ludbrook, I. L. Farrell, M. Kuebel, B. J. Ruck, A. R. H. Preston, H. J. Trodahl, L. Ranno, R. J. Reeves, S. M. Durbin, *Journal of Applied Physics* **106**, 063910 (2009).

91. F. Natali, N. O. V. Plank, J. Galipaud, B. J. Ruck, H. J. Trodahl, F. Semond, S. Sorieul, L. Hirsch, *Journal of Crystal Growth* **312**, 3583-3587 (2010).

92. S. Granville, B. J. Ruck, F. Budde, A. Koo, D. J. Pringle, F. Kuchler, A. R. H. Preston, D. H. Housden, N. Lund, A. Bittar, G. V. M. Williams, H. J. Trodahl, *Physical Review B* **73**, 235335 (2006).

93. H. J. Trodahl, A. R. H. Preston, J. Zhong, B. J. Ruck, N. M. Strickland, C. Mitra, W. R. L. Lambrecht, *Physical Review B* **76**, 085211 (2007).

94. A. R. H. Preston, S. Granville, D. H. Housden, B. Ludbrook, B. J. Ruck, H. J. Trodahl, A. Bittar, G. V. M. Williams, J. E. Downes, A. DeMasi, Y. Zhang, K. E. Smith, W. R. L. Lambrecht, *Physical Review B - Condensed Matter and Materials Physics* **76**, 245120 (2007).

95. T. A. Yamamoto, T. Nakagawa, K. Sako, T. Arakawa, H. Nitani, *Journal of Alloys and Compounds* **376**, 17-22 (2004).

96. P. Pandit, V. Srivastava, M. Rajagopalan, S. P. Sanyal, *Physica B-Condensed Matter* **403**, 4333-4337 (2008).

97. R. A. Degroot, F. M. Mueller, P. G. Vanengen, K. H. J. Buschow, *Physical Review Letters* **50**, 2024-2027 (1983).

98. V. Srivastava, M. Rajagopalan, S. P. Sanyal, *International Journal of Modern Physics B* **25**, 851-862 (2011).

99. J. W. Gerlach, J. Mennig, B. Rauschenbach, *Applied Physics Letters* **90**, 061919 (2007).

100. M. A. Scarpulla, C. S. Gallinat, S. Mack, J. S. Speck, A. C. Gossard, *Journal of Crystal Growth* **311**, 1239-1244 (2009).

101. D. Bonderud, Spintronics Gets Electrons On Their Bikes And Moving Toward Future Binary Technology. http://inventorspot.com/articles/spintronics_gets_electrons_their_bikes_and_moving_toward_future_ (accessed 2010).

102. A. W. Stuart, Y. C. Almadena, T. Daryl, *Spintronics - Spin-Based Electronics*. In *Handbook of Nanoscience, Engineering, and Technology*, A. W. Goddart, Ed. CRC Press: New York, p 8~1 (2003).

103. C. M. Aerts, P. Strange, M. Horne, W. M. Temmerman, Z. Szotek, A. Svane, *Physical Review B* **69**, 045115 (2004).

104. W. R. McKenzie, P. R. Munroe, F. Budde, B. J. Ruck, S. Granville, H. J. Trodahl, *Current Applied Physics* **6**, 407-410 (2006).

105. R. J. Gambino, T. R. McGuire, H. A. Alperin, S. J. Pickart, *Journal of Applied Physics* **41**, 933-934 (1970).

106. P. Wachter, E. Kaldis, *Solid State Communications* **34**, 241-244 (1980).

107. C. Muller, H. Lippitz, J. J. Paggel, P. Fumagalli, *Journal of Applied Physics* **95**, 7172-7174 (2004).

108. A. T. Filip, P. LeClair, C. J. P. Smits, J. T. Kohlhepp, H. J. M. Swagten, B. Koopmans, W. J. M. de Jonge, *Applied Physics Letters* **81**, 1815-1817 (2002).

109. M. Juppo, M. Ritala, M. Leskela, *Journal of The Electrochemical Society* **147**, 3377-3381 (2000).

110. L. T. Lamont, *Solid State Technology* **44**, 81-+ (2001).

111. Y. P. Chen, R. Z. Wang, B. Wang, T. Xing, X. M. Song, M. K. Zhu, H. Yan, *Journal of Crystal Growth* **283**, 315-319 (2005).

112. E. Kondoh, G. Vereecke, M. M. Heyns, K. Maex, T. Gutt, *Journal Of Vacuum Science & Technology A-Vacuum Surfaces And Films* **17**, 650-656 (1999).

113. D. L. Windt, W. L. Brown, C. A. Volkert, W. K. Waskiewicz, *Journal of Applied Physics* **78**, 2423-2430 (1995).

114. C. C. Fang, F. Jones, V. Prasad, *Journal of Applied Physics* **74**, 4472-4482 (1993).

115. J. Ohta, H. Fujioka, H. Takahashi, M. Sumiya, M. Oshima, *Journal of Crystal Growth* **233**, 779-784 (2001).

116. H. A. Castillo, E. Restrepo-Parra, J. M. Velez, W. de la Cruz, *Surface & Coatings Technology* **205**, 3607-3612 (2011).

117. S. M. Rossnagel, H. Kim, I. Ieee, *From PVD to CVD to ALD for interconnects and related applications*. Ieee Computer Soc: Los Alamitos, p 3-5 (2001).

118. T. N. Adarn, S. Bedell, A. Reznicek, D. K. Sadana, A. Venkateshan, T. Tsunoda, T. Seino, J. Nakatsuru, S. R. Shinde, *Journal of Crystal Growth* **312**, 3473-3478 (2010).

119. M. Croci, J. M. Bonard, O. Noury, T. Stockli, A. Chatelain, *Chemical Vapor Deposition* **8**, 89-+ (2002).

120. H. Yang, G. A. Brown, J. C. Hu, J. P. Lu, R. Kraft, A. L. P. Rotondaro, S. V. Hattangady, I. C. Chen, J. D. Luttmer, R. A. Chapman, P. J. Chen, H. L. Tsai, B. Amirhekmat, L. K. Magel, I. I. I. Ieee, In *A comparison of TIN processes for CVD W/TiN gate electrode on 3nm gate oxide*, *International Electron Devices Meeting*, IEEE: New York, 459-462 (1997).

121. Y. Komae, K. Yasui, M. Suemitsu, T. Endoh, T. Ito, H. Nakazawa, Y. Narita, M. Takata, T. Akahane, *Japanese Journal of Applied Physics* **48**, 076509 (2009).

122. A. C. Jones, M. L. Hitchman, *Overview of Chemical Vapour Deposition*. In *Chemical Vapour Deposition: Precursors, Processes and Applications*, A. C. Jones, M. L. Hitchman, Eds. Royal Society of Chemistry: Cambridge, p 7 (2009).

123. J. Y. Zhang, L. J. Bie, I. W. Boyd, *Japanese Journal Of Applied Physics Part 2-Letters* **37**, L27-L29 (1998).

124. P. D. Richard, R. J. Markunas, G. Lucovsky, G. G. Fountain, A. N. Mansour, D. V. Tsu, *Journal Of Vacuum Science & Technology A-Vacuum Surfaces And Films* **3**, 867-872 (1985).

125. T. Suntola, *Materials Science Reports* **4**, 261-312 (1989).

126. L. Niinisto, J. Paivasaari, J. Niinisto, M. Putkonen, M. Nieminen, *Physica Status Solidi a-Applied Research* **201**, 1443-1452 (2004).

127. T. M. Mayer, J. W. Elam, S. M. George, P. G. Kotula, R. S. Goeke, *Applied Physics Letters* **82**, 2883-2885 (2003).

128. N. D. Hoivik, J. W. Elam, R. J. Linderman, V. M. Bright, S. M. George, Y. C. Lee, *Sensors and Actuators a-Physical* **103**, 100-108 (2003).

129. M. Kemell, V. Pore, M. Ritala, M. Leskela, M. Linden, *Journal of the American Chemical Society* **127**, 14178-14179 (2005).

130. S. D. Standridge, G. C. Schatz, J. T. Hupp, *Langmuir* **25**, 2596-2600 (2009).

131. R. L. Puurunen, *Journal of Applied Physics* **97**, 121301 (2005).

132. M. Ritala, M. Leskela, *Atomic Layer Deposition*. In *Handbook of Thin Film Materials*, N. S. Nalwa, Ed. Academic Press: San Diego, Vol. 1 (2002).

133. J. W. Elam, D. Routkevitch, P. P. Mardilovich, S. M. George, *Chemistry of Materials* **15**, 3507-3517 (2003).

134. T. Riedl, T. Winkler, H. Schmidt, J. Meyer, D. Schneidenbach, H. Johannes, W. Kowalsky, T. Weimann, P. Hinze, In *Reliability aspects of organic light emitting diodes, 2010 IEEE International Reliability Physics Symposium (IRPS)*, 327-333 (2010).

135. S. M. Rossnagel, A. Sherman, F. Turner, *Journal of Vacuum Science & Technology B* **18**, 2016-2020 (2000).

136. D. M. Hausmann, E. Kim, J. Becker, R. G. Gordon, *Chemistry Of Materials* **14**, 4350-4358 (2002).

137. Y. Senzaki, S. Park, H. Chatham, L. Bartholomew, W. Nieveen, *Journal of Vacuum Science & Technology A: Vacuum, Surfaces, and Films* **22**, 1175-1181 (2004).

138. X. Y. Liu, S. Ramanathan, T. E. Seidel, *Atomic layer deposition of hafnium oxide thin films from tetrakis(dimethylamino)hafnium (TDMAH) and ozone*. In *Comos Front-End Materials and Process Technology*, T. J. King, B. Yu, R. J. P. Lander, S. Saito, Eds. Materials Research Society: Warrendale, Vol. 765 pp 97-102 (2003).

139. Y. Senzaki, K. Choi, P. D. Kirsch, P. Majhi, B. H. Lee, *AIP conference Proceedings* **788**, 69-72 (2005).

140. J. S. Becker, E. Kim, R. G. Gordon, *Chemistry Of Materials* **16**, 3497-3501 (2004).

141. O. van der Straten, Y. Zhu, K. Dunn, E. T. Eisenbraun, A. E. Kaloyeros, *Journal of Materials Research* **19**, 447-453 (2004).

142. S. Morishita, S. Sugahara, M. Matsumura, *Applied Surface Science* **112**, 198-204 (1997).

143. H. Wojcik, M. Friedemann, F. Feustelt, M. Albert, S. Ohsiekt, J. Metzgert, J. Voss, J. W. Bartha, C. Wenze, In *A comparative study of thermal and plasma enhanced ALD Ta-N-C films on SiO2, SiCOH and Cu substrates, International Interconnect Technology Conference, IEEE 2007*, 19-21 (2007).

144. P. A. Williams, In *Atomic Layer Deposition, SAFC Hitech Global R&D Conference*, UK, (2009).

145. M. Ritala, J. Niinistö, *Atomic Layer Deposition*. In *Chemical Vapour Deposition: Precursors, Processes and Applications*, A. C. Jones, M. L. Hitchman, Eds. Royal Society of Chemistry: Cambridge, p 164 (2009).

146. M. Putkonen, L. Niinistö, *Organometallic Precursors for Atomic Layer Deposition*. In *Precursor Chemistry of Advanced Materials*, R. Fischer, Ed. Springer Berlin / Heidelberg: Vol. 9 pp 125-145 (2005).

147. M. Leskela, M. Ritala, *Journal De Physique Iv* **9**, 837-852 (1999).

148. M. Leskelä, M. Ritala, *Thin Solid Films* **409**, 138-146 (2002).

149. M. Leskela, M. Ritala, *Angewandte Chemie-International Edition* **42**, 5548-5554 (2003).

150. B. H. Lee, S. Cho, J. K. Hwang, S. H. Kim, M. M. Sung, *Thin Solid Films* **518**, 6432-6436 (2010).

151. H. Kim, C. Lavoie, M. Copel, V. Narayanan, D. G. Park, S. M. Rossnagel, *Journal of Applied Physics* **95**, 5848-5855 (2004).

152. K. Kukli, M. Ritala, M. Leskelä, *Chemical Vapor Deposition* **6**, 297-302 (2000).

153. S. K. Kim, C. S. Hwang, S. H. K. Park, S. J. Yun, *Thin Solid Films* **478**, 103-108 (2005).

154. P. C. Rowlette, C. G. Allen, O. B. Bromley, A. E. Dubetz, C. A. Wolden, *Chemical Vapor Deposition* **15**, 15-20 (2009).

155. J. Niinistö, N. Petrova, M. Putkonen, L. Niinistö, K. Arstila, T. Sajavaara, *Journal of Crystal Growth* **285**, 191-200 (2005).

156. R. J. Potter, P. R. Chalker, T. D. Manning, H. C. Aspinall, Y. F. Loo, A. C. Jones, L. M. Smith, G. W. Critchlow, M. Schumacher, *Chemical Vapor Deposition* **11**, 159-169 (2005).

157. H. Kim, A. J. Kellock, S. M. Rossnagel, *Journal of Applied Physics* **92**, 7080-7085 (2002).

158. K. C. Kim, T. J. Anderson, *Advanced Metallization Conference 2005* 451-455 (2006).

159. W. Jeong, Y. Ko, S. Bang, S. Lee, H. Jeon, *Journal of the Korean Physical Society* **56**, 905-910 (2010).

160. B. B. Burton, A. R. Lavoie, S. M. George, *Journal of The Electrochemical Society* **155**, D508-D516 (2008).

161. W. J. Maeng, S. J. Park, H. Kim, *Journal of Vacuum Science & Technology B* **24**, 2276-2281 (2006).

162. Y. Du, S. M. George, *Journal of Physical Chemistry C* **111**, 8509-8517 (2007).

163. K. Kukli, M. Ritala, T. Pilvi, T. Sajavaara, M. Leskelä, A. C. Jones, H. C. Aspinall, D. C. Gilmer, P. J. Tobin, *Chemistry of Materials* **16**, 5162-5168 (2004).

164. M. Ritala, *Applied Surface Science* **112**, 223-230 (1997).

165. J. R. Wank, S. M. George, A. W. Weimer, *Journal of the American Ceramic Society* **87**, 762-765 (2004).

166. P. D. Rouffignac, J. S. Park, R. G. Gordon, *Chemistry of Materials* **17**, 4808-4814 (2005).

167. E. Granneman, P. Fischer, D. Pierreux, H. Terhorst, P. Zagwijn, *Surface & Coatings Technology* **201**, 8899-8907 (2007).

168. M. K. Wiedmann, M. C. Karunarathne, R. J. Baird, C. H. Winter, *Chemistry of Materials* **22**, 4400-4405 (2010).

169. D. R. Lide, *CRC Handbook of Chemistry and Physics*. CRC Press: New York, p 4-64 (2009).

170. Y. Xu, C. B. Musgrave, *Chemical Physics Letters* **407**, 272-275 (2005).

171. Trimethylaluminium - SAFC Hi-tech. http://www.safcglobal.com/etc/medialib/docs/Sigma-Aldrich/General_Information/safc-hitech-trimethylaluminiumforald.Par.0001.File.tmp/safc-hitech-trimethylaluminiumforald.pdf (accessed 2010).

172. M. Ritala, M. Leskela, *Applied Surface Science* **75**, 333-340 (1994).

173. J. J. Ganem, I. Trimaille, I. C. Vickridge, D. Blin, F. Martin, *Nuclear Instruments and Methods in Physics Research Section B: Beam Interactions with Materials and Atoms* **219-220**, 856-861 (2004).

174. S. A. Rushworth, L. M. Smith, A. J. Kingsley, R. Odedra, R. Nickson, P. Hughes, *Microelectronics Reliability* **45**, 1000-1002 (2005).

175. H. H. Horowitz, G. Metzger, *Analytical Chemistry* **35**, 1464-& (1963).

176. K. Gregorczyk, L. Henn-Lecordier, J. Gatineau, C. Dussarrat, G. Rubloff, *Chemistry of Materials* **23**, 2650-2656 (2011).

177. Y. Xu, C. B. Musgrave, *Surface Science* **591**, L280-L285 (2005).

178. D. I. Bazhanov, A. A. Safonov, A. A. Bagatur'yants, A. A. Korkin, *The structure and electronic properties of Zr and Hf nitrides and oxynitrides*. In *Micro- and Nanoelectronics 2003*, K. A. Valiev, A. A. Orlikovsky, Eds. Spie-Int Soc Optical Engineering: Bellingham, Vol. 5401 pp 418-425 (2004).

179. H. Nakagawa, A. Ohta, F. Takeno, S. Nagamachi, H. Murakami, S. Higashi, S. Miyazaki, *Japanese Journal Of Applied Physics Part 1-Regular Papers Short Notes & Review Papers* **43**, 7890-7894 (2004).

180. J. D. Kwon, J. Yun, S. W. Kang, *Japanese Journal of Applied Physics* **48**, 025504 (2009).

181. M. Ritala, P. Kalsi, D. Riihela, K. Kukli, M. Leskela, J. Jokinen, *Chemistry of Materials* **11**, 1712-1718 (1999).

182. D. J. Cardin, M. F. Lappert, C. L. Raston, *Chemistry of Organo-Zirconium and-Hafnium Compounds*. Ellis Horwood Limited: West Sussex, The U.K., (1986).

183. Y. Y. Wu, A. Kohn, M. Eizenberg, *Journal of Applied Physics* **95**, 6167-6174 (2004).

184. N. J. Bae, K. I. Na, H. I. Cho, K. Y. Park, E. Boo, J. H. Bae, J. H. Lee, *Japanese Journal Of Applied Physics Part 1-Regular Papers Short Notes & Review Papers* **45**, 9072-9074 (2006).

185. B. H. Weiller, *Journal of the American Chemical Society* **118**, 4975-4983 (1996).

186. D. M. Hoffman, *Polyhedron* **13**, 1169-1179 (1994).

187. J. W. Elam, M. Schuisky, J. D. Ferguson, S. M. George, *Thin Solid Films* **436**, 145-156 (2003).

188. L. Hiltunen, M. Leskelä, M. Mäkelä, L. Niinistö, E. Nykänen, P. Soininen, *Thin Solid Films* **166**, 149-154 (1988).

189. K. H. Kim, R. G. Gordon, A. Ritenour, D. A. Antoniadis, *Applied Physics Letters* **90**, 212104 (2007).

190. J. S. Becker, R. G. Gordon, *Applied Physics Letters* **82**, 2239-2241 (2003).

191. D. K. Gaskill, N. Bottka, M. C. Lin, *Journal of Crystal Growth* **77**, 418-423 (1986).

192. K. Hieber, *Thin Solid Films* **24**, 157-164 (1974).

193. H. Kim, C. Detavenier, O. van der Straten, S. M. Rossnagel, A. J. Kellock, D. G. Park, *Journal of Applied Physics* **98**, 014308 (2005).

194. K. E. Elers, J. Winkler, K. Weeks, S. Marcus, *Journal of The Electrochemical Society* **152**, G589-G593 (2005).

195. E. J. Kim, D. H. Kim, *Electrochemical And Solid State Letters* **9**, C123-C125 (2006).

196. J. S. Park, H. S. Park, B. D. Kang, *Journal of The Electrochemical Society* **149**, C28-C32 (2002).

197. P. Caubet, T. Blomberg, R. Benaboud, C. Wyon, E. Blanquet, J. P. Gonchond, M. Juhel, P. Bouvet, M. Gros-Jean, J. Michailos, C. Richard, B. Iteprat, *Journal of The Electrochemical Society* **155**, H625-H632 (2008).

198. J. Musschoot, Q. Xie, D. Deduytsche, S. Van den Berghe, R. L. Van Meirhaeghe, C. Detavernier, *Microelectronic Engineering* **86**, 72-77 (2009).

199. H. S. Sim, S.-I. Kim, H. Jeon, Y. T. Kim, *Japanese Journal of Applied Physics* **42**, 6359-6362 (2003).

200. M. Bosund, T. Sajavaara, M. Laitinen, T. Huhtio, M. Putkonen, V. M. Airaksinen, H. Lipsanen, *Applied Surface Science* **257**, 7827-7830 (2011).

201. J. Y. Kim, D. Y. Kim, H. O. Park, H. Jeon, *Journal of the Korean Physical Society* **45**, 1639-1643 (2004).

202. S. P. Krumdieck, *CVD reactors and delivery system tehnology*. In *Chemical Vapour Deposition: Precursors, Processes and Applications*, A. C. Jones, M. L. Hitchman, Eds. Royal Society of Chemistry: Cambridge, p 37 (2009).

203. R. Bankras, J. Holleman, J. Schmitz, M. Sturm, A. Zinine, H. Wormeester, B. Poelsema, *Chemical Vapor Deposition* **12**, 275-279 (2006).

204. J. S. Jur, G. N. Parsons, *Acs Applied Materials & Interfaces* **3**, 299-308 (2011).

205. W. Glime, T. Seidel, *Semiconductor International* **28**, 76-82 (2005).

Chapter 3. Experimental methods

3.1 Introduction

This chapter describes experimental methods used in this project. The ALD deposition was carried out using Oxford Instruments reactors. Film thickness was routinely measured by ellipsometry, the results were validated by weight gain measurements. A Quartz Crystal Microbalance (QCM) has been used to in-situ monitor the mass gain on the crystal surface during ALD deposition. Mass spectrometry has been used to monitor the gas phase composition for molecular and plasma ammonia. Various microscopes including Scanning Electron Microscope (SEM), Transmission Electron Microscope (TEM), Auger Electron Microscope (AES) and Atomic Force Microscope (AFM) have been employed to ascertain film thickness, microstructure, chemical composition and morphology. Medium Energy Ion scattering (MEIS) has been used to quantitatively depth profile chemical composition of the films. MEIS measures the number of atoms per unit area and by combining this information with thickness measurements, film densities were estimated. Film microstructure was investigated using X-Ray Diffraction (XRD), and electrical resistivity was measured by a four point probe.

3.2 Atomic Layer Deposition

Three Oxford Instruments reactors were used for ALD processes, they are OpAL® thermal, OpAL® plasma, and FlexAL® plasma reactors. They are state-of-the-art instruments combining new and established technology intended for research applications. Since these reactors share identical features including the chamber, the

precursor delivery manifold, and the substrate holder, this section mainly describes the experimental setup of the OpAL thermal reactor. Subsequently, the differences in the plasma reactors are introduced. Two OpAL reactors are based at the University of Liverpool, while the FlexAL reactor is based at Oxford Instruments Bristol factory.

Oil back-streaming problem - The OpAL thermal reactor was used as the core instrument to implement nitride thin film processes using thermal ALD. During the first year of this project in 2007, the reactor was supplied by Oxford Instruments with an Alcatel 2063 S/E rotary vane pump using Anderol 555 oil (ISO VG 100) as the lubricant. This is diester based oil and contains oxygen species. The pump was found to have a faulty non-return valve, which means that the pump gives a great degree of oil back-streaming. Although some protection methods were employed such as zeolite and liquid nitrogen traps, oil residuals were inevitably found inside the chamber. Films deposited using this setup with tetrakis(diemethylamino)hafnium and ammonia were found be composed of hafnium and oxygen with non-detectable nitrogen. The oxygen contamination was largely attributed to the oil back-streaming problem. Oxygen rich species in the oil can thermally breakdown and contaminate the films. In the light of this problem, the rotary pump was replaced by Oxford Instruments in early 2009 with an Adixen A103P dry pump. All gas pipes, MFCs, valves, and chamber components have been either replaced or decontaminated.

3.2.1 OpAL thermal reactor

OpAL is an open-load reactor designed for research scale ALD deposition. In outline, it is composed of two bubbling precursor lines, two vapour draw precursor lines, an eight inch substrate holder, and a perpendicular flow chamber equipped with a

showerhead plate. This is schematically illustrated in Figure 3.1 and a picture of the OpAL reactor based at the University of Liverpool is shown in Figure 3.2.

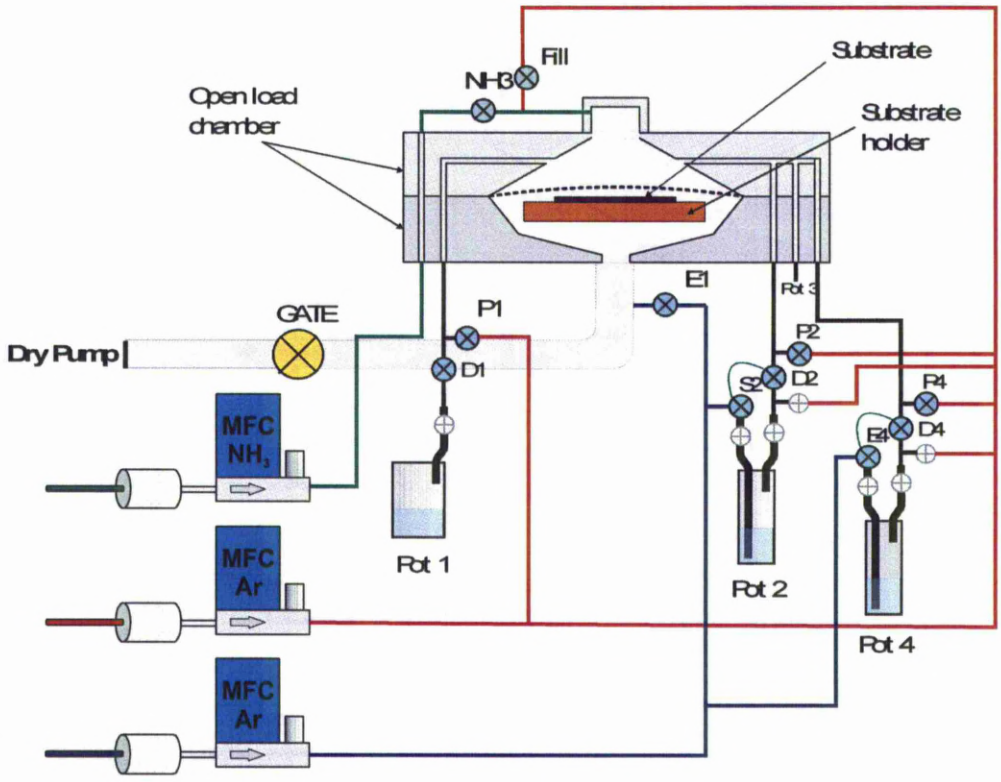

Figure 3.1 A schematic illustration of OpAL thermal reactor, pot 3 is a vapour draw pot that can be considered as the same as pot 1.

Figure 3.2 A picture of the OpAL thermal reactor based at the University of Liverpool.

The reactor was evacuated using an Adixen A103P dry pump, which achieves a base pressure of 4 mTorr. As mentioned in Chapter 2, it is essential to minimise oxygen containing species for nitride deposition. Since the reactor is an open-load system that vents to atmosphere for sample loading, a nitrogen glove box was employed to protect the chamber (Figure 3.2). Dry nitrogen was supplied to the glove box with a flow rate of 6 cm^3/min during the sample loading and un-loading. Silica gel (Fisher scientific) was used as a desiccant inside the glove box and the moisture level was monitored by a relative humidity sensor (Testo 608-H1), a reading as low as 3% was not exceeded.

Although a nitrogen glove box was used, there is still a level of oxygen, water and carbon dioxide in presence. Once the chamber is vented, these species absorb on the chamber walls and they should be removed prior to deposition. This can be done by pumping, or more effectively pumping and purging. A purge refers to an inert gas flow, which helps remove residual molecules in the gas phase and on surfaces. In the current study, the chamber was cycled through an hour long pump-purge sequence (1min pump/1min purge with 250sccm Ar) prior to each deposition to de-gas the chamber. The chamber walls were heated above 100°C to accelerate the desorption process. The chamber leak-up rate, as described in section 2.3.4.2, was regularly checked and a reading of 1 mTorr/min was not exceeded.

The OpAL reactor has three gas lines (Figure 3.1). They were used for precursor dosing (blue), precursor purging (red) and ammonia (green) respectively. Argon (BOC 99.998%) was used for both dosing and purging. Ammonia (Air products, electronic grade) was used as a nitrogen containing co-reactant. Each line has a dedicated MFC (Mass Flow Controller) with the maximum flow rate of 500sccm for the argon lines, and 20sccm for the ammonia line. To minimise oxygen containing

species in these gases, gas purifiers were used on the ammonia (Entegris Gatekeeper CE35KFSK4R) and argon (Entegris Gatekeeper CE35KFI4R) lines. These purifiers are specified to achieve an outflow with H_2O and O_2 levels below 1 ppb.

Precursor and co-reactant doses were controlled using the methods described in Chapter 2. As a gas co-reactant, ammonia was dosed by varying the pulse length with a fixed flow rate (10sccm) as maintained by the MFC. Highly volatile co-reactants such as water and hydrazine were held in a bubbler at room temperature and delivered using vapour draw (pot 1, 3 in Figure 3.1). A high speed ALD valve (Swagelok) was used to achieve accurate dosing, the valve operation time (opening and closing) is 5ms as specified by Swagelok.

Metal precursors were delivered using bubbling due to their relatively low volatility (pot 2, 4 in Figure 3.1). All metal precursors used in this project require heating and this was applied by a heat jacket that wraps the precursor bubbler. Each heat jacket was embedded with resistance coils and a thermo couple. To avoid condensation of the precursor vapour during transport, the delivery manifold between the precursor bubbler and the chamber was also heated with heat jackets. The temperature profile along the heated manifold (100°C) was checked by a handheld thermocouple (RS 1319A), which confirms that there are no cold and hot spots along the delivery line. The reactor chamber is also a part of the delivery pathway (Figure 3.1) and the chamber walls were heated to between 100 and 150°C according to the type of precursor used. The transport temperature for each precursor is specified by the precursor supplier (SAFC-Hitech) and the details are summarised in the each results chapter. The precursor dose was controlled by the bubbling time with a fixed flow rate of 150sccm Ar as advised by Oxford Instruments. It should be noted that in ALD,

the control of flow homogeneity is not required when the deposition is within the self-limiting region as emphasized in Chapter 2.

Step	Control method	Time
Dose Precursor	150sccm Ar → S2 & D2 50sccm Ar → Fill	3s
Purge	200sccm Ar → P2 & Fill	5s
Dose ammonia	10sccm ammonia → NH_3 valve 190sccm Ar → Fill	3s
Purge ammonia	200sccm Ar → Fill	5s
Stabilise flow	150sccm Ar → E1 50sccm Ar → Fill	3s

Table 3.1 A typical ALD cycle when using OpAL thermal reactor.

A typical ALD recipe for nitride deposition is presented in table 3.1, the deposition recipe for each material will be summarized in the result chapters. Firstly, the precursor was dosed using an Ar flow (150 sccm) through S2 and D2 vavles (Figure 3.1). A simultaneous purge (50 sccm) via the Fill valve was used to ensure that the injected precursor is not trapped within the top part of the chamber. The precursor purge was carried out using an argon flow (200sccm) through P2 and Fill valves. The ammonia was then dosed (10 sccm) as a nitrogen containing co-reactant. The ammonia purge (200sccm) was delivered via the Fill valve. Finally, the dosing argon (150sccm) was diverted to the pump via E1 to prepare the MFC for the precursor dosing in the next cycle.

The OpAL reactor is equipped with an 8 inch substrate holder, which can be heated up to 400°C. In order to confirm the heating uniformity, a handheld thermo couple (RS 1319A) was used to measure temperatures across the substrate holder and nearly identical readings have been obtained (Figure 3.3).

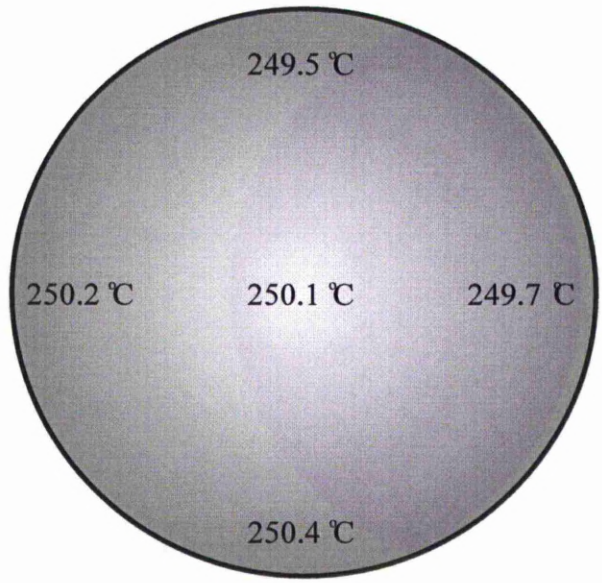

Figure 3.3 Temperature readings across the substrate holder when heated at 250°C.

3.2.2 Plasma reactors

Plasma enhanced (PE) ALD was carried out using either OpAL plasma or FlexAL plasma reactors. They share an identical chamber and manifold design to the OpAL thermal reactor; however, there are differences and the details are summarised in table 3.2. The major difference of the plasma tools is an inductively coupled plasma unit, which is fitted upstream of the substrate holder to allow remote PE ALD (Figure 3.4).

	OpAL thermal	**OpAL plasma**	**FlexAL plasma**
Loading method	Open load	Open load	Separated load chamber
Pump	Dry pump	Dry pump	Turbo pump
Ultimate pressure	4 mTorr	6.7 mTorr	1.35e-3 mTorr
Plasma power	N.A.	Up to 300W	Up to 400W

Table 3.2 Loading method, ultimate pressure and plasma power for the OpAL thermal, OpAL plasma and FlexAL plasma reactors.

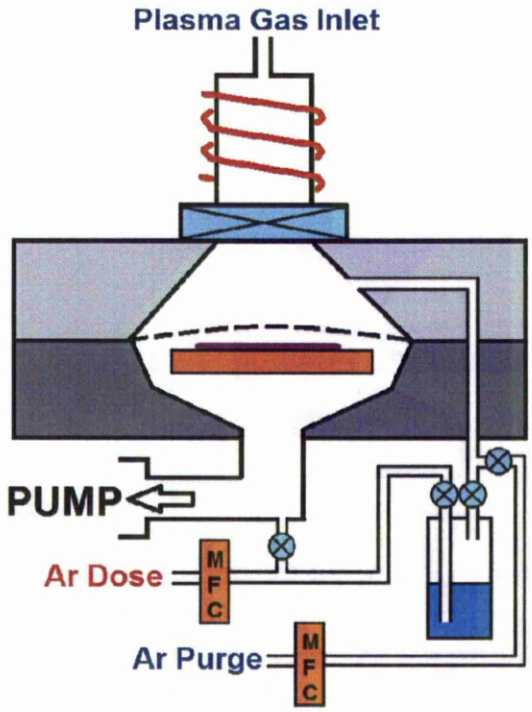

Figure 3.4 A schematic of remote inductively coupled plasma for the OpAL plasma and FlexAL plasma reactors.

The working principle of an inductively coupled plasma (ICP) is very similar to induction heating. In this process, a conductive medium is wrapped by a coil. Radio frequency (RF) power is applied through the coil and generates an oscillating magnetic field. Due to electromagnetic induction, eddy currents are generated within the conductive medium and give rise to high temperatures. In an ICP, the process is similar except that the medium is a gas, the ICP can generate temperatures as high as several thousand degree Kelvin, resulting in the fourth state of matter, plasma.[1] Since gases are not conductive in their natural states, some means of plasma ignition are necessary to provide initial electrons and ions that couple with the magnetic field. Once ignited, the RF power maintains plasma discharge and provides reactive species including both ions and radicals.

During deposition, however, radicals are preferred to ions because ion bombardments etch the sample surface and result in poor roughness of the films.[2] Remote plasma enhanced ALD was developed to solve this problem, in Oxford Instruments plasma reactors, the plasma unit is fitted ~40cm above of the substrate holder. This can minimise the ion density but still maintain a good radical density that is needed for deposition.[3] According to Oxford Instruments, sub-nanometre surface roughness can be achieved when using remote PE ALD. During deposition processes, the metal precursor should not enter the plasma chamber because the high energy plasma power decomposes the precursor and ruins the self-limiting behaviour. To avoid this, a gate valve was used between the plasma and reaction chambers, this can be closed prior to the precursor dosing. Alternatively, a continuous Ar purge can be used from the plasma unit to force a down stream flow so that no metal precursor enters the plasma chamber.

3.2.3 Substrates

The substrate for each deposition was consistently placed at the middle of the substrate holder held in position by glass slides. Three types of substrates including doped silicon, soda lime glass and glassy carbon were used to accommodate different characterisation techniques. 100mm diameter silicon(100) substrates (Compart Technology Ltd. Virgin test grade) were routinely used because silicon has a well defined crystal structure, optical property and surface smoothness. These properties facilitate the chemical composition analysis using MEIS and thickness measurements using ellipsometry, both of which will be discussed below. Silicon is prone to surface oxidation when exposed to air and the wafers were used as-supplied hence with ~20Å of native SiO_2 on the surface. The silicon substrates were heavily doped (either p or n

type) and therefore, they are not suitable for electrical resistivity measurements when depositing conductive films. To accommodate this, Soda lime glass microscope slides measuring 75 × 25 mm were used as the substrates. These were cleaned in an ultrasonic bath using de-ionised water, rinsed with isopropyl alcohol and then dried. Glassy carbon substrates were used to accommodate the Energy Dispersive X-ray (EDX) analysis. EDX was used to qualitatively estimate film composition in this study. Unfortunately, depth profiling is difficult in EDX analysis, meaning that the same element within the film and the substrate is difficult to differentiate. This raises a problem for silicon substrates when investigating silicon incorporation in the film and to solve the problem, glassy carbon substrates (HTW SIGRADUR G) were used when necessary.

3.3. Film characterisation techniques

3.3.1 Ellipsometry

3.3.1.1 Background

Ellipsometry was routinely used in this work as a thickness measurement tool. An ellipsometer detects the change in polarization of incident light after reflection from a surface, and subsequently calculates the film properties including thickness and refractive index. Ellipsometry is an optical technique, offering non-contact, non-destructive measurements and has been widely used in both research and industry.

Light can be described as an electromagnetic wave, and polarization describes the waves' electric field behaviour in space and time. The electric field of a wave is always perpendicular to the direction of propagation. If the field orientation changes

randomly during propagation, the light is unpolarized; if the field orientation is predictable during the course of travel, the light is said to be polarized. Polarized light can be described using x and y components along its propagation direction z (Figure 3.5). There are three types of polarizations including linear, circular and elliptical polarizations. When the two waves on x and y planes have the same amplitude and are in-phase, the light is linearly polarized (Figure 3.5a). When the waves have the same amplitude but are 90^{o} out-of-phase, the light is circularly polarized (Figure 3.5b). When the waves have arbitrary amplitude and phase, the light is elliptically polarized (Figure 3.5c).

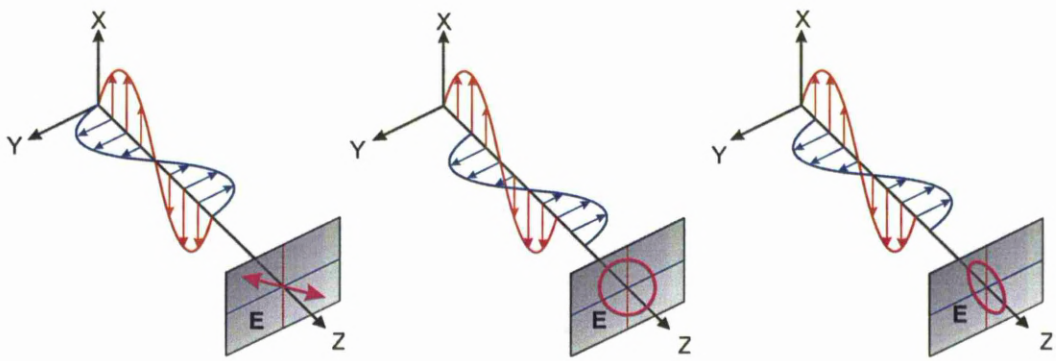

(a) (b) (c)

Figure 3.5 Orthogonal waves demonstrating (a) linear polarisation, (b) circular polarisation, and (c) elliptical polarisation

Light will both reflect and transmit when striking a substrate surface (Figure 3.6). The plane that consists of the incident and reflected beam is defined as the plane of incidence (POI). In a typical ellipsometry measurement, the light source is linearly polarized and is described by its p- component (parallel to POI) and s- component (perpendicular to POI). Each component changes its polarization individually upon reflection, the amount of reflected light, R_p and R_s, can be predicted using Fresnel

equations.[4] The ellipsometer measures the amplitude change (Ψ) and the phase shift (Δ) to determine the ratio of R_p to R_s, this ratio is defined as the complex reflectance ratio and the relation is written as,

$$\rho = \tan(\Psi)\, e^{i\Delta} = R_p/R_s = f(\Theta_I, N_0, N_S) \qquad \text{(Eq. 3.1)}$$

Where Θ_I is the incident angle, N_0 is the ambient refractive index, N_s is the substrate refractive index. In most cases the incidence angle would have been determined prior to the measurement and therefore, N_S can be analytically calculated when Ψ and Δ are measured.

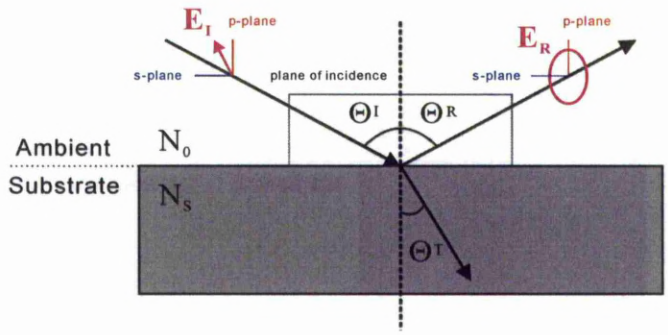

Figure 3.6 The reflection of a linear polarized light on a substrate.

However, in the case of a transparent film on a substrate (Figure 3.7) reflections occur at both top and bottom interfaces of the film, the polarization of reflected light is then determined by the superposition of multiple waves. The R_p to R_s ratio is consequently dependent on properties of the additional layer. The relation is complicated and further explanation is beyond the scope of this study, however, the function can be written as,[5]

$$\rho = \tan(\Psi)\, e^{i\Delta} = R_p/R_s = f(\Theta_I, N_0, N_S, \lambda, N_F, L_F) \qquad \text{(Eq. 3.2)}$$

Where Θ_I is the incident angle, N_0 is the ambient refractive index, N_s is the substrate refractive index, λ is the light wavelength, N_F is the film refractive index, and L_F is the film thickness.

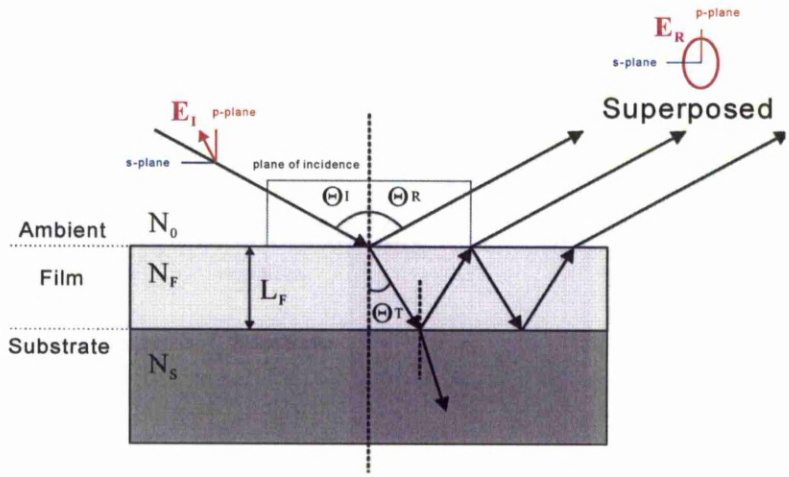

Figure 3.7 The reflection of a linear polarized light on a transparent film on a substrate.

A well designed experiment should allow accurate inputs of Θ_I, N_0, N_S and λ, however, there are two variables (L_F, N_F) and therefore, the equation cannot be solved analytically. Most commercial ellipsometers use a numerical approach and requires an estimation of either L_F or N_F prior to the solution. With some understanding of the film, ellipsometry can accurately determine the thickness and refractive index by measuring Ψ and Δ.

3.3.1.2 Rudolph research Auto EL IV

A Rudolph research Auto EL IV Ellipsometer was used throughout this project to measure film thickness and refractive index. The ellipsometer was operated at a wavelength of 632.8nm generated by a wavelength filter with a white light bulb. The incident angle was fixed at 70^o and a schematic of the ellipsometer is shown in Figure 3.8.

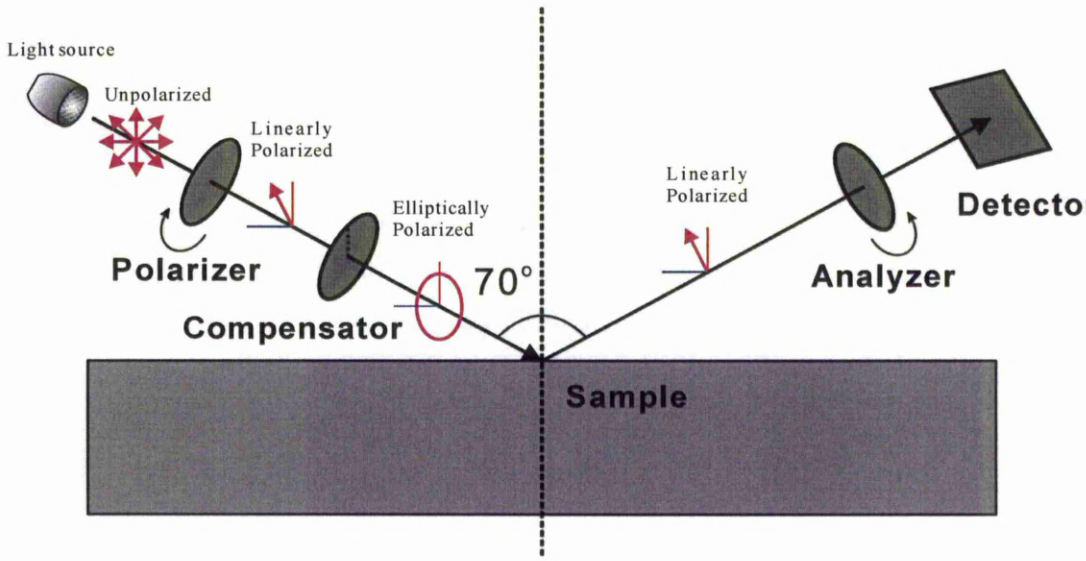

Figure 3.8 A schematic of Rudolph research Auto EL IV Ellipsometer.

The ellipsometer includes a light source, a rotatable polarizer, a compensator, a rotatable analyzer and a photo detector. The light travels along the route of Polarizer (P), Compensator (C), Sample (S) and Analyzer (A) and hence, the configuration is given the name of PCSA. Both the polarizer and analyzer are linear polarizers, which are used to either create or extinguish a linearly polarized beam. Ψ and Δ are correlated to the azimuth of polarizer and analyzer to the incidence plane. The working principle can be summarized as a 'nulling' process as is described below.

The unpolarized light travels through the rotatable polarizer and becomes linearly polarized. A compensator (usually a quarter wave plate) converts the linear polarization into elliptical polarization and previous reports have shown that all polarization states can be achieved after the compensator by rotating the polarizer.[5] The elliptically polarized light reflects off the sample surface and changes its polarization state. The aim is to establish linearly polarized light after reflection by rotating the polarizer. Subsequently this linearly polarized light is extinguished by

another rotatable linear polarizer in the analyzer, with the intensity monitored by a photo detector. The ellipsometer achieves this 'null' position by alternatively rotating the polarizer and analyzer until the intensity of the reflected beam is minimised. Ψ and Δ values are converted using simple linear equations from the azimuths of analyzer and polarizer respectively.

3.3.1.3 Data processing

The calculation of film thickness and refractive index from Ψ and Δ requires a model. In this study, a built-in model of the ellipsometer that describes a single transparent film on silicon was used, however, the deposition occurs on top of the native silicon dioxide and strictly speaking, the layer structure should be film/SiO_2/Si. The effect of the native oxide layer is small because it is very thin (~20Å). To verify this, an additional model written by Kondoh, also known as the ellipsheet was used.[6] This model is suitable for up to three layers on silicon. For the films with thicknesses of ~30nm, the ellipsheet gave nearly identical thickness and refractive index values to the built in model within the measurement tolerance, showing that the effect of the native oxide is small and can be safely neglected.

Ellipsometry was also used to estimate film uniformity. This was done by performing the measurement at ten points across a wafer area. The uniformity is related to the variation between measurements and is defined as,

$$\text{Uniformity} = (1 - \text{Standard deviation/Mean value}) \times 100\%. \qquad \text{(Eq. 3.3)}$$

Errors – The ellipsometer was calibrated on a daily basis and a reference sample of SiO_2 on Si (supplied by Entrepix Thickness 1178Å, R.I. 1.467) was regularly

measured to ensure the accuracy. Although the detection limit of Ψ and Δ were specified to 0.1° and 0.05° respectively by the manufacturer, the rotational mechanism degrades upon usage and an error analysis was performed. Figure 3.9 shows the histogram of Ψ and Δ obtained during ~100 measurements of the reference sample. In overall, both histograms show a Gaussian distribution and the error for Ψ and Δ is ±0.3° and ±0.15° respectively, within which counts lie 97% of the total measurements. The resulting thickness and refractive index variations of the reference sample are ±3Å and ±0.003 respectively. Although this is a very accurate measurement for the reference sample, the errors for thinner films were found to increase dramatically as investigated using the ellipsheet.

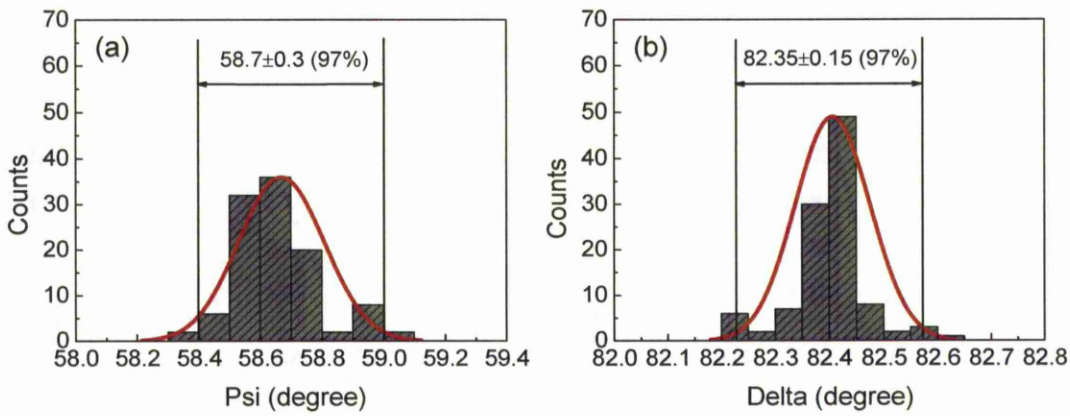

Figure 3.9 Histogram for (a) Psi and (b) Delta from 108 measurements of a SiO_2 reference sample.

Figure 3.10 shows the film thickness and refractive index as a function of Ψ and Δ calculated from the ellipsheet using the single layer model on silicon.[6] It can be seen that the thickness and refractive index values respond differently to Ψ and Δ according to the thickness range, meaning that the corresponding errors also differ according to the thickness range. Figure 3.11 shows the magnifications of Figure 3.10

for different thicknesses, the area inside the blue rectangle represents the error of Ψ and Δ. When the film is thicker than 300Å (Figure 3.11a), the typical error on thickness and refractive index falls within ±10Å and ±0.06 respectively. However, when the film is thinner than 200Å (Figure 3.11b), the error grows significantly for both parameters (thickness ±30Å, refractive index ±0.4). It is therefore, preferred to measure films thicker than 300Å and this principle was followed when depositing samples for thickness measurements. In addition to the uncertainty of Ψ and Δ, the ellipsometry measurements can also be affected by a rough surface or pinholes. These factors were considered minimal because SEM, TEM and AFM experiments have confirmed that they are rarely the case.

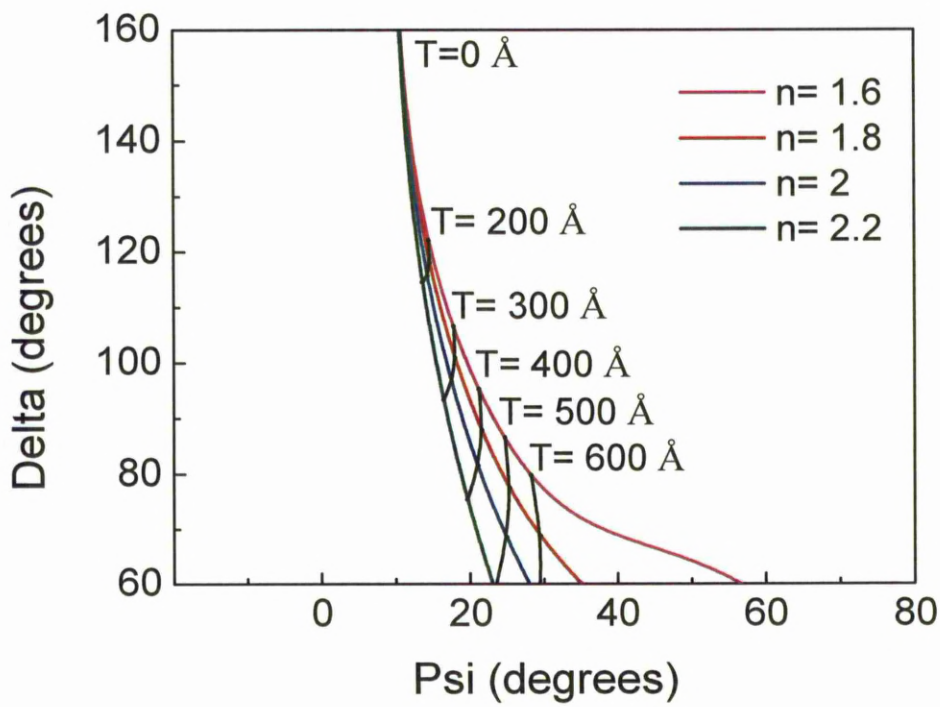

Figure 3.10 Film thickness (T) and refractive index (n) as a function of Ψ and Δ calculated using the ellipsheet.[6]

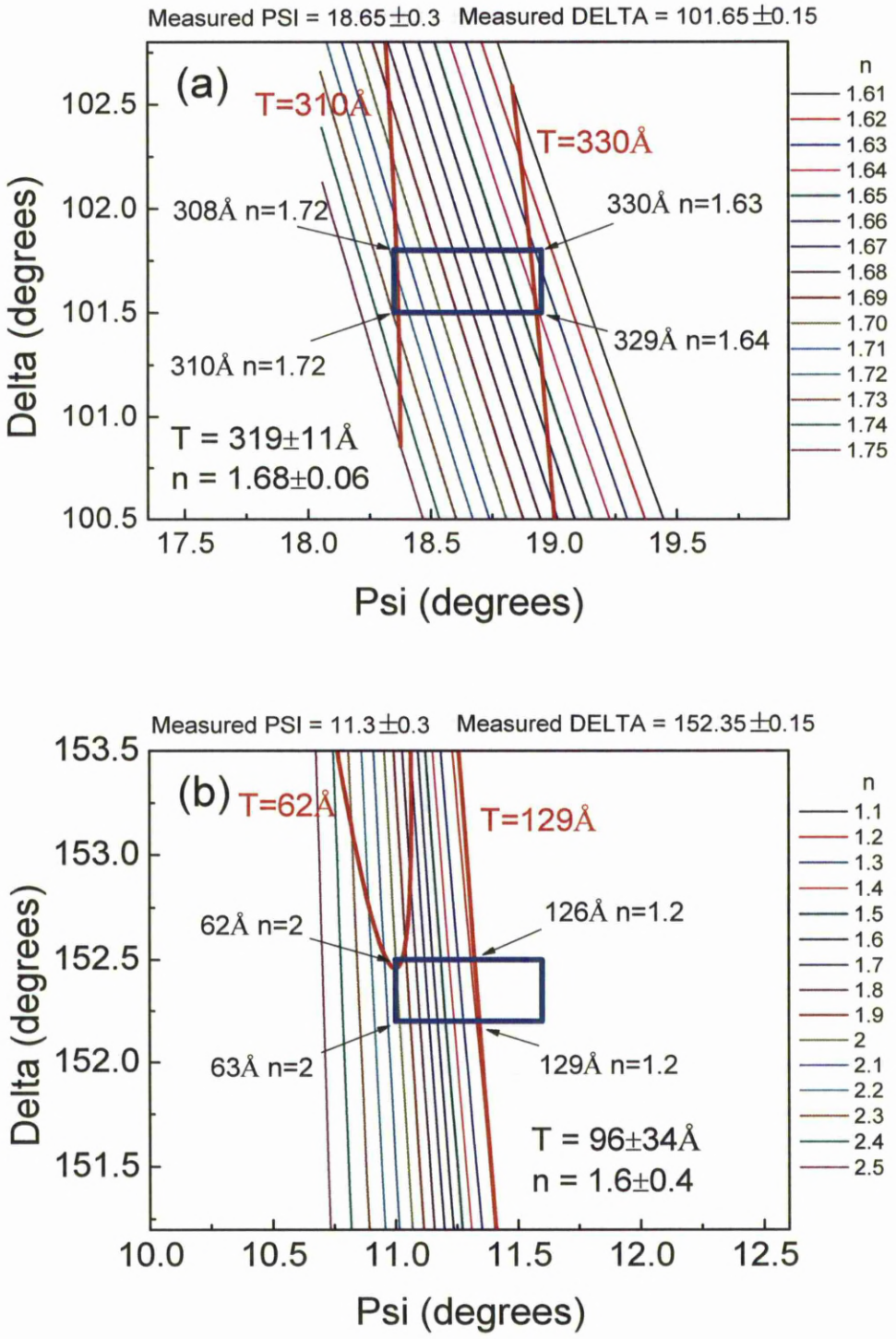

Figure 3.11 Film thickness (T) and refractive index (n) as a function of Ψ and Δ when the approximate film thickness is (a) ~30nm or (b) ~10nm. The area within the blue rectangle indicates the measurement error of Ψ and Δ.

The success of ellipsometry relies on an appropriate model, which means that the technique is an indirect measurement and the results validity should be assessed. This was done by comparing the thickness value obtained by ellipsometry with weight gain, SEM and TEM results. The electron microscopes are believed to be more reliable because they measure thickness as a function of magnification, which is a direct measurement. Selected samples were compared using electron microscopes and the results are summarized in Table 3.3. It can be seen that the ellipsometry thicknesses differ slightly to the SEM and TEM results; however, the variations are within 10% of the mean values. Thus, the thickness measured by ellipsometry was used throughout the thesis to calculate ALD growth rates and the error is estimated to be 10% when films are thicker than 30nm. When the film is thinner than this thickness, the error is calculated from the errors of Ψ and Δ.

Material	**Sample ID**	**Ellipsometry (nm)**	**SEM (nm)**	**TEM (nm)**
TaN	TaN49	30.2±1	28.5±3	
TaN	TaN51	32.5±1	28.0±3	
Ta_3N_5	TaN64	27.5±1	32.0±3	
Hf_3N_4	HfN01	25.8±1	26.5±3	
Hf_3N_4	HfN21	28.0±1		24.0±1
Hf_3N_4	HfN20	11.4±3		10.5±1
Hf_3N_4	HfN15	31.0±1		26.0±1
Hf_3N_4	HfN22	11.3±3		9.4±1
GdN	Run357	49.3±1	53.8±3	

Table 3.3 The thickness of selected samples measured by ellipsometry, SEM and TEM.

3.3.2 Weight gain

A Mettler Toledo XS205 analytical microbalance was used to measure the weight of the deposited film. This was done by measuring the weight of the substrate before and after each deposition. The weight gain is strong evidence of film deposition and the data can be used to extract the layer thickness. In the current work, the weight gain was used to ascertain the ellipsometry thickness measurements. The thickness can be calculated using the equation below,

$$T = \Delta M / A \times \rho \qquad \text{(Eq. 3.4)}$$

Where T is the layer thickness (cm), ΔM is the weight gain (g), A is the surface area for deposition (cm^2), and ρ is the film density (g/cm^3). To use this method, the film was assumed to be uniform and the film density was assumed to be constant.

For each measurement, the balance was reset and the sample was weighted 5 times. The highest and the lowest readings were abandoned and the average of the rest measurements was used to represent the sample weight. To ensure the best accuracy, a 50 mm diameter silicon wafer was employed as a reference sample, which was always weighed in addition to the sample of interest before and after deposition. The weight gain was calculated using,

$$\Delta M = (M_{r1} + M_{s1}) - (M_{r0} + M_{s0}) \qquad \text{(Eq. 3.5)}$$

Where M_{r0} and M_{r1} is the weight of the reference sample before and after deposition, M_{s0} and M_{s1} is the weight of the sample before and after deposition. This method should minimise the measurement shift of the analytical balance at different time.

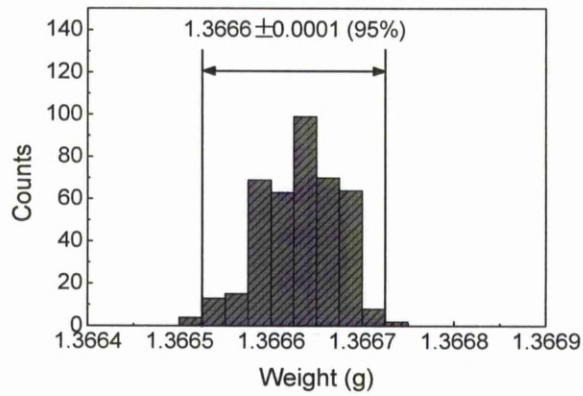

Figure 3.12 A histogram for the measured weigh of a reference sample.

Material	Sample ID	Ellipsometry (nm)	Weight gain (nm)
Ta_2O_5	TaO2	70.6±1	73.5±1.5
TaN	TaN48	30.2±1	25.5±3.5
TaN	TaN49	32.5±1	28.9±3.5
TaN	TaN50	35.2±1	34.9±3.5
TaN	TaN51	33.7±1	31.6±3.5
TaN	TaN52	33.0±1	36.1±3.5
TaN	TaN54	31.2±1	31.0±3.5
TaN	TaN55	30.4±1	30.5±3.5
TaN	TaN58	36.3±1	40.2±3.5
Ta_3N_5	TaN62	22.9±2	19.1±3.5
Ta_3N_5	TaN63	26.3±1	32.3±3.5
Ta_3N_5	TaN64	27.5±1	26.4±3.5
Ta_3N_5	TaN65	27.6±1	29.8±3.5
Ta_3N_5	TaN70	23.7±2	23.1±3.5
Ta_3N_5	TaN71	22.3±2	15.4±3.5

Table 3.4 Thickness obtained by the ellipsometer and the weight gain measurements.

The reference sample has been measured for ~400 times throughout the project and this generated a histogram, which can be used to determine the error of the analytical balance. From Figure 3.12, it is safe to quote that the error limit is ±0.0001g, in which lie the 95% of the total measurements. Given the substrate area and an approximate

density of deposited material, this means that the film thickness should be greater than 30nm to give weight gains greater than 0.001g, which then gives a reasonable signal to noise ratio. This appears to be matching the preferred film thickness for the ellipsometry measurement and most films were deposited with a thickness above 30nm. As mentioned before, the use of the weight gain was to validate the ellipsometry results and table 3.4 summarises the results obtained by both methods for selected samples. It can be seen that a good agreement can be found between two techniques and the ellipsometry data was used for the growth results presented in this work.

3.3.3 Quartz Crystal Microbalance (QCM)

A Quartz Crystal Microbalance (QCM) was used to monitor the mass gain or loss during the cyclic ALD processes. The technique was not only used to provide the mass gain information, but also to elucidate surface reaction mechanisms. QCM relies on the piezoelectric resonance effect. An AC voltage provokes the crystal to oscillate at a frequency that is related to the crystal mass per unit area. A thin film deposited onto the crystal surface can be considered as a part of the crystal, and leads to a frequency change as described by the Sauerbrey equation,

$$\Delta f = -2f_0^2/(\rho_c \times \mu_c)^{1/2} \times \Delta m \qquad \text{(Eq. 3.6)}$$

Where Δf is the change in frequency (Hz), Δm is the change in mass per unit area (g/cm^2), and C_f is the sensitive factor for the crystal used,

$$C_f = 2f_0^2/(\rho_c \times \mu_c)^{1/2} \qquad \text{(Eq. 3.7)}$$

Where f_0 is the natural resonant frequency of the crystal (Hz), ρ_c is the crystal density (g/cm^3), and μc is the crystal shear modulus ($g/cm\ s^2$).

In this study, QCM experiments were conducted using a Maxtex TM-400 thickness monitor with a custom built sensor head installed in the centre of the reactor. The frequency resolution of the monitor is 0.03Hz when operating at 6MHz, and is equivalent to a mass resolution of ~0.4 ng/cm^2. The sampling rate was 10 times per second. As a crystal, quartz is very sensitive to temperature and can only be used up to 250°C.[7] However, most deposition occurred at 300°C in this study and to accommodate this, a Y-11° cut $GaPO_4$ high temperature crystal (Tangidyne) operating at ~6MHz optimised for 0-460°C was installed in the sensor head. This crystal is hundreds of times less temperature sensitive compared to quartz.[7] The mass gain per area was derived using the Sauerbrey equation with a crystal density and sheer modulus of 3.57 g/cm^3 and 2.147 $g/cm\ s^2$ respectively for $GaPO_4$.[8]

Although the crystal manufacturer has stated that the $GaPO_4$ has low temperature sensitivity, the effect of temperature on the measurement was still investigated as a part of the calibration process. The effect of temperature was investigated by purging Ar (200sccm) at 300°C, which was the deposition temperature for in-situ monitoring. The purge flow was used to mimic the pressure during the deposition. Figure 3.13a compares the overall mass gain obtained from 50 TaN ALD cycles with the artificial mass gain driven by the temperature during the same time period. The artefact is less than 1% of the overall result and therefore, the effect of temperature was safely neglected. However, an abrupt pressure change was found to have a significant impact on the measurement. Figure 3.13b shows the artificial mass gain recorded for pump (30s) and purge (30s 200sccm Ar) sequences at 300°C, the pressures were 28 and

200 mTorr respectively. It can be seen that a sudden change in pressure affects the crystal frequency and leads to an inaccurate measurement. However the overall mass change remained close to zero. This is because sufficient rest time was given between each pressure change. Therefore, during the in-situ monitoring, the pressure was maintained constant when possible, however, in the cases of vapour draw where the pressure changes momentarily during dosing, a sufficient rest time (30s) was given to stabilize the crystal oscillation prior to the next step in the ALD recipe.

Having established the preferred monitoring conditions for QCM, the equipment was calibrated using one ALD deposition of TaN at 300°C (1000 cycles) with the mass gain monitored in-situ by the QCM. A silicon substrate was also used simultaneously and the mass gain of the wafer was measured ex-situ by a Mettler Toledo XS205 analytical microbalance. The analytical balance gives a mass gain of 0.00098±0.0001g, while the QCM gives 0.00102g, showing a good agreement between two techniques and confirming the measurement accuracy of the QCM.

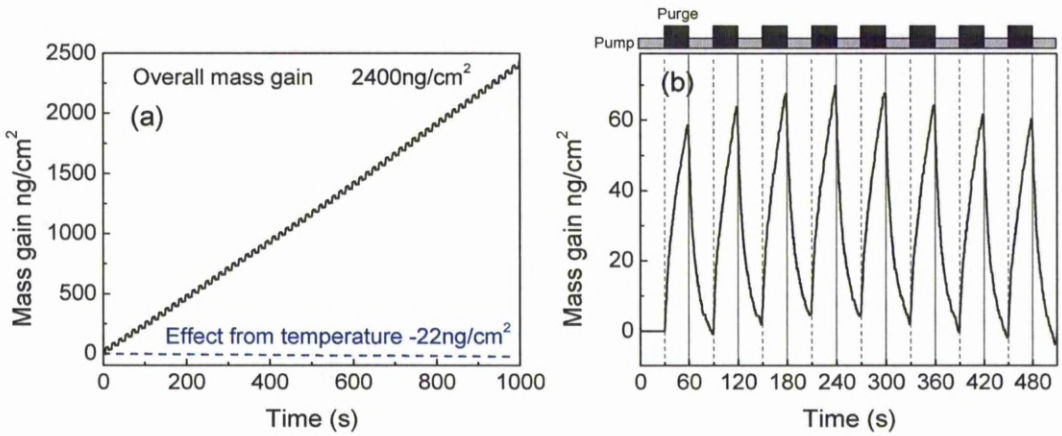

Figure 3.13 (a) Mass gain monitored by the QCM at 300°C for 50 TaN ALD cycles and for an Ar purge (200sccm) to investigate the effect from temperature; (b) Mass gain monitored during a pump (30s) and purge (30s, 200sccm Ar) sequence, the pressures were 28 and 200 mTorr respectively.

3.3.4 Mass spectrometry

Mass spectrometry was used to compare the gas phase composition between the molecular ammonia and plasma ammonia. The technique has provided an insight into the reactive species involved in PEALD. Mass spectrometer uses a filament to ionise the sampling species. The ions are subsequently separated by electromagnetic fields in an analyzer according to their mass to charge ratio (m/Q). Only the ions with the desired m/Q can pass the analyzer and these ions are counted by a detector.

Mass spectrometry experiments were conducted using a HPQ2 Residual Gas Analyzer (RGA) (MKS instruments). It was fitted on a separate chamber evacuated to 8×10^{-7} mbar using a turbo pump. A leak valve was used between the mass spectrometer chamber and the reaction chamber to provide sampling species. The sampling pressure was maintained at 1×10^{-5} mbar when flowing ammonia. The intensities for masses between 1 and 50 were measured and five scans (~2 min per scan) were recorded for each sampling condition.

3.3.5 Electron Microscopes

In this study, electron microscopes including SEM, TEM and AES were used to ascertain the film thickness, film morphology, microstructure and chemical composition. Electron microscopes rely on the signals generated when a high energy electron beam interacts with the sample, and these signals used in the current thesis are summarized in Figure 3.14.

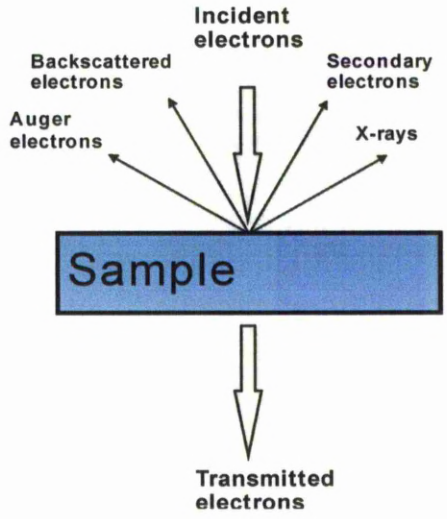

Figure 3.14 Signals that may be used in electron microscopes when a high-energy electron beam interacts with the sample.

3.3.5.1 Scanning Electron Microscope

SEM can be considered as an analogue of reflected light microscopes, but uses an electron beam with its short wavelength instead of light for imaging. SEM detects both secondary electrons and backscattered electrons, these are generated when a focused electron beam interacts with the sample surface. The interaction region generating secondary electrons is within a few nanometres of the surface and therefore, they can be used for imaging. SEM mainly detects secondary electrons and the yield at a given beam spot is recorded to represent the contrast for a pixel. When the beam scans over an area, the contrast information for each pixel is gathered and an image is subsequently formed.

A Jeol JSM-7001F field emission SEM was used to measure the thickness of selected samples and to investigate surface morphology. The experiment was conducted by Karl Dawson (University of Liverpool) using an acceleration voltage of 30kV, a beam current of ~250pA, and a working distance of ~7mm. The sample was cleaved and

mounted with the cross section parallel to the sample holder by conductive tapes. The sample holder is equipped with a goniometer to allow examinations under all orientations. An SEM picture for Ta_3N_5 on silicon is shown in Figure 3.15.

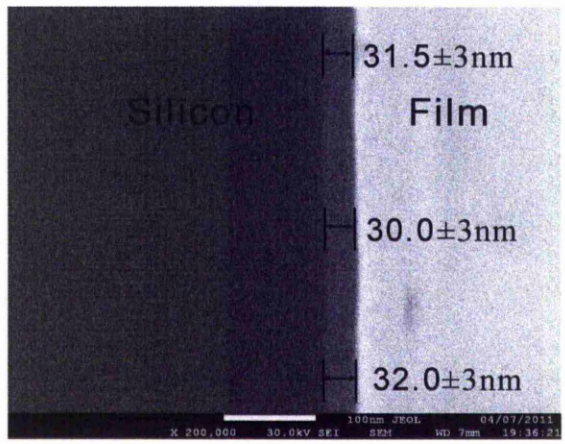

Figure 3.15 A SEM picture for a Ta_3N_5 film on silicon (TaN64).

3.3.5.2 Energy Dispersive X-ray (EDX) Analysis

X-rays are generated when a high energy electron beam interacts with the sample (Figure 3.14). The phenomenon is attributed to the interactions between an incident electron and the inner shell electrons of the target atom.[9] If an inner shell electron is knocked out by the incident electron, the atom is excited. This state is not stable and the atom will relax within a short period of time, if the atom relaxation is achieved by a jump of an outer shell electron into the inner shell vacancy, an elemental specific x-ray is emitted. This raises the possibility of composition analysis using the x-ray spectrum.

Energy dispersive x-ray (EDX) analysis is able to detect the x-ray spectrum and is often employed in SEMs or TEMs. It should be noted that the region of the material that generates x-rays is quite large, typically within a few micrometers of the

surface.[9] In the current study, this means that signals from the substrates were inevitably detected because all films deposited were thinner than 200nm. Depth profiling is also difficult within this thickness range. Therefore, EDX results were used to qualitatively determine the chemical composition.

A Jeol JSM-6610A SEM equipped with an Oxford Instrument Inca X-act model 51 EDX detector was used for the work reported in chapter 6. The X-rays were generated using an incident beam with an acceleration voltage of 30kV. The working distance of the EDX detector was ~10mm. The X-ray spectrum with the energy from 0 to 10eV was collected for two minutes. The elements to be detected are tantalum, gadolinium, silicon, oxygen, nitrogen and carbon. Table 3.4 summarizes the primary peaks of these elements, and fortunately, they do not overlap. The carbon feature in the EDX spectrum should be treated with care because the microscope uses rotary and diffusion pumps to achieve vacuum, which means that organic oil species would contribute to a background carbon signal.

	Ta	Gd	Si	O	N	C
Primary peak energy (keV)	L_{α} 8.146 $L_{\beta1}$ 9.343 $L_{\beta2}$ 9.652	L_{α} 6.057 $L_{\beta1}$ 6.713 $L_{\beta2}$ 7.103	K_{α} 1.740 $K_{\beta1}$ 1.829	K_{α} 0.525	K_{α} 0.392	K_{α} 0.277

Table 3.5 Primary X-ray emission energies for tantalum, gadolinium, silicon, oxygen, nitrogen and carbon.[10]

3.3.5.3 Other microscopes - TEM and AES

Selected films were examined using transition electron microscopy (TEM) to investigate the film thickness and microstructure. Cross section specimens were used for imaging, they were prepared conventionally by gluing two samples with the

surface of interest facing each other, the stack was sliced and mechanically polished to ~50 μm. A Gatan ion miller (model 691) was subsequently used to thin the cross-section specimen until transparent, Ar^+ beams with an energy of 5keV and an incident angle of 5° was used for ion milling. The TEM studies were conducted at the University of Liverpool by Robert Murray using a Jeol 2000 FX TEM operating with an acceleration voltage of 200kV. An example TEM picture for Hf_3N_4 on silicon is shown in Figure 3.16.

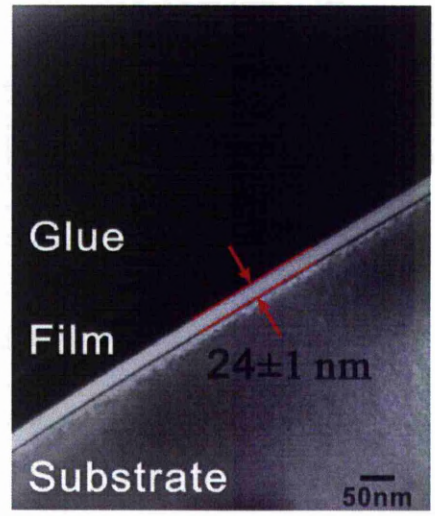

Figure 3.16 A TEM picture for Hf_3N_4 on silicon (HfN21 FX3067).

A few Auger Electron Spectroscope (AES) experiments were also carried out to depth profile chemical composition for thick films (>30nm), this was done to compensate the thickness limitation of MEIS analysis (20nm), which will be introduced below. AES experiments were conducted at Hangyang University (South Korea) by Prof. Hyeongtag Jeon using a PHI-680 AES with a 10keV electron beam. And a 2keV Ar^+ ion gun was employed in order to sputter the films with a sputter rate of 7.1nm per minute.

3.3.6 Atomic Force Microscopy (AFM)

Atomic force microscope (AFM) was used to assess the film topography. The technique was used to confirm that films deposited using ALD have a smooth surface (typically sub-nanometre roughness). Arithmetical mean roughness (Ra) was used to express the smoothness and is equal to the average of sample height deviations.

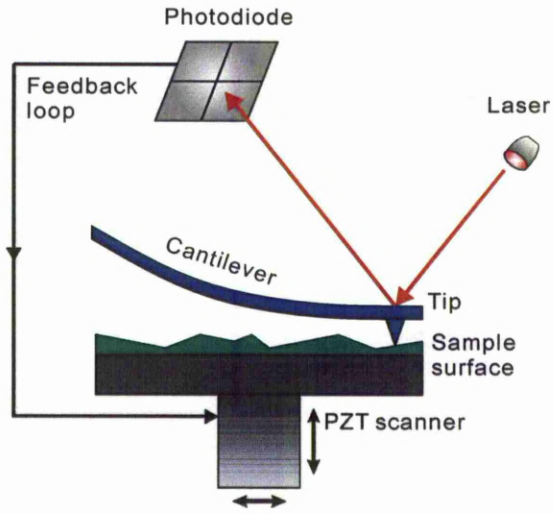

Figure 3.17 A schematic of AFM.

Compared to electronic microscopes, AFM offers sub-nanometre vertical resolution without sample preparation. It relies on the various forces between the probing tip and surface atoms. They may include interatomic, frictional, magnetic and electrostatic forces. Figure 3.17 shows a schematic of AFM operating in a 'contact mode'. A tip supported by a cantilever is used to probe the sample surface and its position is controlled by the voltages applied to three axis piezoelectric transducers (PZT) fitted at the sample holder. To image the topography, the tip is lowered to the surface and the cantilever bends against the sample, the degree of this bending is monitored by a photodiode that detects the position of a laser reflected from the tip. The AFM keeps

the laser beam in the middle of the photodiode by controlling the voltage applied to the PZT. The recorded voltage is converted to the sample height and the surface topography is viewed after the tip scans over a given area.

In this study a Nanoscope IIIa (Digital Instrument) AFM was used to measure the surface roughness of deposited films. Images were recorded in contact mode using a silicon nitride tip (Veeco nanoprobe NP-S20) with a scan frequency of 0.5Hz and over areas from 1 to 10 μm^2 (512 lines). The AFM was calibrated by Tim Joyce (University of Liverpool) using a reference sample (Veeco) and the surface roughness of silicon substrates was measured prior to the actual experiments. Figure 3.18 shows an AFM micrograph for a silicon substrate. This is a featureless picture and the surface roughness (Ra) was found to be 0.3nm. Although the single crystal silicon should be atomically flat, the measured roughness may be attributed to the vibrations during the measurement.

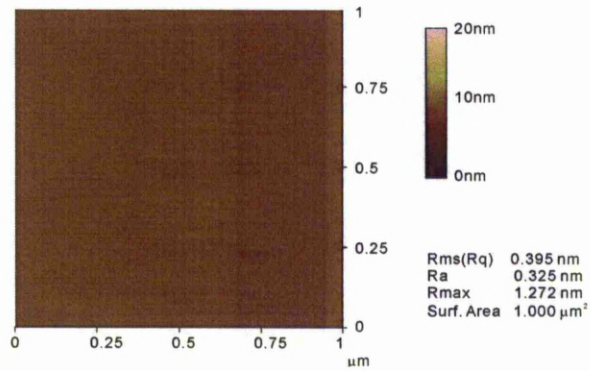

Figure 3.18 An AFM image for a silicon(100) substrate.

3.3.7 Medium Energy Ion Scattering (MEIS)

3.3.7.1 Background

Medium Energy Ion Scattering (MEIS) was used as the key technique to depth profile film chemical composition and to estimate film density when combined with thickness measurements (ellipsometry, SEM or TEM). The MEIS experiments were carried out at the Daresbury Laboratory of the Council of the Central Laboratory of the Research Councils (CCLRC).[11] MEIS is a modification from a more commonly known technique, Rutherford Backscattering Spectroscopy (RBS), but with much lower operation energy. The typical ion beam energy for MEIS is between 50 and 400 keV, compared with 1 to 2 MeV in RBS. This confinement favours a significant enhancement in depth and angle resolution with low damage to the sample.

Element detection - MEIS uses a mono-energetic, collimated H^+ or He^+ beam to collide atoms in the sample, the elastic collisions result in scattered ions with a spread of remaining energy and scattering angles. The energy after an elastic collision is described using a kinematic factor, K, and the overall relation is written as,[12]

$$K = \frac{E_1}{E_0}\left[\frac{(M_2^2 - M_1^2 \sin^2\theta)^{\frac{1}{2}} + M_1 \cos\theta}{M_2 + M_1}\right]^2 \qquad \text{(Eq. 3.8)}$$

Where E_0 is the incident bean energy, E_1 is the remaining beam energy after collision, M_1 is the atomic mass of an incident ion, M_2 is the atomic mass of a target atom, and θ is the scattering angle. By measuring the resulted energy at a fixed scattering angle, M_2 is calculated and the corresponding element can be determined.

Quantification - Quantitative analysis is achieved by measuring the scattering counts for a specific element, however, scattering cross sections should be taking into account because different elements have different scattering yields. The detailed calculation of scattering cross sections is complicated and is beyond the scope of this thesis. In MEIS, the scattering cross section is proportional to the square of the atomic number for each element.[12] During data interpretation, this is normalized to give a relative atomic ratio calculated using the equation below,

$$\frac{R_1}{R_2} = \frac{C_1}{C_2}\left(\frac{Z_2}{Z_1}\right)^2 \qquad \text{(Eq. 3.9)}$$

Where R, C and Z are the relative atomic fraction, scattering counts and the atomic number respectively, of elements 1 and 2.

Depth profile - Ions travelling within the sample are subject to interactions with electrons and atomic nuclei in the target, resulting in inelastic energy loss of the ion. The energy loss is related to the path length of the ion, and is commonly described by the stopping power (eV/Å). This allows MEIS to convert the lost energy into thickness and consequently determine the depth of elastically collided atoms. The estimation of stopping power requires knowledge of the target material and its density. Since it is difficult to estimate thin film densities, bulk material densities are generally used. This leads to an inaccurate converted thickness because most thin films densities are significantly lower than the bulk value. However, if the film thickness is measured by another technique (TEM, SEM or Ellipsometry), the process can be reversed to calculate the actual density using the equation below,[13]

$$Thickness_{MEIS} \times Density_{MEIS} = \frac{atoms}{cm^2} = Thickness_{Real} \times Density_{Real} \text{ (Eq. 3.10)}$$

3.3.7.2 Experimental procedure

The details of the MEIS facilities at Daresbury have been previously described by Werner[12] and Bailey,[14] this section only introduces the experimental procedure. Figure 3.19 shows a schematic of the MEIS experiment. A mono-energetic ion beam strikes atoms in the sample and results in scattered ions, whose energy is subsequently measured by a detector at a fixed angle. As indicated by Eq. 3.8, parameters including the ion mass, ion incident energy and scattering angle should be well defined for the experiment. MEIS facilities at Daresbury allows either H+ or He+ ions as the source and the incident energy may be tuned from 50 to 200 keV. These ions are significantly smaller than the target atoms, meaning that some ions may travel in the material without being scattered. This effect is mostly dominant when the ion beam is aligned with crystallographic planes in a single crystal material, resulting in smaller scattering counts compared to random orientations. These special alignments are called open channels. In the current work, MEIS relies on the crystallographic planes of the Si(100) substrate to accurately determine the scattering angle. The scattering angle is related to both beam-in and beam-out angles (θ_1, θ_2 in Figure 3.19). The beam-in angle is aligned by controlling the sample orientation relevant to the incident beam until the scattering count for silicon is minimised. Take the alignment to the Si {-1-11} for example, the beam was firstly aligned to Si {001} crystallographic plane, which is the perpendicular plane to the Si surface. The sample was then rotated 54.7° around the c-axis to make the beam roughly aligned to the Si {-1-11} plane. The final adjustments were made by fine tuning the orientation of the sample to the beam until the counts on the detector is minimised. The beam-out angle is determined by an angle sensitive detector, which collects counts over an angle range of 27° and the

direction with the minimum counts represents the open channel. This method accurately determines the scattering angle and minimises signals from the silicon substrate.

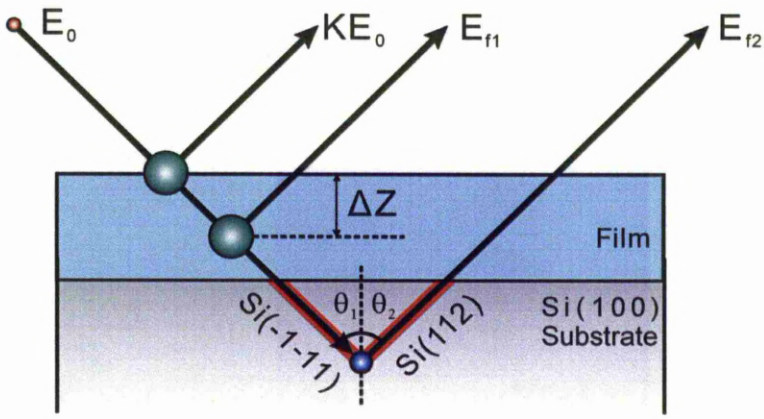

Figure 3.19 A schematic of the MEIS measurement, E_0 is the incident beam energy, K is the kinematic factor, E_f is the energy after both elastic and inelastic collisions; in this particular case $\theta_1+\theta_2=90^o$.

Once ions are scattered off the sample, the resulted beam energy, ion counts, and scattering angle are all analysed by a Toroidal Electrostatic Analyzer (TEA) (Figure 3.20). Ions entering the TEA are deflected by the electric field of two charged plates that bends 90° towards the detector. The position that the ion strikes the detector is consequently relevant to its scattering angle and energy. The counts of ions striking each position on the detector are recorded on a computer. The analyser has a 27° acceptance angle with an angular resolution of 0.3°, the energy resolution ΔE/E is ~ 0.35%.[12] During a measurement, a fixed dose of incident ions, typically within the range of microcoulombs is given, and the corresponding scattering counts, energy, and angles are recorded.

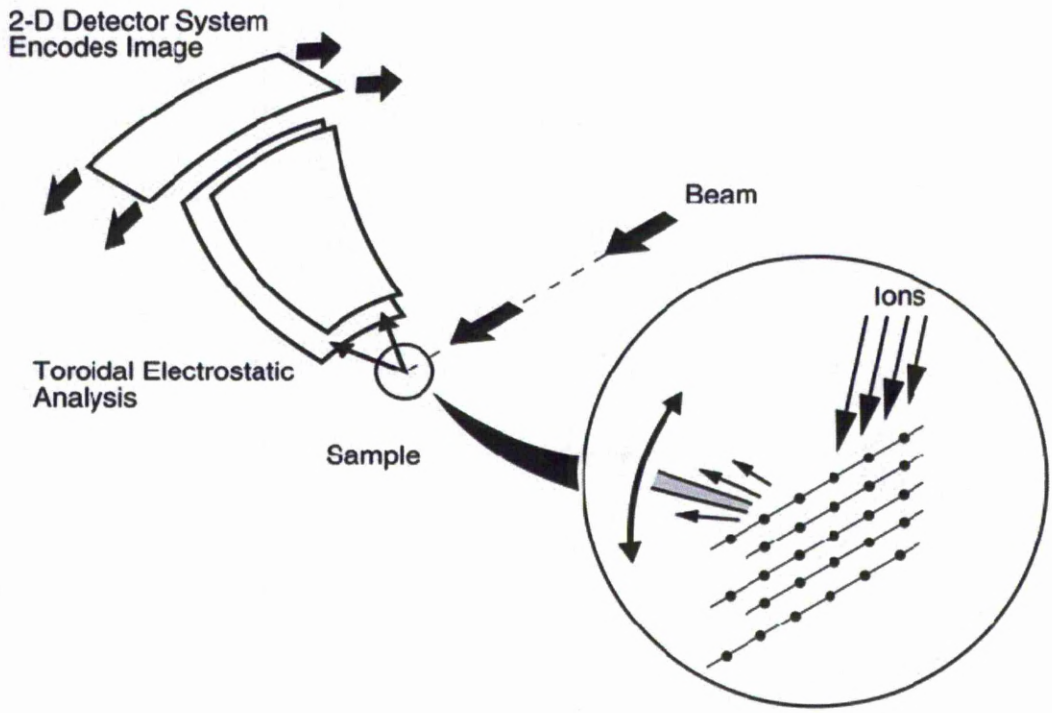

Figure 3.20 A schematic of MEIS analyzer.[12]

3.3.7.3 Experimental parameters

The experimental parameters used in this project were specifically chosen for nitride characterisation. In a typical nitride film deposited in this study, the elements of interest may include a metal (m_a ranges from 64 to 73), nitrogen (m_a=14), oxygen (m_a=16), and carbon (m_a=12). The major challenge for MEIS is to differentiate the light elements whose atomic masses are close to each other. The scattering configurations chosen should allow the maximum peak separation of these elements on the spectrum to avoid ambiguity of the results.

As illustrated in Eq. 3.8, the scattering energy (peak position) is dependent on the incident energy, the incident ion mass, and the scattering angle. The scattering energy is proportional to the incident energy and therefore, the maximum beam energy of 200 keV was used to ensure a wider separation between peaks. The effects of the

latter two can be described by the kinematic factor, K, and are illustrated in Figure 3.21a. A better separation between K values can be achieved when using He^+ ions rather than H^+ ions, it can also be done by increasing the scattering angle. However, the scattering angle in MEIS is also restricted by the possible open channels in silicon. The beam-in angle was chosen to be Si {-1-11} because this channel is easy to find. Figure 3.21b shows the possible beam-out channels with the corresponding scattering angles. It can be seen that Si {112} direction allows the maximum separation of the K values and this configuration was used throughout the project. The problem of a large scattering angle is the decrease of scattering yields, which means that longer time is required to obtain a MEIS spectrum. Each nitride MEIS spectrum presented in the current work requires more than half-day to acquire and thus only selected samples were characterised by MEIS. The full details of the MEIS experimental conditions are summarized in Table 3.5. The films for MEIS experiments were deposited with a target thickness of 10nm, this is because thick films result in peak overlapping, which leads to ambiguity of the spectrum. A thick film also raises challenges in the alignments to the Si channels.

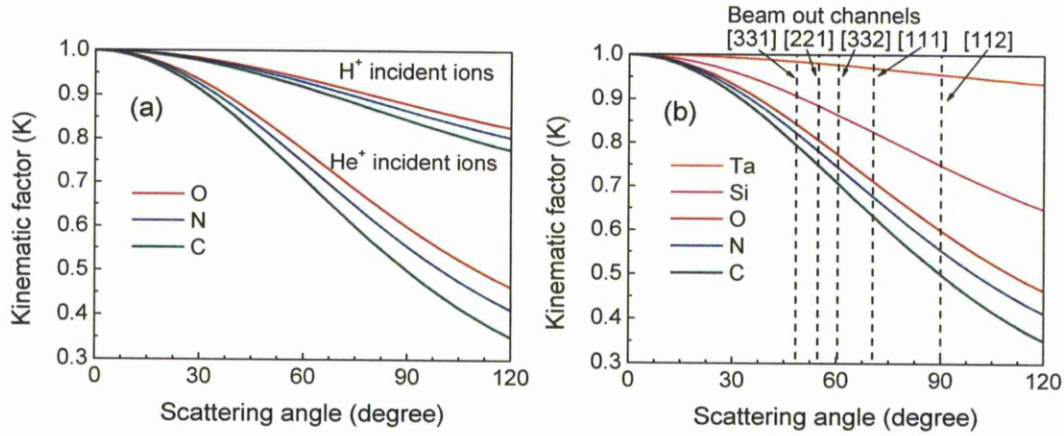

Figure 3.21 The change of Kinematic factors when using (a) either H+ or He+ ions (b) He+ ions at various scattering angles, the dot lines show the possible beam-out channels when the incident beam is aligned to Si{-1-11}.

Parameter	Value
Ion source	He^+
Beam energy	200 keV
Beam current	60 nA
Beam-in orientation	Si{-1-11}
Beam-out orentation	Si{112}
Scattering angle	90°
Dose	6-10 μC

Table 3.6 Measurement parameters for MEIS experiments.

3.3.7.4 Data processing

By changing the voltages applied to the plates in the analyzer, the full energy data is collected and Figure 3.22a shows the MEIS raw spectrum for a ~10nm TaN film on Si (100) substrate. The different colour represents scattering counts. Taking a cross section of the data along the angular axis gives the counts vs scattering angle spectrum (Figure 3.22b), the dip at 90° scattering angle represents the Si {112} beam-out direction. Taking a cross section along the energy axis at this angle gives the energy spectrum for the desired scattering configuration (Figure 3.22c).

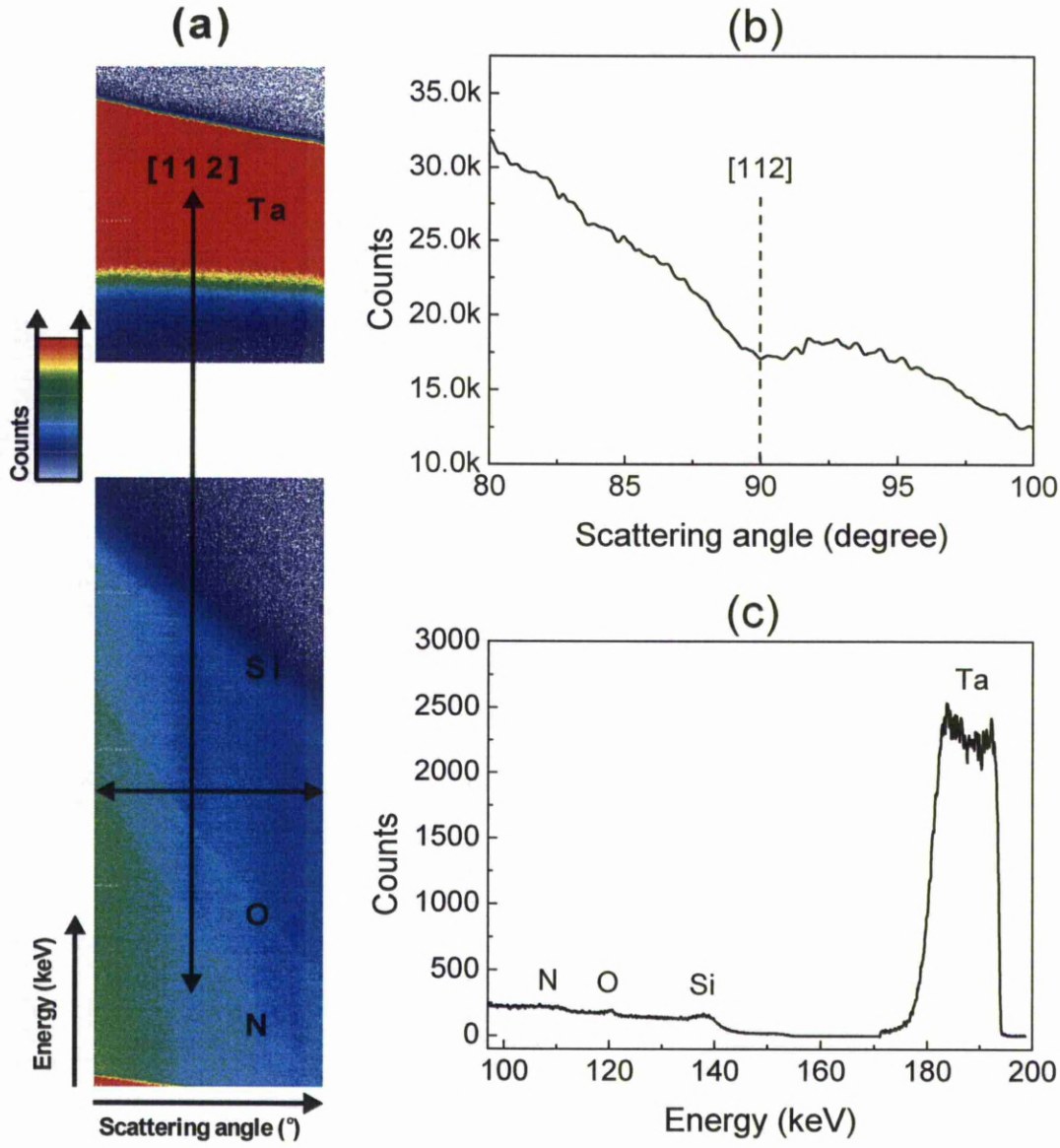

Figure 3.22 (a) MEIS raw data for a TaN film on Si (100); two arrows indicate (b) the angular cut and (c) energy cut along the Si {112} beam-out direction.

Two techniques were used to interpret the energy spectra, they are depth profiling and SINMRA simulation. In depth profiling, the kinematic factors were firstly used to identify the element of each peak. Depth information was subsequently obtained using the stopping power. The stopping power of He^+ in the corresponding material was simulated by SRIM 2008,[15] bulk material densities were used for simulations and an example is shown in Figure 3.23. The energy to depth conversion was made by a numeric computer program described by Werner.[12] The results are represented as the

thickness bars above each peak in the energy spectrum (Figure 3.24). By subtracting the silicon background, normalizing the scattering cross sections, and re-plotting the energy axis to the thickness, a depth profile spectrum is produced (Figure 3.25). The major error introduced in the result interpretation is the subtraction of the Si background, and this has been taking into consideration by using error bars. Typically speaking, the metal elements, oxygen, nitrogen and carbon have errors of ±1.5%, ±5%, ±8%, and ±10% respectively. Another method to interpret the data is the SIMNRA simulation,[16] which simulates the energy spectrum by inputting layer structures. The results were obtained when the simulated spectrum matches the experimental data, an example is also shown in Figure 3.24.

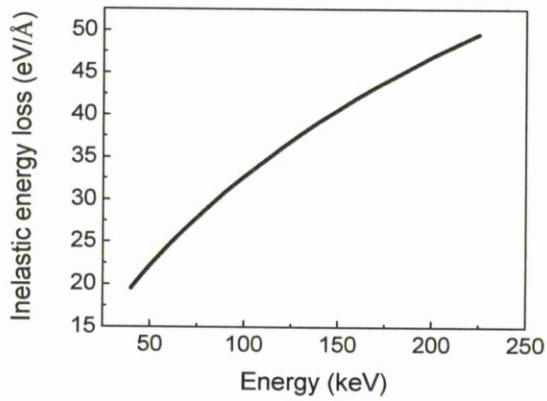

Figure 3.23 The stopping power of He^+ in TaN (density 13.7 g/cm^3).

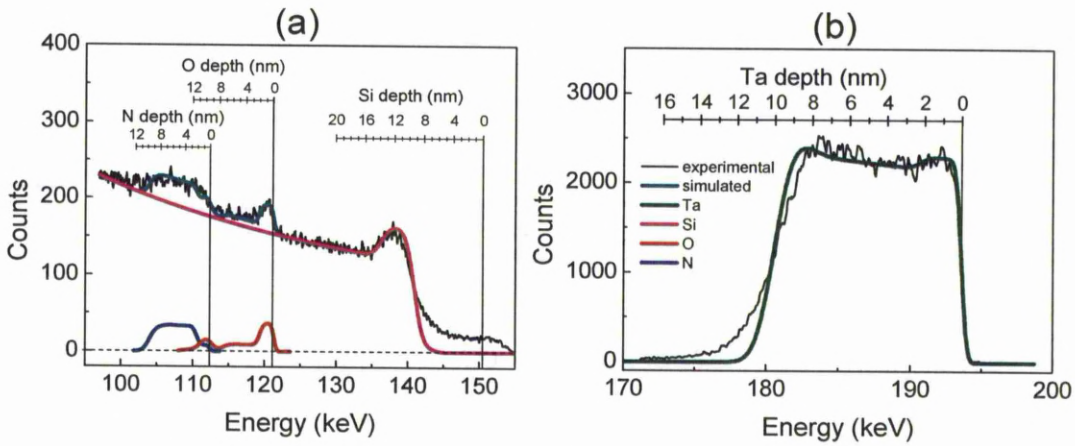

Figure 3.24 An energy spectrum showing the energy to depth conversion using the numeric

method described by Werner;[12] the colour lines shows SIMNRA simulations to the raw data. The spectrum is displayed in (a) low and (b) high energy ranges.

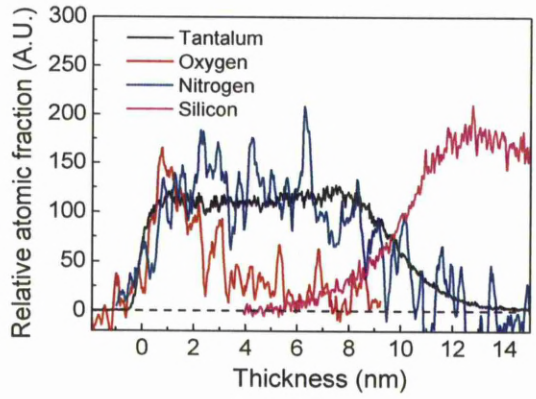

Figure 3.25 A depth profiling spectrum for TaN on silicon.

3.3.8 X-ray Diffraction (XRD)

X-ray diffraction was employed to access the microstructure of the films deposited by ALD. XRD detects the constructive interference of x-rays reflecting off (hkl) crystallographic planes. A schematic of this process is shown in Figure 3.26. Monochromatic x-rays strike the crystallographic planes with an angle θ to the surface. If the reflected x-rays are in phase the waves interfere constructively and the amplitude is raised, which can be subsequently quantified by a detector located also at an angle θ to the surface. The constructive wave requires the path length (AB+BC) in Figure 3.26 to be one or more wavelength (λ) of the incident X-ray. This length can be used to trigonometrically calculate the distance between two or more parallel (hkl) crystallographic planes, d_{hkl}, and the relation is described by the Bragg's law,

$$n\lambda = 2d_{hkl} \sin\theta \qquad \text{(Eq. 3.11)}$$

where n is the integer, d_{hkl} is the atomic spacing of the (hkl) planes (Å), λ is the x-ray wavelength (Å) and θ is the diffraction angle (°).

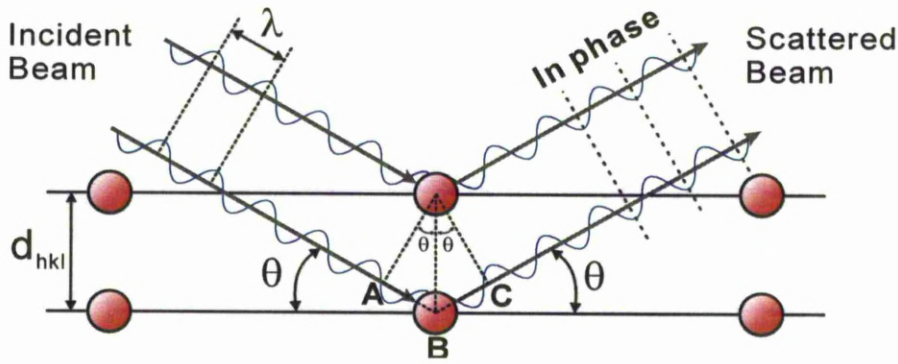

Figure 3.26 Geometry for X-ray diffraction

The technique requires the wavelength of the incident light to be smaller than the d spacing, which is approximately a few angstroms in many cases. X-rays generated from copper (K_α λ=1.5405Å) are the most widely used for XRD. Since the set of plane spacing in a crystal is usually a unique characteristic, XRD may be used as an analytical tool to indicate composition and to determine the crystal structure.

All XRD experiments in this study were carried out using a Rigaku Miniflex diffractometer with Cu *Kα* source in θ/2θ Bragg Brentano configuration. The sample thicknesses were over 30nm to ensure good signals. A 'fixed-time' method was used for each scan, the x-ray intensity was collected for 5s at a fixed 2θ angle, which steps with a 0.01° interval until the desired angular range is scanned. This measurement condition has been optimised for thin film characterisation and was adopted from the work reported by Marshall.[17] The X-ray diffractometer was also calibrated by P. Marshall using a SiO_2 powder sample.[17] The experimental diffraction patterns were compared with the reference spectra from the Cambridge Structure Database (CSD) and the corresponding crystal structure were determined.

3.3.9 Four point probe

For conductive films, the electrical resistivity was measured using a four point probe. Figure 3.27 shows a schematic of the measurement, a constant current flow is given between the probe 1 and 4, while the voltage between the probe 2 and 3 is measured. If the film thickness, h, is significantly smaller (typically 40%) than the probe spacing, d, and the measurement is performed well away from the sample edge (r>4d), the sheet resistance R_S (Ω/□) can be calculated using the equation below,[18]

$$R_S = 4.53 \times \frac{V}{I} \qquad \text{(Eq. 3.12)}$$

The electrical resistivity, ρ (Ω.cm) can be obtained if the thickness (h) is known,

$$\rho = R_s \times h \qquad \text{(Eq. 3.13)}$$

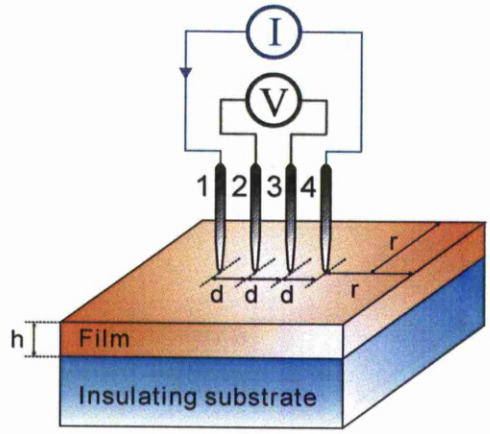

Figure 3.27 A schematic of a four point probe measurement.

Four point probe measurements were conducted using a Signatone probe head (SP4-50085TFS) and a Keithley 2400 source meter. The probe was placed onto the sample using a thread based supporting arm, which ensures a consistent probing pressure and

ohmic contacts. Films thicker than 30nm were prepared for the measurement because thin films (<10nm) lead to electron scattering at the interfaces, which increase the resistivity.[19] The measurement consistency was accessed using a TaN film (100nm) deposited on soda-lime glass. ~100 measurements were performed with a current of 20 μA, for each measurement the probe was reloaded onto the sample and the current was reset. This has resulted in a voltage histogram shown in Figure 3.28. The voltage resolution, ΔV/V is 3.5% and a similar error was obtained for all measurements when the measured voltage lies between 10^{-4} and 1 V. Figure 3.29 shows that measurements taken outside this range are unreliable, which can be attributed to the detection limitation of the voltmeter. Based upon the voltage error, the corresponding resistance error was calculated and ΔR/R was found to be 7% (Figure 3.30).

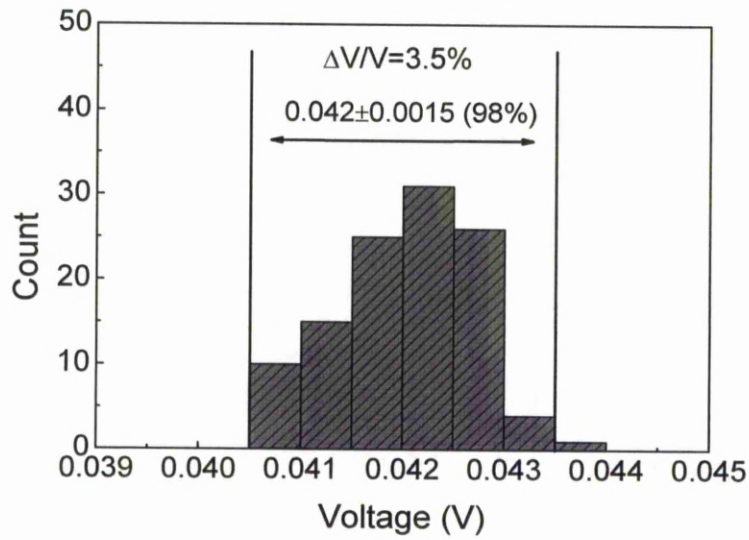

Figure 3.28 A histogram for ~100 voltage measurements on a TaN film on glass using a current of -20μA.

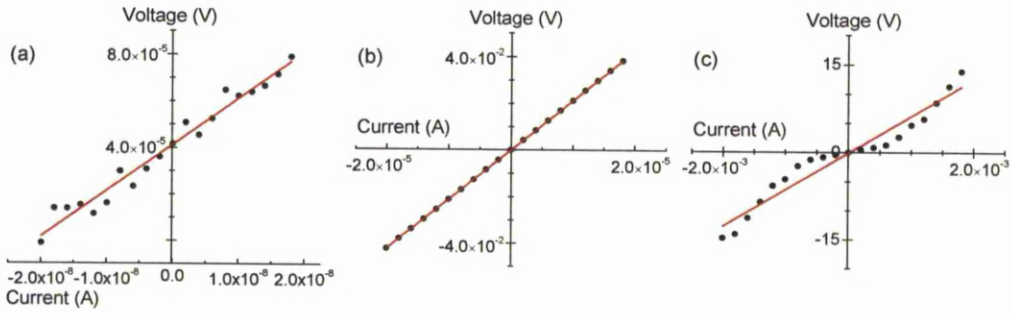

V/I = 2000Ω V/I = 2100Ω V/I = 6300Ω

Figure 3.29 Voltage as a function of current for a TaN film on glass at a voltage range of (a) 10^{-5} V, (b) 10^{-2} V and (c) 10 V.

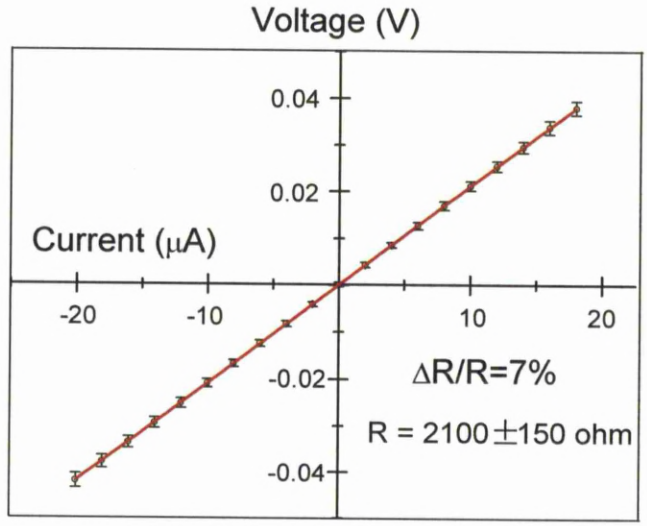

Figure 3.30 Voltage as a function of current showing the error of resulted resistance.

It was suspected that soda lime glass substrates are not suitable for the electrical measurement due to the possible sodium diffusion to the film. This was investigated using multiple insulating substrates during one ALD deposition of TaN (~30nm) at 300°C, they include SiO_2, sapphire, Ta_2O_5, and soda-lime glass. The resulted resistance values (Table 3.6) show a good agreement within the measurement tolerance. Due to its availability, soda-lime glass slides were used as the substrate for four point probe measurements throughout the study. The glass slides were cleaned in

an ultrasonic bath using de-ionised water, rinsed with isopropyl alcohol and then dried.

Substrates	100nm SiO_2 on Si	Sapphire	100nm Ta_2O_5 on Si	Soda lime glass
Resistance of the TaN film (Ω)	6000±420	6600±460	5900±410	6400±450

Table 3.7 The resistance for TaN films deposited on various substrates during one ALD deposition.

3.4 References

1. T. Manning, W. Grow, Inductively coupled plasma atomic emission spectrometry. http://www.mrfn.org/ucsb/chem/icp.pdf (accessed 2010).

2. M. Ritala, J. Niinistö, *Atomic Layer Deposition*. In *Chemical Vapour Deposition: Precursors, Processes and Applications*, A. C. Jones, M. L. Hitchman, Eds. Royal Society of Chemistry: Cambridge, p 164 (2009).

3. J. L. van Hemmen, S. B. S. Heil, J. H. Klootwijk, F. Roozeboom, C. J. Hodson, M. C. M. van de Sanden, W. M. M. Kessels, *Journal of The Electrochemical Society* **154**, G165-G169 (2007).

4. J. Humlicek, *Polarized Light and Ellipsometry*. In *Handbook of ellipsometry*, H. G. Tompkins, E. A. Irene, Eds. Springer: Heidelber, p 72 (2005).

5. D. Gonçalves, E. A. Irene, *Química Nova* **25**, 794-800 (2002).

6. E. Kondoh, Spreadsheet Ellipsometry. http://www.ccn.yamanashi.ac.jp/~kondoh/ellips_e.html (accessed Aug-2010).

7. J. W. Elam, M. J. Pellin, *Analytical Chemistry* **77**, 3531-3535 (2005).

8. R. Sreenivasan, T. Sugawara, K. C. Saraswat, P. C. McIntyre, *Applied Physics Letters* **90**, 102101 (2007).

9. P. J. Goodhew, F. J. Humphreys, R. Beanland, *Electron microscopy and analysis*. Third ed.; Taylor & Francis: London, (2001).

10. Phoenix batch process ALD reactor - Cambridge nanotech. http://www.cambridgenanotech.com/products/phoenix.php (accessed July-2011).

11. The Medium Energy Ion Scattering Facility. http://www.dl.ac.uk/MEIS/ (accessed Jun-2011).

12. M. Werner, Ph.D. thesis, *Damage formation and annealing studies of low energy ion implantation in silicon using medium energy ion scattering*, University of Salford, Salford, (2006).

13. Rutherford Backscattering Spectrometry (RBS) theory tutorial. http://www.eaglabs.com/training/tutorials/rbs_theory_tutorial/density.php (accessed 10-Aug-2010).

14. P. Bailey, T. C. Q. Noakes, D. P. Woodruff, *Surface Science* **426**, 358-372 (1999).

15. SRIM 2008. http://www.srim.org/ (accessed 10-Dec-2009).

16. M. Mayer, *AIP conference Proceedings* **475**, 541-544 (1999).

17. P. Marshall, Ph.D. thesis, *Optical and surface characterization of oxide and nitride thin films*, University of Liverpool, Liverpool, (2005).

18. Four point probe. http://www.four-point-probes.com/short.html (accessed Jun-2010).

19. D. L. Smith, *Thin film deposition: Principles and Practise*. Mcgraw-Hill: Columbus, (1995).

Chapter 4. Tantalum nitride

In this chapter, thermal ALD has been investigated for the deposition of tantalum nitride. A comparison has been made between ammonia and monomethylhydrazine (MMH) as a nitrogen co-reactant. The process using MMH has resulted in highly resistive nitrogen rich tantalum nitride. The process using ammonia, by contrast, has resulted in electrically conductive tantalum mono nitride, the film resistivity exhibits the lowest value compared with previous thermal ALD studies in the literature.

4.1 Introduction

Tantalum nitride (TaN_x) is a versatile material, with a main stoichiometry ranging from the mono nitride, TaN, to the nitrogen rich, Ta_3N_5 phase.[1] The physical properties including density, colour appearance and electrical property are significantly affected by the nitrogen content. The bulk densities of TaN and Ta_3N_5 are 13.7g/cm^3[2] and 9.85g/cm^3[3] respectively. TaN has a grey colour[4], whilst Ta_3N_5 has a yellow colour.[5] The electrical resistivity of TaN can be as low as 0.25 mΩ.cm at ambient temperature (300K) making it a good conductor, whereas Ta_3N_5 exhibits significantly higher resistance, typically higher than 6,000 mΩ.cm.[6] Theoretical calculations suggest that the higher resistivity of Ta_3N_5 is due to the formation of tantalum vacancies, which decreases the density of states at the Fermi level.[7]

TaN_x is thermodynamically very stable with respect to copper,[8] and has been extensively studied as a diffusion barrier between copper interconnects and silicon for Very Large Scale Integration (VLSI) based circuits.[9-13] Although the diffusion barrier property of TaN_x improves with the nitrogen content,[9,14-17] the higher

resistivity increases the overall resistance of the interconnects. This is detrimental to the device performance, because a higher resistance leads to more power consumption and heat generation during operation. Thus, conductive TaN is currently required,[18-20] however, Kim et al. has argued that when the device dimensions shrink, the overall interconnect resistance will largely rely on the interconnects themselves rather than being affected by a diffusion barrier and therefore, Ta_3N_5 may become advantageous in the future.[9] In addition, TaN_x has many other applications, for example, TaN has been investigated as a gate electrode,[21-23] a work function tuning layer,[24] thin film resistors,[25] and as a non-magnetic interlayer in non-volatile magnetic random access memories (MRAM).[26] Ta_3N_5 has also been used in photonic structures, such as inverse opals because of its high refractive index (3.0) and partial transparency in the visible wavelengths.[27] It has also been used for photocatalysis[28] and photoelectrolysis.[29]

The adoption of any material for applications in microelectronics is heavily dependent on thin film deposition technology. The deposition method employed must produce high quality, uniform, pinhole free films with the desired stoichiometry and thickness. In many modern devices, the films must be conformal over high aspect ratio features, such as the trench structures in dynamic random access memory (DRAM) cells, where TaN can be used as a gate electrode.[30] The thermal budget of the deposition process may also be an important consideration when temperature sensitive parts of the device have been formed prior to deposition.[31] As introduced in Chapter 2, Atomic Layer Deposition (ALD) can fulfil these requirements and as a result is becoming increasingly popular as a thin film deposition technique for microelectronics and many other applications.[32-34]

ALD deposition of TaN_x has previously been reported using various Ta precursors. The halide precursors including TaF_5,[35] $TaCl_5$,[17,36] and $TaBr_5$[37] have been most widely studied, however, these tend to form corrosive hydrogen halides by-products, which can damage the deposition equipment. Halide precursors also require relatively high deposition temperatures (>400°C) to prevent halide incorporation within the film.[36] To overcome these challenges, amide-based precursors such as pentakis(dimethylamino)tantalum (PDMAT) $Ta\{N(CH_3)_2\}_5$,[38] pentakis(ethylmethylamino)tantalum (PEMAT) $Ta\{N(CH_3C_2H_5)\}_5$,[39] and (tertbutylimido)tris(diethylamido)tantalum (TBTDET) $Ta\{N(C_2H_5)_2\}_3\{NC(CH_3)_3\}$[40] have been developed for TaN_x ALD. Amides allow lower deposition temperatures because they undergo a transamination-like reaction with co-reactants such as ammonia.[41] Recent theoretical calculations showed that the nitride formation can be driven by low barrier (10.6 and 27.6 kcal/mol) ligand exchange mechanisms between an amide precursor and ammonia, in addition, amine by-products may also catalyse the nitride formation and therefore provide favourable reaction thermodynamics.[42] Carbon and hydrogen are potential impurities when using amide precursors; however, efficient transamination-like reactions exchange the carbon rich amide group in the precursor with ammonia and therefore, these contaminants should be minimised. Carbon content as low as 2% have been reported in Ta_3N_5 films deposited with PDMAT and ammonia at 275°C.[38]

A major challenge in the ALD of TaN_x is the control of the nitride stoichiometry, especially in the deposition of TaN. Because the oxidation states of the metal in the precursor are Ta(V) or Ta(IV) and the required oxidation state in TaN is Ta(III), a reduction reaction is necessary. A range of nitrogen co-reactants including ammonia (NH_3),[38] hydrazines,[31,40] and nitrogen/hydrogen mixed radicals[17] have been studied

in the ALD deposition of TaN_x. Hydrogen radicals can achieve the reduction in Plasma Enhanced (PE) ALD,[17] however, very few reports are available on the deposition of TaN using thermal ALD. This is partially due to the difficulty of finding a suitable precursor-reactant combination for the reduction reaction. Ammonia is the most widely used nitrogen co-reactant in thermal ALD of nitrides, however, previous studies have only been able to obtain nitrogen rich Ta_3N_5 when ammonia was used with either tantalum halide[36] or amide[43] precursors. Reductants such as zinc[36] and trimethylaluminium (TMA)[37] have been used with ammonia to produce conductive TaN, however, transport of zinc vapour requires high temperatures (>400°C) and the use of TMA results in both Al (12 at.%) and C (22 at.%) impurities. Hydrazines are another class of nitrogen co-reactants that can be used for nitride ALD and offer superior reactivity to ammonia.[44] The high reactivity of hydrazine based co-reactants means that lower temperature processes are possible, which has been demonstrated for the ALD of TaN_x with TBTDET[40] and $TaCl_5$.[31]

In this chapter, the thermal ALD of TaN_x using PDMAT and either ammonia or monomethylhydrazine (MMH) are compared. In contrast to previous thermal ALD studies, where ammonia based ALD produces semi-insulating Ta_3N_5, this study demonstrates that conductive TaN can be deposited using ammonia without the need for any additional reductant. The use of MMH as a co-reactant is reported and it is shown that semi-insulating Ta_3N_5 can be produced. The growth behaviour has been studied as a function of the growth conditions, and has been analysed in detail using a quartz crystal microbalance (QCM) to elucidate the chemisorption of PDMAT.

4.2 Results and discussion

TaN_x films were deposited on 100mm diameter p-type Si(100) substrates used as-supplied without any additional surface preparation. Soda lime glass slides measuring 75 × 25 mm were also used as the substrates for electrical resistivity measurements. The depositions of TaN_x using thermal ALD with PDMAT (SAFC Hitech) and either ammonia (Electronic grade, Air Products), or MMH (SAFC Hitech) were carried out in an OpAL thermal reactor, and the growth parameters are summarised in Table 4.1. During each step of the ALD cycle, the overall gas flow into the reactor was maintained at 200sccm to keep the pressure approximately constant at ~200 mTorr except during MMH doses, where the pressure changed to ~250mTorr momentarily (within 1s) due to the high vapour pressure of MMH. The initial growth experiments (not shown), using purge lengths of 5, 10 and 15s, resulted in nearly identical films and therefore a purge time of 5s was used.

Reactor, leak rate and cleaning method	OpAL thermal ALD reactor, 1mTorr/min, 1 hour Ar pump and purge		
PDMAT transport temperatures	75°C (bubbler) - 90°C (manifold) - 100°C (chamber walls)		
Substrate temperature	200-375°C		
PDMAT doses	150sccm 0-8s		
PDMAT purge	200sccm 5s		
Co-reactant	**Without co-reactant**	**Ammonia**	**MMH**
Co-reactant doses	N.A.	10sccm 0-12s	0-30ms vapour draw
Co-reactant purge	200sccm 5s		

Table 4.1 Growth parameters for the depositions of TaN_x using thermal ALD with PDMAT and either ammonia, MMH or without a co-reactant.

4.2.1 Growth characteristics

The effects of deposition temperature (Figure 4.1) on the growth of tantalum nitride with PDMAT (6s dose) and either ammonia (3s) or MMH (20ms) were investigated. Tests were also conducted without any co-reactant to assess the thermal decomposition of PDMAT. In the absence of a co-reactant, growth rate remains close to zero between 200 and 300°C but increases rapidly to 0.7 Å/cycle at 375°C, indicating that PDMAT undergoes thermal decomposition at temperatures above 300°C. This is consistent with the previous work using PDMAT reported by Maeng et al..[43]

The growth rate for the ammonia process clearly increases with temperature, rising to 0.24 Å/cycle at 200°C, to 0.6 Å/cycle at 300°C and to 1.1 Å/cycle at 375°C (Figure 4.1), indicating a CVD growth mechanism. At temperatures above 300°C, thermal decomposition is expected to contribute to the deposition rate too. Thermal decomposition often results in high levels of carbon from the ligands and this is confirmed in the MEIS analysis of the films grown at 375°C (table 4.2), which shows a carbon incorporation level of 27±10 at.%. The increasing growth rate observed between 200 and 300°C is not related to thermal decomposition of the precursor, but is indicative of thermal activation of the reactions between the PDMAT and the ammonia.

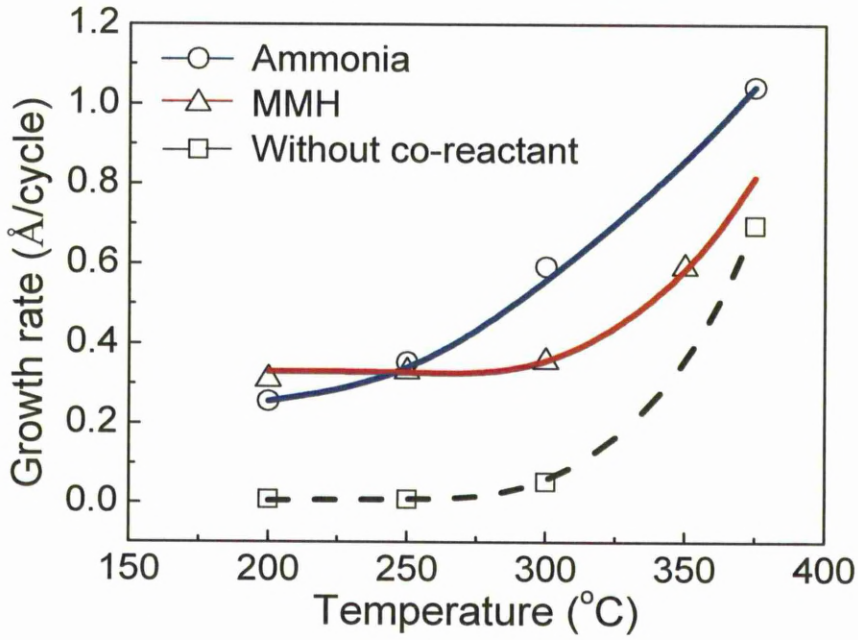

Figure 4.1 Growth rate as a function of deposition temperature using 6s PDMAT doses with either 3s ammonia doses, 20ms MMH doses, or without co-reactant. Error is ±0.03 Å/cycle.

For the MMH, the growth rate at 200°C is ~0.3 Å/cycle, which is slightly higher than the growth rate using ammonia and indicates the superior reactivity of MMH. The higher reactivity of MMH can be explained by the weak N-N bonding in hydrazines compared with the strong N-H bonding in ammonia, which can be represented by radical formation enthalpies, ΔH°, with a value of 297 and 461 kJ/mol for hydrazine and ammonia respectively.[44] At temperatures between 200 and 300°C the growth rate plateaus out, providing a good ALD temperature window. Once again, the growth rate increases at temperatures above 300°C due to thermal decomposition of the PDMAT.

The observed difference between the growth rate for the two processes at temperatures below 300°C is consistent with the ALD study reported by Burton et al. using TBTDET and either ammonia or hydrazine.[40] In this study, the authors observe an ALD window for the hydrazine process between 180 and 220°C, whilst they do not

see a temperature plateau for the ammonia process at all. For ammonia, it is speculated that growth rate is controlled by surface chemistry, which is limited by the thermal reactivity of ammonia. In contrast, hydrazines are generally much more reactive and hence require significantly less energy to react on the surface. As a result, the MMH process is limited by surface reaction sites rather than chemical reactivity, resulting in an ALD window.

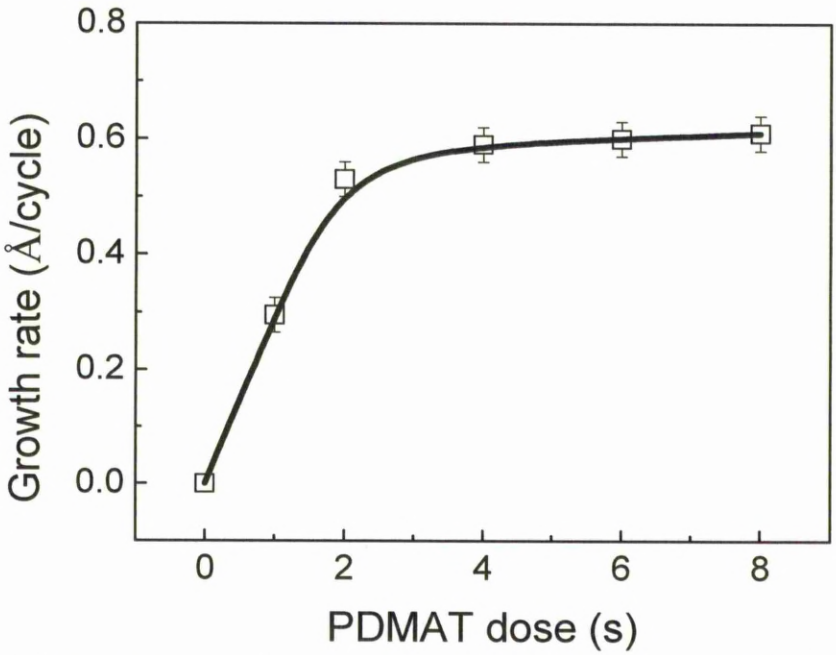

Figure 4.2 Growth rate as a function of PDMAT dose for ammonia (3s) based ALD at 300°C.

The effect of PDMAT dose was investigated by varying the dose between 0 and 8s at a fixed growth temperature of 300°C with 3s ammonia doses. The growth rate (Figure 4.2) increases readily between 0-2s doses to 0.53 Å/cycle and then saturates at 0.6 Å/cycle for doses above 4s. This confirms that PDMAT is a good self-limiting precursor for ALD growth, in agreement with previous studies.[43] Self-limiting ALD provides large area uniformity, and the thickness uniformity was assessed by ellipsometry using films deposited for 600 ALD cycles under saturative conditions.

The thickness variation was small and the uniformity was 96±1% across 100mm diameter wafers (Figure 4.3).

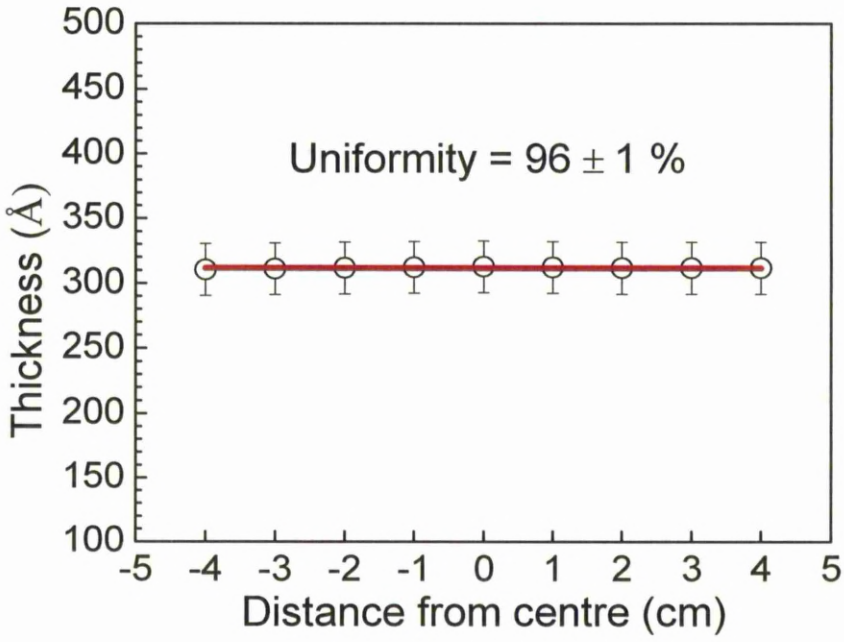

Figure 4.3 Thickness measured by the ellipsometry across the film deposited on a 100mm diameter Si wafer using 600 cycles of 6s PDMAT with 6s ammonia at 300°C.

The effects of co-reactant dose were investigated by varying either ammonia (0-12s) or MMH (0-30ms) doses at 300°C with alternating 6s PDMAT exposures (Figure 4.4). The growth rate for the ammonia process increases as the dose increased from 0 to 3s and saturates at 0.63 Å/cycle. Similarly, the process using MMH reaches a self-limiting rate of 0.4 Å/cycle at 10ms doses.

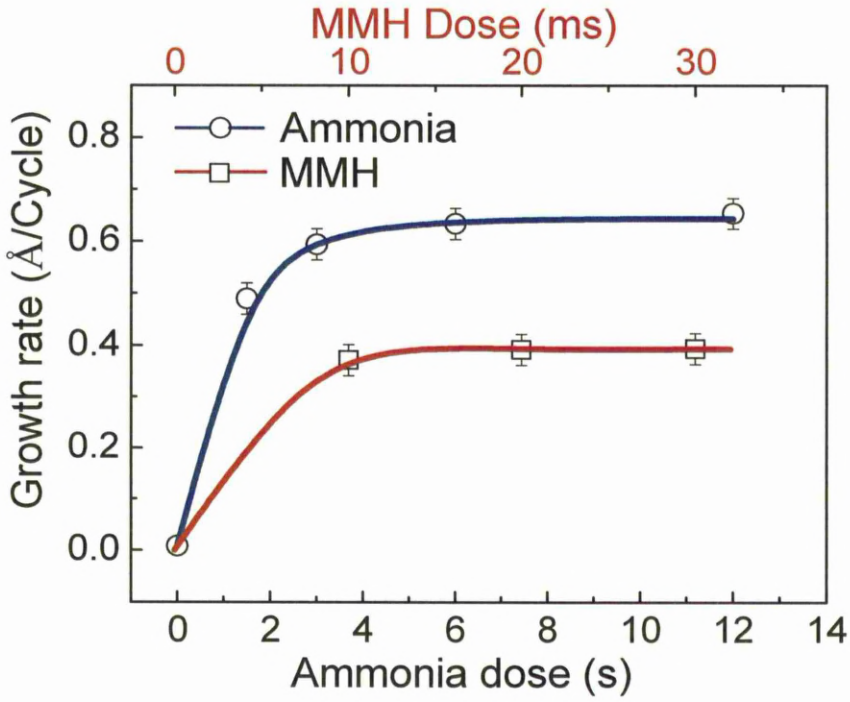

Figure 4.4 Growth rate as a function of either ammonia or MMH doses at 300°C using PDMAT (6s).

4.2.2 QCM analysis

It is clear (Figure 4.4) that the saturated growth rate for MMH is lower than that for ammonia. To investigate this further, in-situ QCM measurements were carried out for ammonia (12s) and MMH (20ms) processes at 300°C using 6s PDMAT doses and 15s purges. The long purges were used to ensure stabilization of the QCM crystal. Figure 4.5a shows the mass gain during 10 ALD cycles for each co-reactant, both of which follow overall linear dependence on the number of cycles. The observed mass gain is in a good agreement with ex-situ weight gain measurements on Si(100). Figure 4.5b shows the average mass gain and mass loss for each ALD cycle obtained by averaging over 10 cycles. These data confirm that the lower growth rate for the MMH process is related to a lower mass gain in the PDMAT chemisorption, which

indicates that fewer surface reaction sites are available on the MMH terminated surface.

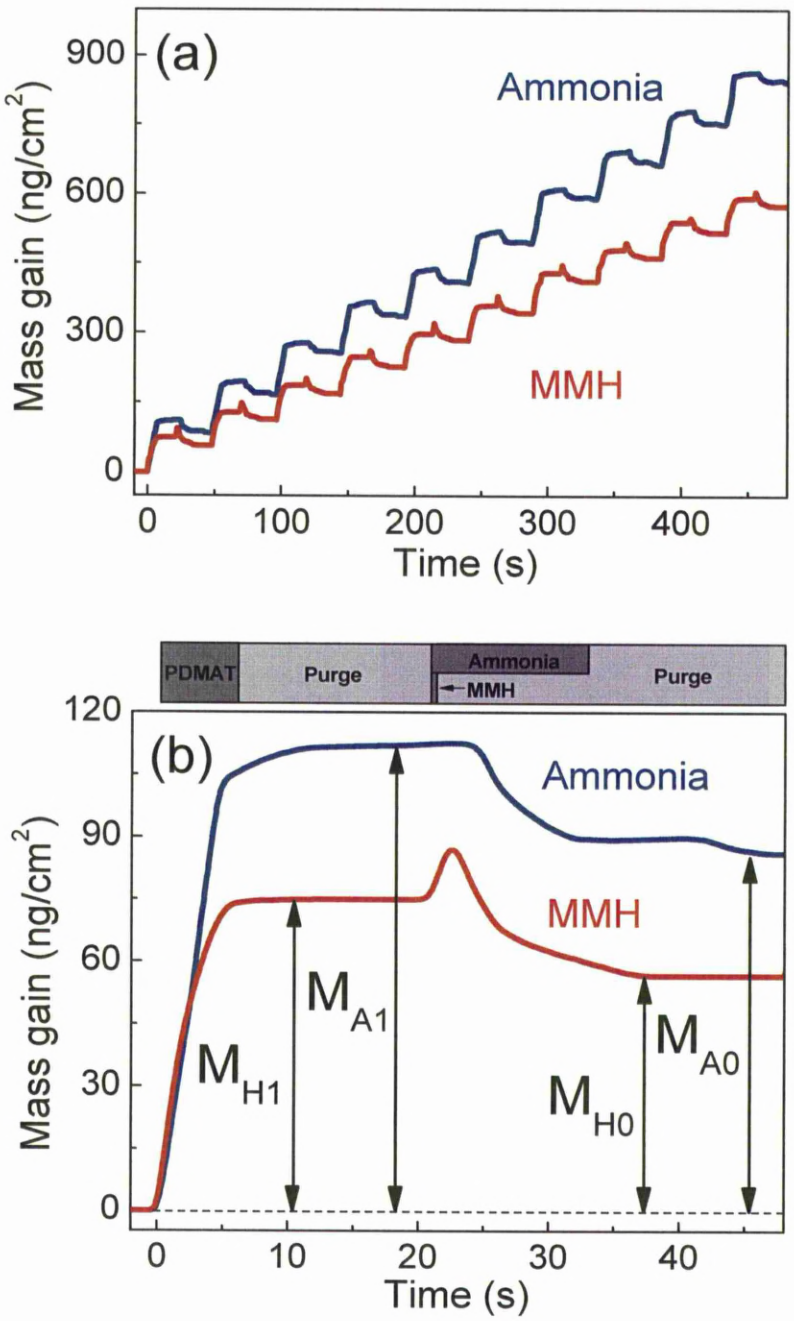

Figure 4.5 (a) QCM data for 10 cycles of either ammonia or MMH based ALD at 300°C; (b) Detailed view of QCM data for one ALD cycle using either co-reactant at 300°C. The ALD cycle for ammonia and MMH is 6s-15s-12s-15s and 6s-15s-0.02s-26.98s respectively.

In the deposition process using PDMAT and ammonia (Figure 4.5b), the PDMAT exposure results in an average mass gain of 113 ng/cm^2 and corresponds to chemisorption of PDMAT molecules on the surface. The chemisorption of PDMAT is likely to be driven by reactions between surface groups (–NH or –NH_2) and the dimethylamido ligands (–NMe_2). In this type of exchange reaction, schematically illustrated in Figure 4.6, $HNMe_2$ is produced as a gaseous leaving group during the chemisorption. The resulting mass gain (M_{A1} in Figure 4.5b) corresponds to the mass of PDMAT molecules (401 g/mol) absorbing on the QCM crystal minus the $HNMe_2$ leaving groups (45 g/mol). For each PDMAT molecule, one or more side groups may react with the surface, resulting in a mass gain proportional to (401-45n), where n is the number of reacted dimethylamido ligands per PDMAT.

The subsequent ammonia exposure results in an average mass loss of 27 ng/cm^2 (Figure 4.5b) and corresponds to the transamination-like reaction of the remaining side groups (Figure 4.6). The completed ALD cycle gives an overall average mass gain of 86 ng/cm^2 (M_{A0} in Figure 4.5b), which corresponds to the mass of TaN_x plus hydrogen related surface groups deposited on the crystal. MEIS measurements, which will be discussed below, show that the TaN_x films deposited with ammonia are TaN (195 g/mol), therefore the ratio of M_1/M_0, is equal to (401-45n)/(195+n). From the QCM data for the ammonia process, we obtain a ratio of 113/86 = 1.31 for M_1/M_0. Hence the average number of leaving groups (n) during the chemisorption process is estimated to be 3.1. In other words, approximately three side groups react with the surface during the first half of the ALD cycle and the remaining two react with the ammonia dose during the second half of the process.

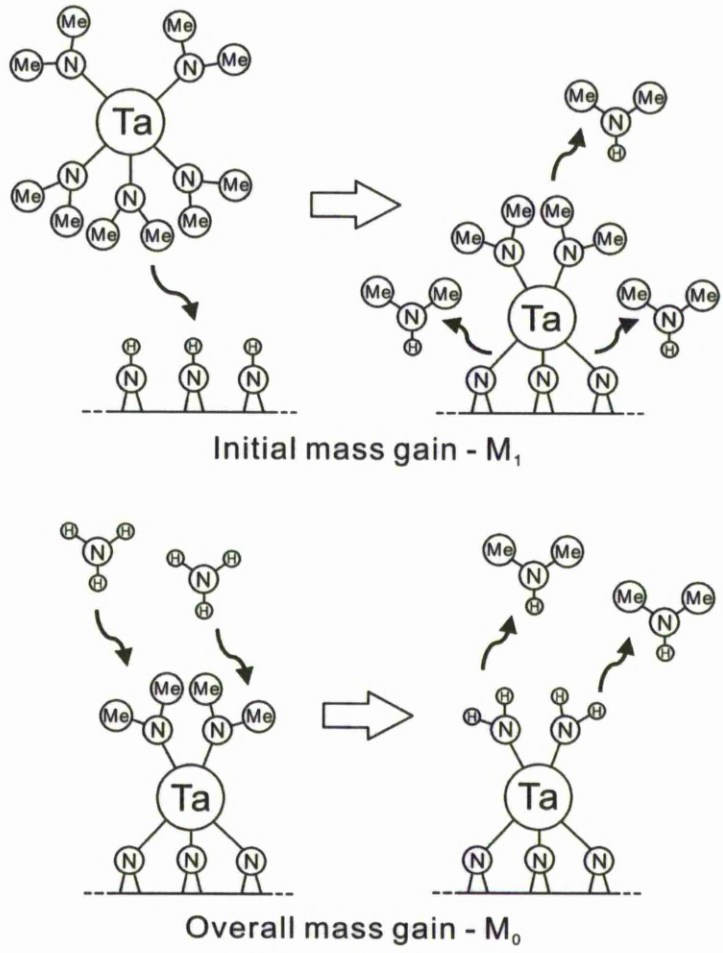

Figure 4.6 One possible surface reaction that corresponds to the observed QCM mass gain and mass loss during the ALD using PDMAT and NH_3.

In the deposition using MMH (Figure 4.5b), the mass gain during the PDMAT dose (M_{H1}) is 75 ng/cm^2, which is significantly lower than the ammonia process. The subsequent MMH dose is accompanied by a peak in the QCM data (Figure 4.5b). The peak is an artefact due to the pressure spike from the MMH dose. This has been illustrated in section 3.2.3 that an abrupt pressure change leads to false signals in QCM measurement and therefore, the peak associated with the MMH dose is an artefact. The crystal stabilizes within 20s after the MMH dose, which eventually leads to a mass loss of 20 ng/cm^2, meaning that the overall average mass gain (M_{H0}) per

cycle is 55 ng/cm^2. The surface species left behind by the MMH exposures could range from low mass –NH groups up to higher mass –NMe groups, however, the low carbon incorporation in these films (Figure 4.8b) indicates that the latter is unlikely. Methylamino –NMe surface groups would have a similar acidity to the amide groups on the PDMAT, therefore, an exchange reaction is unlikely to occur and hence carbon incorporation would be expected to be high. The low carbon levels indicate that the –NMe groups are cleanly removed following the MMH dose. Hence, it is reasonable to assume that –NH surface groups are largely responsible for the chemisorption of PDMAT.

MEIS measurements show that the TaN_x films deposited using the MMH process are Ta_3N_5 (613 g/mol or 204.3 g/mol for each Ta atom), hence the ratio of M_1/M_0 is equal to (401-45n)/(204.3+n). From the QCM data, we obtain a ratio of 75/55 = 1.36, and from this, estimate that n is 2.7. The lower initial mass gain and the slightly lower value of n obtained for the MMH process indicates that fewer surface sites are available for the chemisorption with MMH than with ammonia.

MMH molecules are significantly larger than ammonia molecules (Figure 4.7), with a van der Waals volume of 52.5 and 22.9 Å^3 respectively.[45] A larger molecule generally has a higher steric hindrance, which blocks the reaction site and prevents chemical reactions. This means less surface reaction sites would be available on the MMH terminated surface than the ammonia terminated surface, which is in a good agreement with the QCM results. Therefore, steric hindrance of the co-reactant plays a significant role in determining the number of available sites on the surface and hence the lower growth rates.

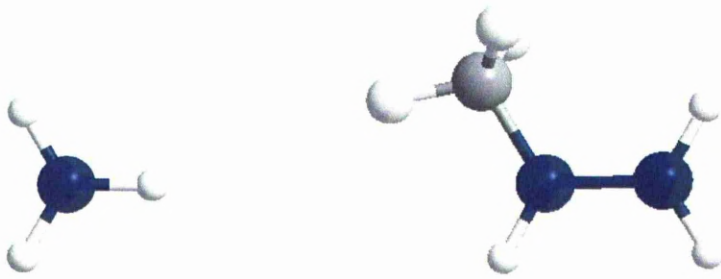

Ammonia MMH

Figure 4.7 Molecular structures for ammonia and MMH; Blue, white and grey spheres represent nitrogen, hydrogen and carbon atoms respectively.

4.2.3 Chemical composition

In this study, the appearance of the film when viewed in transmission was found to vary depending on growth conditions – particularly the co-reactant used. Films grown on glass using MMH were observed to have a yellow appearance, while many of the films grown using ammonia were grey. A correlation between the colour and the conductivity was also noted, with grey films displaying good conductivity. The correlation between colour and composition of TaN_x is well known, TaN and Ta_2N have been reported to be grey [4], whereas Ta_3N_5 is yellow [5].

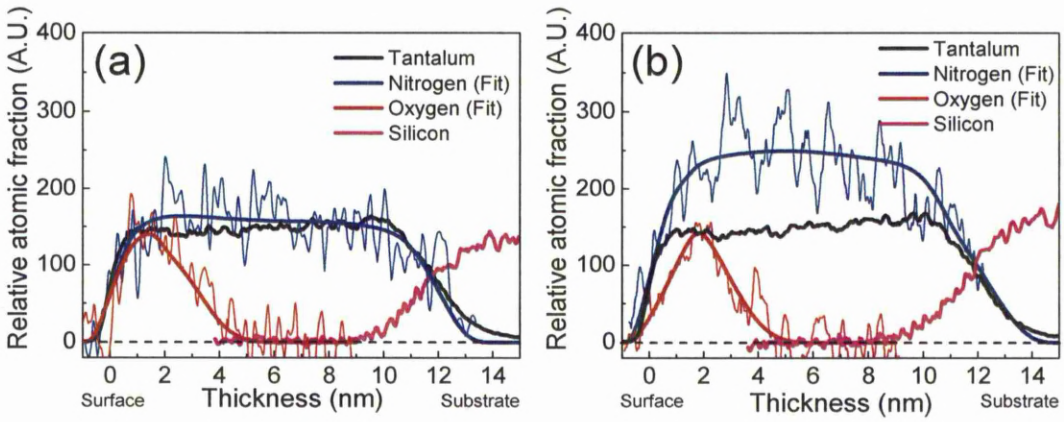

Figure 4.8 MEIS depth profiles of film deposited using PDMAT (6s) and either (a) 3s ammonia for 200 cycles or (b) 20ms MMH for 250 cycles at 300°C. Data were taken for a dose of 6μC.

Selected films were analysed using MEIS to provide quantitative composition depth profiles and film densities. The energy-to-depth conversion was carried out using the stopping powers of He^+ in TaN assuming a density of 13.7 g/cm^3.[2] Figure 4.8a shows the MEIS depth profile for a film deposited using the ammonia process at 300°C (using 200 cycles with 6s PDMAT and 3s ammonia doses) and clearly shows tantalum, nitrogen and oxygen features. The tantalum and nitrogen feature spans over a thickness range of 12nm, and the Ta:N ratio is close to 1:1, which is in a good agreement with the stoichiometry of TaN. The surface oxygen feature in the top 4nm of the film can be attributed to post growth absorption of oxygen-containing species from air. Within the bulk of the film, at depths of 4-8nm, oxygen levels are in the noise of the signal, which indicating that there is less than 5 at.% oxygen. Based on the ellipsometry and MEIS derived thickness measurements,[46] the film density was estimated to be 11.3 g/cm^3, which is ~80% of the bulk density for TaN (13.7 g/cm^3).

A MEIS profile (Figure 4.8b) was also obtained for films deposited using the MMH process (at 300°C using 250 cycles with 6s PDMAT and 20ms MMH doses).

However, the films were found to be nitrogen rich with a Ta:N ratio of 1:1.6, which is in good agreement with the stoichiometry of Ta_3N_5. The film density was found to be 9.8 g/cm^3, and is close to the bulk density for Ta_3N_5. No carbon was detected in either sample by MEIS, which has a theoretical detection limit of ~2%.[47] The low carbon incorporation shows that the carbon containing groups in PDMAT have been efficient removed in the processes using both co-reactants. This can be attributed to transamination-like reactions,[41,42] which exchanges an amide group with nitrogen co-reactants and therefore, films with low carbon contamination have been deposited.

Co-reactant	Temp. (°C)	Density (g/cm^3)	Bulk film composition (at. %)				Figure No. in Appendix I
			Ta	N	O	C	
Ammonia	200	9.6±1	37±1.5	36±8	27±5	BDL	Figure 1
Ammonia	300	11.3±1	49±1.5	51±8	BDL	BDL	Figure 2
Ammonia	375	9.5±1	26±1.5	27±8	20±5	27±10	Figure 3
MMH	200	9.0±1	35±1.5	57±8	8±5	BDL	Figure 4
MMH	300	9.8±1	38±1.5	62±8	BDL	BDL	Figure 5

Table 4.2 Summary of density and chemical composition for the films deposited using PDMAT (6s) with either ammonia (3s) or MMH (20ms) at the temperature range from 200 to 375°C. The bulk film composition were quoted at a thickness range of 4-8nm. (BDL - below the detection limit).

The effect of growth temperature on film composition and density using either co-reactants was also studied by MEIS. The results are summarised in Table 4.2 and the Figures are attached in appendix I, the bulk film composition is based on averaged data from 4-8nm depth range. For the films deposited with ammonia, the Ta:N ratio is almost independent of temperature and remains at 1:1. Carbon incorporation is below the detection limit at temperatures below 300°C, indicating complete ligand removal. However, carbon contamination increases to 27±10 at.% at 375°C, which is consistent with thermal decomposition of PDMAT.

The oxygen impurity level is high at 200 and 375°C, but is below the detection limit at 300°C. The minimal oxygen level at 300°C demonstrates that the reactor, carrier gas, precursor and ammonia contain negligible oxygen species and therefore, the oxygen detected in the films deposited at other temperatures is unlikely to be incorporated during deposition, but during post deposition exposures to air. The high oxygen content in the films grown at 200 and 375°C can be correlated to the lower film densities, which leads to deeper oxygen penetration into the film during post deposition exposure to air. It is postulated that the low density at 200°C is due to the insufficient reactivity of ammonia at this temperature, which is also indicated by the low growth rate at 200°C (Figure 4.1). A low growth rate indicates a poor reaction kinetics, which may give rise to dangling bonds and defects. Consequently, films with a low density were deposited. At 375°C, the incorporation of decomposed precursor by-products results in vacancies and reduced density.

For the MMH process, Ta:N ratio is also consistent at 200 and 300°C with a value of 1:1.6. Although a trace level of oxygen (8±5 at.%) was observed in the films deposited at 200°C, the oxygen incorporation is significantly lower than those deposited with ammonia at the same temperature (27±5 at.%). This confirms that the films are more stable during post deposition exposures to air if they were deposited with the MMH rather than ammonia at 200°C. The ability of depositing good quality films at low temperatures is the advantage of the MMH process and is due to the high reactivity of the MMH, which has also been indicated by the growth results in Figure 4.1.

4.2.4 Electrical properties and crystallography

The resistivities of ~30nm thick films deposited on glass were studied using four-point probe measurements. A four-point probe result for TaN is shown in Figure 4.9. It can be seen that the voltage and current strictly follow a linear relationship. Highly repeatable resistance values have been obtained for all films.

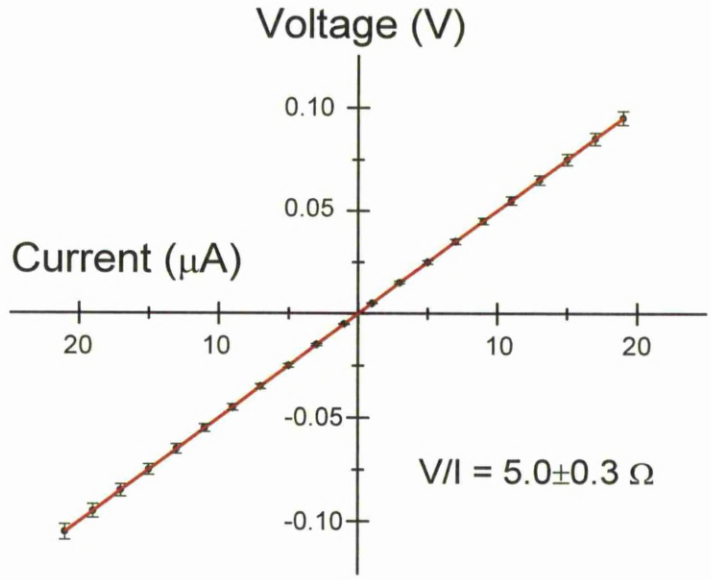

Figure 4.9 Four-point probe result for a film (~31nm) deposited at 300°C with 6s PDMAT and 12s ammonia doses.

The resistivity as a function of deposition temperature was investigated. Table 4.3 summarizes the resistivity for films (~30nm) deposited at different temperatures with 6s PDMAT and either 20ms MMH or 12s ammonia doses. Films deposited with ammonia have immeasurable resistivities at growth temperatures below 250°C. However, they became more conductive as the growth temperature increased, the resistivity was found to be 70±5 mΩ.cm at 300°C and 20±1 mΩ.cm at 350°C. The immeasurable resistivities at low deposition temperatures are due to oxygen ingress of the films. Ta_2O_5 is a good dielectric[23] and the resistivity of TaN films would be

expected to increase if oxygen is added to the material. The resistivity at a deposition temperature of 300°C correlates with previously published values for TaN.[40] At a deposition temperature of 350°C, MEIS indicates high carbon incorporation and as a result, the resistivities are partly attributed to tantalum carbide, which is also a good conductor.[15]

Growth temp. (°C)	Resistivity (Ω.cm)	
	MMH	Ammonia
200°C	Immeasurable	Immeasurable
250°C	300±20	Immeasurable
300°C	4±0.3	0.070±0.005
350°C	0.120±0.008	0.020±0.001

Table 4.3 Electrical resistivity for the films (30nm) deposited at different temperatures 6s PDMAT dose and either 20ms MMH or 12s ammonia doses.

The resistivities measured for the films deposited using MMH show a very similar trend. The resistivities were immeasurable at the growth temperature of 200°C but the films became more conductive at higher temperatures. The resistivity of films deposited at 300°C is ~4 Ω.cm and correlates well with the previous published values for Ta_3N_5.[6] At the highest temperature (350°C), the resistivity reduced significantly. This is believed to be a consequence of carbide formation when thermal decomposition of PDMAT takes place at this temperature.

Selecting the optimum growth temperature of 300°C, the effect of ammonia dose on the resistivity of films was investigated (Figure 4.10a). The resistivity decreases rapidly as the ammonia dose was increased, but as with the growth rate, it tends to saturate as the ammonia dose is increased above 6s. The resistivity reduces rapidly from ~1 Ω.cm for 1.5s doses down to ~70 mΩ.cm for 12s exposures. The main factor affecting resistivity is believed to be film density, which increased from 11.3 to

12.1 g/cm^3 when the ammonia dose increases from 3 to 12s. This increase in density inhibits oxygen ingress into the films during post growth exposure to air and hence inhibits the formation of insulating oxide. It may also reduce the number of vacancy defects within the film and hence gives rise to higher carrier mobility. For the MMH process (Figure 4.10b), the resistivity also saturates with the increasing MMH doses with a saturated resistivity of 4 Ω.cm.

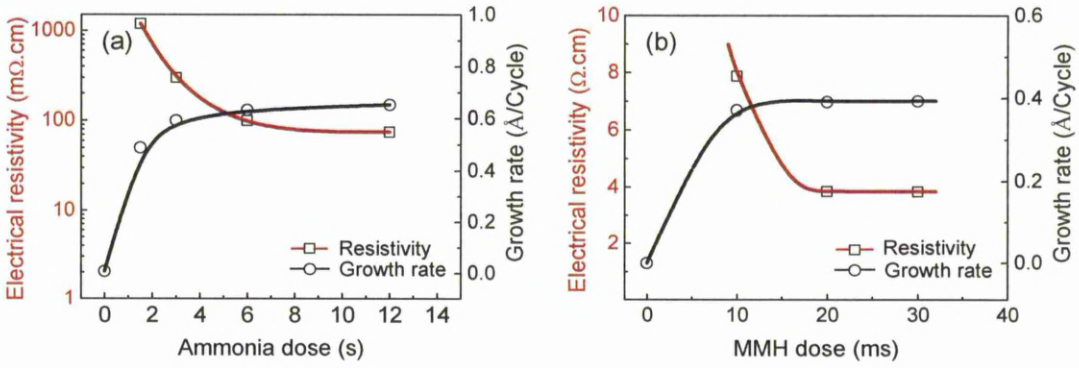

Figure 4.10 The electrical resistivity as a function of either (a) the ammonia dose or (b) the MMH dose at a deposition temperature of 300°C using 6s PDMAT. The growth rate is also shown for comparison. The error on growth rate is ±0.03Å/cycle, the error on resistivity $\Delta\rho/\rho$ is ±7%.

Although the resistivity of the most stoichiometric TaN films (70 mΩ.cm) remains somewhat higher than published values obtained using PEALD,[48] they are lower than previous thermal ALD studies and further improvements can be made using post growth heat treatments.[49] Previous ALD deposition experiments using PDMAT and ammonia reported insulating N-rich films,[38,43] the previous best results obtained by thermal ALD was the process using TBTDET and hydrazine, which has resulted in TaN resistivities of ~200 mΩ.cm.[40]

XRD results were obtained for the films (~100nm thick) deposited with both co-reactants across the studied temperature range. The films were found to be amorphous below 250°C, however, as the growth temperature increases to 300°C, the films deposited with ammonia start to crystallize into a face centred cubic structure (Figure 4.11). Films deposited using the MMH remained amorphous for all growth temperatures and may be attributed to the high nitrogen fraction, which is known to inhibit crystallisation of nitrogen rich TaN_x sputtered films.[14] The amorphous nature of these films could be advantageous for diffusion barrier applications as grain boundaries promote diffusion.[50,51]

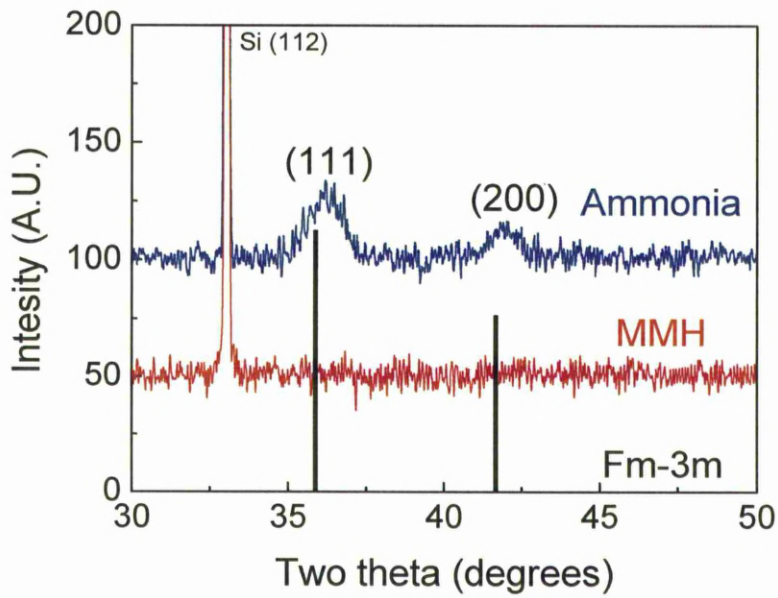

Figure 4.11 X-Ray diffraction patterns for the films (100nm) deposited using PDMAT (6s) and either ammonia (12s) or MMH (20ms) at 300°C. The reference pattern for the (111) and (200) feature of cubic TaN (JCPDS card number 89-5196) is also shown with a space group label of Fm-3m.

For the ammonia sample deposited at 300°C (Figure 4.11), two clear peaks were observed at 36.3° and 42.1°, which correspond closely with the (111) and (200) peaks of fcc TaN respectively (JCPDS card number 89-5196), indicating a polycrystalline

film with random orientations. The peaks are offset from the bulk reference pattern by 0.4° indicating that the lattice parameter is slightly smaller (2.47Å) than the bulk value of TaN (2.50Å). One plausible explanation is the intrinsic stress, which is due to insufficient temperature and relaxation for the material to achieve a perfect crystal structure. It seems is very likely that an annealing process could improve the crystal structure. The crystallite size, estimated using the Debye-Scherrer method, is ~5nm. TaN films with a similar crystallite size have been previously deposited using CVD,[52] although they were polycrystalline, the Cu/TaN/Si structure was reported to be stable after 1 hour annealing at 550°C in hydrogen atmosphere.[52] These films had significantly lower densities (7.2g/cm^3) than the TaN films deposited in the current study (12.1g/cm^3). Low density films have a large number of defects and voids, both of which can facilitate diffusion.[53] Thus, the TaN films deposited in this study is expected to have a similar or better diffusion barrier property to the reference.[52]

4.3 Summary

Thermal ALD of conductive TaN and insulating Ta_3N_5 has been demonstrated using PDMAT with either ammonia or MMH respectively. Both processes exhibit good self-limiting behaviour, with growth rates of 0.6 and 0.4 Å/cycle at 300°C for the ammonia and MMH respectively. Films deposited with ammonia at 300°C were found to be cubic TaN, with high conductivity (70 mΩ.cm) and densities comparable to the bulk values. During this ALD process, tantalum must undergo a reduction reaction from Ta(V) to Ta(III) to form TaN. Ammonia is able to reduce PDMAT to produce TaN without the need for an additional reductant.

Although conductive TaN is currently preferred for the applications as diffusion barriers, the significance of the MMH process presented here, which produces Ta_3N_5 should not be overlooked. This low temperature (200°C) MMH process, which is well within the processing temperature window required for microelectronics,[31] produces amorphous films that are expected to be a better diffusion barrier than those deposited using ammonia at the same temperature.

4.4 References

1. N. Terao, *Japanese Journal of Applied Physics* **10**, 248-259 (1970).

2. D. R. Lide, *CRC Handbook of Chemistry and Physics*. CRC Press: New York, p 4-64 (2009).

3. G. Brauer, J. Weidlein, J. Strahle, *Zeitschrift Fur Anorganische Und Allgemeine Chemie* **348**, 298-& (1966).

4. B. Mehrotra, J. Stimmell, *Journal of Vacuum Science & Technology B* **5**, 1736-1740 (1987).

5. R. Fix, R. G. Gordon, D. M. Hoffman, *Chemistry of Materials* **5**, 614-619 (1993).

6. K. Hieber, *Thin Solid Films* **24**, 157-164 (1974).

7. C. Stampfl, A. J. Freeman, *Physical Review B* **67**, 064108 (2003).

8. M. Wittmer, *Applied Physics Letters* **36**, 456-458 (1980).

9. H. Kim, C. Detavenier, O. van der Straten, S. M. Rossnagel, A. J. Kellock, D. G. Park, *Journal of Applied Physics* **98**, 014308-8 (2005).

10. K. Holloway, P. M. Fryer, C. Cabral, J. M. E. Harper, P. J. Bailey, K. H. Kelleher, *Journal of Applied Physics* **71**, 5433-5444 (1992).

11. J. O. Olowolafe, C. J. Mogab, R. B. Gregory, M. Kottke, *Journal of Applied Physics* **72**, 4099-4103 (1992).

12. T. Oku, E. Kawakami, M. Uekubo, K. Takahiro, S. Yamaguchi, M. Murakami, *Applied Surface Science* **99**, 265-272 (1996).

13. W. L. Yang, W. F. Wu, D. G. Liu, C. C. Wu, K. L. Ou, *Solid-State Electronics* **45**, 149-158 (2001).

14. D. J. Willmott, *Journal of Applied Physics* **43**, 4865-4871 (1972).

15. D. Gerstenberg, C. J. Calbick, *Journal of Applied Physics* **35**, 402-407 (1964).

16. C. S. Shin, Y. W. Kim, D. Gall, J. E. Greene, I. Petrov, *Thin Solid Films* **402**, 172-182 (2002).

17. H. Kim, A. J. Kellock, S. M. Rossnagel, *Journal of Applied Physics* **92**, 7080-7085 (2002).

18. H. Kim, C. Cabral, C. Lavoie, S. M. Rossnagel, *Journal of Vacuum Science & Technology B* **20**, 1321-1326 (2002).

19. K. Holloway, P. M. Fryer, *Applied Physics Letters* **57**, 1736-1738 (1990).

20. C. K. Hu, J. M. E. Harper, *Materials Chemistry and Physics* **52**, 5-16 (1998).

21. S. Gopalan, K. Onishi, R. Nieh, C. S. Kang, R. Choi, H. J. Cho, S. Krishnan, J. C. Lee, *Applied Physics Letters* **80**, 4416-4418 (2002).

22. J. K. Schaeffer, S. B. Samavedam, D. C. Gilmer, V. Dhandapani, P. J. Tobin, J. Mogab, B. Y. Nguyen, J. B. E. White, S. Dakshina-Murthy, R. S. Rai, Z. X. Jiang, R. Martin, M. V. Raymond, M. Zavala, L. B. La, J. A. Smith, R. Garcia, D. Roan, M. Kottke, R. B. Gregory, *Journal of Vacuum Science & Technology B* **21**, 11-17 (2003).

23. C. Chaneliere, J. L. Autran, R. A. B. Devine, B. Balland, *Materials Science and Engineering: R: Reports* **22**, 269-322 (1998).

24. W. P. Bai, S. H. Bae, H. C. Wen, S. Mathew, L. K. Bera, N. Balasubramanian, N. Yamada, M. F. Li, D. L. Kwong, *IEEE Electron Device Letters* **26**, 231-233 (2005).

25. C. L. Au, W. A. Anderson, D. A. Schmitz, J. C. Flassayer, F. M. Collins, *Journal of Materials Research* **5**, 1224-1232 (1990).

26. T. Yeh, D. Swanson, L. Berg, P. Karn, *IEEE Transactions on Magnetics* **33**, 3631-3633 (1997).

27. A. Rugge, J. S. Park, R. G. Gordon, S. H. Tolbert, *The Journal of Physical Chemistry B* **109**, 3764-3771 (2004).

28. M. Tabata, K. Maeda, M. Higashi, D. Lu, T. Takata, R. Abe, K. Domen, *Langmuir* **26**, 9161-9165 (2010).

29. X. Feng, T. J. LaTempa, J. I. Basham, G. K. Mor, O. K. Varghese, C. A. Grimes, *Nano Letters* **10**, 948-952 (2010).

30. N. Ramaswamy, V. Ananthan, D. Hwang, R. Iyer, C. Mouli, A. McTeer, S. Tang, K. Parekh, T. Owens, Y. P. Kim, N. Palaniappan, J. Li, S. Groothuis, G. Haller, S. Wang, In *Metal Gate Recessed Access Device (RAD) for DRAM Scaling, IEEE Workshop on Microelectronics and Electron Devices*, 42-44 (2007).

31. M. Juppo, M. Ritala, M. Leskela, *Journal of The Electrochemical Society* **147**, 3377-3381 (2000).

32. R. L. Puurunen, *Journal of Applied Physics* **97**, 121301 (2005).

33. T. Suntola, *Materials Science Reports* **4**, 261-312 (1989).

34. M. Ritala, M. Leskela, *Atomic Layer Deposition*. In *Handbook of Thin Film Materials*, N. S. Nalwa, Ed. Academic Press: San Diego, Vol. 1 (2002).

35. Y. J. Kwon Jung-Dae, Kang Sang-Won, *Japanese Journal of Applied Physics* **48**, 025504 (2009).

36. M. Ritala, P. Kalsi, D. Riihela, K. Kukli, M. Leskela, J. Jokinen, *Chemistry of Materials* **11**, 1712-1718 (1999).

37. P. Alen, M. Juppo, M. Ritala, T. Sajavaara, J. Keinonen, M. Leskela, *Journal of The Electrochemical Society* **148**, G566-G571 (2001).

38. Y. Y. Wu, A. Kohn, M. Eizenberg, *Journal of Applied Physics* **95**, 6167-6174 (2004).

39. N. J. Bae, K. I. Na, H. I. Cho, K. Y. Park, E. Boo, J. H. Bae, J. H. Lee, *Japanese Journal Of Applied Physics Part 1-Regular Papers Short Notes & Review Papers* **45**, 9072-9074 (2006).

40. B. B. Burton, A. R. Lavoie, S. M. George, *Journal of The Electrochemical Society* **155**, D508-D516 (2008).

41. B. H. Weiller, *Journal of the American Chemical Society* **118**, 4975-4983 (1996).

42. S. Somani, A. Mukhopadhyay, C. Musgrave, *The Journal of Physical Chemistry C* **115**, 11507-11513 (2011).

43. W. J. Maeng, S. J. Park, H. Kim, *Journal of Vacuum Science & Technology B* **24**, 2276-2281 (2006).

44. D. K. Gaskill, N. Bottka, M. C. Lin, *Journal of Crystal Growth* **77**, 418-423 (1986).

45. Reaxys. http://www.reaxys.com/ (accessed 23-Fab-2011).

46. J. O. Olowolafe, C. J. Mogab, R. B. Gregory, M. Kottke, *Journal of Applied Physics* **72**, 4099-4103 (1992).

47. J. A. van den Berg, G. Carter, D. G. Armour, M. Werner, R. D. Goldberg, E. J. H. Collart, P. Bailey, T. C. Q. Noakes, *Applied Physics Letters* **85**, 3074-3076 (2004).

48. H. Kim, C. Lavoie, M. Copel, V. Narayanan, D. G. Park, S. M. Rossnagel, *Journal of Applied Physics* **95**, 5848-5855 (2004).

49. R. Sreenivasan, T. Sugawara, K. C. Saraswat, P. C. McIntyre, *Applied Physics Letters* **90**, 102101 (2007).

50. J. F. Kang, H. Y. Yu, C. Ren, N. Sa, H. Yang, M.-F. Li, D. S. H. Chan, X. Y. Liu, R. Q. Han, D.-L. Kwong, *Journal of The Electrochemical Society* **154**, H927-H932 (2007).

51. A. E. Kaloyeros, E. Eisenbraun, *Annual Review of Materials Science* **30**, 363-385 (2000).

52. S. L. Cho, K. B. Kim, S. H. Min, H. K. Shin, S. D. Kim, *Journal of The Electrochemical Society* **146**, 3724-3730 (1999).

53. H. C. M. Knoops, L. Baggetto, E. Langereis, M. C. M. van de Sanden, J. H. Klootwijk, F. Roozeboom, R. A. H. Niessen, P. H. L. Notten, W. M. M. Kessels, *Journal of The Electrochemical Society* **155**, G287-G294 (2008).

Chapter 5. Hafnium nitride

This chapter focuses on the investigation of nitride deposition using PEALD and its differences with thermal ALD. Thin films of hafnium nitride have been deposited using PEALD and compared with a thermal process. No previous report is available in the literature for such direct comparison, and the results presented here show that PEALD have some advantages to thermal ALD: PEALD allows the deposition of higher density films within a shorter cycle time by reducing the required purge length.

5.1 Introduction

Hafnium and tantalum are adjacent elements in period 6 of the periodic table. Their nitrides, HfN_x and TaN_x have very similar properties. HfN_x has two stoichiometric forms, the mono nitride form, HfN, is a conductor,[1,2] whilst the nitrogen rich Hf_3N_4 form is reported to be insulating [3-5] or semiconducting.[6,7] These stoichiometric nitrides have excellent thermal stability,[8] high resistance to oxygen diffusion,[9] and they are chemically stable with respect to hafnium oxide,[10] which is currently being employed as the high-k dielectric material in CMOS devices. In addition, it is feasible to deposit both hafnium oxide and nitride in a two stage ALD process using a common organometallic precursor.[3,11] Stoichiometric HfN can exhibit very low resistivities ($33\mu\Omega.cm$)[2] and could, therefore be used as a electrical contact material or as an interlayer between the gate oxide and gate metal to prevent inter-diffusion. In contrast, insulating Hf_3N_4 could be used as a dielectric material and also as a buffer layer between the high-k dielectric and the substrate to prevent oxidation of the silicon or inter-diffusion at the interface.

Despite their potential uses in CMOS gate stacks, as well as other conceivable applications such as a adhesion layer[12] and hardness coating,[13] thin film HfN_x has not been widely explored in the scientific literature. A handful of papers have reported more conventional methods of depositing HfN_x films using techniques such as reactive magnetron sputtering,[7,14,15], reactive-sputtering,[16] sputtering,[17,18] chemical vapour deposition,[19-21] and pulsed laser deposition.[1] Deposition of Hf_3N_4 has been reported using thermal ALD with either tetrakis(diemethylamino)hafnium (TDMAH)[3] or tetrakis(ethylmethylamino)hafnium (TEMAH),[22,23] and ammonia. Conductive HfN has been deposited using PEALD with TEMAH and Ar/H_2 plasma. A mixed H_2/N_2 plasma has been used with TDMAH, where both HfN and Hf_3N_4 have been deposited by adjusting the H_2 to N_2 partial pressure.[24] Hf_3N_4 has also been deposited with TDMAH and pure N_2 plasma.[25] From the literature data, it is clear that both thermal and PE ALD process can deposit HfN_x, however, the differences between these techniques remain unclear due to the lack of a systematic study. This has been investigated in the current work.

In this research, deposition was firstly carried out using thermal ALD with TDMAH and molecular ammonia, which resulted in films with a low density, and they were prone to oxidation during post-deposition exposure to air. Subsequently, deposition was carried out using PEALD with TEMAH and an ammonia plasma, the thermal process with molecular ammonia was also carried out for a direct comparison. The use of ammonia plasma has not been reported previously, and it has been found to produce films with a superior density than those deposited with molecular ammonia. The PEALD process also has an added advantage of shorter purge times, which significantly reduces the overall cycle length. Mass spectrometry indicates that these

features are attributed to the reactive species involved in the PEALD process, namely hydrogen and nitrogen radicals.

5.2 Results and discussion

5.2.1 Thermal ALD of HfN_x

Hafnium nitride films were deposited on 40×40mm square p-type Si(100) substrates. Thermal ALD study was conducted using an OpAL thermal ALD reactor with TDMAH and ammonia and the growth parameters are summarised in Table 5.1.

Reactor, leak rate and cleaning method	OpAL thermal ALD reactor, 1mTorr/min, 1 hour Ar pump and purge	
TDMAH transport temperatures	40°C (bubbler) – 70°C (manifold) - 100°C (chamber walls)	
Substrate temperature	100-400°C	
TDMAH doses	150sccm 0-1s	
TDMAH purge	250sccm 12s	
Co-reactant	**Without co-reactant**	**Ammonia**
Co-reactant doses	N.A.	0-10sccm 1.5s
Co-reactant purge	250sccm 5-15s	

Table 5.1 Growth parameters for the thermal ALD of HfN_x using TDMAH with either ammonia or without any co-reactant.

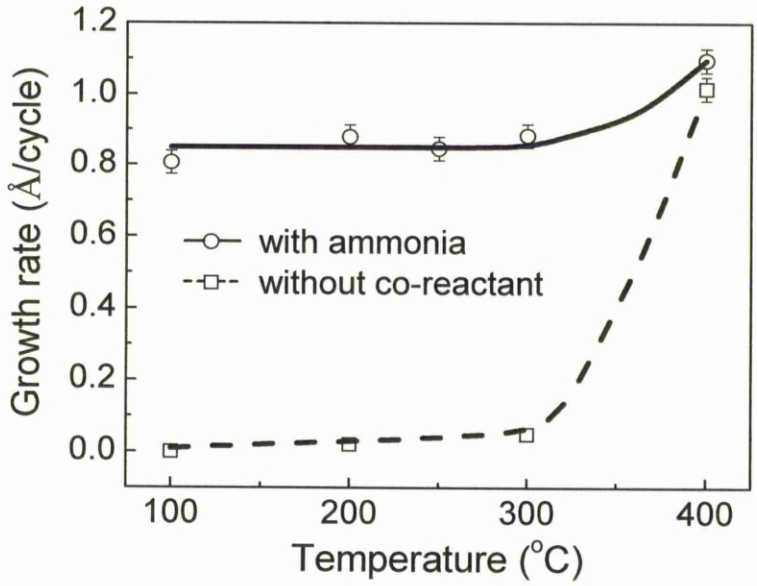

Figure 5.1 Growth rate as a function of deposition temperature using 300 ALD cycles with 0.5s TDMAH doses and either 2.5sccm ammonia doses or without any co-reactant. The co-reactant purge length was 15s.

The effects of growth temperature (Figure 5.1) were investigated between 100 and 400°C. The growth rates were corroborated using 300 ALD cycles with 0.5s TDMAH doses and either 2.5sccm ammonia or without any co-reactant. In the absence of a co-reactant, growth rate is close to zero below 300°C, but increases rapidly to 1.1 Å/cycle at 400°C. The near zero growth rate below 300°C shows that the current experimental setup meets the basic requirement for nitride deposition, namely, an environment that is free of reactive oxidant. Any oxidant, such as oxygen or water, would lead to oxide reactions with TDMAH and result in non-zero growth rates at these temperatures.[11] This is not observed in the current study and therefore, the reaction chamber and carrier gases contain negligible oxidant. The high growth rate above 300°C indicates that TDMAH suffers from thermal decomposition, and is

consistent with the previous PEALD of hafnium nitride using TDMAH and N_2 plasma reported by Jeong et al..[25]

For the films deposited with ammonia (Figure 5.1), a stable growth rate of ~0.9 Å/cycle was observed at temperatures between 100 and 300°C, providing an ALD temperature window. The growth rate, increases again at temperatures higher than 300°C due to the thermal decomposition of TDMAH. The observation of an ALD window is consistent with the previous ALD deposition of HfN_x using TDMAH and ammonia.[3]

Selecting the optimal temperature of 300°C, which provides the most thermal energy to the nitridation reaction within the ALD window, the effects of the TDMAH dose (Figure 5.2) were investigated. The films were grown using 100 ALD cycles with 5sccm ammonia doses and either 5 or 15s co-reactant purge. With a co-reactant purge length of 5s, the growth rate increases dramatically from 0 to 2 Å/cycle at TDMAH doses of 0.2-0.65s, showing that the growth rate is not saturative, but is dependent on the total flux of TDMAH molecules. This is due to an insufficient co-reactant purge length, which leads to an incomplete removal of reaction by-products and excessive co-reactant molecules in the chamber. These chemical species react with TDMAH in the gas phase during the subsequent ALD cycle, resulting in a gas phase CVD-like deposition rather than a saturative one. With an extended purge length of 15s (Figure 5.2), the growth rate clearly becomes self-limiting. After the initial increase from 0-0.9 Å/cycle between 0 and 0.5s, the growth rate plateaus at ~1 Å/cycle for longer doses, showing good self-limiting behaviour; this is consistent with the previous ALD depositions of HfN_x using TDMAH and ammonia.[3]

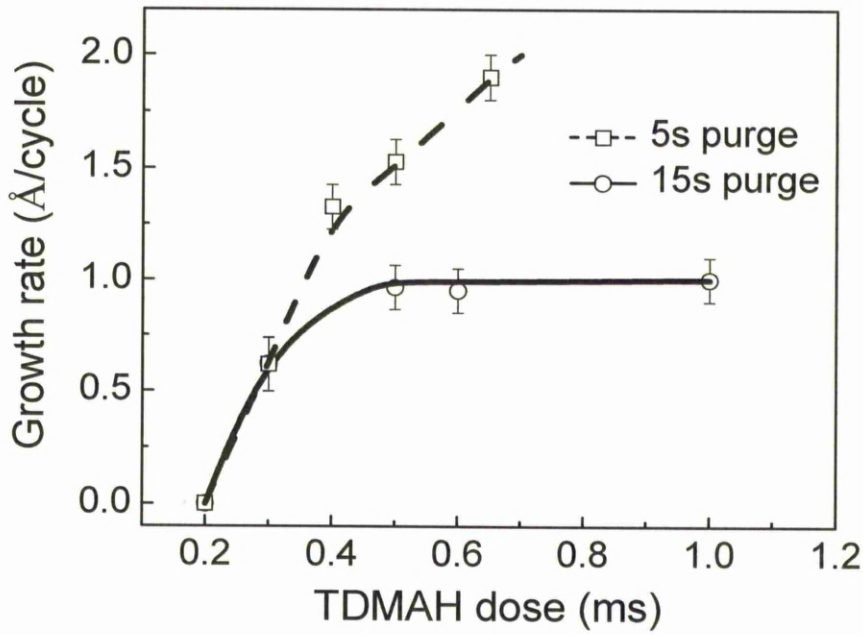

Figure 5.2 Growth rate as a function of TDMAH dose for the ALD deposition at 300°C using 100 ALD cycles with 5sccm ammonia doses. The effect of co-reactant purge length was investigated at 5 and 15s.

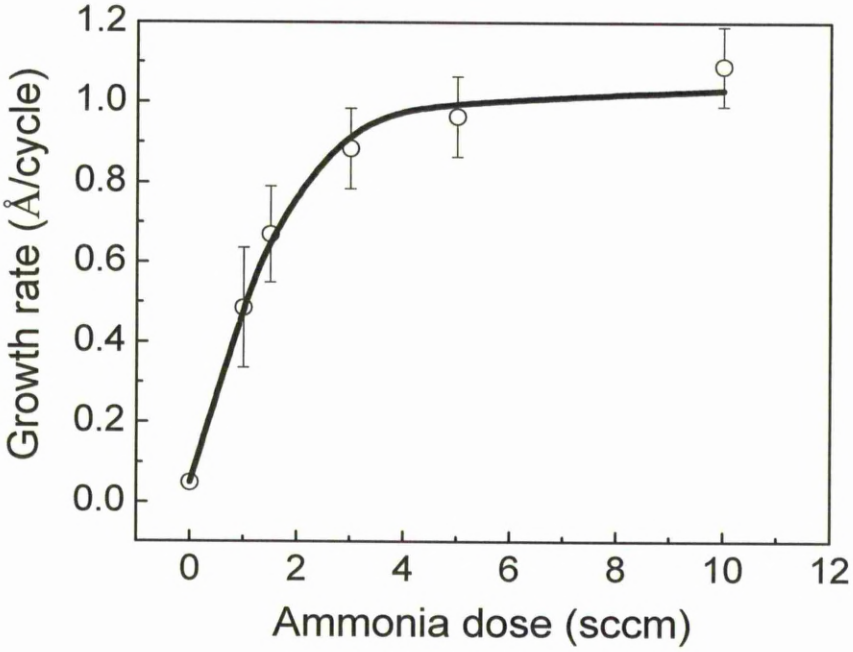

Figure 5.3 Growth rate as a function of ammonia dose for the ALD deposition at 300°C using 100 ALD cycles with 0.5s TDMAH and 15s co-reactant purge.

The ammonia co-reactant also displays a good self-limiting behaviour. Figure 5.3 shows the change of the growth rate when varying ammonia doses from 0-10sccm with 0.5s TDMAH doses and a 15s co-reactant purge. The growth rate initially increases from 0-0.9 Å/cycle between 0-2.5sccm ammonia doses and then saturates at ~1 Å/cycle, providing good self-limiting behaviour.

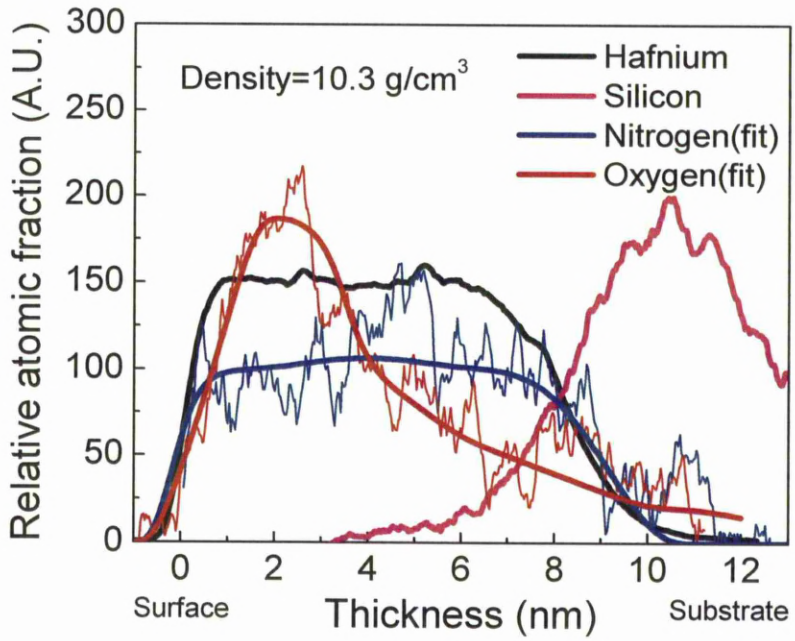

Figure 5.4 The MEIS depth profile of a film deposited using 110 cycles of 0.6s TDMAH, 5sccm ammonia and 15s co-reactant purge at 300°C. Data were gathered for a dose of 6μC.

The chemical composition of the films were analysed by MEIS. All energy-to-depth conversion in this chapter was carried out using the stopping powers of He^+ in HfN with a density of 13.8 g/cm^3.[26] Figure 5.4 shows a MEIS depth profile for a film deposited at 300°C using 110 cycles of 0.6s TDMAH and 5sccm ammonia. Hf, N, O were detected, however, no carbon was seen with a practical detection limit of ~10%. Both hafnium and nitrogen features are present over a thickness range between 0 and 8nm, the Hf:N ratio was found to be 0.6, which disagrees with both stoichiometric

phases of HfN and Hf_3N_4. The oxygen content was found to be high near the film surface but gradually decreases towards the film bulk. The density of the film was found to be ~10.3 g/cm^3, and is ~70% of the bulk density (13.8 g/cm^3). This is considered to be a low density for thin films[27] and is largely responsible for the observed oxygen incorporation as discussed below.

The shape of the oxygen feature indicates that the film suffered from oxygen ingress during post-deposition exposure to air. If the oxygen was incorporated during the ALD deposition, the oxygen signal in MEIS would distribute uniformly throughout the film, which is not observed and hence is less likely the case. The low nitrogen incorporation compared with hafnium shows that the film is non-stoichiometric, which can be attributed to partial oxidation of the film when exposed to air. Consequently an intermixture of hafnium oxynitride (HfN_xO_y) was formed near the surface. This oxidation is largely attributed to the low density. A low density film means a higher number of defects in the layer, previous study has argued that the metal to nitrogen bonds are particularly weak at these defects, which can give rise to oxidation.[28] The correlation between oxidation rate and film density has been previously studied for TiN films deposited by sputtering, where the film density was controlled by growth conditions.[27,28] These papers show that at room temperature, the oxidation rate of TiN films (60-200nm) varies correspondingly to the film density, with lower density films more prone to oxidation.[27,28] The films in the current study were exposed to air several days prior to the MEIS characterisation and therefore can be oxidised during this period.

Depth (nm)	Composition (at.%)			
	Hf	N	O	C
0	23	3	64	10
8.5	30	25	39	6
25.5	37	48	5	10

Table 5.2 AES composition for the film (~30nm) deposited by thermal ALD with 300 cycles of 0.6s TDMAH, 5sccm ammonia and 15s co-reactant purge at 300°C.

In order to extract the nitride stoichiometry in the bulk part of the film, thick samples were prepared and analysed by AES (Table 5.2). AES experiment was carried out by Gary Critchlow at Loughborough University for the film (30nm) deposited at 300°C using 300cycles with 0.6s TDMAH and 5scccm ammonia doses. Hf, O, N, and C were detected. The oxygen incorporation is high near the surface but decreases to ~5% at a depth of ~25nm. The nitrogen incorporation is low near the surface but increases towards the film bulk, at a depth of ~25nm the Hf:N ratio found to be ~1:1.3, which is in a good agreement with the nitrogen rich, Hf_3N_4 stoichiometry. This shows that the film has suffered from oxygen ingress during post-deposition exposure to air, and a layer of oxynitride has been formed near the surface, in a good agreement with MEIS. AES also detected a level of carbon contamination (~10%), which can be attributed to an incomplete reaction between TDMAH and ammonia, a trace level of carbon rich ligands can be trapped in the films. These ligands occupy extra space and are also partly responsible for the observed low density. Both carbon incorporation and low film density indicate that the surface reaction between TDMAH and ammonia is not optimum for the deposition of high density films. Further studies using alternative co-reactants with a superior reactivity to ammonia are required.

5.2.2 Thermal vs. plasma enhanced ALD

PEALD provides highly reactive radicals and supplies additional energy to ALD surface reactions,[29] which may overcome the limitations of thermal ALD processes using co-reactants such as ammonia. In the following section, a comparison was made between thermal and PE ALD. Films were deposited on 100mm diameter P type Si(100) substrates. Deposition was carried out using a FlexAL plasma ALD reactor with TEMAH and either molecular ammonia or an ammonia plasma. TEMAH was used instead of TDMAH due to the availability. Previous study using TEMAH show that the optimum deposition temperature is 300°C[30] and this was adopted in the current study. All growth parameters are summarised in Table 5.3, chamber pressure in FlexAL was maintained at 40mTorr by a butterfly valve. Growth rates were corroborated from the thickness of the films deposited using 300 ALD cycles.

Reactor, leak rate and cleaning method	FlexAL plasma ALD reactor, 1mTorr/min, 5 minutes Ar pump and purge	
TEMAH transport temperatures	80°C (bubbler) – 120°C (manifold) - 150°C (chamber walls)	
Substrate temperature	300°C	
TEMAH doses	250sccm 0-1.2s	
TEMAH purge	250sccm 5s	
Co-reactant	**Molecular ammonia**	**Plasma ammonia**
Co-reactant doses	10sccm 3s	0-30sccm 3s **400W**
Co-reactant purge	250sccm 15s	250sccm 5s

Table 5.3 Growth parameters for the depositions of HfN_x using thermal and PE ALD with TEMAH and either molecular ammonia or an ammonia plasma.

5.2.2.1 Growth characteristics

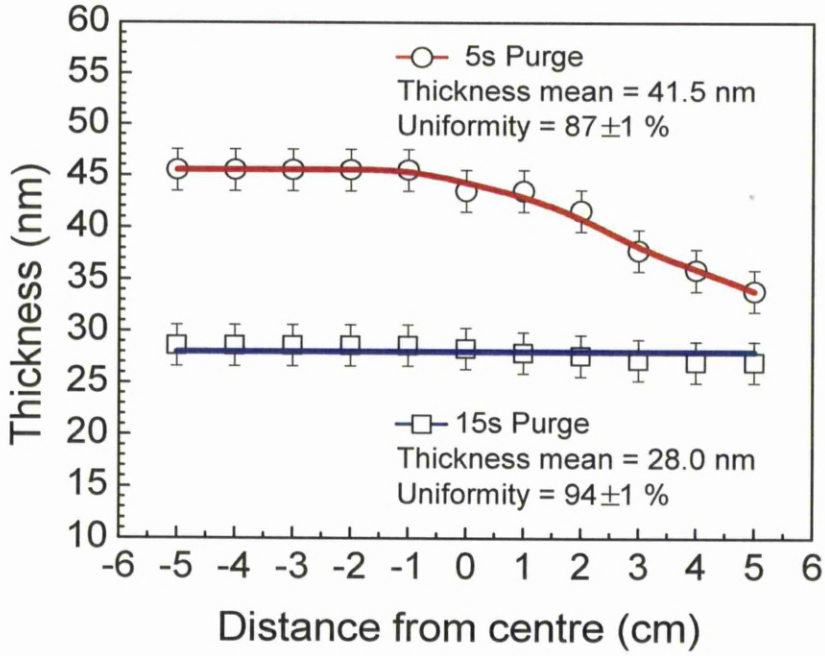

Figure 5.5 Thickness measured at multiple points of HfN_x films deposited on a 100mm diameter silicon substrate using 300 ALD cycles of TEMAH (1s) and molecular ammonia (10sccm 3s) with either 5s or 15s purge.

The effect of co-reactant purge time (either 5 or 15s) was investigated using the processes with TEMAH (1s) and either an ammonia plasma (10sccm) or molecular ammonia (10sccm). In thermal ALD (Figure 5.5), a 5s purge results in films with poor uniformity (87±1%) and a high growth rate. The growth rate was found to be 1.3 Å/cycle, and is significantly higher than the saturated growth rate of ~1 Å/cycle (Figure 5.8). This shows that a 5s purge is insufficient to separate precursor and co-reactant doses, leading to gas phase CVD-like reactions and resulting in a high growth rate with poor uniformity. With an extended purge of 15s (Figure 5.5), the growth rate reduces to ~1 Å/cycle and the uniformity improves to 94±1%, showing that the deposition is driven by self-limiting surface reactions. It is worth noting that this

observation is similar to the thermal ALD process using TDMAH and ammonia (Figure 5.2) that a long purge length is required to achieve self-limiting behaviour.

In PEALD by contrast, a 5s purge is sufficient to achieve self-limiting deposition with a growth rate of ~1 Å/cycle and a film uniformity of 95±1%. These results confirm that by changing the nitrogen co-reactant from molecular ammonia into an ammonia plasma, the required purge time for self-limiting growth has been significantly reduced. The reason was investigated using in-situ gas phase analyses by mass spectrometry.

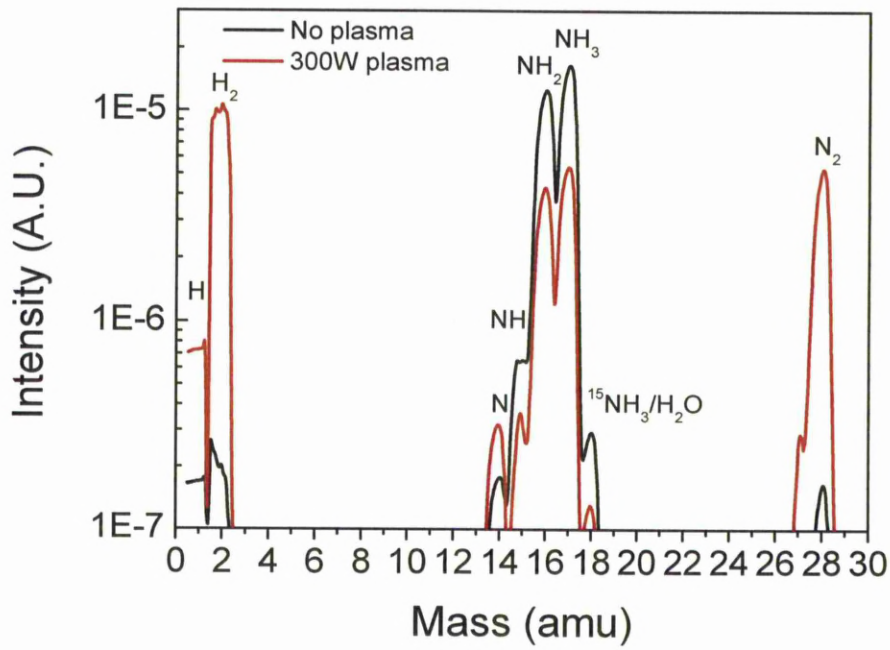

Figure 5.6 Mass spectrometry results of a continuous ammonia flow (10sccm) with and without 300W plasma power.

Mass spectrometry was used to compare the gas phase composition of plasma ammonia and molecular ammonia. The ammonia flow rate was maintained at 10sccm and the plasma power was increased from 0 to 300W. Figure 5.6 shows the spectra

obtained for the ammonia with and without 300W plasma power, peaks at the mass 1(H), 2(H_2), 14(N), 15(NH), 16(NH_2), 17(NH_3), 18($^{15}NH_3/H_2O$) and 28(N_2) were detected. The intensities of these peaks as a function of the plasma power are shown in Figure 5.7.

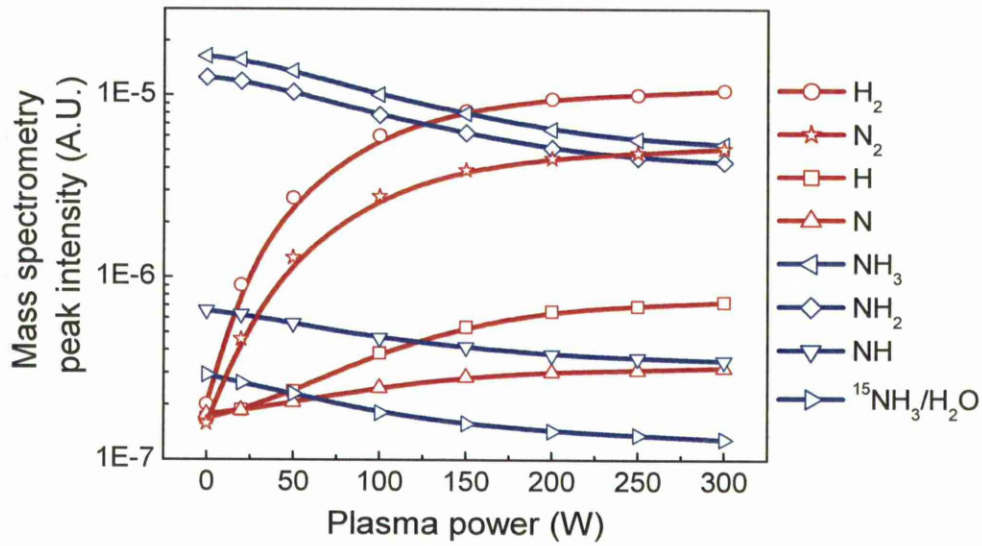

Figure 5.7 Mass spectroscopy peak intensities recorded for the mass 1(H), 2(H_2), 14(N), 15(NH), 16(NH_2), 17(NH_3), 18($^{15}NH_3/H_2O$) and 28(N_2) as a function of the plasma power.

From Figure 5.7, it is clear that increasing plasma power results in decreasing intensities for ammonia related species (NH_3, NH_2, NH and $^{15}NH_3$), and increasing intensities for both hydrogen (H and H_2) and nitrogen (N and N_2) related species. In mass spectrometry, if the pressure is maintained constant, the peak intensity is proportional to molecule/atom quantity. Therefore, the observed results are interpreted as a decomposition of molecular ammonia by the plasma energy, forming nitrogen and hydrogen radicals. These radicals are very reactive and tend to recombine into molecules once they left the inductively coupled plasma chamber.[31] In an ALD cycle, while a fraction of these radicals participate in the surface reactions with TEMAH and form nitride, the majority of radicals recombine into H_2 and N_2

molecules. They are believed to be chemically inert to TEMAH at 300°C and therefore, the purge length in the PEALD process could be dramatically reduced. For this reason, a purge length of 5s was chosen in the rest of the study when using PEALD for the deposition of HfN_x.

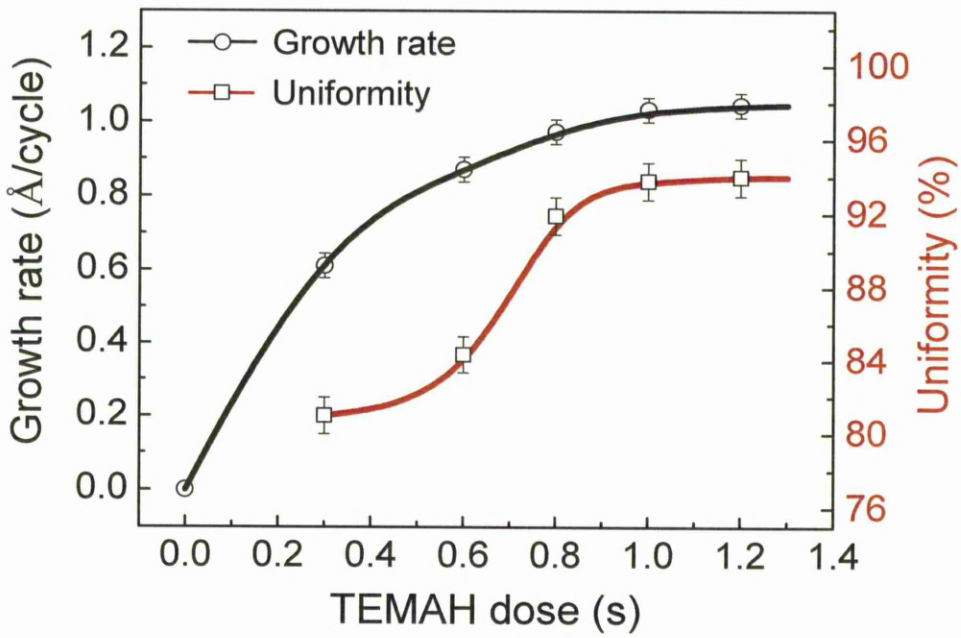

Figure 5.8 Growth rate and film uniformity as a function of TEMAH dose when using 300 ALD cycles with 10sccm plasma ammonia doses at 300°C.

To study the self-limiting behaviour, the effect of the TEMAH dose was investigated using 300 ALD cycles with 10sccm plasma ammonia doses (3s). The growth rate, as shown in Figure 5.8, increases from 0 to 0.9 Å/cycle between 0 and 0.8s, and plateaus above 1 Å/cycle. In addition, the film uniformity shows a similar trend, improving from 81% to 92% between 0.3 and 0.8s doses, further plateaus at 95%. These results confirm that TEMAH is a good self-limiting precursor for ALD. The growth rates for thermal and PE ALD using 1s TEMAH and 10sccm ammonia are very similar; with a growth rate of ~1 Å/cycle.

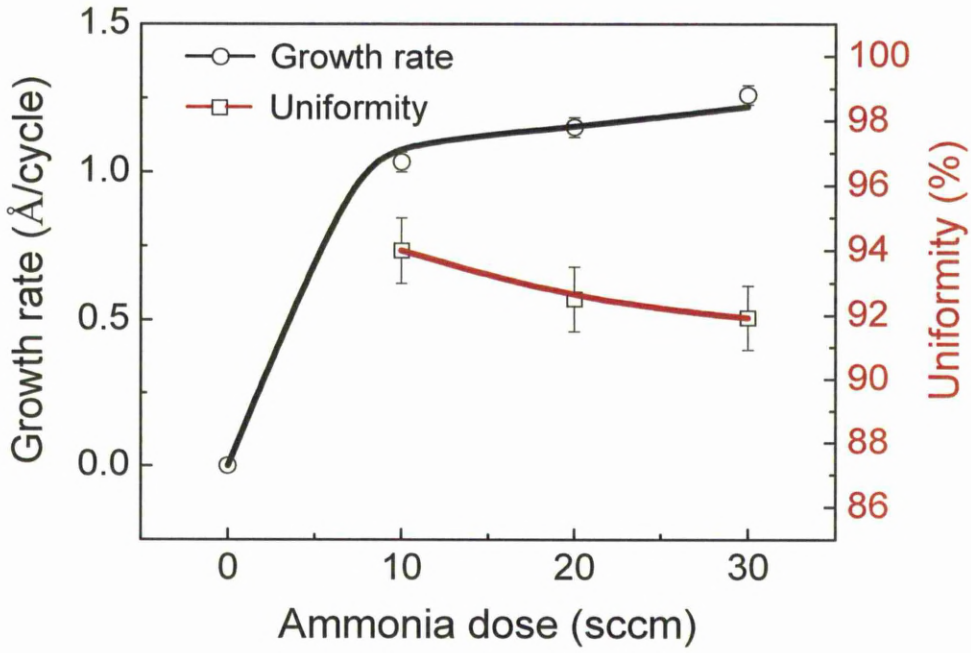

Figure 5.9 Growth rate and film uniformity as a function of plasma ammonia dose when using 300 ALD cycles with 1s TEMAH doses at 300°C.

The effect of ammonia plasma doses was also investigated by varying the ammonia flow rate at a fixed 3s dose using 300 ALD cycles with 1s TEMAH doses (Figure 5.9). After the initial increase, the growth rate reaches 1 Å/cycle at 10sccm doses and slowly rises to 1.2 Å/cycle at 30sccm doses. Similar behaviours of this slow increase within the saturation region has also been observed in the hafnium oxide ALD study using TEMAH and either H_2O or ozone.[11] Although no explanation was provide in this literature, some insights were raised by the change of uniformity in the current study. The uniformity (Figure 5.9) ascertained by ellipsometry, is 94% at 10sccm but decreases to 92% at 30sccm. The increasing growth rate and decreasing uniformity are indicative of insufficient purging at higher ammonia doses. There could be residual reactive species in the gas phase that combine with the subsequent pulse of TEMAH, resulting in higher growth rate and reduced uniformity. However, because a good uniformity has been achieved at low doses, this was not investigated further, and

a flow rate of 10sccm ammonia was chosen for the comparison between thermal and PE ALD.

5.2.2.2 Composition analysis

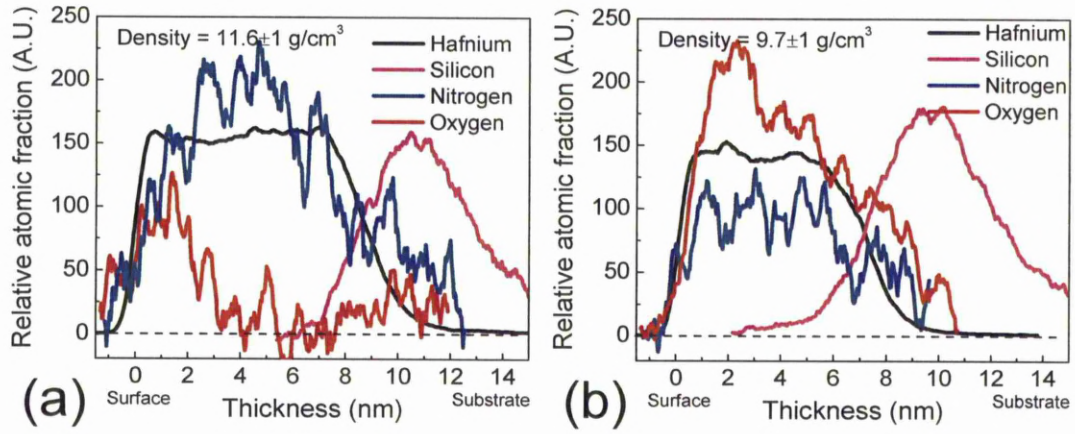

Figure 5.10 MEIS depth profiles for the films deposited using 100 cycles with 1s TEMAH and either (a) 10sccm plasma ammonia or (b) 10sccm molecular ammonia at 300°C.

Selected films were characterised using MEIS and TEM to investigate the chemical composition and to extract film density. Figure 5.10 (a) shows the MEIS depth profile for a film deposited using 100 cycles with 1s TEMAH and 10sccm plasma ammonia at 300°C. Hafnium, nitrogen and oxygen signals were detected, no carbon was seen with a detection limit of ~10%. The hafnium and nitrogen features are present from 0 to 8nm with a Hf:N ratio close to 1:1.3, which is consistent with the stoichiometry of Hf_3N_4. The oxygen content is high near the surface (0-4nm); however, it decreases dramatically into the film bulk; at a depth of 6nm, the oxygen signal is close to the background noise, meaning that the oxygen incorporation is below ~5 at.%. At a depth of 10nm, the signal rises again and this is due to the oxygen content from the

SiO_2 layer on the Si substrate. The density of this film was found to be 11.6±1 g/cm^3, which is 84% of the bulk density (13.8 g/cm^3).

Figure 5.10 (b) shows the MEIS depth profile for a film deposited using 100 cycles with 1s TEMAH and 10sccm molecular ammonia at 300°C. Hafnium, nitrogen and oxygen were evident in the layer again. The hafnium and nitrogen signals were detected at 0-8nm, however, the nitrogen content is significantly lower than the film deposited with plasma. The oxygen signal, by contrast, is seen across the entire depth of the film; the oxygen content is high near the surface, but gradually decreases towards the film bulk. The low nitrogen and the high oxygen content is attributed to a low film density, which was found to be 9.7 g/cm^3 and is ~70% achievement of the bulk density (13.8 g/cm^3). This is similar to the film deposited using thermal ALD with TDMAH and molecular ammonia (Figure 5.4). As explained in section 5.2.1, the low density leads to oxygen ingress when the film was exposed to air, and in this particular case, the oxygen has completely penetrated to a depth of 8nm. The film deposited using PEALD show an oxygen penetration of only ~4nm, and is attributed to its high density.

It is clear that PEALD yields higher film density compared with thermal ALD, which has also been observed in the previous PEALD studies of Ta_2O_5[32] and HfO_2.[33] This can be attributed to the extra kinetic energy of the adsorbate species generated by the plasma discharge. First principle calculations have been used previously to compare the ammonia plasma and molecular ammonia processes. The analysis shows that the reaction between metal precursors and an ammonia plasma is spontaneous; however, the reaction with molecular ammonia requires external energy,[29] in the present case, the thermal energy. In PEALD, the radical forms of hydrogen and nitrogen are more

reactive than molecular ammonia, providing a more favourable reaction kinetics with TEMAH. A more favourable reaction kinetics may enhance the mobility of surface species for them to find the most vacant site during reactions. If the mobility of the surface species is insufficient in thermal ALD, they may block reaction sites and give rise to defects, which reduce the overall density. Furthermore, because radicals have smaller sizes than molecular ammonia, they may lead to a surface with denser reaction sites, which facilitates a closer packing density of chemisorbed TEMAH molecules, improving the film density.

The refractive index (λ=632.8nm) of films (~30nm) deposited using an ammonia plasma was found to be 2.40±0.05, which is higher than those deposited using molecular ammonia with a refractive index of 2.13±0.05. The higher refractive index may be attributed to a higher film density, since there are more materials to give polarizibility. It may also be attributed to low oxygen incorporation in the PEALD films. In transition metal oxynitrides, the refractive index is expected to decrease when nitrogen atoms are substituted by oxygen.[34] The polarizability of metal-oxygen bonds tends to be higher than that of metal-nitrogen bonds, leading to a lower polarizability of the metal-oxides and thus a lower refractive index.[34] A similar decrease in refractive index has also been observed in the deposition of Hf_3N_4 and Zr_3N_4 when oxygen is incorporated in the films.[3,35]

5.2.2.3 Microstructure and electrical properties

The microstructure of the films deposited using both thermal and plasma process was investigated using XRD and TEM. X-ray diffraction analysis of all films shows the absence of any diffraction features, indicating that they are effectively amorphous. However in XRD, the insensitivity of the equipment can also cause the absence of diffraction peaks and to disprove this, the nitride films deposited using molecular ammonia were annealed in air at 800°C for 10 minutes. Given sufficient temperature and an oxygen rich environment, the film was converted into HfO_2 with a monoclinic structure as illustrated in Figure 5.11. This shows that the diffractometer was sensitive to crystal structure and the as-deposited nitride films are effectively amorphous.

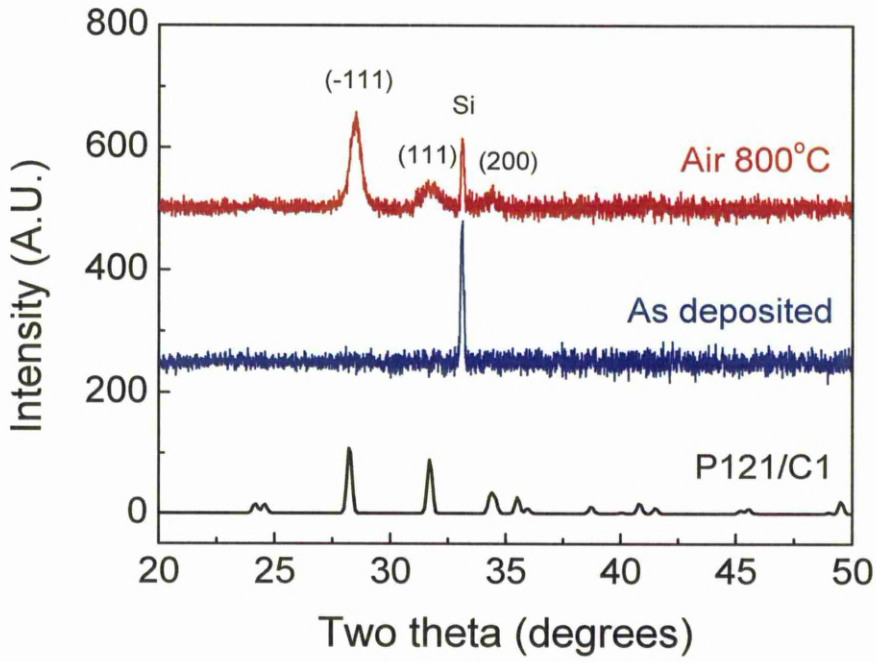

Figure 5.11 XRD for the as-deposited film prepared using 1s TEMAH with 10sccm molecular ammonia and after air anneal at 800°C, a monoclinic HfO_2 reference spectrum was also given (P121/C1).[36]

The amorphousness was also confirmed by TEM, and a dark-field micrograph for the film deposited using 300 cycles with TEMAH (1s) and molecular ammonia (10sccm) is shown in Figure 5.12. The film has a featureless microstructure, and no crystalline structure is evident. The same TEM results have also been observed with the films deposited using PEALD (Not shown). For the films to be used as a diffusion barrier, an amorphous microstructure is preferred to a polycrystalline one, because diffusion and current leakage can occur along grain boundaries.[37]

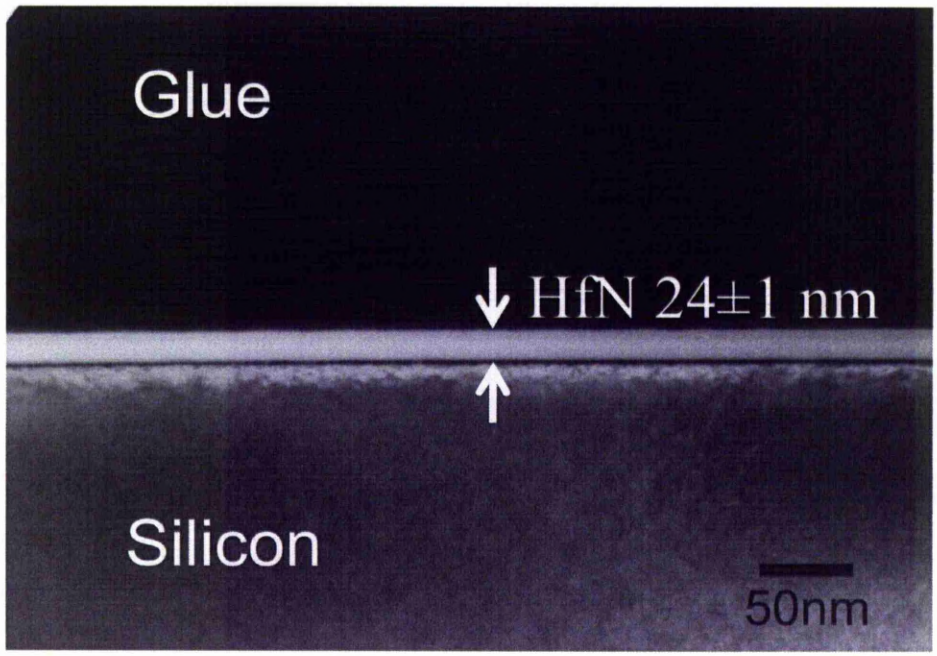

Figure 5.12 A TEM micrograph for the film deposited using 300 cycles of TEMAH (1s) and molecular ammonia (10sccm) at 300°C.

All four-point probe measurements for the films (30nm) on P-type silicon result in immeasurable voltage using the current ranging from 2 nA to 2 mA. This confirms that all films deposited are insulators and have successfully functioned as a dielectric to stop current flow in the silicon substrate, which is expected with the Hf_3N_4 stoichiometry.[3] The insulating nature of the films may also be attributed to oxygen ingress because HfO_xN_y is also a good dielectric.[38]

5.2.2.4 Thermal stability

In the manufacture of electronic devices, post-deposition annealing is often employed to reduce defects, improve physical properties and therefore enhance layer functionalities. For hafnium nitride, the film can be used as a diffusion barrier.[16] This requires the layers to be thermodynamically stable in contact with silicon at high temperatures, and ideally with interconnect materials such as copper and nickel as well. In this work, the stability of PEALD films on silicon was analysed.

MEIS was used to study the thermal stability of Hf_3N_4. Firstly, a film deposited at 300°C using 100 cycles with 1s TEMAH and 10sccm plasma ammonia was characterised; the film was then annealed in the MEIS sample transfer chamber ($1x10^{-9}$ mbar) for 10 minutes at temperatures of 500, 600, 700 and 800°C. A MEIS spectrum was recorded at each annealing stage.

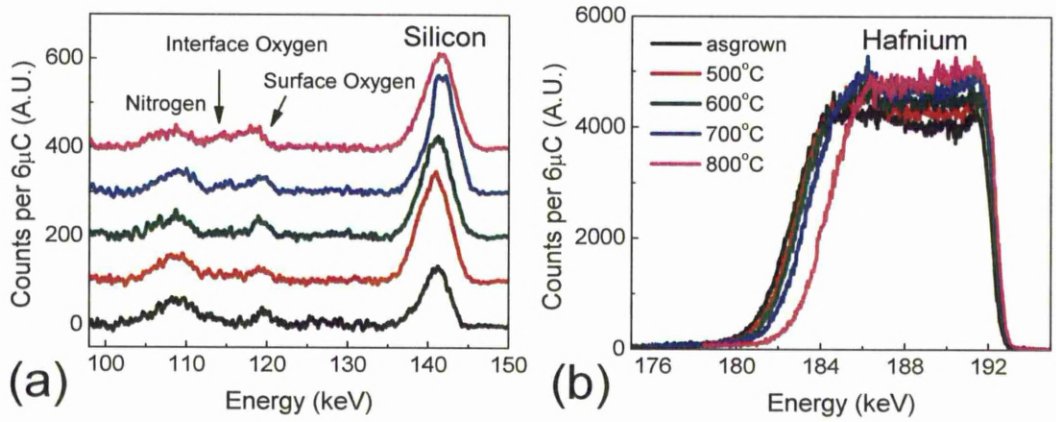

Figure 5.13 The MEIS spectrum for the as-deposited film using 100 cycles with 1s TEMAH and 10sccm plasma ammonia at 300°C and after in-situ annealing at 500,600,700 and 800°C. The spectra are displayed in (a) low and (b) high energy ranges due to high scattering yield for hafnium.

Figure 5.13 shows the MEIS spectra of as-deposited and annealed films. At the high-energy end of each spectrum (Figure 5.13b), the hafnium signal is observed. The front edge of this feature is near 192keV, and represents the surface of the film; the back edge for each annealing temperature is between 182 and 185keV, and represents the interface between Hf_3N_4 and SiO_2. With increasing annealing temperature, it is clear that the width of the hafnium feature reduces, and the scattering counts increase. This confirms that the film thickness is physically reducing; however, the number of hafnium atoms that occupies a unit area is increasing, meaning that the film is undergoing a densification process. The thickness determined by MEIS reduces from 8.8 to 7.5nm; and the film density increases from ~11.6 to ~12.8 g/cm^3, achieving ~92% of the bulk density (13.8 g/cm^3). The significance of the results, however, is not the evidence of densification, but rather the confirmation that little, if any, inter-diffusion occurs between hafnium and silicon. At the energy between 180 and 185keV, the hafnium back edges can be seen, and the gradient of this feature represents the Hf-Si interface quality. If any diffusion occurs, then this gradient will decrease. However, it remains identical across the annealed temperature range, and confirms that no effective inter-diffusion occurs between hafnium and silicon up to 800°C within the detection limit of MEIS. Therefore, the Hf_3N_4 thin films deposited using PEALD are thermodynamically very stable with respect to silicon up to 800°C after 10 minutes annealing.

At low energies (Figure 5.13a), however, oxygen migration was observed. The low end of the spectra remains identical up to 600°C; but at 700°C, oxygen from the surface (120keV) and the SiO_2 interface (114keV) start to move towards the film bulk; the diffusion is more evident at 800°C, causing a decrease of nitrogen content and an increase of oxygen content within the film bulk. Oxygen is more

electronegative than nitrogen and consequently, it migrates easily in the film when the annealing temperatures are sufficient.[38,39] However in a real device, this is less likely to occur, because surface cleaning and device packing can be employed to eliminate both interface and surface oxygen.[40]

XRD of the films annealed in vacuum up to 800°C displayed no diffraction pattern, indicating that these films retain an amorphous microstructure after annealing up to 800°C. This property is highly desirable from the application point of view, and confirms that the process reported in this study has potential to be employed in the manufacture of electronic devices.

5.3 Summary

To summarise, a direct comparison has been made between thermal and PE ALD processes using TEMAH precursor with either molecular ammonia or an ammonia plasma. Self-limiting behaviour has been observed for both TEMAH and ammonia half-reactions. Some advantages were found for the PEALD compared with the thermal ALD process: PEALD allows shorter purge time, which significantly reduces the cycle length; PEALD also results in higher film density. The densities of the films deposited by PEALD and thermal ALD are 11.6 and 9.7 g/cm^3 respectively. In-situ mass spectrometry measurements have indicated that these process characteristics are attributed to the nature of the co-reactants, namely, radicals of hydrogen and nitrogen in the case of PEALD. The reactivity and the short life time of these radicals are responsible for the observed advantages using PEALD.

All films deposited in the current study are amorphous. The films deposited by PEALD have a density of 11.6 g/cm^3 and post-deposition vacuum annealing has been exploited to increase the density to 12.8 g/cm^3. The films remain amorphous and stable with no inter-diffusion to silicon up to 800°C, making them a good candidate for diffusion barrier applications.

5.4 References

1. R. A. Araujo, X. H. Zhang, H. Y. Wang, *Journal Of Vacuum Science & Technology B* **26**, 1871-1874 (2008).

2. L. E. Toth, *Transition Metal Carbides and Nitrides* Academic Press Inc: New York, (1971).

3. J. S. Becker, E. Kim, R. G. Gordon, *Chemistry Of Materials* **16**, 3497-3501 (2004).

4. W. W. Wang, T. Nabatame, Y. Shimogaki, *Japanese Journal Of Applied Physics Part 2-Letters & Express Letters* **45**, L1183-L1185 (2006).

5. R. Fix, R. G. Gordon, D. M. Hoffman, *Chemistry of Materials* **3**, 1138 (2002).

6. J. Lannon, Jr., C. Pace, S. Goodwin, S. Solomon, P. Bryant, *Journal of Vacuum Science & Technology A: Vacuum, Surfaces, and Films* **22**, 1730-1733 (2004).

7. M. H. Lin, S. Y. Chiou, *Japanese Journal Of Applied Physics Part 1-Regular Papers Short Notes & Review Papers* **43**, 3340-3345 (2004).

8. M. Wittmer, *Journal Of Vacuum Science & Technology A-Vacuum Surfaces And Films* **3**, 1797-1803 (1985).

9. H. Y. Yu, H. F. Lim, J. H. Chen, M. F. Li, C. X. Zhu, C. H. Tung, A. Y. Du, W. D. Wang, D. Z. Chi, D. L. Kwong, *Ieee Electron Device Letters* **24**, 230-232 (2003).

10. J. W. Lim, S. J. Yun, *Electrochem. Solid-state Letter* **7**, F45-F48 (2004).

11. X. Y. Liu, S. Ramanathan, T. E. Seidel, *Atomic layer deposition of hafnium oxide thin films from tetrakis(dimethylamino)hafnium (TDMAH) and ozone*. In *Comos Front-End Materials and Process Technology*, T. J. King, B. Yu, R. J. P. Lander, S. Saito, Eds. Materials Research Society: Warrendale, Vol. 765 pp 97-102 (2003).

12. A. Grill, P. R. Aron, *Thin Solid Films* **108**, 173-180 (1983).

13. W. D. Sproul, *Thin Solid Films* **118**, 279-284 (1984).

14. D. Deniz, J. M. E. Harper, *Journal Of Vacuum Science & Technology A* **27**, 63-66 (2009).

15. H. Gueddaoui, S. Maabed, G. Schmerber, M. Guemmaz, J. C. Parlebas, *European Physical Journal B* **60**, 305-312 (2007).

16. K. L. Ou, *Microelectronic Engineering* **83**, 312-318 (2006).

17. M. Y. Liao, Y. Gotoh, H. Tsuji, J. Ishikawa, *Journal Of Vacuum Science & Technology A* **22**, 214-220 (2004).

18. Y. Gotoh, M. Y. Liao, H. Tsuji, J. Ishikawa, *Japanese Journal Of Applied Physics Part 2-Letters* **42**, L778-L780 (2003).

19. W. W. Wang, T. Nabatame, Y. Shimogaki, *Microelectronic Engineering* **85**, 320-326 (2008).

20. W. W. Wang, T. Nabatame, Y. Shimogaki, *Thin Solid Films* **498**, 75-79 (2006).

21. W. W. Wang, T. Nabatame, Y. Shimogaki, *Advanced Metallization Conference 2004 (Amc 2004)* 621-626 (2004).

22. K. H. Kim, R. G. Gordon, A. Ritenour, D. A. Antoniadis, *Applied Physics Letters* **90**, 212104 (2007).

23. Y. Senzaki, K. Choi, P. D. Kirsch, P. Majhi, B. H. Lee, *AIP conference Proceedings* **788**, 69-72 (2005).

24. E. J. Kim, D. H. Kim, *Electrochemical And Solid State Letters* **9**, C123-C125 (2006).

25. W. Jeong, Y. Ko, S. Bang, S. Lee, H. Jeon, *Journal of the Korean Physical Society* **56**, 905-910 (2010).

26. D. R. Lide, *CRC Handbook of Chemistry and Physics*. CRC Press: New York, p 4-64 (2009).

27. K. Hinode, Y. Homma, M. Horiuchi, T. Takahashi, *Journal Of Vacuum Science & Technology A-Vacuum Surfaces And Films* **15**, 2017-2022 (1997).

28. S. Logothetidis, E. I. Meletis, G. Stergioudis, A. A. Adjaottor, *Thin Solid Films* **338**, 304-313 (1999).

29. S. B. Clendenning, S. Park, H. S. Simka, S. Shankar, In *Nitrogen-mediated ALD of metallic nickel: film deposition and mchanistic insights, 10th Internation Conference of Atomic Layer Deposition*, Korea (South), (2010).

30. Y. Senzaki, S. Park, H. Chatham, L. Bartholomew, W. Nieveen, *Journal of Vacuum Science & Technology A: Vacuum, Surfaces, and Films* **22**, 1175-1181 (2004).

31. H. C. M. Knoops, E. Langereis, M. C. M. van de Sanden, W. M. M. Kessels, *Journal of The Electrochemical Society* **157**, G241-G249 (2010).

32. W. J. Maeng, S. J. Park, H. Kim, *Journal of Vacuum Science & Technology B* **24**, 2276-2281 (2006).

33. J. Kim, S. Kim, H. Jeon, M. H. Cho, K. B. Chung, C. Bae, *Applied Physics Letters* **87**, 053108 (2005).

34. S. Venkataraj, D. Severin, S. H. Mohamed, J. Ngaruiya, O. Kappertz, M. Wuttig, *Thin Solid Films* **502**, 228-234 (2006).

35. S. Venkataraj, O. Kappertz, R. Jayavel, M. Wuttig, *Journal of Applied Physics* **92**, 2461-2466 (2002).

36. S. J. Henderson, O. Shebanova, A. L. Hector, P. F. McMillan, M. T. Weller, *Chemistry of Materials* **19**, 1712-1722 (2007).

37. J. F. Kang, H. Y. Yu, C. Ren, N. Sa, H. Yang, M.-F. Li, D. S. H. Chan, X. Y. Liu, R. Q. Han, D.-L. Kwong, *Journal of The Electrochemical Society* **154**, H927-H932 (2007).

38. T. Das, C. Mahata, G. K. Dalapati, D. Z. Chi, G. Sutradhar, P. K. Bose, C. K. Chia, S. Y. Chiam, J. S. Pan, Z. Zhang, C. K. Maiti, *Semiconductor Science and Technology* **25**, 125009 (2010).

39. F. Tessier, R. Marchand, *Journal of Solid State Chemistry* **171**, 143-151.

40. International Technology Roadmap for semiconductors (ITRS). http://www.itrs.net/ (accessed 2010).

Chapter 6. Gadolinium nitride

This chapter reports on a pioneering search for the ALD deposition of gadolinium nitride. This material has potential applications in spintronic devices. Gd nitride is very difficult to synthesise and previous studies have shown that it can convert to oxide when exposed to air at ambient temperature. ALD deposition of such challenging materials has not been previously reported. The current study investigates both thermal and PE ALD processes for the deposition of gadolinium nitride films. Gd nitride films with a 1:1 Gd:N ratio and low oxygen and carbon incorporation were successfully deposited.

6.1 Introduction

Spintronic devices are strong candidates for the next generation of logic devices. They exploit the spin of the carriers as well as their charge to register 'on' and 'off' binary states. A major challenge in integrating spin-based devices with charge-based ones is to find suitable materials that are both ferromagnetic and semiconducting. This criterion has to be attained in order to enable an efficient injection of spin-polarized carriers into semiconductors.[1] Rare-earth (RE) nitrides are potential candidates for this purpose. Their magnetic property arises from the highly localized and progressively filled 4*f* electron shell of RE metals across the period, which is also true of RE compounds.[2] Amongst the RE nitrides, gadolinium mono-nitride (GdN) has been the most thoroughly studied since the late 60's. Historically, there have been conflicting and contradictory reports on the magnetic[3-6] and electrical[7,8] properties of GdN. This was partially due to poor sample preparation techniques, which give rise to defect and impurity in GdN films or non-stoichiometric material. However, GdN

has now been widely accepted to be both ferromagnetic[3-6] and semiconducting.[9-11] GdN has a Curie temperature of ~70K and a large magnetic moment of 7 Bohr magnetons (μ_B) per Gd^{3+}.[12,13] Recent measurements have also revealed the semiconductor nature of GdN, which has a narrow band gap both below and above its Curie temperature.[14] These findings encourage further exploration of GdN and processes for integrating it with current semiconductor technology. Establishing an ALD deposition process that is capable of incorporating GdN within current VLSI fabrication schemes represents a significant advance in the field.

The deposition of GdN is challenging due to the high affinity of gadolinium to oxygen. Gerlach et al. show that a 55nm GdN film can convert to oxide when exposed to air at ambient temperature within a few tens of seconds.[15] Oxygen contamination largely inhibits the ferromagnetic properties of GdN,[16,17] therefore, it is of utmost importance to grow films with high purity and to avoid post-growth oxidation. GdN has previously been deposited by MBE,[15,18] PVD,[19,20] and PLD.[10] In addition, GdN CVD has also been recently reported by two groups, one using $GdCl_3$ and NH_3 at a deposition temperature of 1000°C,[21] and the other using single source CVD with a gadolinium guanidinate precursor at 850°C.[22] In comparison with these deposition techniques, ALD offers lower deposition temperature, high conformability, large area uniformity and sub-nanometer thickness control.[23,24] To date, there has been no previous ALD study of any RE nitride.

Precursors - Suitable precursors for CVD or ALD of any rare-earth films are currently very limited and for nitride growth, this selection is further restricted. The precursors must not only be volatile to enable transport, but they must also be oxygen-free, both in terms of purity and ligand structure. Any oxygen source within the

reactor during growth can lead to preferential oxidation reactions and hence high levels of oxygen incorporation. The simple RE alkylamides $Ln(NR_2)_3$ are unstable and involatile, hence they cannot be used.[25] However, a number of oxygen-free RE precursors, including cyclopentadienyls (Cp),[26] silylamides $(N(SiR_3)_2)$,[27] and amidinate-based (amd)[28] precursors have been developed and reported for the deposition of RE oxides. For example, Gd_2O_3 was deposited with tris(methylcyclopentadienyl)gadolinium,[26] $Gd(MeCp)_3$; and PrO_x was deposited with tris(silylamide)praseodymium,[27] $Pr\{N(SiMe_3)_2\}_3$, although in the latter case, silicon impurities were found in the bulk of the film. Yttria (Y_2O_3) has also been deposited with tris(*N*,*N*'-diisopropylacetamidinate)yttrium,[28] $Y(^iPr_2amd)_3$. Gd sources based on these ligand structures could be suitable for GdN ALD, subject to their reactivity with nitrogen co-reactants.

In this study, $Gd(MeCp)_3$ was employed because of its high volatility. This precursor has previously been used for the deposition of Gd_2O_3 by ALD, and although it does not fully self-limit due to thermal decomposition, it can still produce high quality films with good uniformity.[26] In the current study, the oxide process was firstly repeated to establish the precursor transport parameters. For the nitride, a comprehensive investigation using both thermal and PE ALD was conducted. In thermal ALD, either ammonia or MMH was used as the nitrogen co-reactant and the results show that they are not suitable for use with the $Gd(MeCp)_3$. In PEALD, both H_2/N_2 mixed plasma and N_2 plasma were investigated; the latter case produced GdN thin films with low oxygen incorporation. Therefore, the $Gd(MeCp)_3$ work mainly focuses on the GdN PEALD process using N_2 plasmas. The growth behaviour was investigated by varying deposition parameters. The film composition, microstructure and surface morphology were characterised using MEIS, AES, XRD and AFM

respectively. GdN films with a 1:1 Gd:N ratio, low oxygen and carbon incorporation, amorphous microstructure, and smooth surface have been deposited.

The thermal ALD process with $Gd\{N(SiMe_3)_2\}_3$ and MMH was also investigated. Despite the fact that oxygen and silicon incorporation was detected in the films, the study shows that $Gd\{N(SiMe_3)_2\}_3$ is a self-limiting precursor and there is a reaction between $Gd\{N(SiMe_3)_2\}_3$ and MMH. The oxygen source is identified to be the THF used during the precursor synthesis and it is anticipated that further work in precursor development is required. If the pure $Gd\{N(SiMe_3)_2\}_3$ can be made, the process reported here may deposit $GdSi_xN_y$.

6.2 Results and discussion

6.2.1 $Gd(MeCp)_3$ thermal ALD

Films were deposited on 50×50mm P type Si(100) substrates used as-supplied without any additional surface preparation. Consequently the wafer surfaces consist of a ~20Å thick native oxide. The deposition of Gd-based materials using thermal ALD with $Gd(MeCp)_3$ (supplied by SAFC-Hitech) and either de-ionized water, ammonia, or MMH were carried out in an OpAL thermal reactor and the growth parameters were summarised in Table 6.1. The growth rates presented in this chapter were all corroborated from the films deposited with 300 ALD cycles. Since rare-earth nitrides are highly susceptible to oxidation even at room temperature,[15] films were capped with a protective TaN layer. The TaN cap layers were deposited at 300°C using 300 ALD cycles with PDMAT and ammonia (10sccm). The {PDMAT dose - purge - ammonia dose - purge -} pulse sequence were {6s - 5s - 6s - 5s -}. These parameters

have been optimised for the deposition of high quality TaN layers as demonstrated in Chapter 4.

Reactor, leak rate and cleaning method	OpAL thermal ALD reactor, 1mTorr/min, 1 hour Ar pump and purge			
$Gd(MeCp)_3$ transport temperatures	135°C (bubbler) - 140°C (dosing pipes) - 140°C (chamber walls)			
Substrate temperature	150-300 °C			
$Gd(MeCp)_3$ doses	150sccm 2s			
$Gd(MeCp)_3$ purge	250sccm 3s			
Co-reactant	**Without co-reactant**	**Water**	**Ammonia**	**MMH**
Co-reactant doses	N.A.	20ms vapour draw	10sccm 6s	20ms vapour draw
Co-reactant purge	250sccm 3s			

Table 6.1 Growth parameters for the deposition of Gd-based oxide and nitride using thermal ALD with $Gd(MeCp)_3$ and either water, ammonia or MMH.

Oxide – The Gd_2O_3 process using $Gd(MeCp)_3$, reported by Niinistö et al.,[26] was repeated in the current study to establish the precursor transport conditions. Films were deposited at temperatures between 150 and 300°C using $Gd(MeCp)_3$ and either 20ms water doses or without any co-reactant. In the absence of a co-reactant, growth rate increases in a linear fashion with temperature (Figure 6.1), indicating that the $Gd(MeCp)_3$ suffers from thermal decomposition within this temperature range. This is consistent with previous work,[26] where $Gd(MeCp)_3$ was used as a source for Gd_2O_3 ALD and no clear ALD temperature window was observed. The growth rate of films deposited with water is also shown in Figure 6.1. The growth rate has values of ~0.24-0.58 Å/cycle for the temperature range 150-300°C and is consistently higher

than the growth without any co-reactant, indicating a reaction between $Gd(MeCp)_3$ and water.

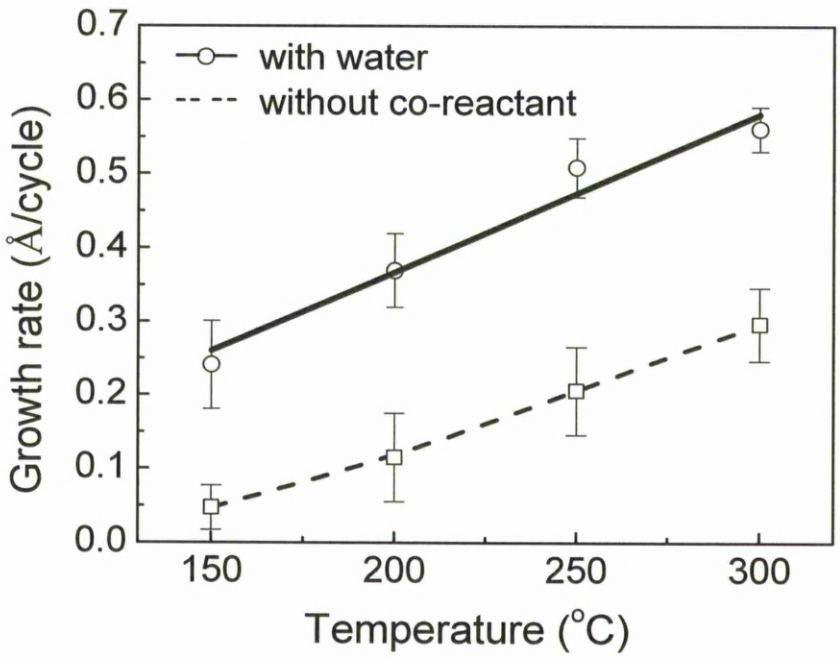

Figure 6.1 Growth rate as a function of growth temperature for the ALD deposition using $Gd(MeCp)_3$ with either water or without any co-reactant.

MEIS was used to confirm the chemical composition of films deposited with water. Figure 6.2 shows the MEIS depth profile of a film deposited with $Gd(MeCp)_3$ and water at 250°C using 300 ALD cycles. The energy-to-depth conversion was carried out using the stopping powers of He^+ in Gd_2O_3 (bulk density 7.1 g/cm^3).[29] Gadolinium and oxygen were detected and the ratio of Gd:O was found to be ~1:1.5, which is in a good agreement with Gd_2O_3. Combined with the ellipsometry thickness measurement, the actual film density was estimated to be 5.8±1 g/cm^3, which is considered as a reasonable value since thin film densities are often smaller than the bulk value (7.1 g/cm^3).[29] XRD (Figure 6.3) shows that the films deposited with water are cubic Gd_2O_3, which is in a good agreement with the previous deposition of

Gd_2O_3.[26] These results confirm the success in the precursor transport and oxide deposition, further work can be carried out for the search of suitable nitride processes.

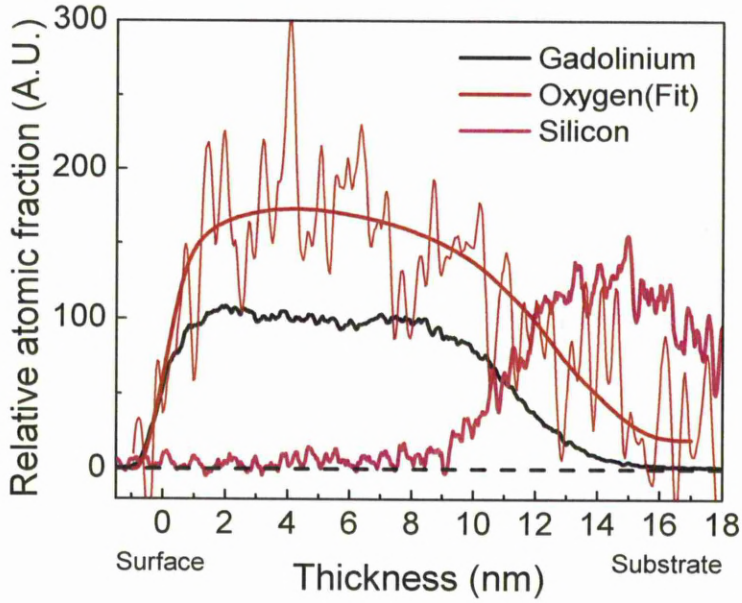

Figure 6.2 MEIS depth profile for a thin film deposited with $Gd(MeCp)_3$ and water at 250°C using 300 ALD cycles.Data was taken for a dose of 2μC.

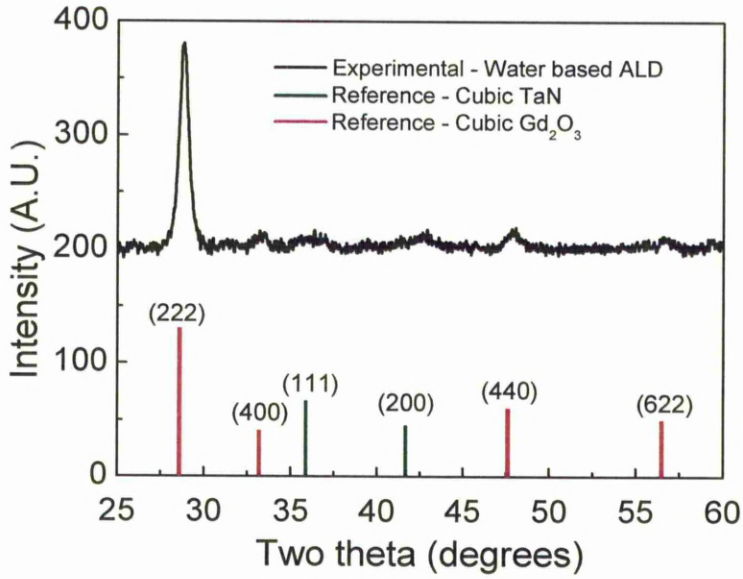

Figure 6.3 XRD of the film (~70nm) deposited on silicon with $Gd(MeCp)_3$ and water at 300°C with a TaN capping layer. The reference diffraction patterns for cubic Gd_2O_3[30] and cubic TaN (JCPDS card number 89-5196) are also shown.

Nitride - Although Gd_2O_3 can be deposited with $Gd(MeCp)_3$ and water, the deposition of GdN using thermal ALD remains challenging. The thermal ALD growth using either of the nitrogen sources shows low growth rates compared to the deposition with water. For example, the growth rates for the various depositions using ammonia, MMH and water at 250°C were 0.22±0.06, 0.20±0.06 and 0.50±0.04 Å/cycle respectively. The deposition without any co-reactant has a growth rate of 0.20±0.06 Å/cycle due to thermal decomposition alone. It is clear that the nitrogen co-reactants have not reacted with the $Gd(MeCp)_3$ precursor and that the observed deposition can largely be attributed to thermal decomposition.

Selected films for each co-reactant were analysed with MEIS to determine their chemical composition. Films were deposited with a target thickness of ~10nm for the Gd layers and with a further ~5nm of TaN as a protective cap. Figure 6.4 shows MEIS spectra for the films deposited with $Gd(MeCp)_3$ with ammonia (400 cycles), MMH (400 cycles) at 250°C and for comparison, the film deposited with water (200 cycles) was also characterised. SIMNRA was used to interpret the spectra and to deconvolue overlapping peaks, the results for the films deposited with water and ammonia are also shown in Figure 6.5 and 6.6 respectively. Due to the layer roughness, the interface quality between the layers, and the straggling effect of ions in MEIS, the SIMNRA fittings are not optimum. The thickness extracted from peak deconvolution in Figure 6.5 and 6.6 has an error of ±1nm.

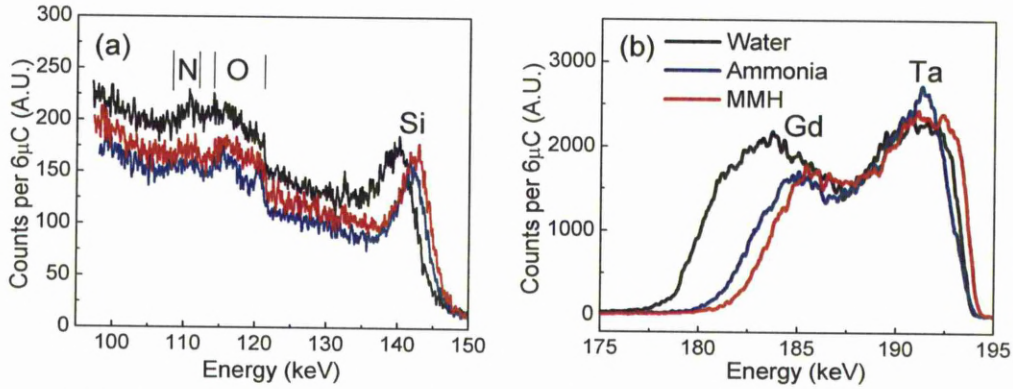

Figure 6.4 MEIS raw spectra for films deposited with $Gd(MeCp)_3$ and either ammonia (400 cycles), MMH (400 cycles) or water (200 cycles) at 250°C. All films were capped with a ~5nm TaN cap layer. The spectra are displayed in (a) low- and (b) high-energy ranges.

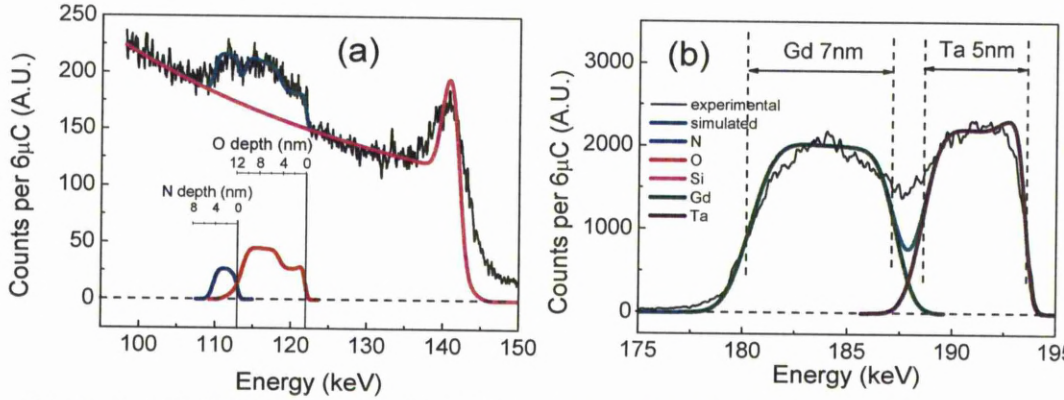

Figure 6.5 SIMNRA fittings for the MEIS spectrum of the film deposited with water (200 cycles) at 250°C. The spectrum is displayed in (a) low- and (b) high-energy ranges.

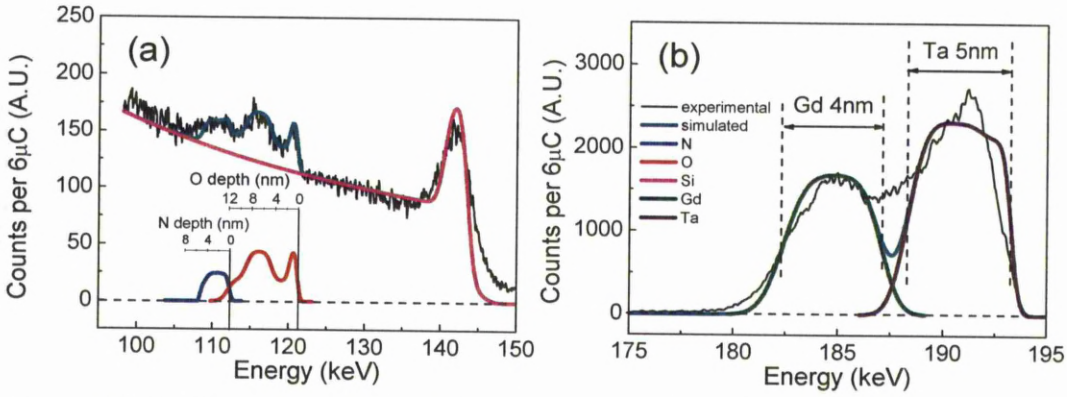

Figure 6.6 SIMNRA fittings for the MEIS raw spectrum of the film deposited with ammonia (400 cycles) at 250°C. The spectrum is displayed in (a) low- and (b) high-energy ranges.

From high to low energy (Figure 6.4), tantalum, gadolinium, silicon, oxygen and nitrogen signals can be assigned. At the energy of 185 keV, gadolinium peaks can be

seen. Despite the longer growth cycles, the width of the gadolinium feature (Figure 6.4b) is significantly narrower for ammonia and MMH compared with water, which corresponds to a thickness of 4, 3 and 7nm respectively. A surface oxygen peak (Figure 6.4a) is clearly visible at the energy of 120 keV and can be attributed to oxygen species absorbed on the surface of the TaN. A dip in the oxygen feature, which is particularly evident in the ammonia sample, corresponds to the TaN layer. The oxygen features for all samples clearly continue to penetrate through the depth of the remaining film material. The oxygen incorporation in both the ammonia or MMH samples is similar to the water sample, with a Gd:O ratio of ~1:1.5. At the energy of 111 keV, a nitrogen peak is visible and can be attributed to the TaN layer, however, this feature discontinues after 107 keV in each sample, which corresponds to the edge of TaN layer. No significant nitrogen incorporation was detected in the Gd layer.

These results indicate unfavourable reaction thermodynamics between nitrogen co-reactants and $Gd(MeCp)_3$. This could be attributed to unmatched acidity constants (pK_a) between the MeCp complex and these co-reactants. The acidity constant, pK_a, of cyclopentadiene and ammonia are 15.5 and 33 respectively.[31] The pK_a of cyclopentadiene was used as an approximation for the MeCp group due to the availability in literature, and the pK_a of MMH is likely to have a similar value as ammonia. A forward reaction requires a close match of the pK_a between precursor and co-reactant. For example, water has a pK_a of 15.7,[31] which matches the pK_a of the MeCp group and hence Gd_2O_3 can be deposited using water and $Gd(MeCp)_3$.[26] Neither ammonia, nor MMH are able to extract the MeCp group from the Gd precursor, and therefore the reaction is unfavourable. The high oxygen contamination in the films is most likely from trace levels of oxygen within the process and carrier gas supplies. Although significant effort has been made to minimize sources of

oxygen within the reactor, it is likely that the partially decomposed Gd precursor acts as an oxygen getter on the surface. As a result, the thermal ALD approach using $Gd(MeCp)_3$ with either ammonia or MMH was found to be unsuitable for the deposition of GdN within the temperature range studied.

6.2.2 $Gd(MeCp)_3$ PEALD

PEALD provides highly reactive radicals and supplies additional energy to ALD surface reactions,[32] which may overcome the limitations of thermal ALD processes using co-reactants such as ammonia and MMH. PEALD using $Gd(MeCp)_3$ with either H_2/N_2 plasma or pure N_2 plasma was investigated using an OpAL plasma reactor and the growth conditions are summarised in Table 6.2. Unfortunately, there were no gas purifiers available on the gas lines of the OpAL plasma reactor, the Ar (BOC zero grade), H_2 (Linde gas 99.995%) and N_2 (BOC zero grade) gases were used as supplied. Films for characterisations were capped with a protective TaN layer deposited at 300°C using 100 ALD cycles with PDMAT and H_2/N_2 plasma (30/5sccm 300W) The {PDMAT dose - purge - plasma dose - purge -} pulse sequence were {6s - 5s - 3s - 5s -}.

The growth rates were corroborated from the films deposited without a capping layer. This was suspected to introduce an error on measured thickness because the thickness can change when converting from Gd nitride to Gd oxide. However, this effect was found to be minimal. The thickness was compared for films with and without a capping layer when deposited using the identical conditions, the films with a capping layer are consistently 5nm thicker than those without a capping layer. The difference is in a good agreement with the thickness of the capping layer. This means that the film thickness has been retained regardless of the presence of a capping layer, showing post-deposition exposure to air has a minimal effect on the film thickness.

Reactor, leak rate and cleaning method	OpAL plasma ALD reactor, 1mTorr/min, 1 hour Ar pump and purge + H_2 plasma	
$Gd(MeCp)_3$ transport temperatures	135°C (bubbler) - 140°C (dosing pipes) - 140°C (chamber walls)	
Substrate temperature	150-300 °C	
$Gd(MeCp)_3$ doses	150sccm 2s	
$Gd(MeCp)_3$ purge	250sccm 3s	
Co-reactant	H_2/N_2 plasma	N_2 plasma
Co-reactant doses	5/30sccm 5s **300W**	60sccm 0-10s **300W**
Co-reactant purge	250sccm 3s	

Table 6.2 Growth parameters for the deposition of GdN using PEALD with $Gd(MeCp)_3$ and either H_2/N_2 plasma or N_2 plasma.

6.2.2.1 N_2 vs. H_2/N_2 plasma

EDX measurements show that the films deposited with N_2 plasma (Figure 6.7a) have high levels of nitrogen incorporation with little oxygen; but for H_2/N_2 mixed plasma (Figure 6.7b), shows significant oxygen with undetectable nitrogen incorporation. X-ray diffraction (Figure 6.8) confirms that the crystal structure of as-deposited films using H_2/N_2 plasma is consistent with cubic Gd_2O_3, whereas the films deposited with N_2 plasma are effectively amorphous. Films deposited using the same mixed plasma process with PDMAT rather than $Gd(MeCp)_3$ produced TaN with only ~2 at.% oxygen as illustrated in Figure 6.15 by AES, which indicates that reactor integrity and gas purity are suitable for nitride deposition.

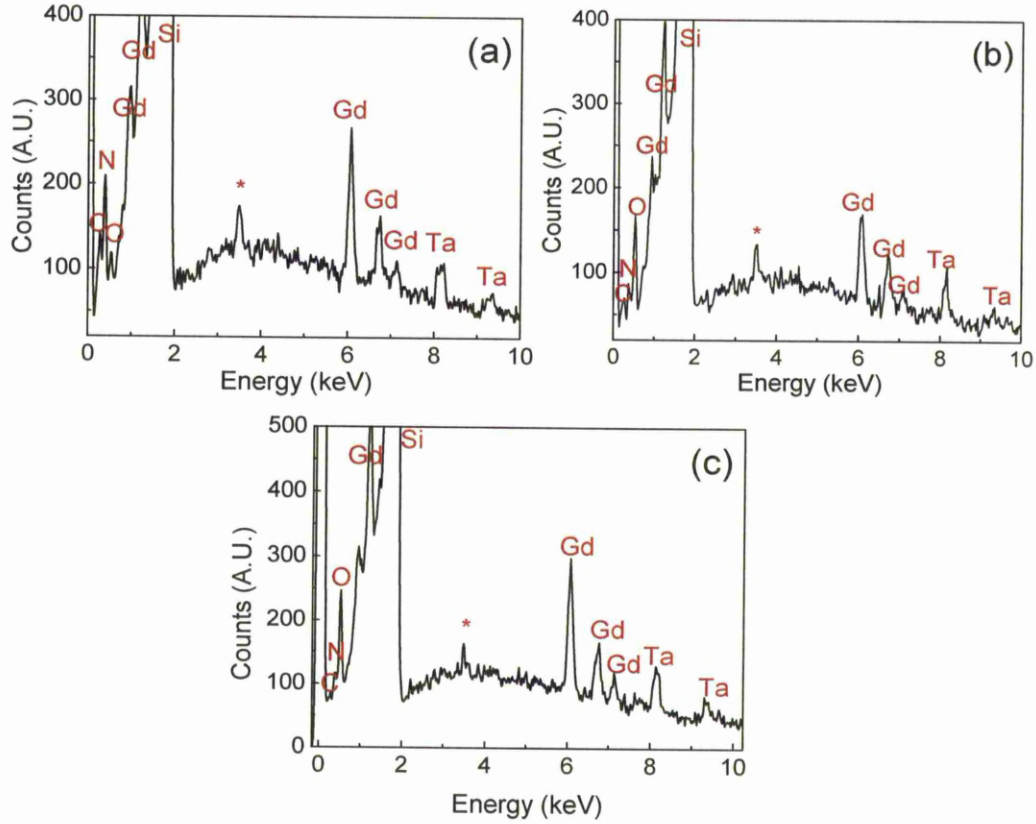

*Figure 6.7 EDX for the film (~70nm) deposited with (a) N_2 plasma (5s), and (b) H_2/N_2 plasma (c) H_2 plasma (5s 60sccm) at 200°C. * is a feature associated with the Si substrate.*

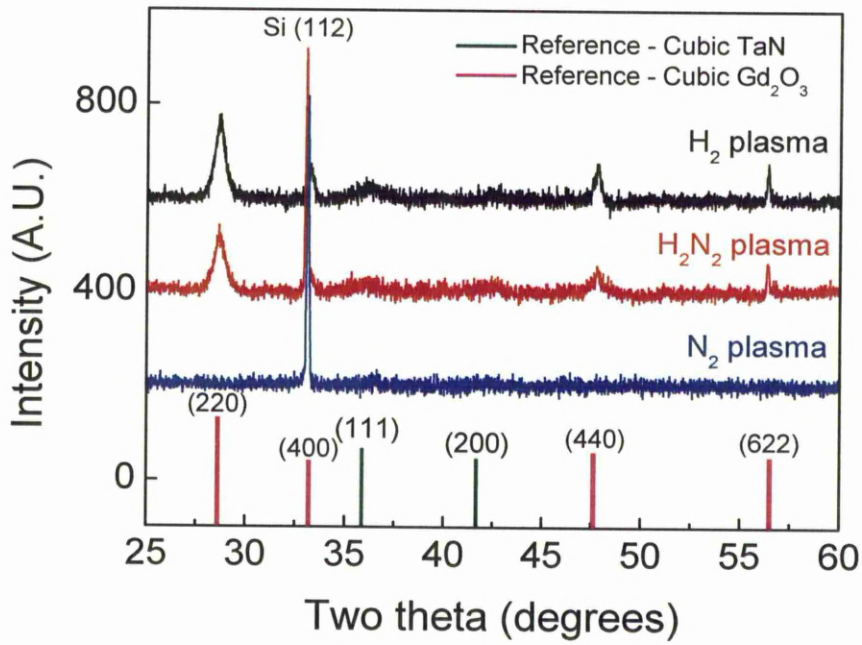

Figure 6.8 XRD for the film (70nm) deposited with H_2, H_2/N_2 and N_2 plasma at 200°C; reference diffraction patterns for cubic Gd_2O_3[30] and cubic TaN are also shown.

Further thin film deposition was carried out using $Gd(MeCp)_3$ with pure-hydrogen plasma, and the EDX results show that oxide films were formed (Figure 6.7c). XRD analysis also confirms that the films deposited with pure H_2 plasma have a cubic Gd_2O_3 structure (Figure 6.8). These results confirm that the oxide formation using H_2/N_2 mixed plasma is linked to the hydrogen plasma and its interaction with the $Gd(MeCp)_3$. Hydrogen radicals are expected to act as strongly reducing agents. This means that they are likely to disassociate the MeCp ligands from the Gd metal centre. If this happens, then highly unstable Gd metal cores will be left, which are highly susceptible to reactions with even small traces of oxygen impurities.[15] The bare metal cores will essentially act as oxygen getters. In the case of the TaN process using PDMAT, the nitrogen from the amine group is less likely to be stripped away by the hydrogen radicals to expose the bare metal centre hence avoiding the gettering effect. Previous studies have shown that TaN can be deposited using amine-based precursor and radicals from a pure hydrogen plasma, without the need for an additional nitrogen source.[33] To avoid the oxide formation with the H_2/N_2 mixed gas plasma, the rest of this section will focus on hydrogen free plasma growth.

6.2.2.2 N_2 plasma process – Growth characteristics

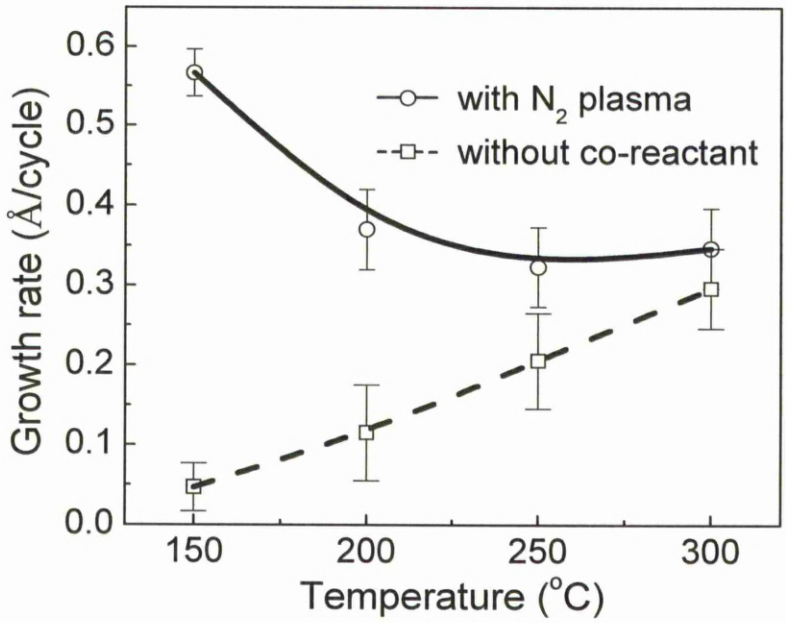

Figure 6.9 Growth rate as a function of growth temperature for the PEALD using $Gd(MeCp)_3$ and either N_2 plasma (5s) or without co-reactant.

The growth rate is shown as a function of deposition temperature for the N_2 plasma process in Figure 6.9. The growth rate at 150°C is ~0.56 Å/cycle, which is significantly higher than the growth rate without the plasma step, however, it decreases and stabilizes at ~0.33 Å/cycle for temperatures above 200°C. Although the growth curve between 200 and 300°C suggests an ALD window, it is clear that the thermal decomposition contributes to the overall deposition and hence, this is a non-ideal ALD process. In PEALD, the inverse relationship between growth rate and temperature has also been previously observed in the PEALD of SiO_2,[34] Al_2O_3,[35] and TiO_2[36] using O_2 plasma. Although no explanation was given in these papers, some possible insights are raised by the EDX analysis in the current study.

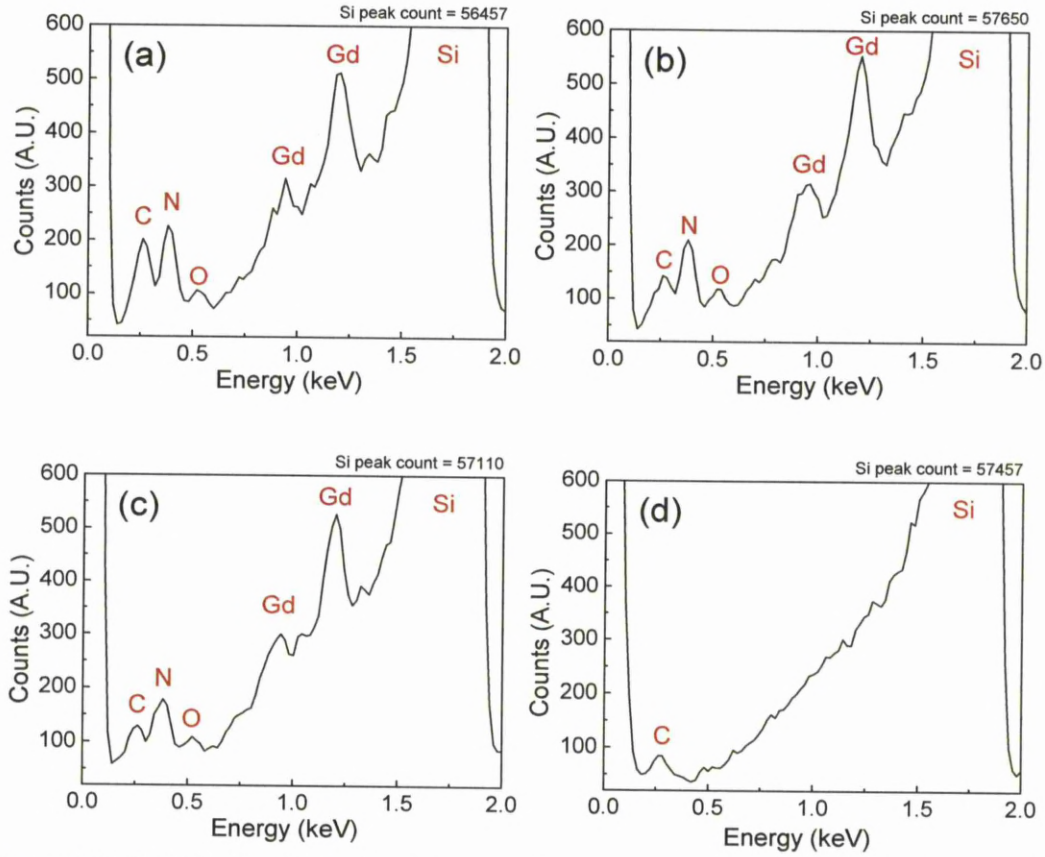

Figure 6.10 EDX for the films (70nm) deposited using N_2 plasma (5s) at (a) 150°C, (b) 200°C and (c) 250°C. (d) the EDX performed on a silicon substrate.

Figure 6.10 shows the EDX analysis for the films deposited at 150, 200 and 250°C, the samples were prepared with a similar thickness of ~70nm. The EDX spectrum for each sample was recorded three times at different locations and repeatable results were obtained. As emphasised in Chapter 3, carbon levels in EDX should be treated with care because the rotary pump used in the SEM can contribute to a background carbon signal. For this reason, a silicon substrate was used as a reference sample to extract the background carbon signal (Figure 6.10d).

Gd, N, O, C and Si were detected for the films deposited at different temperatures. The peak intensities for Gd, N, O and Si features remain almost identical for all deposition temperatures. However, a significantly higher carbon peak can be observed for the films deposited at 150°C (Figure 6.10a) than those deposited at higher

temperatures (Figure 6.10b,c), whose carbon peaks are close to the background level. These results show that more carbon has been incorporated in the films deposited at 150°C than those deposited at higher temperatures. The high carbon incorporation and high growth rates observed at 150°C are most likely due to incomplete reactions and by-product re-absorption. If the thermal energy at 150°C is insufficient to drive a complete reaction between $Gd(MeCp)_3$ and N_2 plasma, carbon rich ligands would be trapped in the film and consequently increase the thickness and carbon incorporation. The low temperature may also give rise to by-products condensation on the deposition surface, which also results in carbon impurity and higher growth rate. The stabilized growth rate at temperatures above 200°C (Figure 6.9) is due to a more complete reaction when additional thermal energy is given. This has resulted in a significant reduction in carbon incorporation, which was confirmed by EDX of the films deposited at 200 and 250°C (Figure 6.10).

Although the thermal decomposition of $Gd(MeCp)_3$ takes place in addition to the surface reactions, the films are uniform and the thickness variation is small. The thickness uniformity over a 40×40mm square area is 83% at 150°C, however, this improve readily to 95% at temperatures above 200°C (Figure 6.11). The best uniformity obtained in the current study is consistent with the previous oxide study using $Gd(MeCp)_3$ and H_2O,[26] which shows that $Gd(MeCp)_3$ chemisorbs uniformly. The poor uniformity at lower temperature can be explained by localized incomplete reactions, as a consequence of the uniformity of the plasma gas flow. Previous study has shown that the radical distribution of an inductively coupled plasma is not uniform.[37] This means that the reactions at different locations on the substrate receive different amount of plasma energy, at 150°C these locations receiving insufficient plasma energy would suffer incomplete reactions, which lead to different

thicknesses and affect the uniformity. At higher temperatures, the additional thermal energy compensates the non-uniform plasma power, the reactions at all locations can receive sufficient energy and therefore, the uniformity has been improved. Another possible explanation to the poor uniformity at lower temperature is the by-product re-absorption or condensation, which would be more dominant at lower temperatures.

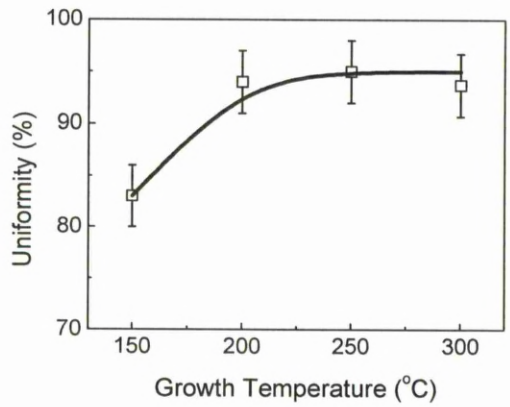

Figure 6.11 Thickness uniformity over a 40×40mm square for films deposited using N_2 plasma (5s) as a function of deposition temperature.

The effect of nitrogen plasma dose was investigated at a fixed growth temperature of 200°C for 0-10 second plasma exposures. The growth rate (Figure 6.12) clearly increases when the plasma exposure is introduced, however, after an initial peak at short exposures; the growth rate decreases towards a steady value of ~0.35 Å/cycle. The high growth rate at low plasma exposure times is again an indication of the incomplete exchange reaction between nitrogen radicals and $Gd(MeCp)_3$. A similar growth behaviour has been reported for TaN deposited using PEALD with $TaCl_5$ and H_2/N_2 plasma, where high chlorine contamination was found when the plasma exposure was insufficient.[38] This indicates that in the present study, a N_2 plasma exposure time longer than 5s is required to deposit GdN films with low carbon

incorporation and this principle has been followed when preparing the films for characterisations.

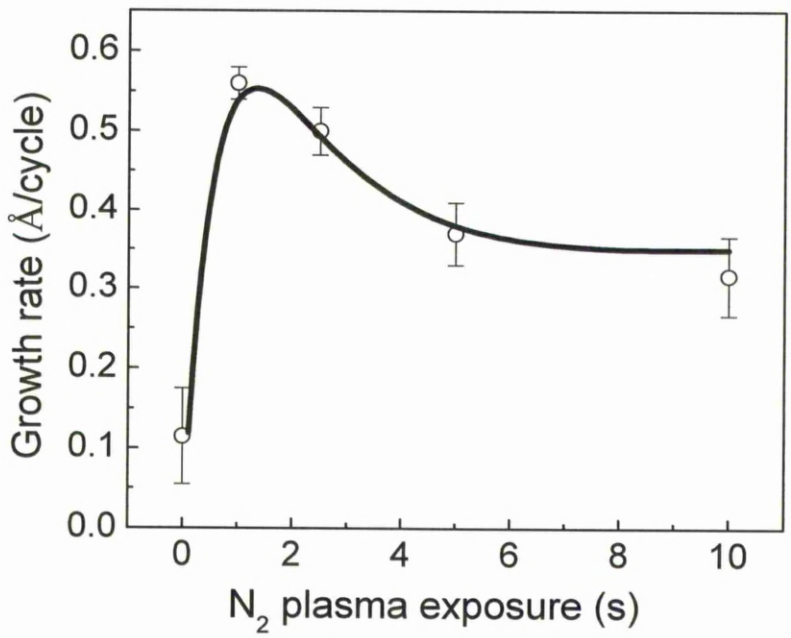

Figure 6.12 Growth rate as a function of N_2 plasma exposure at 200°C for the PEALD using $Gd(MeCp)_3$ and N_2 plasma.

6.2.2.3 N_2 plasma process – Chemical composition

Selected films were analyzed in more detail using MEIS and AES to provide quantitative composition depth profiles through the films. Figure 6.13 shows the MEIS spectrum of a sample deposited at 200°C with 5s plasma doses. The film consists of a ~15nm thick GdN layer produced using 500 ALD cycles and a ~5nm TaN capping layer (300cycles). The energy-to-depth conversion was carried out using the stopping powers of He^+ in TaN and GdN, with a density of 13.7 and 9.1 g/cm^3 respectively.[29] SIMNRA was also employed for peak fitting and deconvolution.

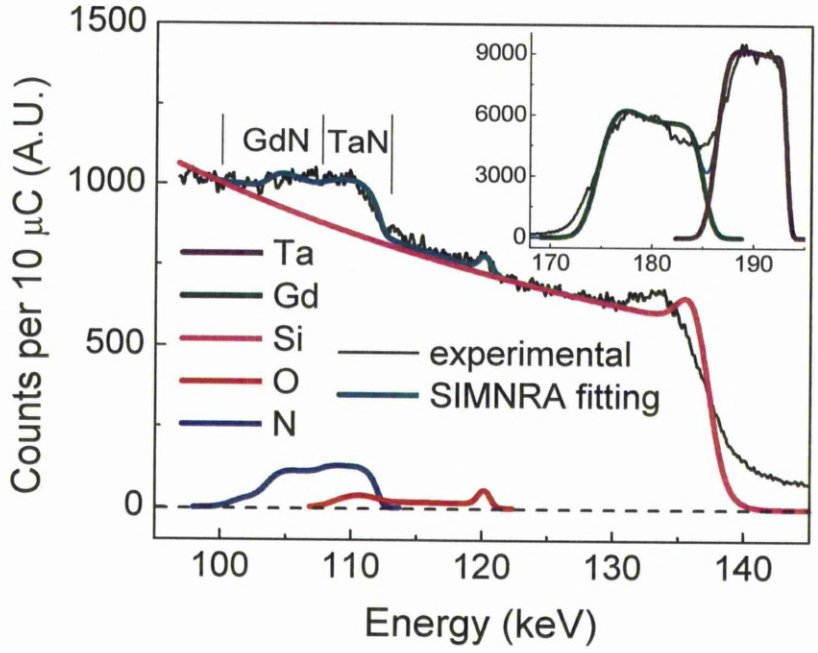

Figure 6.13 MEIS spectrum (low energy end) fitted with the SIMNRA simulation of GdN thin film deposited at 200°C with N_2 plasma (exposure time 5s). The film was capped with TaN. The inset shows the high energy end of the MEIS spectrum.

The high energy region of the MEIS spectra (Figure 6.13 inset) shows a tantalum peak (193.2-186.2 keV), which partially overlaps with the gadolinium feature (185-174.3 keV). From the width of the gadolinium peak extracted by deconvoluting the two peaks and the thickness measured by ellipsometry, film density is estimated to be 6.1±1 g/cm^3, which is around 70% of the bulk density.

At lower MEIS energies, silicon, oxygen and nitrogen features can be assigned, however, no carbon feature is observed, which, if present in the GdN layer, should appear at ~98 keV. Due to the signals from double charged ions in MEIS, the current spectra is only displayed to 96 keV, meaning that the carbon incorporation within the first ~4nm of the GdN layer is below the practical detection limit (~9 at.%). The oxygen feature, which spans from 120.7 keV to 106.4 keV, is made up of three main regions. At the high energy edge (120.7 keV), a peak is observed, which can be

attributed to surface oxygen on the TaN layer surface with a penetration of ~2nm into the surface. This surface oxygen is probably due to OH-groups absorbed when the sample was removed from the ALD reactor. The middle region of the oxygen feature is reasonably flat and represents oxygen at around 5 at.% within the bulk of the TaN and GdN layers. Finally, on the low energy side of the oxygen feature, a second small peak is observed (although it is partly obscured by the rising nitrogen edge); this can be attributed to oxygen within the native SiO_2 layer and at the interface between the GdN layer and the Si substrate. It should be noted that in the current process, the nitrogen and argon gases were used as supplied without any purification, trace levels of oxygen impurity in these gases may contribute to the observed oxygen incorporation in the film bulk (~5%). It is therefore anticipated that further improvements can be made by additional gas purification steps.

The nitrogen feature spans from 111.7 to 100 keV and can be attributed to nitrogen in the TaN (111.7-107 keV) and in the GdN (107-100 keV). Within the bulk of the GdN layer, the Gd:N ratio is found to be close to 1:1, which indicates a mono-nitride stoichiometry. Unfortunately, the nitrogen feature tails off from mid way through the GdN layer towards the SiO_2 interface. The decrease in nitrogen and increase in oxygen is evidence of the formation of an intermediate layer of GdO_xN_{x-1} when GdN grows on SiO_2. The same phenomenon is also observed in the GdN film deposited with MBE where an oxide substrate is used.[15] It is likely, that a significant improvement in the quality of the GdN layer could be made by removing the native SiO_2 and any absorbed oxygen species from the substrate before deposition. Despite these interface issues, the estimated bulk composition of the GdN layer is found to have a Gd:N ratio close to 1:1.

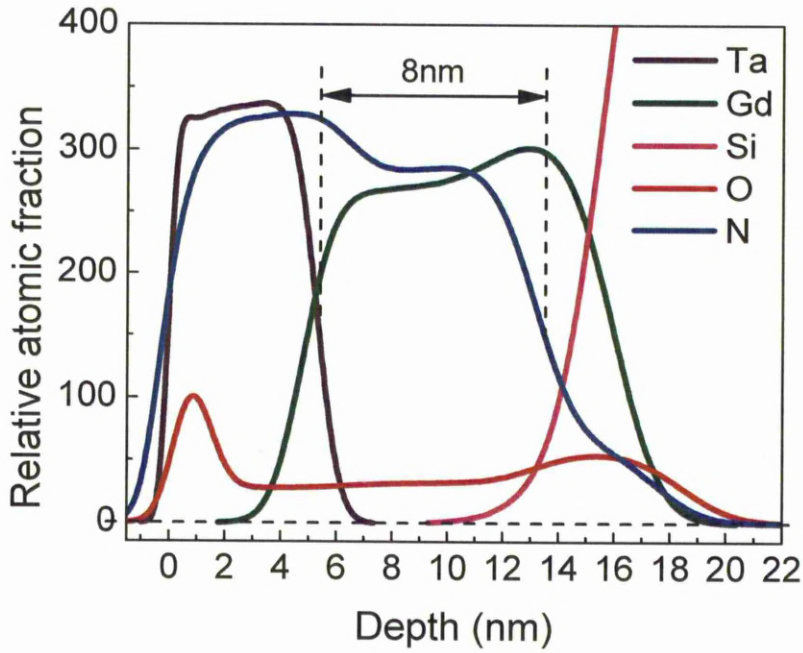

Figure 6.14 Depth profile of the SIMNRA simulation obtained from Figure 6.13, which is the MEIS of GdN film deposited at 200°C with N_2 plasma (exposure time 5s).

MEIS is a powerful technique for surface and interface analysis in thin films, however, with a material system such as GdN, where a protective cap is essential and interface layers are relatively thick, the GdN layer that was not affected by the interfaces is rather thin in the MEIS spectrum. Figure 6.14 shows the depth profiling of the SIMNRA simulation obtained from Figure 6.13, it can be seen that only 8nm of GdN can be used to extract the Gd:N ratio. Alternative techniques are required to fully assess the bulk properties of the deposited material. AES was performed by Hyeongtag Jeon from Hanyang University (South Korea)[39] to ascertain the depth composition of thicker films deposited at 200°C using 5s plasma doses. The details of the AES experiment can be found in Chapter 3.

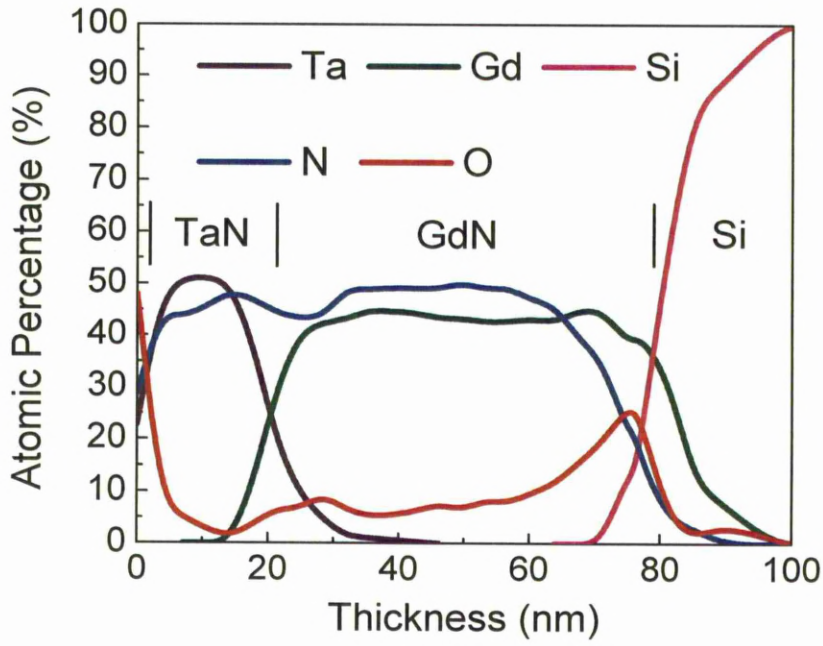

Figure 6.15 AES depth profiling of GdN film deposited with N_2 plasma (5s) at 200°C, film thickness was estimated from the sputtering rate (7.1nm/min) and time.

Figure 6.15 shows the AES depth profile of the GdN sample deposited at 200°C, this sample has a ~70nm thick layer of GdN grown on SiO_2/Si(100) with a ~20nm thick TaN cap. Ta, Gd, N, O and Si were detected, however, no carbon was seen. The Gd:N ratio in the bulk of the GdN layer is 1:1.08 with around ~6 at.% oxygen, which is in a good agreement with the MEIS. The nitrogen signal is almost constant through the bulk of the TaN and GdN layers, however, the tail edge of the nitrogen signal is clearly offset from the tail edge of the gadolinium signal. This offset, indicates interactions between the GdN layer with the oxide substrate, possibly oxygen diffusion from the native oxide into the Gd layer, resulting in the formation of Gd-oxynitride interlayer, in a good agreement with the MEIS data.

6.2.2.4 N_2 plasma process – microstructure and morphology

The XRD analysis for the films deposited at 200°C is shown in Figure 6.8, where no diffraction pattern can be seen, identical results were obtained for films deposited at other temperatures (not shown). These results show GdN films deposited in the current study are effectively amorphous; this can be attributed to the low deposition temperature compared to other techniques. The absence of any diffraction pattern also ascertains that there is effectively no crystallized oxide formed in the films deposited by N_2 plasma.

AFM shows that the as-deposited films are very smooth. Figure 6.16 shows the AFM image of a ~70nm film deposited by N_2 plasma at 200°C, the surface roughness, Ra, was found to be 0.7nm when the substrate roughness is 0.3nm. GdN films (1μm thick) deposited by CVD were reported to have a surface roughness of 60nm.[21] A smooth surface is desired in spintronic devices as it has been reported to significantly improve the device performance.[40] The sub-nanometre surface roughness of the film deposited in this study is therefore, an added advantage of ALD.

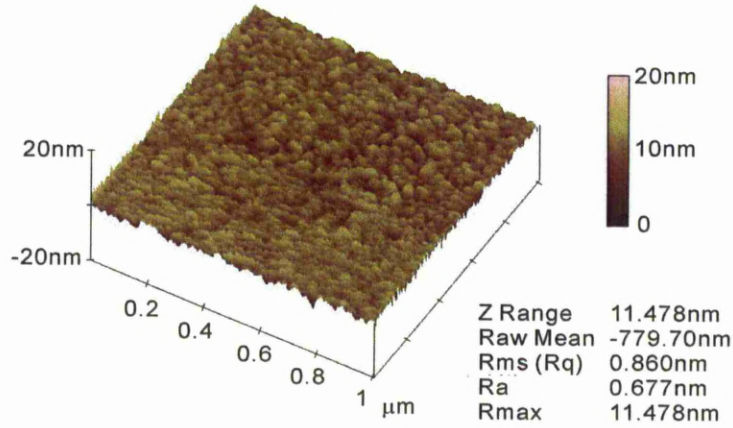

Figure 6.16 AFM image of a 1 by 1 μm² area on the GdN film deposited using PEALD with $Gd(MeCp)_3$ and N_2 plasma (5s) at 200°C. The film has a thickness of 70nm.

6.2.3 $Gd\{N(SiMe_3)_2\}_3$ thermal ALD

The thermal ALD study using $Gd\{N(SiMe_3)_2\}_3$ (supplied by SAFC-Hitech) and either ammonia or MMH was conducted using the OpAL thermal reactor, the growth conditions are summarised in Table 6.3. The co-reactant dosing conditions were adopted from the results presented in chapter 4, which has demonstrated that they are sufficient to saturate the surface area in the reactor. Films were deposited on 50×50 mm square P type Si (100) substrates and glassy carbon substrates (HTW SIGRADUR G). As explained in Chapter 3, the glassy carbon substrates were used to accommodate EDX analysis to determine the silicon incorporation in the film. TaN capping layer was also employed and was deposited using the method described in the section 6.3.1.

Reactor, leak rate and cleaning method	OpAL thermal ALD reactor, 1mTorr/min, 1 hour Ar pump and purge		
$Gd(N(SiMe_3)_2)_3$ transport temperatures	140°C (bubbler) - 150°C (dosing pipes) - 150°C (chamber walls)		
Substrate temperature	150-350 °C		
$Gd(N(SiMe_3)_2)_3$ doses	150sccm 2-13s		
$Gd(N(SiMe_3)_2)_3$ purge	250sccm 5-60s		
Co-reactant	**Without co-reactant**	**Ammonia**	**MMH**
Co-reactant doses	N.A.	10sccm 6s	20-30ms vapour draw
Co-reactant purge	250sccm 5-60s		

Table 6. 3 Growth parameters for the deposition of GdN using thermal ALD with $Gd\{N(SiMe_3)_2\}_3$ and either ammonia or MMH.

The results show that the growth rates for ammonia are significantly low, typically close to the growth rates without any co-reactant. For example, the growth rates for the films deposited with MMH, ammonia and without any co-reactant at 200°C were 0.7±0.03, 0.3±0.05 and 0.4±0.05 Å/cycle respectively, a similar result has also been observed at 300°C. The low growth rates have also been confirmed by the EDX analysis (Figure 6.17), which only detected a trace level of gadolinium in the films deposited using ammonia at either 200°C or 300°C after 1800 cycles, whereas the films deposited with MMH using the same temperatures and cycle length exhibit good Gd incorporation, showing a significantly higher growth rate.

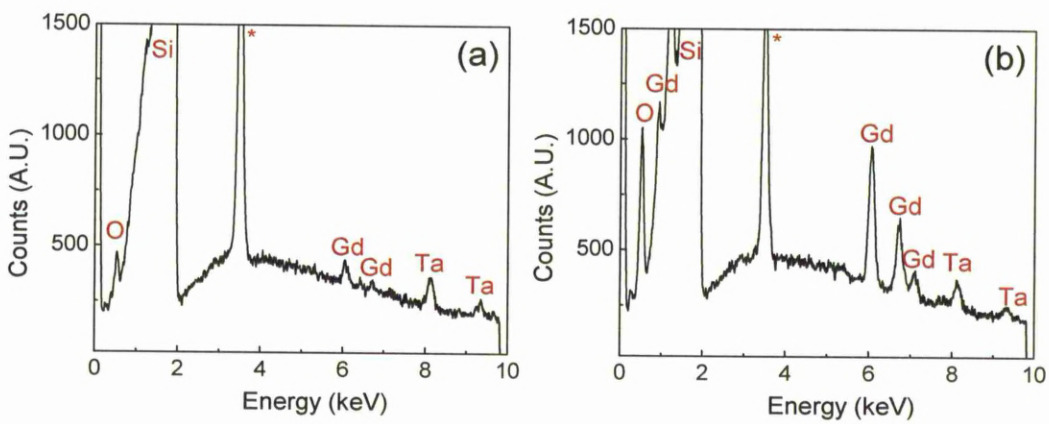

*Figure 6.17 EDX for the films deposited at 200°C using 1800 cycles with $Gd\{N(SiMe_3)_2\}_3$ (5s) and either (a) ammonia or (b) MMH. Both precursor and co-reactants purges were 30s. * is a feature associated with the Si substrate.*

These results indicate that the reaction between $Gd\{N(SiMe_3)_2\}_3$ and ammonia is thermodynamically unfavourable. The reactivity of ammonia relies heavily on the deposition temperature. This has been demonstrated by the work presented in Chapter 4 that a deposition temperature of 300°C is required to obtain high density TaN films using PDMAT and ammonia, the films deposited at lower temperatures exhibit poor densities with lower growth rates. The same may apply to the $Gd\{N(SiMe_3)_2\}_3$ study

that a deposition temperature of 200°C is insufficient to drive the reaction between $Gd\{N(SiMe_3)_2\}_3$ and ammonia, meaning that more thermal energy is required. However, the growth results of $Gd\{N(SiMe_3)_2\}_3$, which are presented in Figure 6.18, show that this precursor displays desorption behaviour at high temperatures (above 300°C), resulting in low growth rates.[27] This means that increasing the growth temperature is unpractical when using $Gd\{N(SiMe_3)_2\}_3$, deposition must be conducted at low temperatures to allow adsorption of the precursor. The reactivity of ammonia and the absorption of the precursor do not share a common temperature window and thus, the process was unsuccessful. However, as demonstrated in chapter 4, the MMH has a superior reactivity than ammonia at temperatures as low as 200°C and therefore, films have been deposited with $Gd\{N(SiMe_3)_2\}_3$ and MMH. For this reason, the rest of the section discusses the MMH based process.

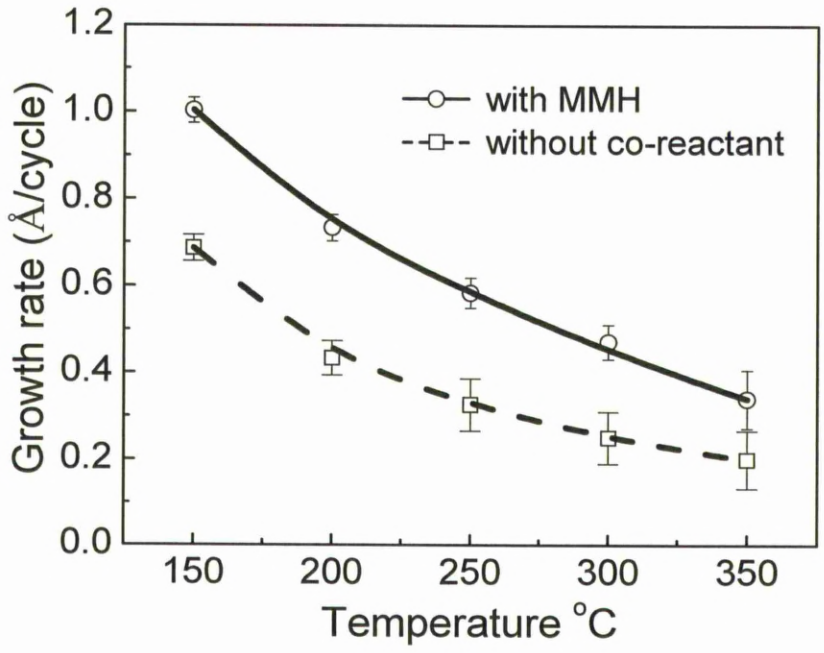

Figure 6.18 The growth rate as a function of growth temperature for the 300 cycles ALD using $Gd\{N(SiMe_3)_2\}_3$ with either MMH or without any co-reactant. The ($Gd\{N(SiMe_3)_2\}_3$ – purge – MMH – purge –) sequence was (5s – 30s – 20ms – 30s –).

The effect of deposition temperature was investigated using $Gd\{N(SiMe_3)_2\}_3$ and either MMH or without any co-reactant between 150 and 350°C using the ($Gd\{N(SiMe_3)_2\}_3$ – purge – MMH – purge –) sequence of (5s – 30s – 20ms – 30s –). In the absence of a co-reactant (Figure 6.18), growth rate was found to be inversely dependent on the temperature, decreasing from ~0.7 Å/cycle at 150°C to 0.2 Å/cycle at 350°C. This is consistent with previous work reported by Kukli et al.,[27] where $Pr\{N(SiMe_3)_2\}_3$ was used as a source for Pr-oxide ALD. In this study, the authors found that the growth rate decreases dramatically with increasing temperature and no film could be deposited at temperatures higher than 400°C. The high growth rates at low temperatures could be attributed to either thermal decomposition or condensation of the precursor, however, the self-limiting behaviour observed at 200°C (Figure 6.19) confirms that the former is unlikely. The precursor decomposition would lead to CVD-like reactions and result in increasing growth rate with increasing precursor doses. Figure 6.19 shows that this is not the case, the growth rate saturates with increasing precursor doses and hence, the high growth rates at the low temperatures are believed to be a consequence of precursor condensation. The growth rates of films deposited with MMH are higher than those deposited without any co-reactant at all temperatures, indicating a reaction between $Gd\{N(SiMe_3)_2\}_3$ and MMH.

In order to answer the question whether $Gd\{N(SiMe_3)_2\}_3$ is suitable for self-limiting ALD, the effect of dose was studied. The experiment was carried out at 200°C due to the low growth rates at higher temperatures, the $Gd\{N(SiMe_3)_2\}_3$ dose was varied between 0 and 13s with 20ms MMH and either 5 or 30s purge. With a short purge of 5s (Figure 6.19), the growth rate increases dramatically from 0 to 1.1 Å/cycle for the $Gd\{N(SiMe_3)_2\}_3$ dose between 0 and 9s, showing that the growth rate is not saturative but dependent on the total flux of $Gd\{N(SiMe_3)_2\}_3$. This is due to an insufficient

purge, which results in precursor overlapping and CVD-like reactions. With a longer purge (30s), the growth rate clearly becomes saturative (0.7 Å/cycle) for doses higher than 5s, showing that $Gd\{N(SiMe_3)_2\}_3$ is a self-limiting precursor. A similar saturative growth rate has also been observed with increasing MMH doses. An additional film was deposited with 9s $Gd\{N(SiMe_3)_2\}_3$ doses, 30ms MMH doses, and 30s purge, the resulted growth rate remains at ~0.7 Å/cycle, showing that both $Gd\{N(SiMe_3)_2\}_3$ and MMH half-reactions are self-limiting.

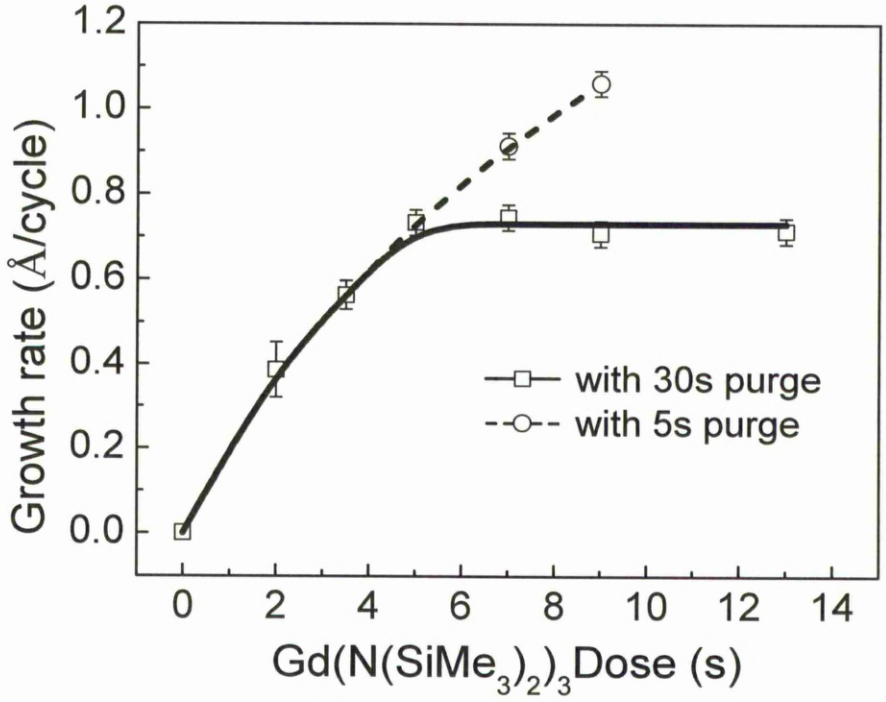

Figure 6.19 The growth rate as a function of $Gd\{N(SiMe_3)_2\}_3$ dose at 200°C with 20ms MMH and either 5s or 30s purge.

The effect of purge was studied in more detail at 200°C using the ($Gd\{N(SiMe_3)_2\}_3$ – purge – MMH – purge –) sequence of (9s – n – 20ms – n –), where n was varied between 5 to 60s. The growth rate decreased between 5 and 30s and then plateaus at longer times. The high growth rates at low purges indicate insufficient purge time to

remove excessive precursors and by-products in the gas phase, resulting in a CVD-like process. The saturated growth rates at high purges (>30s) show that the self-limiting deposition has been achieved using $Gd\{N(SiMe_3)_2\}_3$. The results outlined above conflicts with the paper reported for $Pr\{N(SiMe_3)_2\}_3$[27], where no self-limiting behaviour was observed. This is most likely due to the limited experimental range covered by those authors, in which a purge length of 0.5s was used without justifying that it is sufficient to eliminate gas phase reactions.

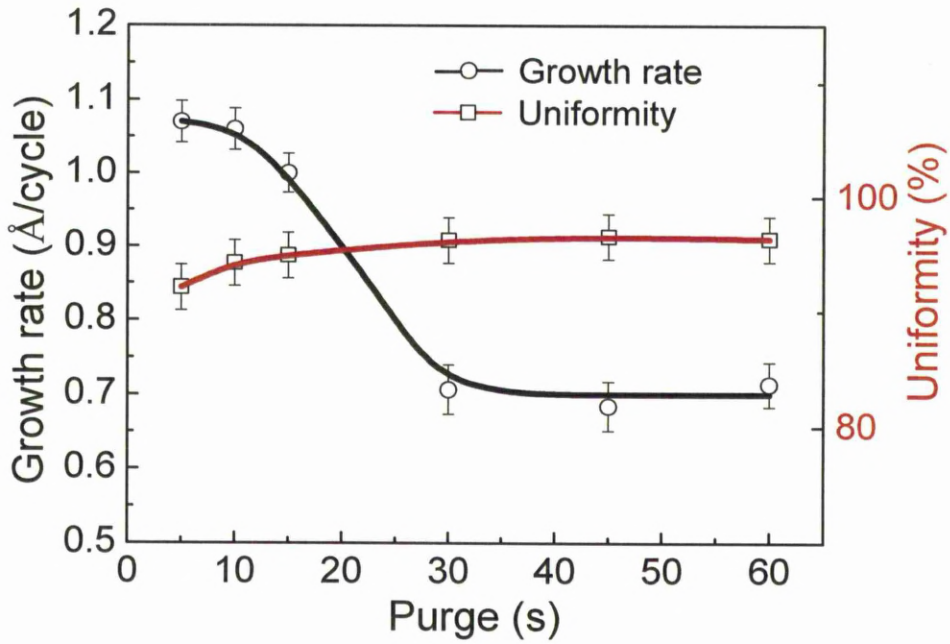

Figure 6.20 The growth rate and film uniformity (40×40mm) as a function of purge time for the ALD deposition using $Gd\{N(SiMe_3)_2\}_3$ with MMH at 200°C. The ($Gd\{N(SiMe_3)_2\}_3$ – purge – MMH – purge –) sequence was (9s – n – 20ms – n –), where n was varied 5-60s.

In ALD, self-limiting growth offers excellent uniformity and this has been observed in this study. The uniformity across a 40×40mm square (Figure 6.20) is poor at 5s purge, however, gradually improves when the purge increases and eventually achieves ~96% when the purge is greater than 30s. A similar trend was also observed with the increasing $Gd\{N(SiMe_3)_2\}_3$ dose when using a purge of 30s (Figure 6.21). The

uniformity increasing from 80% to 94% between 0-5s and further saturates at 96%. These results further confirm that $Gd\{N(SiMe_3)_2\}_3$ is a good ALD precursor for self-limiting deposition.

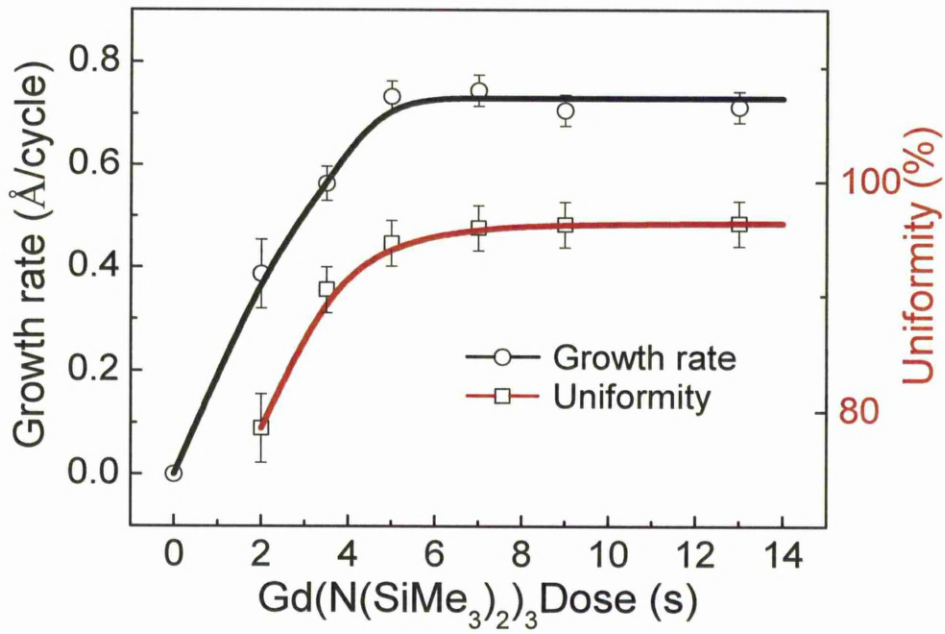

Figure 6.21 The growth rate as a function of $Gd\{N(SiMe_3)_2\}_3$ dose for the ALD deposition with MMH at 200°C. The ($Gd\{N(SiMe_3)_2\}_3$ – purge – MMH – purge –) sequence was (ns – 30s – 20ms – 30s –), where n was varied from 0-13s.

The growth results outlined above show that precursor transport is successful and that precursor absorption onto the substrate is self-limiting. Unfortunately, EDX shows that the films deposited with MMH (~100nm) are predominantly composed of gadolinium, oxygen and silicon. Figure 6.22a shows the EDX of films deposited on silicon at 200°C, whereas Figure 6.22b shows the EDX of same film but deposited on the glassy carbon substrate. In both cases, no nitrogen signal can be detected and high levels of gadolinium and oxygen are seen. In the EDX of the film deposited on glassy carbon (Figure 6.22b), a clear peak can be seen at the energy of 1.7 keV, which may be assigned to silicon K_α and K_β features. However, this feature may also be assigned

to tantalum M_α, which is also near 1.7 keV. According to Oxford Instruments, the tantalum M_α feature has a similar intensity as the tantalum L_α feature, which is seen as a small peak at 8.15 keV. The peak at 1.7 keV has a significantly larger intensity than the peak at 8.15 keV, showing that the contribution of tantalum M_α to the peak at 1.7 keV is small and silicon is incorporated in the film. The presence of silicon and the absence of nitrogen indicate a partial decomposition of the silylamine group during the reaction. Similar silicon incorporation has also been reported for the oxide ALD using $Pr\{N(SiMe_3)_2\}_3$.[27]

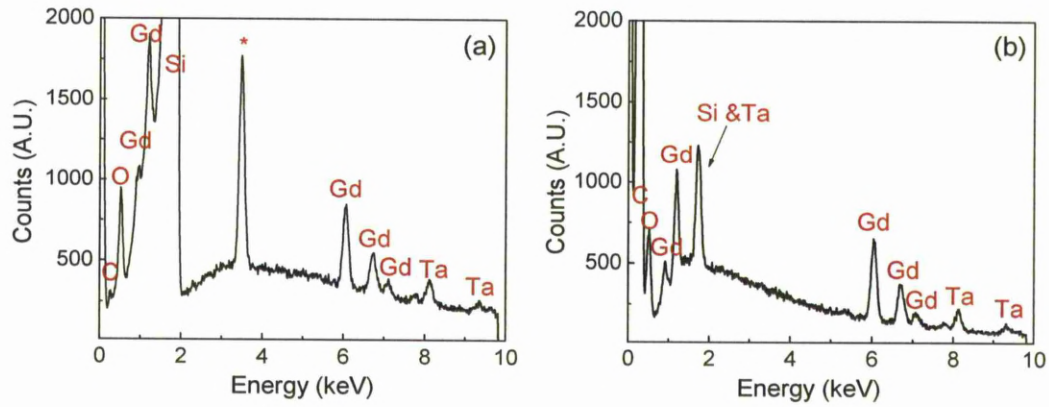

*Figure 6.22 EDX for the films (~100nm) deposited with $Gd\{N(SiMe_3)_2\}_3$ (5s) and MMH at 200°C on (a) silicon and (b) carbon substrates. No nitrogen is found in the films. * is assigned to a unique feature associated with the silicon substrate.*

The high oxygen content in the film is most likely linked with the purity of the $Gd\{N(SiMe_3)_2\}_3$ precursor. In this study, the possible oxygen sources are the chamber leakage and the impurities in Gd precursor, carrier gas and MMH. Based upon the results presented in chapter 4, the reaction chamber, the carrier gas and MMH are believed to contain negligible oxygen because the PDMAT and MMH process has resulted in Ta_3N_5 films with oxygen incorporation below the detection limit of MEIS (5%). This means that the $Gd\{N(SiMe_3)_2\}_3$ precursor is highly likely to be the oxygen

source. According to SAFC-Hitech, tetrahydrofuran (THF), an oxygen containing molecule, was used as the solvent to prepare the $Gd\{N(SiMe_3)_2\}_3$ precursor. Although some sublimation steps were taken to minimise the THF incorporation, the impurity level of the precursor was not characterised and therefore, the $Gd\{N(SiMe_3)_2\}_3$ used can be contaminated with oxygen.

The growth rate of the MMH process is consistently higher than the process without any co-reactant (Figure 6.19), indicating that there is a reaction between the MMH and the $Gd\{N(SiMe_3)_2\}_3$. If the Gd precursor was pure, the reaction between $Gd\{N(SiMe_3)_2\}_3$ and MMH would probably leads to $GdSi_xN_y$ depending on whether the silylamine groups cleave off cleanly. However, if the Gd precursor was contaminated with oxygen, the nitride formation would be unlikely due to the high affinity of Gd to O.[15] It is therefore anticipated that the contamination level of the $Gd\{N(SiMe_3)_2\}_3$ should be assessed and further purification steps should be developed to improve the precursor purity, these are beyond the scope of this study and are not treated further.

6.3 Summary

GdN films with a 1:1 Gd:N ratio have been successfully deposited at low temperatures by a PEALD based process using $Gd(MeCp)_3$ and nitrogen plasma. Although the process is not fully self-limiting due to partial decomposition, films with low oxygen and carbon incorporation, good uniformity (95%), and smooth surface (R.a.=0.7nm) have been obtained. It is anticipated that further improvement could be made by substrate cleaning and gas purifications. The present study has considered a wide range of nitrogen co-reactant and has demonstrated the first successful GdN

deposition using an ALD based processes. This approach might also be used for the deposition of other RE nitrides. Thermal ALD GdN processes using $Gd(MeCp)_3$ and ammonia or hydrazine are unsuccessful due to unfavourable reaction thermodynamics.

$Gd\{N(SiMe_3)_2\}_3$ processes with both ammonia and MMH were also investigated. Although the process using ammonia is thermodynamically unfavourable, the results indicate a reaction between $Gd\{N(SiMe_3)_2\}_3$ and MMH. Unfortunately, the deposited films were predominantly composed of gadolinium, oxygen and silicon. The silicon incorporation was attributed to partial breakdown of silylamine groups, where the oxygen contamination was attributed to the possible THF contamination in the precursor. Despite these issues, the significance of this study should not be overlooked. The results show that $Gd\{N(SiMe_3)_2\}_3$ exhibits a saturative growth rate with increasing precursor doses, showing good self-limiting behaviour. If the oxygen contamination in the Gd source can be removed, $GdSi_xN_y$ may be deposited in a self-limiting manner.

6.4 Reference

1. A. W. Stuart, Y. C. Almadena, T. Daryl, *Spintronics - Spin-Based Electronics*. In *Handbook of Nanoscience, Engineering, and Technology*, A. W. Goddart, Ed. CRC Press: New York, p 8~1 (2003).

2. J. Rhyne, T. McGuire, *IEEE Transactions on Magnetics* **8**, 105-130 (1972).

3. G. Busch, P. Junod, O. Vogt, F. Hulliger, *Physics Letters* **6**, 79-80 (1963).

4. G. Busch, *Journal of Applied Physics* **38**, 1386-1394 (1967).

5. T. R. McGuire, R. J. Gambino, S. J. Pickart, H. A. Alperin, *Journal of Applied Physics* **40**, 1009-1010 (1969).

6. R. A. Cutler, A. W. Lawson, *Journal of Applied Physics* **46**, 2739-2744 (1975).

7. R. Didchenko, F. P. Gortsema, *Journal of Physics and Chemistry of Solids* **24**, 863-870 (1963).

8. J. Q. Xiao, C. L. Chien, *Physical Review Letters* **76**, 1727 (1996).

9. S. Granville, B. J. Ruck, F. Budde, A. Koo, D. J. Pringle, F. Kuchler, A. R. H. Preston, D. H. Housden, N. Lund, A. Bittar, G. V. M. Williams, H. J. Trodahl, *Physical Review B* **73**, 235335 (2006).

10. B. M. Ludbrook, I. L. Farrell, M. Kuebel, B. J. Ruck, A. R. H. Preston, H. J. Trodahl, L. Ranno, R. J. Reeves, S. M. Durbin, *Journal of Applied Physics* **106**, 063910 (2009).

11. F. Natali, N. O. V. Plank, J. Galipaud, B. J. Ruck, H. J. Trodahl, F. Semond, S. Sorieul, L. Hirsch, *Journal of Crystal Growth* **312**, 3583-3587 (2010).

12. D. X. Li, Y. Haga, H. Shida, T. Suzuki, Y. S. Kwon, G. Kido, *Journal of Physics: Condensed Matter* **9**, 10777 (1997).

13. D. X. Li, Y. Haga, H. Shida, T. Suzuki, *Physica B: Condensed Matter* **199-200**, 631-633 (1994).

14. H. J. Trodahl, A. R. H. Preston, J. Zhong, B. J. Ruck, N. M. Strickland, C. Mitra, W. R. L. Lambrecht, *Physical Review B* **76**, 085211 (2007).

15. J. W. Gerlach, J. Mennig, B. Rauschenbach, *Applied Physics Letters* **90**, 061919 (2007).

16. R. J. Gambino, T. R. McGuire, H. A. Alperin, S. J. Pickart, *Journal of Applied Physics* **41**, 933-934 (1970).

17. P. Wachter, E. Kaldis, *Solid State Communications* **34**, 241-244 (1980).

18. M. A. Scarpulla, C. S. Gallinat, S. Mack, J. S. Speck, A. C. Gossard, *Journal of Crystal Growth* **311**, 1239-1244 (2009).

19. F. Leuenberger, A. Parge, W. Felsch, K. Fauth, M. Hessler, *Physical Review B* **72**, 014427 (2005).

20. E. Shalaan, H. Schmitt, *Optics Communications* **260**, 588-594 (2006).

21. J. R. Brewer, Z. Gernhart, H. Y. Liu, C. L. Cheung, *Chemical Vapor Deposition* **16**, 216-219 (2010).

22. A. P. Milanov, T. B. Thiede, A. Devi, R. A. Fischer, *Journal of the American Chemical Society* **131**, 17062-17063 (2009).

23. R. L. Puurunen, *Journal of Applied Physics* **97**, 121301 (2005).

24. M. Ritala, M. Leskela, *Atomic Layer Deposition*. In *Handbook of Thin Film Materials*, N. S. Nalwa, Ed. Academic Press: San Diego, Vol. 1 (2002).

25. A. C. Jones, H. C. Aspinall, P. R. Chalker, *Chemical vapour deposition of metal oxides for microelectronics applications*. In *Chemical Vapour Deposition: Precursors, Processes and Applications*, A. C. Jones, M. L. Hitchman, Eds. Royal Society of Chemistry: Cambridge, p 381 (2009).

26. J. Niinistö, N. Petrova, M. Putkonen, L. Niinistö, K. Arstila, T. Sajavaara, *Journal of Crystal Growth* **285**, 191-200 (2005).

27. K. Kukli, M. Ritala, T. Pilvi, T. Sajavaara, M. Leskelä, A. C. Jones, H. C. Aspinall, D. C. Gilmer, P. J. Tobin, *Chemistry of Materials* **16**, 5162-5168 (2004).

28. P. D. Rouffignac, J. S. Park, R. G. Gordon, *Chemistry of Materials* **17**, 4808-4814 (2005).

29. D. R. Lide, *CRC Handbook of Chemistry and Physics*. CRC Press: New York, p 4-64 (2009).

30. Z. Heiba, H. Okuyucu, Y. S. Hascicek, *Journal of Applied Crystallography* **35**, 577-580 (2002).

31. J. Clayden, N. Greeves, S. Warren, P. Wothers, In *Organic Chemistry*, Oxford University Press: Oxford, p 196 (2001).

32. S. B. Clendenning, S. Park, H. S. Simka, S. Shankar, In *Nitrogen-mediated ALD of metallic nickel: film deposition and mchanistic insights, 10th Internation Conference of Atomic Layer Deposition*, Korea (South), (2010).

33. J. S. Park, H. S. Park, B. D. Kang, *Journal of The Electrochemical Society* **149**, C28-C32 (2002).

34. J. W. Lim, S. J. Yun, J. H. Lee, *ETRI Journal* **27**, 118-121 (2005).

35. J. W. Lim, S. J. Yun, *Electrochem. Solid-state Letter* **7**, F45-F48 (2004).

36. J. W. Lim, S. J. Yun, J. H. Lee, *Electrochem. Solid-State Letter* **7**, F23-F76 (2004).

37. H. Fukumoto, I. Fujikake, Y. Takao, K. Eriguchi, K. Ono, *Plasma Sources Science & Technology* **18**, 045027 (2009).

38. H. Kim, A. J. Kellock, S. M. Rossnagel, *Journal of Applied Physics* **92**, 7080-7085 (2002).

39. Personal communication, H. Jeon, AES results of the GdN film deposited with $Gd(MeCp)_3$ and N_2 plasma. 2010.

40. W. F. Shen, D. Mazumdar, X. J. Zou, X. Y. Liu, B. D. Schrag, G. Xiao, *Applied Physics Letters* **88**, 182508 (2006).

Chapter 7. Conclusions and suggestions for possible future work

7.1 Tantalum nitride

Tantalum nitride has been identified in the literature as a good candidate for diffusion barriers and gate electrodes in microelectronic devices. Currently, the conductive mono-nitride is desirable and its deposition was a challenge in the previous thermal ALD studies of TaN_x. In the current study, the deposition of conductive TaN (Ta:N=1:1) and highly resistive Ta_3N_5 (Ta:N=1:1.6) has been demonstrated using thermal ALD with PDMAT and either ammonia or MMH as a co-reactant respectively.

The growth temperature of the ALD processes using PDMAT is limited to 300°C as higher temperatures lead to thermal decomposition of the PDMAT, resulting in CVD-like growth and carbon contamination in the films. The ammonia process shows absence of an ALD temperature window, however, the MMH process shows a temperature window between 200 and 300°C. The absence of an ALD window for the ammonia process was attributed to the insufficient reactivity of ammonia at low temperatures, which results in a reactivity limited growth rate. The ALD window observed with the MMH process was attributed to the high reactivity of MMH at low temperatures, which results in a chemisorption limited growth rate. Both processes exhibit saturative growth rates with increasing doses of PDMAT, ammonia, and MMH, showing good self-limiting behaviour. At the optimum deposition temperature of 300°C, the growth rates were 0.6 and 0.4 Å/cycle for the ammonia and MMH based processes respectively.

QCM analysis has been employed to study the detailed growth at 300°C, and the mass gain results correlates well with the growth rates obtained by the ellipsometry measurements. The low growth rate in the MMH based process was due to poor chemisorption of PDMAT molecules on the surface, which indicates an insufficient number of reaction sites on the MMH terminated surface. Mass gain and mass loss observed in the QCM measurements have been used to elucidate the chemisorption mechanisms of PDMAT. On average, one PDMAT molecule chemisorbs onto the ammonia terminated surface by reacting ~3.1 dimethylamido ligands, whereas on the MMH terminated surface, it chemisorbs by reacting ~2.7 dimethylamido ligands. This supports the hypothesis that fewer surface sites are available in the MMH terminated surface compared to the ammonia terminated surface. The lack of reaction sites can be attributed to the steric hindrance of the MMH molecules.

Films deposited in this study show good correlations between their chemical composition, colour appearance, electrical resistivity, and microstructure if crystallized. The mono nitride was found to have a grey appearance with low resistivities (<0.2 Ω.cm), whereas the nitrogen rich nitride was found to have a yellow appearance with high resistivities (>6 Ω.cm). Films deposited with ammonia at 300°C were found to be cubic TaN with the best resistivity of 70 mΩ.cm, which is lower than the values reported in previous thermal ALD studies of TaN. During this ALD process, tantalum must undergo a reduction reaction from Ta(V) to Ta(III) to form TaN. Ammonia is able to reduce PDMAT to produce TaN without the need for an additional reductant. This contradicts with the previous papers and is the first time that the reduction of a tantalum precursor has been achieved by ammonia. Although conductive TaN is currently preferred for the applications as diffusion barriers, the significance of the MMH based process presented here, which produces Ta_3N_5,

should not be overlooked. This low temperature (200°C) process produces amorphous films that are expected to be a better diffusion barrier than those deposited with ammonia at the same temperature. This was attributed to the high reactivity of MMH.

7.2 Hafnium nitride

Hafnium nitride is another transition metal nitride and has also been previously identified as a good candidate for diffusion barriers and gate electrodes in microelectronics. Although HfN_x has been previously deposited using both thermal and PE ALD, the differences between these techniques were unclear due to the lack of a systematic study. In the current work, a direct comparison has been made between thermal and PE ALD for the deposition of HfN_x, and the process characteristics of PEALD has been identified.

In the thermal ALD process using TDMAH and ammonia, an ALD temperature window was observed between 100 and 300°C, higher temperatures lead to thermal decomposition of the precursor. At 300°C, growth rates are saturative with increasing TDMAH and ammonia doses, showing good self-limiting behaviour. However, as-deposited films were found to contain oxygen, which is attributed to oxygen ingress during post-deposition exposures to air, and a layer of HfO_xN_y was formed within ~10nm from the surface. The low film density (10.3 g/cm^3), which gives rise to large number of defects and dangling bonds, is largely responsible for the oxygen ingress.

A direct comparison has been made between thermal and PE ALD using TEMAH with either molecular ammonia or an ammonia plasma. Self-limiting behaviour has been observed for both TEMAH and ammonia half-reactions. Some advantages were

found for the PEALD process compared with the thermal ALD process: PEALD allows shorter purge time, which significantly reduces the cycle length; PEALD also results in higher film density. The density of the films deposited by PEALD and thermal ALD are 11.6 and 9.7 g/cm^3 respectively. This has significantly improved film stability during post-deposition exposures to air. The oxygen penetration in the films deposited by PEALD was less than 4nm from the surface, whereas oxygen penetration in the films deposited by thermal ALD was greater than 10nm.

In-situ mass spectrometry measurements have indicated that these process characteristics are attributed to the nature of the co-reactants, namely, radicals of hydrogen and nitrogen in the case of PEALD. The reactivity and the short life time of these radicals are believed to be responsible for the high film density and short purge time observed in the PEALD processes. It should however, be noted that a short life time of the co-reactant is an advantage when depositing films on plane substrate, but can be a limitation when depositing films on high-aspect ratio structures as radicals may not be able to reach the bottom of the trench and hence, the conformality can be affected for PEALD processes.

Films deposited by both processes have a nitrogen rich, Hf_3N_4 stoichiometry and low oxygen and carbon incorporations in the film bulk. Four point probe measurements indicate that these films are dielectric, in a good agreement with the expected electrical behaviour of the nitrogen rich nitride. XRD results show that all films are amorphous and this has been confirmed by TEM. The thermal stability of Hf_3N_4 films deposited by PEALD on silicon has been assessed by post-deposition vacuum annealing. MEIS show that the films undergo a densification process with the densities increase from 11.6 to 12.8 g/cm^3. No inter-diffusion between Hf and Si has

been observed and the films remain amorphous up to 800°C, making them a good candidate for diffusion barrier applications.

7.3 Gadolinium nitride

Gadolinium nitride, as a member of rare-earth nitrides, is a ferromagnetic semiconductor and has potential applications in spintronic devices. No previous attempt of producing these nitrides by ALD has been reported. In this thesis, a search for an ALD process for the deposition of GdN has been conducted. GdN films with a 1:1 Gd:N ratio have been successfully deposited at low temperatures by a PEALD based process using $Gd(MeCp)_3$ and nitrogen plasma. Although the process is not fully self-limiting due to partial decomposition of $Gd(MeCp)_3$, films with low oxygen and carbon incorporation, good uniformity (95%), and smooth surface (R.a.=0.7nm) have been obtained. It is anticipated that further improvement could be made by substrate cleaning and gas purifications. Thermal ALD processes using $Gd(MeCp)_3$ and ammonia or hydrazine were unsuccessful due to unfavourable reaction thermodynamics. The acidity constant of the MeCp group and either ammonia or MMH are incompatible and therefore, a forward reaction to form nitride is unfavourable.

ALD processes using $Gd\{N(SiMe_3)_2\}_3$ with either ammonia or MMH were also investigated. The process using ammonia is thermodynamically unfavourable, however, the results indicate that a reaction between $Gd\{N(SiMe_3)_2\}_3$ and MMH does take place. Unfortunately, the as-deposited films were predominantly composed of gadolinium, oxygen and silicon. The silicon incorporation was attributed to partial breakdown of silylamine groups, while the oxygen contamination was attributed to

THF contamination in the precursor. THF was used by SAFC-Hitech as a solvent to prepare the $Gd\{N(SiMe_3)_2\}_3$, although purification steps have been used to remove the solvent, it is likely that some traces remained. Despite these issues, the significance of this study should not be overlooked. The results show that $Gd\{N(SiMe_3)_2\}_3$ exhibits a saturative growth rate with increasing precursor doses, showing good self-limiting behaviour. If the oxygen contamination in the Gd source can be removed, $GdSi_xN_y$ may be deposited in a self-limiting manner. It should however be noted that the precursor purification is not a trivial process would probably require a different synthesis route which does not introduce THF or similar oxygen sources.

7.4 Suggestions for possible future work

The research carried out in this thesis has raised further questions which are beyond the scope of the current study, but would be worthwhile pursuing in the future.

It has been shown in chapter 4 that tantalum mono-nitride and nitrogen rich nitride has been deposited using the ammonia and MMH based processes respectively. Although the MEIS, XRD and electrical results confirm that the reduction of the tantalum precursor has been achieved using ammonia without additional reductant, the mechanism is still unclear. In-situ monitoring techniques including infrared spectroscopy and x-ray photoelectron spectroscopy could identify surface species, in-situ analysis using mass spectroscopy could characterise gas phase composition and diagnose reaction by-products. These would provide additional experimental evidence to the reduction reaction and hopefully the mechanism can be elucidated.

At the optimum growth temperature of 300°C, the growth rate of the MMH process was lower than the ammonia process. This was attributed to steric hindrance of the co-reactant molecules, which restricted the surface reaction sites and hence reduced the growth rate. The steric hindrance and the reactivity of hydrazines can be modified by adding more side groups to the basic hydrazine (Figure 7.1). The N-N bond strength would be weaker when adding more side groups to the basic hydrazine and thus make the co-reactant more reactive.[1] Additional side groups on the basic hydrazine would increase the steric hindrance and hence decrease the reaction kinetics. The exact effect of different hydrazines in ALD deposition is currently unclear in the literature. A systematic study using different hydrazines with a consistent metal precursor would answer the question. Both growth behaviour and the resulted nitride phase are worth investigating because other hydrazines may reduce the tantalum precursor and deposit conductive TaN. Carbon incorporation should also be assessed because additional groups on the basic hydrazine may decompose during the process and introduce carbon contamination into the film.

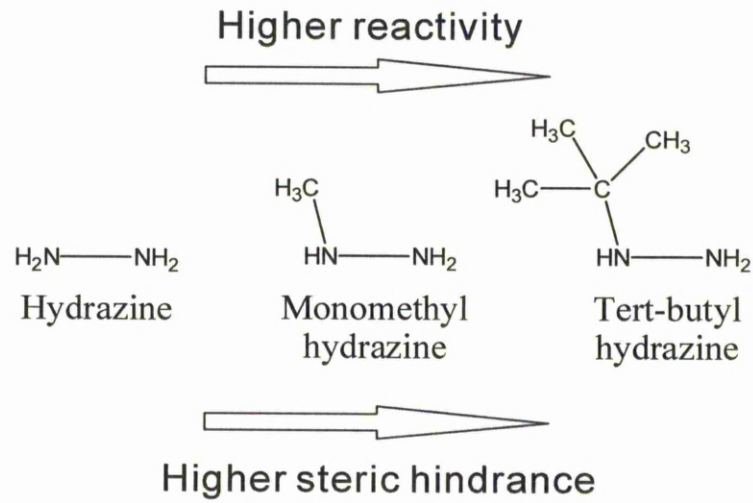

Figure 7.1 The change of reactivity and steric hindrance when adding different groups on the basic hydrazine.

In addition, to fully adopt the TaN and Ta_3N_5 processes reported in chapter 4 to a real device, the diffusion barrier properties, work functions and high aspect ratio coatings should be assessed subject to the application. The diffusion barrier property can be investigated by depositing Si/TaN_x/Cu structure, and investigating the sheet resistance and XRD diffraction patterns of the layer stack as a function of annealing temperatures. The Si-Cu diffusion would lead to higher sheet resistances due to the formation of resistive copper silicide, which if crystallized, can also be detected by XRD. MEIS and AES may also be used to depth profile the chemical composition. The work function of the conductive nitride may be studied by fabricating the TaN/dielectric/Si capacitor structures and studying the capacitance-voltage curves.

The work reported in chapter 5 shows that films deposited using thermal ALD with ammonia exhibit low density. One possible future work in thermal ALD is to try hydrazine based co-reactants, which may improve the quality of resulted films.

The comparison between thermal and PE ALD clearly demonstrates the advantages of PEALD in terms of film density and required purge time when depositing films on plane substrates. If the films are to be used as a diffusion barrier, further research should be carried out to investigate high aspect ratio coatings using PEALD. The literature data shows that conformal coatings using PEALD is particularly challenging. To date, the best reported result is the PEALD process of Ta, with an aspect ratio of 15:1 (trench diameter ~100nm).[2] This is low compared with thermal ALD and is due to the short life time of radicals, some may not be able to reach the bottom of the trench.[3] Further study, which optimises the deposition pressure, radical flux, plasma power, and plasma expose time, may yield a better result. The roadmap of semiconductors indicates that that by 2015,[4] the aspect ratio for the global wiring

will increase to 20:1 (trench diameter 2-4μm) and therefore, conformal coatings on these structures are necessary for the application as a diffusion barrier.

By searching the literature, another point of interest is raised for PEALD – batch processes. Several reports and commercial ALD reactors are available for the thermal batch ALD processes,[5-7] however, to date, none has been reported using PEALD. The difficulty is again associated with the short life time of the radicals. A successful PEALD batch process would significantly increase the throughput and opens up a new manufacturing route for the deposition of challenging materials such as nitrides and metals using ALD. A recent European based research project has already taken this on board.[8]

The results reported in chapter 6 have achieved the first GdN deposition using an ALD based process. A trace level of oxygen (5%) was detected in the film bulk, however, it is anticipated that the oxygen impurity can be reduced by surface cleaning prior to the deposition and additional gas purification steps. To fully adopt the GdN layer in spintronics, the functional properties including the Curie temperature, magnetic moment, and band gap of the GdN films should also be assessed in the future.

In the PEALD process using $Gd(MeCp)_3$ and N_2 plasma, it was speculated that the film uniformity was affected by the uniformity of the plasma. Further optimisation can be made for a more uniform plasma. The uniformity of a plasma is highly desirable in remote dry etching processes and compared with this field, less optimisations have been considered for the plasma source used in PE ALD. It is

therefore anticipated that some knowledge can be transferred from the etching process and help the development of a more uniform plasma in PE ALD.

The ALD process using $Gd\{N(SiMe_3)_2\}_3$ with MMH exhibits self-limiting behaviour, however, the process did not deposit nitride due to the possible contamination in the Gd precursor. The purity of the $Gd\{N(SiMe_3)_2\}_3$ should be assessed to confirm the impurity level, further purification steps should be developed to improve the purity of the precursor. For the deposition of challenging materials such as rare-earth nitride using ALD, further research in precursor development is needed for better and purer precursors. Alternative oxygen free precursors are required, which can overcome the limitations of precursor decomposition in the work reported for $Gd(MeCp)_3$, and the silicon incorporation in the work reported for $Gd\{N(SiMe_3)_2\}_3$. One possible candidate is amidinate based precursor and this can be investigated in the future.

7.5 Reference

1. D. M. Golden, R. K. Solly, N. A. Gac, S. W. Benson, *International Journal of Chemical Kinetics* **4**, 433-448 (1972).

2. H. Kim, J. C. Cabral, C. Lavoie, S. M. Rossnagel, *Journal of Vacuum Science & Technology B: Microelectronics and Nanometer Structures* **20**, 1321-1326 (2002).

3. H. C. M. Knoops, E. Langereis, M. C. M. van de Sanden, W. M. M. Kessels, *Journal of The Electrochemical Society* **157**, G241-G249 (2010).

4. International Technology Roadmap for semiconductors (ITRS). http://www.itrs.net/ (accessed 2010).

5. Phoenix batch process ALD reactor - Cambridge nanotech. http://www.cambridgenanotech.com/products/phoenix.php (accessed July-2011).

6. Picosun 200mm batch production ALD system. http://www.picosun.com/pdf/Picosun_Press_Release_30112009ENG_P200B.pdf (accessed July-2011).

7. E. Granneman, P. Fischer, D. Pierreux, H. Terhorst, P. Zagwijn, *Surface & Coatings Technology* **201**, 8899-8907 (2007).

8. A. Gschwandtner, HALE & RAPID : High Throughput Atomic Layer Chemical Vapour Deposition Batch Equipment using Remote Plasma Enhanced Processing and In-Situ Chamber Clean. http://cordis.europa.eu/fetch?CALLER=PROJ_ICT&ACTION=D&DOC=8&CAT=PROJ&QUERY=013135122455:53a6:49bdd02b&RCN=63301 (accessed July-2011).

Appendix I – MEIS depth profiles for Chapter 4

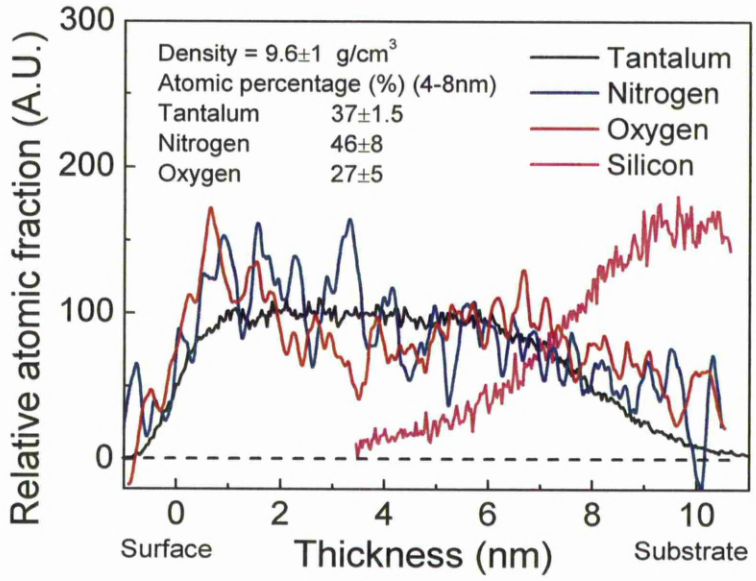

Figure 1 MEIS depth profiles of film deposited using 6s PDMAT and 3s ammonia for 300 cycles at 200°C. Data were taken for a dose of 6μC.

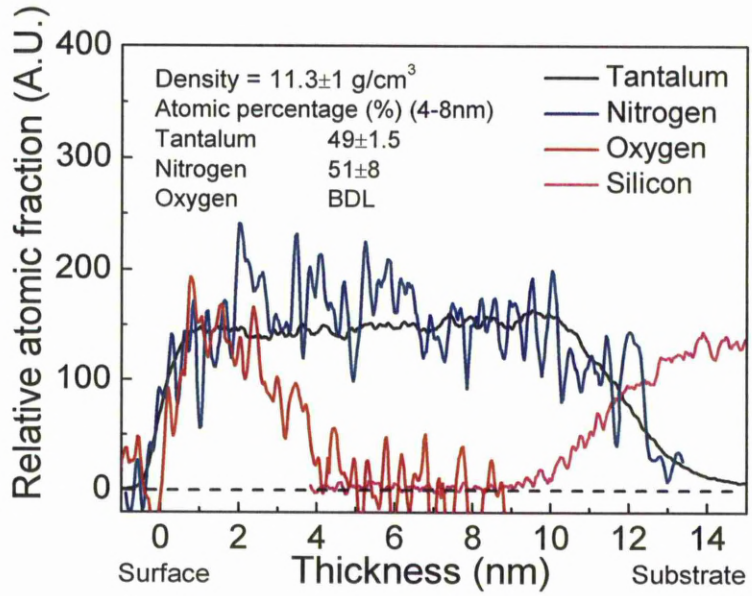

Figure 2 MEIS depth profiles of film deposited using 6s PDMAT and 3s ammonia for 200 cycles at 300°C. Data were taken for a dose of 6μC.

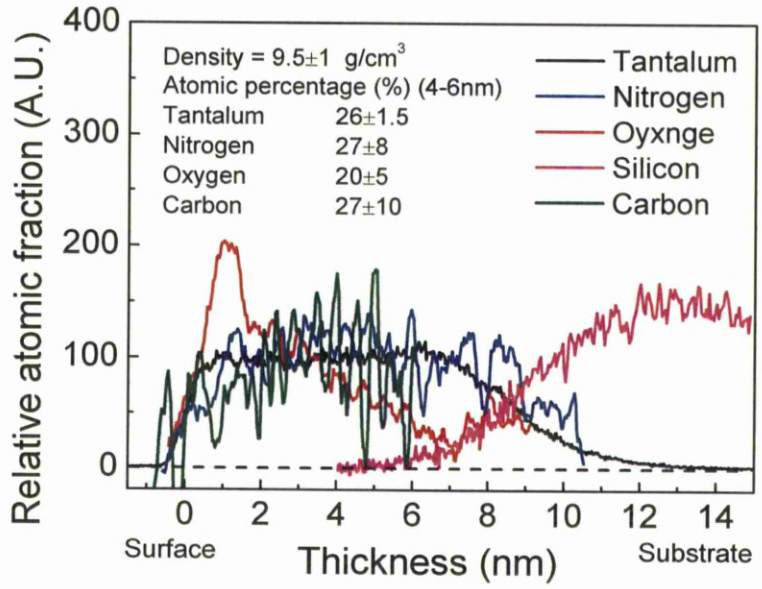

Figure 3 MEIS depth profiles of film deposited using 6s PDMAT and 3s ammonia for 100 cycles at 350°C. Data were taken for a dose of 6μC.

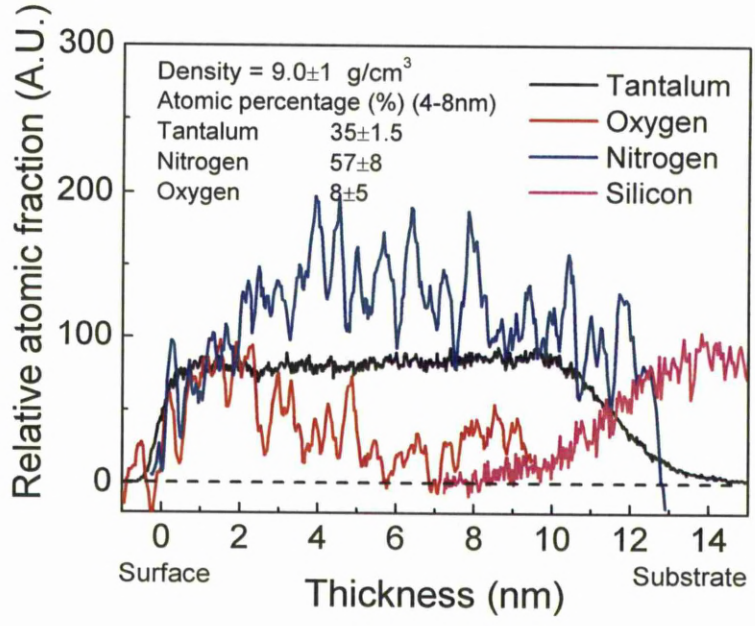

Figure 4 MEIS depth profiles of film deposited using 6s PDMAT and 20ms MMH for 250 cycles at 200°C. Data were taken for a dose of 6μC.

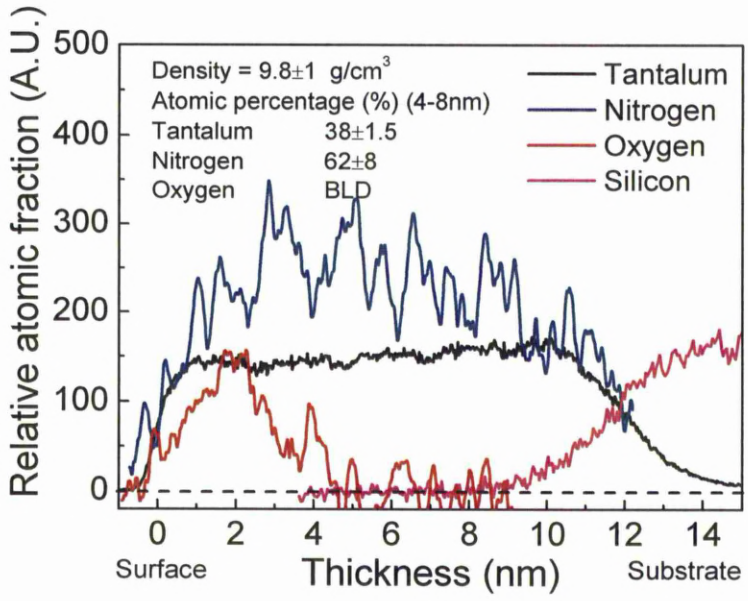

Figure 5 MEIS depth profiles of film deposited using 6s PDMAT and 20ms MMH for 250 cycles at 300°C. Data were taken for a dose of 6μC.